MAGNETIC FLUCTUATIONS IN THE REVERSED FIELD PINCH

By

David Brotherton-Ratcliffe

RHC LIBRARY
CLASS No. T BPP Bro
ACC. No. 616, 113
Date ACQ. Feb. '85

A thesis submitted for the degree of Doctor of Philosophy of the University of London

Department of Physics,
Royal Holloway College,
Egham, Surrey.

June 1984

ProQuest Number: 10097541

All rights reserved

INFORMATION TO ALL USERS
The quality of this reproduction is dependent upon the quality of the copy submitted.

In the unlikely event that the author did not send a complete manuscript
and there are missing pages, these will be noted. Also, if material had to be removed,
a note will indicate the deletion.

ProQuest 10097541

Published by ProQuest LLC(2016). Copyright of the Dissertation is held by the Author.

All rights reserved.
This work is protected against unauthorized copying under Title 17, United States Code.
Microform Edition © ProQuest LLC.

ProQuest LLC
789 East Eisenhower Parkway
P.O. Box 1346
Ann Arbor, MI 48106-1346

ABSTRACT

Arrays of edge magnetic coils and an insertable magnetic probe have been used to study the behaviour of the magnetic fluctuations in the HBTX1A Reversed Field Pinch.

EDGE COILS: In the sustainment phase of the discharge poloidal arrays of edge coils show that the superficially random fluctuations can be attributed almost entirely to global modes of poloidal mode number $m = 0$ and 1 provided account is taken of the toroidal distortion of these instabilities. A toroidal array of edge coils discloses a broad spectrum of toroidal mode numbers with a peak at $|n| \approx 10$ and significant variation with time and frequency. Cross correlation between signals from poloidal and toroidal edge coil arrays establishes that the $|n| \approx 10$ is $m = 1$, a set of helical modes resonant inside the reversal surface and also shows the presence of $m = 0$, $|n| \approx 0$. Timescales of the measured fluctuations indicate that the instabilities are probably resistive in character and mode amplitudes are such that island overlap and magnetic field ergodization should occur. The energy confinement time due to stochastic transport, estimated directly from the measured fluctuations, is consistent with that experimentally observed.

Studies of the edge magnetic fluctuations have been applied to discharges of differing conditions and in the termination and current set-up phases. Results show that, although systematic trends in the amplitude of the fluctuations occur, mode numbers and frequencies appear invarient with respect to changes in plasma current and filling pressure. At high values of Θ an $|n| \approx 3$ mode becomes of equal significance to the $m = 1$, $|n| \approx 10$ modes. Estimates of the safety factor indicate that, although the observed timescale of this mode would label it resistive, it is not resonant. The structure of the global fluctuations in the current set-up phase appears very similar to that during sustainment, although the amplitude is higher. In the termination phase the fluctuations show several differences in the frequency and mode numbers. However, after reversal is lost, the observed frequencies correspond to resistive timescales rather than the Alfven timescale expected for ideal modes.

INSERTABLE PROBE: A statistical method for determining the radial amplitude distributions of instabilities is presented. This is used to analyse probe data from which it is possible to distinguish three types of instability. At low frequencies (4-20 kHz) the dominant internal fluctuations are to be associated with the global $m = 1$, $|n| \approx 10$ resistive modes seen by the edge coils. These modes possess a radial structure in agreement with that predicted by a linear tearing mode stability analysis of the measured equilibrium. At similar amplitudes to these modes there is also a short correlation component ($\Lambda_r \approx 3$ cm) which is peaked in the central regions of the discharge. At high frequencies (>30 kHz) this local turbulence dominates over the global modes. Finally, at about 1/4 the peak power of the dominant global modes and with a similar frequency dependence, an $m = 1$ mode with some ideal characteristics is observed. Stability calculations show that ideal modes that are either destabilised by a resistive shell or whose growth rates are reduced by a resistive liner would have the same radial structure and timescales as this mode.

To Thea

ACKNOWLEDGEMENTS

First of all I would like to thank my initial Culham supervisor Dr Ian Hutchinson for the constant help and encouragement he has always extended to me. I would also like to thank Dr Hugh Bodin, my second Culham supervisor, for his guidance and invaluable comments concerning my research. In addition, I am indebted to my Royal Holloway supervisor Dr Eric Wooding.

I would like to thank, principally for the many useful discussions I have had,but also, in some cases, for active contribution, Marco Malacarne, Dr Chris Gimblett, Paul Noonan, Jeremy Webber, Dr Paddy Carolan, Professor Michael Rusbridge and Dr Mike Bevir. I would also like to thank the remainder of the HBTX1A team for their kind help and support.

Finally I would like to thank the U.K.A.E.A for their financial support and the facilities extended to me at the Culham laboratory.

R.H.C.
LIBRARY

SPECIFICATION OF THE AUTHOR'S CONTRIBUTION

The work reported in this thesis was done principally by the author but in some areas in participation with others. The purpose of this section is to delinearate clearly those areas which comprise solely the original research of the author and those areas where others were involved.

Proceeding by order of chapter, the extension of standard statistical techniques outlined in chapter 3 is due to the author and Marco Malacarne. The technique of correlation matrix fitting was developed purely by the author. Likewise chapter 4 comprises work due only to the author. Chapter 5, however, should be regarded as a 50-50 split between the author and Marco Malacarne. The analysis of probe data in chapter 6 is the work solely of the author. However, the linear stability analysis of this chapter was carried out in conjunction with Dr Chris Gimblett. It should be stressed that the author was not responsible for the running and maintenance of the HBTX1A machine which has a technical staff for this purpose.

CONTENTS OF THESIS

INTRODUCTION

This thesis presents an experimental study of the magnetic fluctuations in the Reversed Field Pinch (RFP) HBTX1A using arrays of edge coils, an insertable probe and statistical analysis techniques.

In the RFP fluctuations are thought to be of importance concerning the plasma behaviour. A prime example is the phenomenon of self-reversal, where a reversed toroidal field is created and sustained by the growth and interaction of instabilities. Such 'turbulence', which manifests itself in fluctuations of the discharge parameters, such as the temperature, density and magnetic field, is also widely believed to be responsible for the RFP's anomalous confinement properties. Studying the fluctuations in an RFP thus offers a way to the understanding of these two key phenomena; field reversal and transport.

In contrast to the Tokamak where the dominant fluctuations are usually temporally coherent, the RFP is characterised by fluctuations showing little periodicity in time. For this reason statistical techniques such as correlation and spectrum analysis have been employed in this thesis in the analysis of the fluctuation measurements. These techniques allow the discrimination of spatial and temporal structures not directly apparent from the measurements themselves.

We will see that, although the magnetic fluctuations in HBTX1A appear to be temporally incoherent, their spatial structure is fairly coherent. In addition the majority of the fluctuations may be shown to be explicable in terms of fluid theory. A possible cause for the anomalous energy transport is offered in terms of ergodic field line behaviour due to the overlap of magnetic islands associated with the dominant fluctuations. On the subject of field-reversal, tentative evidence is found that reversal is sustained by a quasi-cyclic process involving the same modes responsible for the stochastic transport.

In chapters 1 and 2 we review the theoretical and experimental background of the study of fluctuations in the RFP. Chapter 1 deals with theory and chapter 2, with experiment. The theory chapter starts with the particle formalism and shows how, in some cases, this can lead to a useful fluid theory. In this way we are led to the MHD equations for one fluid. Instabilities are discussed in terms of this fluid model and the linearised perturbation theory is introduced. In particular we will draw the distinction between 'ideal' and 'resistive' modes and discuss the formation of magnetic islands. The overlap of these islands is seen to lead to field line stochasticity and the resulting effect on radial energy transport is discussed. The dominant quasi-linear effects of plasma instabilities are mentioned principally in terms of results from fluid codes. Lastly theoretical models concerning the important property of field reversal are discussed in some detail (e.g. Taylor's relaxation theory, the Tangled Discharge model and the Mean Field Electrodynamics model).

In the 'experimental' review of chapter 2 previous work on fluctuation measurements is discussed. In particular we will review the work performed on ZETA and MK IV TORUS, where various types of insertable probes were employed and interpretation concentrated mainly on small-scale fluctuations and fully developed (fluid-like) turbulence. Similar studies, concentrating on large-scale fluctuations, on the series of fast programmed pinches, in particular HBTXI, are also reviewed. Finally a brief discussion of contemporary measurements on machines other than HBTX1A is given.

Chapter 3 is devoted to a discussion of the experimental and theoretical techniques used in this thesis. The first section deals with experimental aspects, discussing the HBTX1A machine, the insertable magnetic probe and the arrays of edge coils. Methods of data acquisition are also briefly reviewed. The second section deals with the techniques of data analysis used in this thesis. We start by reviewing correlation and spectrum analysis. This is then applied to the problem of interpreting data obtained

from the edge coils and the insertable probe. In the case of the edge coils, the poloidal and toroidal mode spectra are introduced. Various ways of obtaining the toroidal spectrum (for instance by correlation techniques, linear deconvolution, or Maximum Entropy) are presented and the relative advantages of each method are discussed. This naturally leads to a discussion of the 'Association' spectrum which approximates the two-dimensional mode power spectrum under certain assumptions. Lastly, using the probe data, a method is developed for determining the radial structure of the many instabilities present in the plasma by way of a correlation matrix fitting technique.

The basic measurements, about which this thesis revolves, are described in chapters 4,5 and 6. Chapter 4 is concerned with the derivation of the equilibrium magnetic fields from probe data. The results of this chapter facilitate the interpretation of the fluctuation measurements to be reported in chapters 5 and 6. For instance the measured q profile allows one to distinguish whether a certain (observed) helicity is resonant or non-resonant. In addition the equilibrium fields may be tested for linear stability and the outcome of such tests compared with fluctuation measurements. Chapter 4 should thus be viewed as providing an essential background for the interpretation of the measurements of chapters 5 and 6.

Chapter 5 deals with the edge coil measurements. Here we present a detailed study of the fluctuation activity at the plasma edge in the sustainment phase of the discharge using the analysis techniques discussed in chapter 3. This is then extended for different time regions of the discharge; the termination and set-up phases. Differences in the structure of the dominant global instabilities are discussed. Then results from parameter scans are presented showing how the fluctuations evolve with pinch parameter, plasma current and filling pressure. Finally, we discuss the results at length, presenting the consequences of our observations in terms of anomalous transport and reversal mechanisms.

Chapter 6 returns to the insertable probe. Here we discuss the internal structure of the fluctuations. By the technique of correlation matrix fitting developed in chapter 3 we are able to derive the radial structures of the dominant instabilities. These are compared with the results from a linear stability analysis of the measured equilibrium field profiles (obtained in chapter 4) and with the edge coil measurements.

Chapter 7 brings all the results together and discusses the observations and deductions as a whole and in relation to previous investigations. In this way the contribution of this thesis to the current understanding of the subject is outlined. Further areas of investigation are also discussed.

CHAPTER 1

REVIEW OF THEORY

1.1 OVERVIEW OF THEORETICAL PLASMA MODELS

Fluctuations in the magnetic field of a plasma arise from many types of plasma instability which are, in principle, describable by a set of governing equations which constitute a mathematical model of the plasma. In this thesis extensive use will be made of the predictions of a relatively simple single fluid model. It is thus appropriate to review the derivation of this model from the much wider 'particle' description, stressing the various approximations employed. The reader familiar with such a derivation may wish to proceed to section 1.2.

1.1.1 Particle Theory

The task of theoretical plasma physics is to provide an understanding of the behaviour of an ensemble of interacting ions and electrons in the presence of an electromagnetic field, which may be self-generated or applied. Perhaps the most obvious way towards such an understanding is through a knowledge of the behaviour of an individual charged particle in an electromagnetic field. In principle this problem is far simpler than the many-particle problem and in cases of low collisionality can provide a fruitful avenue. Such an approach is termed 'Orbit Theory' [1].

When collisions between the particles of a plasma cannot be ignored orbit theory cannot provide an adequate framework for the understanding of plasma phenomena. In this case a statistical approach is fruitful. Instead of attempting to describe the phase-space trajectories of individual particles, we now consider the average properties of a given species of

particle. So we smear out the particles,α so that they no longer have discrete velocities but are described by a distribution function $f_\alpha(\underline{r},\underline{v},t)$ such that $f_\alpha(\underline{r},\underline{v},t)d\underline{r}d\underline{v}$ represents the number of particles in the region $(\underline{r},\underline{r}+d\underline{r})$ having velocities $(\underline{v},\underline{v}+d\underline{v})$ at the time t. '$f_\alpha(\underline{r},\underline{v},t)$' is thus the density of particles α in a 6-D phase space. By considering a closed region in this phase space it is possible to derive a generalised continuity equation for f_α. In the collisionless limit this is the Vlasov equation:

$$\frac{\partial f_\alpha}{\partial t} + \underline{v}.\frac{\partial f_\alpha}{\partial \underline{r}} + \frac{\partial}{\partial \underline{v}}.\{\underline{F}_\alpha f_\alpha/m_\alpha\} = 0 \ , \qquad - (1.1)$$

where $\underline{F}_\alpha$ is the force acting on the particles α each having mass m_α. When collisions are considered the RHS of this equation is simply replaced by a term $(\partial f_\alpha/\partial t)_{coll}$. This form is known as the Boltzmann equation.

In principle the Boltzmann equation coupled to Maxwell's equations provide a complete set of equations determining f_α for any number of particle species. These equations provide a very detailed and complete picture of plasma behaviour. On the one hand they contain microscopic information about the orbits of the individual charged particles and on the other hand they accurately describe macrosopic phenomena. It is thus hardly surprising that the model is mathematically intractable, even with numerical techniques, for many of the realistic problems posed in the fusion field.

1.1.2 MAGNETOHYDRODYNAMICS

The realisation that the Boltzmann-Maxwell set of equations could not be applied to many of the more realistic problems led to the development of simpler models with narrower physical content. Ideal [2] and resistive [3,4] Magnetohydrodynamics (MHD) are particularly successful examples, capable of describing a wide range of macroscopic plasma

phenomena and yet remaining mathematically tractable.

1.1.2.1 Two-Fluid Equations

The first step to a simplification of the Boltzmann-Maxwell system of equations is the formulation of the two-fluid equations. Here we consider just two particle species, ions and electrons. Then we rewrite the resulting two Boltzmann equations by taking moments of the form:

$$\int \Xi \{ \frac{\partial f_\alpha}{\partial t} - (\frac{\partial f_\alpha}{\partial t})_{coll} \} d\underline{v} \quad , \qquad - (1.2)$$

where $\Xi = 1$, $m_\alpha \underline{v}$ and $m_\alpha \underline{v}^2/2$. This gives three equations for each α (=i,e) corresponding to the conservation of mass, momentum and energy. Together with the Maxwell relations, these are the two-fluid equations:

$$\frac{dn_\alpha}{dt} + n_\alpha \nabla . \underline{v}_\alpha = 0 \qquad - (1.3)$$

$$n_\alpha m_\alpha \frac{d\underline{v}_\alpha}{dt} - q_\alpha n_\alpha (\underline{E} + \underline{v}_\alpha \times \underline{B}) + \nabla . \underline{\underline{P}}_\alpha = \underline{R}_\alpha \qquad - (1.4)$$

$$\frac{3}{2} n_\alpha \frac{dT_\alpha}{dt} + \underline{\underline{P}}_\alpha : \nabla \underline{v}_\alpha + \nabla . \underline{h}_\alpha = Q_\alpha \qquad - (1.5)$$

$$\nabla \times \underline{E} = -\partial \underline{B}/\partial t \qquad - (1.6)$$

$$\nabla \times \underline{B} = \mu_o e(n_i \underline{v}_i - n_e \underline{v}_e) + \frac{1}{c^2} \frac{\partial \underline{E}}{\partial t} \qquad - (1.7)$$

$$\nabla . \underline{E} = \frac{e}{\varepsilon_o} (n_i - n_e) \qquad - (1.8)$$

$$\nabla . \underline{B} = 0 \quad . \qquad - (1.9)$$

Here n, q, $\underline{E}$, $\underline{B}$, c , ε_o and μ_o are respectively the density, charge, electric field, magnetic field, light velocity, vacuum permittivity and vacuum permeability.

In the above equations we have assumed that $\underline{F}_\alpha$ in equation 1.1 is simply the Lorentz force and that ions and electrons have the same charge.

Equation 1.3 expresses the conservation of mass. Equation 1.4 expresses conservation of momentum, the LHS representing transfer of momentum between like particles and from the electromagnetic field and the RHS representing momentum transfer between unlike particles. In this equation $\underline{\underline{P}}$ is the total pressure tensor. Equation 1.5 is the energy conservation equation. This states that a change in the energy of either the ions or the electrons must come from the heat generated due to unlike collisions, Q_α, and is independent of the electromagnetic field. Here T_α represents the temperature of the species α and $\underline{h}_\alpha$ is the heat flux due to random motion. The remaining equations (1.6-1.9) are simply the Maxwell relations.

The two-fluid equations derive directly from the Boltzmann-Maxwell system and are thus exact. However, they do not constitute a complete set, since as yet we have not introduced any method for closing the sequence of higher order moments. Hence no matter how many moments we care to take (as per equation 1.2) there will always be too few equations to determine all the variables. In order to establish a useful model we must thus close the equations with further assumptions.

1.1.2.2 The MHD Equations

The derivation of the MHD equations from the two-fluid equations requires the following steps. First of all the Maxwell equations are replaced by their low-frequency form ($\varepsilon_o \to 0$) which eliminates the displacement current $\varepsilon_o \partial \underline{E}/\partial t$ and the charge $\varepsilon_o \nabla . \underline{E}$. Neglect of the displacement current constrains electromagnetic waves of interest to have phase velocities much less than that of light and excludes relativistic motion. In addition, the neglect of $\varepsilon_o \nabla . \underline{E}$ dictates charge neutrality ($n_e = n_i \equiv n$) and restricts attention to plasma phenomena of frequencies much less than the electron plasma frequency $\omega << \omega_{pe} \equiv (n_e^2/m_e\varepsilon_o)^{1/2}$ and length scales much longer than the Debye length $L >> \lambda_d \equiv v_{Te}/\omega_{pe}$.

The second approximation that is made is the neglect of electron inertia in the momentum equation ($m_e \to 0$). This means that time scales of interest must be long compared with those of the electron plasma frequency ω_{pe} and the electron cyclotron frequency $\omega_{ce} \equiv eB/m_e$ and that length scales must similarly be much greater than the electron larmor radius $r_{le} \equiv v_{Te}/\omega_{ce}$ and the Debye length λ_d.

Both the neglect of high frequencies in Maxwell's equations and the neglect of electron inertia in the momentum equation are assumptions which are very well satisfied when considering the macroscopic behaviour of fusion plasmas. However it should be noted that the latter assumption precludes a complete description of a class of long wavelength modes called Drift waves [5,6] which are strongly affected by resonant particles moving along the field lines.

The next step in the derivation of the MHD equations is to combine the individual ion and electron equations into a set of single fluid equations. This is accomplished by introducing single fluid variables. Thus the total mass density is defined as:

$$\rho = m_i n \ , \qquad - (1.10)$$

since we ignore m_e. Likewise the fluid velocity is given by:

$$\underline{v} = \underline{v}_i \ . \qquad - (1.11)$$

The current density is then defined as:

$$\underline{J} = en(\underline{v}_i - \underline{v}_e) \ . \qquad - (1.12)$$

Finally the single fluid pressure and temperature are written:

$$p = p_e + p_i = 2nT \qquad - (1.13)$$

$$2T = T_e + T_i \ . \qquad - (1.14)$$

We may then rewrite the two-fluid equations in terms of these single fluid variables. Now if we assume that both the ions and electrons are collision dominated then the ion and electron distribution functions will be

Maxwellian and in this case established theory [7] may be used to close the equations by expressing higher order moments in terms of transport coefficients. In particular, under the additional approximations of large collisionality but small resistivity we may derive the Ideal MHD equations:

$$\text{Continuity} : \frac{D\rho}{Dt} + \rho\nabla.\underline{v} = 0 \qquad - (1.15)$$

$$\text{Motion} : \rho\frac{D\underline{v}}{Dt} = -\underline{J} \times \underline{B} + \nabla p = 0 \qquad - (1.16)$$

$$\text{Energy} : \frac{Dp}{Dt} = -\gamma p\nabla.\underline{v} \qquad - (1.17)$$

$$\text{Convection} : \frac{\partial\underline{B}}{\partial t} = \nabla \times (\underline{v} \times \underline{B}) \qquad - (1.18)$$

$$\text{Ampere's Law} : \nabla \times \underline{B} = \mu_o\underline{J} \ , \qquad - (1.19)$$

where γ is the ratio of the specific heats and $D/Dt \equiv \partial/\partial t + (\underline{v}.\underline{\nabla})$ is the 'substantive' or 'convective' derivative.

It turns out that for fusion type plasmas ($n \approx 10^{12}$-$10^{16}cm^{-3}$, $T \approx 0.1$-$10keV$) strictly speaking this model is invalid since the collisionality criterion is not satisfied. However there is overwhelming empirical evidence [8,9,10,11] that Ideal MHD provides a rather accurate description of a broad class of plasma phenomena. The reasons for this necessitate a detailed discussion of the perpendicular MHD model which is valid for plasmas of fusion interest and yet makes almost the same predictions as ideal MHD. The interested reader is referred to the excellent review article by J.P.Freidberg [2].

An important generalisation of Ideal MHD is the inclusion of resistivity, η. This modifies the convection equation by including a resistive diffusion term:

$$\frac{\partial\underline{B}}{\partial t} = \nabla \times (\underline{v} \times \underline{B}) - \nabla \times (\frac{\eta}{\mu_o}\nabla \times \underline{B}) \qquad - (1.20)$$

and in addition an ohmic heating term supplements the energy equation:

$$\frac{Dp}{Dt} + \gamma p \nabla . \underline{v} = (\gamma - 1)\eta |\underline{J}|^2 \ . \qquad - (1.21)$$

Now at first sight, including resistivity would not seem to make a great deal of difference since fusion plasmas are almost infinitely conducting. However, the resistive MHD equations permit fundamentally different types of motion than the ideal equations. To see this one must realise that the ideal convection equation implies that the magnetic flux is convected with the fluid so that the flux through any contour following the material motion remains constant in time. This is known as Alfven's theorem [12] and effectively dictates that the magnetic topology must remain invariant. Now adding resistivity, however small this is, relaxes this topological constraint and allows field lines to break and reconnect. A similar problem arises in fluid mechanics [13] where, in the inviscid fluid theory, vortex lines are constrained to move with the fluid but with the introduction of even infinitesmal viscosity this constraint is relaxed and fundamentally different motions can ensue.

So we see that a small amount of resistivity introduced into the convection equation can yield new phenomena. However, if η really is small the ohmic heating term can become negligible in which case the resistive MHD energy equation is simply the adiabatic gas law (1.17). In some cases the energy equation can be replaced by the condition of incompressibility, $\nabla . \underline{v} = 0$. This approximation allows the definition of velocity stream functions [14] and hence lowers the number of dependent variables rendering the equations more tractable both analytically and numerically.

1.2 THE REVERSED FIELD PINCH

By a simple consideration of the MHD equations it may be shown that, for a plasma of finite extent and (small mass), no equilibrium is possible without the application of external fields. This dictates the need for some form of confinement system in a potential fusion reactor [see 15,16,17,18]. One such system is the Reversed Field Pinch which is a class of toroidal pinch in which the toroidal field, B_ϕ, reverses near the edge of the plasma. Unlike the Tokamak, where $B_\phi >> B_\theta$ (B_θ is the poloidal magnetic field) the RFP has $B_\phi \approx B_\theta$. As we will see in section 1.3 this makes the RFP potentially unstable to many plasma instabilities. Nevertheless a reversed toroidal field acts to stabilise these instabilities and as a result it is thought that the RFP may be able to sustain far higher plasma pressure than the Tokamak. Together with the weak toroidal field this makes the RFP a very plausible confinement system.

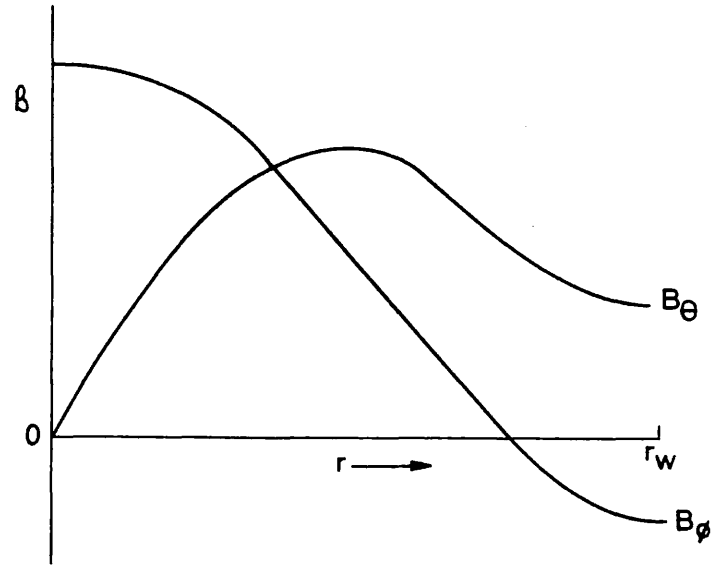

Figure 1.1 Toroidal (B_ϕ) and Poloidal (B_θ) magnetic field variation with radius (r) for a typical RFP.

Figure 1.1 shows a typical RFP field configuration and for comparison figure 1.2 shows a similar diagram for the Tokamak. In order to characterise, in a simple fashion, the types of RFP fields possible, the

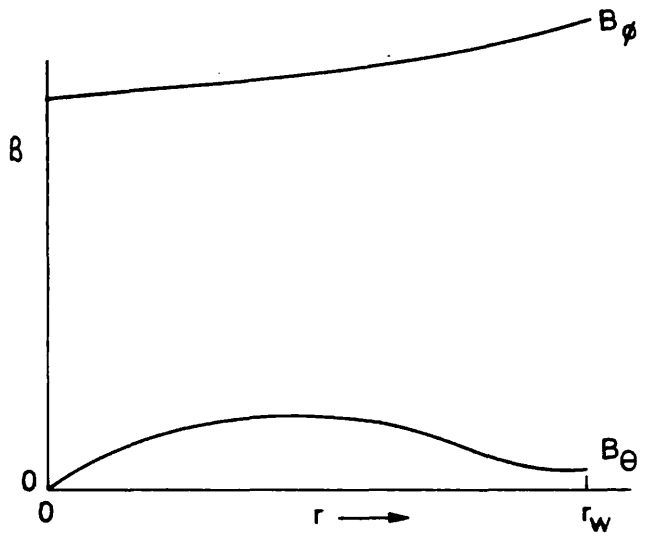

Figure 1.2 Toroidal (B_ϕ) and Poloidal (B_θ) magnetic field variation with radius (r) for a typical Tokamak.

following parameters are often used:

$$\Theta \equiv \frac{B_\theta(a)}{\langle B_\phi \rangle} \qquad - (1.22)$$

$$F \equiv \frac{B_\phi(a)}{\langle B_\phi \rangle} \quad , \qquad - (1.23)$$

where a is the plasma radius and triangular brackets indicate radial average. Θ is known as the Pinch parameter and measures the relative magnitudes of the current and toroidal flux. For The RFP $\Theta \approx 1$ whereas for the Tokamak $\Theta << 1$. The parameter F is known as the Field-reversal ratio and simply indicates how reversed the toroidal field is. For typical RFP configurations $F \approx -0.2$. For the Tokamak $F \approx 1$. Another important parameter is the plasma poloidal beta defined as:

$$\beta_\theta \equiv \frac{2\mu_0 \langle p \rangle}{B_\theta^2(a)} \, . \qquad - (1.24)$$

This is a measure of how much plasma kinetic pressure can be supported by a given magnetic pressure. Obviously, for a reactor, β_θ should be as large as possible. Current values for the RFP, as we will see in chapter 4., are about 10%.

The basic pinch equilibrium is the pressureless fully relaxed minimum energy state given by Taylor [19] which has Bessel function fields

(BFM)(see section 1.6 of this chapter):

$$B_\phi = B_o J_o(\mu r) \qquad - (1.25)$$

$$B_\theta = B_o J_1(\mu r) \ . \qquad - (1.26)$$

The parameter μ is related to θ (= $2\theta/a$) and is constant over r. The model gives a reversed field when $\mu r > 2.405$ and predicts the ratio $|\underline{J}|/|\underline{B}|$ to be constant with r.

Many other models for the RFP field configurations exist, some more realistic and others less so. Particularly fruitful are the Bessel Vacuum Model (BVM) and the Modified Bessel Function Model (MBFM) [20]. In these models the standard Bessel function description is used in the inner regions of the plasma but in the outer regions account is taken of the non-uniformity of $|\underline{J}|$ which must, in reality, fall to zero at the walls. Both these models thus specify a sensible $\mu(r)$ profile and then solve the force-free relation $\nabla x\underline{B}=\mu(r)\underline{B}$ for the fields.

1.3 LINEAR INSTABILITY THEORY

An unstable plasma is one in which an initial perturbation will always grow. On the other hand a stable plasma is one in which an initial perturbation will always decay. By instability we refer to the condition of an unstable plasma and also to the form and behaviour of the growing departure from the equilibrium situation.

A very powerful tool for investigating the stability of general systems is the energy principle. This states that if the potential energy of a system is increased for all perturbations then the system is stable whereas if the potential energy is decreased for any one form of the perturbation then the system is unstable.

1.3.1 The Linear Theory

In principle the MHD equations provide a complete description of how an initial perturbation to an equilibrium configuration will evolve. However, since the equations are non-linear, an analytic treatment along these lines is seldom fruitful. It should be noted that this is not necessarily true for numerical studies. To gain insight into the physics of instabilities one thus restricts attention to such times when the perturbations are small in comparison with the neighbouring equilibrium. In this case the MHD equations describing the instabilities are linear and hence are analytically far more tractable than their non-linear counterparts.

Another frequent simplification that is made is to study instabilities in a (periodic) cylindrical rather than a toroidal geometry (figure 1.3). This simplifies the algebra considerably while essentially predicting similar results to more complete toroidal investigations. It should be noted, however, that this approximation precludes a class of toroidal instabilities known as ballooning modes [21].

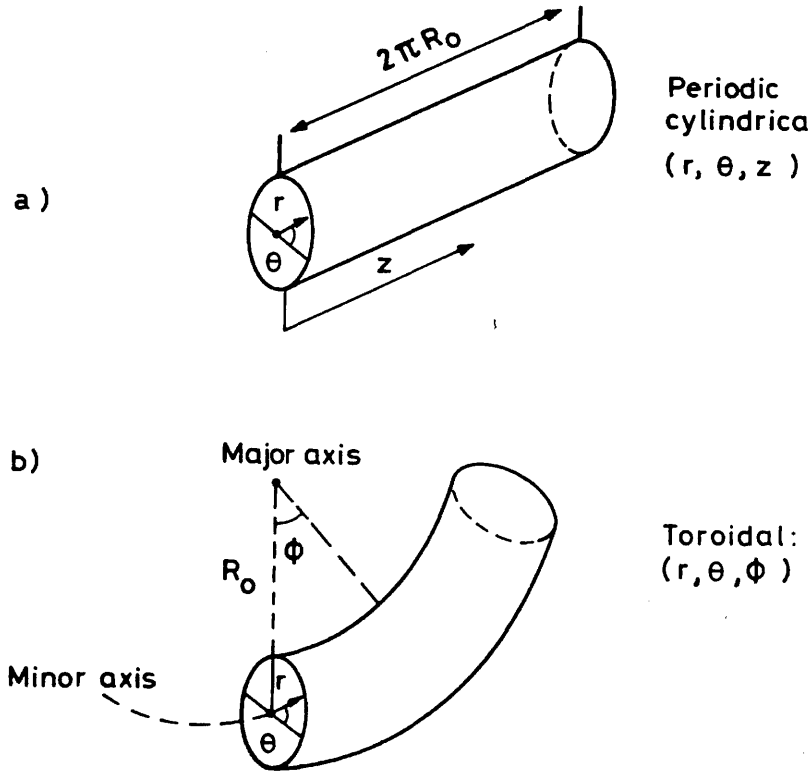

Figure 1.3 Toroidal and periodic cylindrical geometric systems.

The analytical technique used in the linear theory is perturbation analysis. This consists of writing each dependent variable in the MHD equations as an equilibrium and perturbation component. Thus the velocity field, $\underline{v}$, would be written:

$$\underline{v} = \underline{v}_0 + \tilde{\underline{v}} \qquad - (1.27)$$

where $\underline{v}_0$ represents the equilibrium velocity flow and $\tilde{\underline{v}}$, the velocity perturbation. Then the assumption that the perturbed quantities are smaller than the neighouring equilibrium allows us to neglect non-linear terms such as $\tilde{\underline{v}}.\tilde{\underline{v}}$ or $\tilde{\underline{v}}.\tilde{\underline{B}}$ etc and so we are led to a set of linear differential equations describing the perturbation. In a cylindrical geometry we may fourier analyse in space and time, taking the θ, z and t dependence of all perturbed quantities to be:

$$e^{\Gamma t + i(m\theta + kz)} , \qquad - (1.28)$$

where Γ, m and k are respectively the growth rate, poloidal mode number and longitudinal wavenumber. The ratio m/n (where $n \equiv kR_0$ is the toroidal mode number) is known as the helicity of the perturbation.

1.3.2 Ideal Instabilities

Ideal MHD instabilities may be conveniently divided into two classes. The first are fixed boundary [22] or internal instabilities where the plasma boundary remains fixed and the second are free boundary [22] or external instabilities where the plasma surface is allowed to move. In the first case, to determine the stability of a given equilibrium, only the potential energy associated with the plasma need be investigated whereas in the second case the potential energy of the vacuum fields must also be taken into account. In the RFP fixed boundary modes represent the most important instabilities.

1.3.2.1 Fixed Boundary Modes

The linearised ideal MHD equations may be combined into a single relation [23] for the perturbed displacement:

$$\underline{\xi}(r,t) = \int_0^t \tilde{\underline{v}}(r,\tau)d\tau \ . \qquad - (1.29)$$

This relation reads:

$$\rho \frac{\partial^2 \underline{\xi}}{\partial t^2} = \nabla(\gamma p \nabla.\underline{\xi} + \underline{\xi}.\nabla p) + (\nabla x \underline{B})x(\nabla x(\underline{\xi} x \underline{B}))$$

$$+ (\nabla x(\nabla x(\underline{\xi} x \underline{B})))x\underline{B} = F(\underline{\xi}) \quad , \qquad - (1.30)$$

where the operator F may be shown to be Hermitian. After a little algebra equation 1.30 can be transformed into:

$$\frac{\partial}{\partial t}\{ \frac{1}{2} \iiint_{V_{plasma}} \rho \, (\frac{\partial \underline{\xi}}{\partial t})^2 d\underline{r} - \frac{1}{2} \iiint_{V_{plasma}} \underline{\xi}.F(\underline{\xi})d\underline{r}\} = 0 \quad , \qquad - (1.31)$$

which simply states that the rate of change of kinetic (first term) and potential (second term) energies must be the same. As we noted above, by examining whether the potential energy of a system increases or decreases when it is perturbed, we may learn if the system is stable. Hence much insight into the stability problem may be gained by a careful formulation of the second term in this equation. A particularly fruitful form is that given by Furth et al [24] which reads:

$$\delta W = \frac{1}{2} \iiint_{V_{plasma}} \{ |\tilde{\underline{B}}_\perp|^2 + \left|\tilde{\underline{B}}_\parallel - \underline{B}\,(\underline{\xi}.\nabla p)/|\underline{B}^2|\right|^2 + \gamma p|\nabla.\underline{\xi}|^2$$

$$+ \frac{\underline{J}.\underline{B}}{|B^2|} . (\underline{B}x\underline{\xi}).\tilde{\underline{B}} - 2\underline{\xi}.\nabla p \underline{\xi}.\underline{\kappa} \}d\underline{r} \quad , \qquad - (1.32)$$

where κ is the curvature and '$\perp$' and '$\parallel$' indicate perpendicular and parallel

to the equilibrium field.

The first three terms in this expression are respectively the energy stored in Alfven, magnetosonic and sound waves. Clearly all are positive definite and hence are stabilising. The last two terms, however, are not in general positive and can thus decrease the potential energy and drive instabilities. The first of these terms represents instabilities driven by parallel current (kink modes) while the second represents modes driven by the interaction of pressure and curvature and are known as Suydam or interchange modes.

If we fourier analyse in space (θ,z) we may use the calculus of variations to minimise δW with respect to ξ_θ and ξ_z. This tells us that δW is minimised by velocity perturbations obeying the equation $\nabla.\underline{\xi}=0$ which in turn allows a simplified form of δW to be derived in terms of ξ_r alone:

$$\delta W = \frac{\pi}{2\mu_o}\int_0^{r_w}\{ f\ (\frac{\partial \xi_r}{\partial r})^2 + g\xi_r^2\}dr$$

where $$f(r) = \frac{r(mB_\theta + krB_z)^2}{(m^2 + k^2r^2)} ,$$

$$g(r) = \frac{2\mu_o k^2r^2}{(m^2 + k^2r^2)}\frac{dp}{dr} + \frac{(m^2 + k^2r^2 - 1)}{r(m^2 + k^2r^2)}(mB_\theta + krB_z)^2$$

$$+ \frac{2k^2r}{(m^2 + k^2r^2)^2}(k^2r^2B_z^2 - m^2B_\theta^2) , \qquad - (1.33)$$

and r_w is the wall radius.

Clearly the first term in the integrand is positive definite and so this always represents a stabilising term. The second term, however, is not constrained to be positive and so may be destabilising. For the case of $m = 0$ the second term simplifies to the following form:

$$g(r) = 2\mu_o\frac{dp}{dr} + B_z^2(k^2r^2 + 1)/r . \qquad - (1.34)$$

This dictates that, in the absence of pressure gradients, all $m = 0$ ideal

modes are stable. Further, if the pressure gradient is included, it must be negative to be destabilising. However, since the second term in 1.34 is positive definite, a large enough toroidal field, B_z or a high enough k will always produce stabilisation. In addition, as g becomes less negative, so the range of the instability will decrease. This is because if δW is only slightly negative then the integrand will only be negative for large ξ_r. Thus, as the toroidal wavenumber or the applied toroidal field increases pressure driven m = 0 modes will get more and more localised. In reality dissipative and kinetic effects such as finite Larmor radius limit this localisation.

For the case of m = 1 it is possible to perform a similar analysis as above. In particular Shafranov [25] has shown that if dp/dr is negative the ensuing instabilities are not local but are of a global nature being contained within the entire plasma region where nq < 1 ($q \equiv rB_z/R_oB_\theta$ is the safety factor). If, on the other hand, the Kruskal-Shafranov limit [26,27], nq > 1, is satisfied then these modes are stable. For m > 1 the picture is similar to that of m = 0.

The Suydam Criterion

From the energy principle it is possible to derive a necessary condition for the stability of a given equilibrium to pressure driven ideal modes. First we must note that the radius, r_s, where $mB_\theta/r_s + kB_z = 0$ represents a regular singularity of the ideal MHD equations. At this surface, perturbations require the least energy to bend field lines and so this surface is energetically most favourable for a given fourier mode to occur.

If we define $x = r - r_s$ then at this surface:

$$f(x) = \frac{x^2}{2} \left.\frac{\partial^2 f}{\partial x^2}\right|_{r_s} + \ldots \quad . \qquad - (1.35)$$

Now, the Schwartz inequality [28] may be used to dictate that:

$$\int_a^b (x^2\{\frac{\partial \xi_r}{\partial r}\}^2 - \frac{\xi^2}{4})dx \geq 0 \ , \qquad - (1.36)$$

where a and b are two points either side of the singular surface at which $\xi_r|_a = \xi_r|_b = 0$. Thus for δW to be positive definite this inequality implies:

$$\int_a^b \xi^2\{ \frac{1}{8} \frac{\partial^2 f}{\partial x^2}\Big|_{r_s} + g(r_s)\}dx > 0 \qquad (a,b \text{ small}) \ . \qquad - (1.37)$$

In turn, for this to be true, the integrand must also be positive definite and hence, after a little algebra, we arrive at the Suydam criterion [29]:

$$-\frac{dp}{dr} < \frac{rB_z^2}{8\mu_o}\{\frac{q}{q'}\} \ . \qquad - (1.38)$$

Essentially this criterion says that if you raise the shear of the magnetic field at a certain radius, pressure driven modes, whose singular surface is at this radius, can be stabilised. In toroidal geometry this criterion maps to the Mercier criterion [30]:

$$\frac{r}{4}\{\frac{1}{q}\frac{dq}{dr}\}^2 + \frac{2\mu_o}{B_\phi^2}(\frac{dp}{dr})(1-q^2) > 0 \ . \qquad - (1.39)$$

In pinches $q << 1$ and so toroidal effects do not modify the cylindrical results. In Tokamaks, however, the term $(1-q^2)$ is generally negative and so stability is possible without shear. In general, comparing the ideal stability of pinches and Tokamaks, the former are stabilised by conducting walls and magnetic shear, while the latter depend mainly on periodicity and toroidal effects with shear playing a role for localised modes.

Newcomb's Method

A general method for testing an arbitrary cylindrical equilibrium for stability to internal modes has been given by Newcomb [31]. Since this technique is used extensively in chapter 6 we will briefly review the relevant theory.

The starting point is the equation for $\delta W(\xi_r)$, equation 1.33. By minimising δW with respect to ξ_r we obtain the Euler-Lagrange equation for the lagrangian $L = -\delta W$:

$$\frac{d}{dr}(f\frac{d\xi_r}{dr}) - g\xi_r = 0 \quad . \qquad - (1.40)$$

The solution of this equation represents the smallest value of δW and hence the most unstable ξ_r. However, it is not possible to solve this equation and then simply substitute ξ_r into equation 1.33 to determine δW since in general there will not exist a solution for ξ_r under the appropriate boundary conditions. To guarantee a solution the growth rate Γ must be included and an Euler-Lagrange equation derived for the Lagrangian:

$$L = \Gamma^2 \int \frac{1}{2} \rho^2 \xi^2 d\underline{r} - \delta W \ . \qquad - (1.41)$$

First of all consider the case where m and n are such that there exists no singular surface. Then equation 1.40 is non-singular and has two independent solutions of the form $\xi_r=\alpha\xi_1(r)+\beta\xi_2(r)$. Now, as we have discussed above, $\xi_1(r)$ can be chosen to be regular at the origin but in general $\xi_1(a) \neq 0$. Similarly $\xi_2(r)$ can be chosen so that $\xi_2(a) = 0$ but in general $\xi_2(r)$ is not regular at $r = 0$.

The main result we will show is that if $\xi_1(r)$ has a zero anywhere within the interval $[0,a]$ a trial function for ξ_r may be constructed which, on substitution into equation 1.33, gives a negative δW and thus instability. On the other hand, if there are no such zeros then $\delta W > 0$ and there is

stability. The analysis is based on the separation theorem which applies to Sturm-Liouville forms [32] such as equation 1.40. This theorem proves that the zeros of any two independent solutions of a Sturm-Liouville equation interlace.

Consider the trial function shown in figure 1.4(a) using ξ_1 and ξ_2 in the inner and outer regions of the discharge respectively. Here it is assumed that ξ_1 has just one zero at r_1 (this does not affect the generality of the argument). Now the above theorem tells us that ξ_2 must then have a zero at r_2 such that $0 < r_2 < r_1$. In addition, ξ_2 may not have a second zero in the range $r_2 < r < a$.

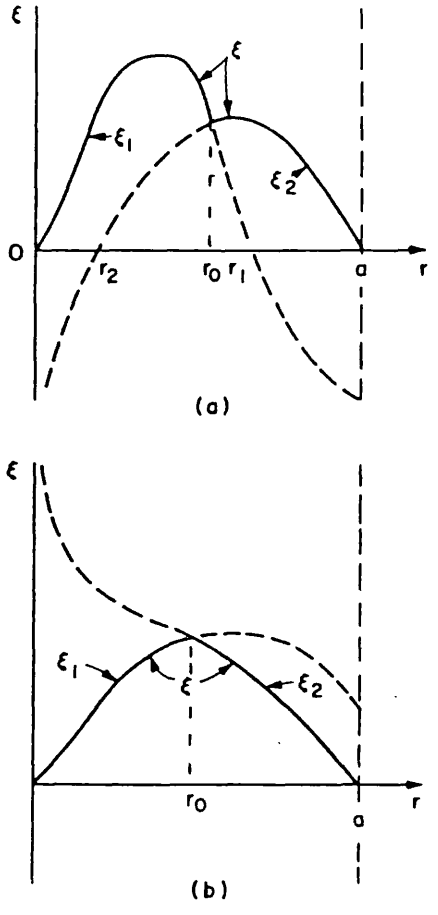

Figure 1.4 Trial functions illustrating Newcomb's method showing (a) instability and (b) stability for the case of no resonances in the range $0 \leq r \leq a$.

Substituting the above trial function into equation 1.33 gives an expression for δW:

$$\delta W \propto \Omega \, (\xi_1'(r_0) - \xi_2'(r_0)) \equiv \Omega s, \qquad - (1.42)$$

where Ω is a positive function and r_0 is the intersection point of ξ_1 and ξ_2. Now because of the separation theorem $s < 0$ and so $\delta W < 0$ which implies instability. If now we consider the case where ξ_1 has no zeros in the interval (0,a) the only type of trial function we may construct is that shown in figure 1.4(b) which gives $s > 0$ and so predicts stability. Thus the condition that ξ_1 has no zeros in the interval (0,a) is a necessary and sufficient condition for stability.

In the case where the Euler-Lagrange equation is singular due to the existence of singular surfaces the above analysis may be extended to each interval between the singularities. Then the necessary and sufficient condition for stability for a given m and n is that the Suydam criterion be satisfied in each interval and ξ_1 has no zeros in each interval.

Other Stability Criteria

The Suydam criterion provides a necessary condition for stability to pressure driven modes. In addition to these modes, however, there also exist current driven instabilities which depend for their stability on the profile of pitch, $P = R_0 q$. Figure 1.5 shows the four possible types of basic pitch variation. It can be shown by a consideration of equation 1.33 that some of these forms are always unstable. For instance (a) shows a pitch minimum which is always destabilising to a mode located in the vicinity of the minimum. This may be seen to be true by the construction of an $m = 1$ trial function which is constant in the region of the pitch minimum and falls sharply to zero at the two singular surfaces. Equation 1.33 then shows δW to be negative. It is interesting to note that if the pressure gradient is negative then consideration of the Suydam criterion shows a pitch minimum to be destabilising to pressure-driven modes as well.

The pitch variation in figure 1.5(b) is similar to that for Tokamaks. As with pressure driven modes, if $nq < 1$, then there is instability for the

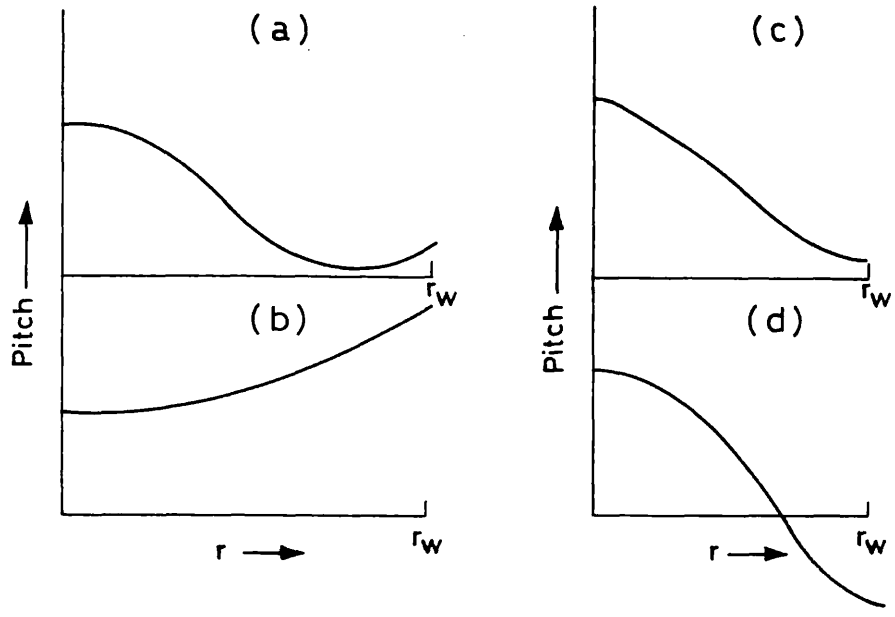

Figure 1.5 The four basic types of pitch variation:
(a) Exhibiting a minimum in the outer regions as in the stabilised pinch surrounded by a vacuum region,
(b) monotonically increasing as in the Tokamak,
(c) monotonically decreasing as in the stabilised pinch with currents extending to the wall and
(d) decreasing and changing sign as in the RFP.

cylindrical case but not necessarily for the toroidal case. The pitch profile of 1.5(c) corresponds to that of a stabilised pinch. If a vacuum region surrounds the plasma then there will always be a pitch minimum and hence instability. A pitch minimum occurs in this case because, in the plasma region, the pitch will be decreasing owing to the paramagnetic nature of the pinch and the pitch of a vacuum field is always increasing for positive B_θ and B_z since $B_\theta \propto 1/r$ and $B_z \propto$ constant. Thus if the toroidal field, B_z, is made to reverse in the outer regions of the discharge, as in the RFP, a vacuum region will now be associated with decreasing pitch and so there will be no pitch-minimum and the configuration can be stable (figure 1.5(d)).

By further consideration of equation 1.33 it is possible to show the total longitudinal flux:

$$\Phi = \int_0^{r_w} 2\pi R_0 B_z dr, \qquad - (1.43)$$

must be greater than zero for stability. Hence, in the RFP, as the field reversal is increased so the wall position for stability becomes smaller.

At the minor axis the shear and pressure gradient are zero and the local stability thus depends on how the second derivatives of these quantities behave. The condition for stability to current driven instabilities is:

$$\frac{P}{2}\frac{d^2P}{dr^2}\bigg|_{r\to 0} < \frac{-4}{8+m^2} . \qquad - (1.44)$$

For the BFM the LHS of this expression is -1/2 and so for $m > 0$ this criterion is satisfied. For on-axis pressure driven instabilities a modified Suydam criterion may be derived which states that the second derivative of pressure must be zero or negative. Hence Suydam stability on axis requires a flat or hollow pressure distribution.

1.3.2.2 Free Boundary Modes

In early experiments on pinches the plasma was observed to contort into various helical shapes due to the growth of instabilities which deformed the plasma surface. Inevitably the onset of such behaviour signalled the termination of the discharge since these modes generally grew exponentially until confinement was lost. In RFP's these modes are generally far less important than fixed boundary instabilities since usually a conducting wall is close to the plasma edge. Nevertheless, historically these modes played a very important role and so we will briefly review them.

As with fixed boundary instabilities we may assign mode numbers m and n to a given perturbation (assuming a cylindrical geometry). Figure 1.6 shows an example of an $m = 0$, $n \neq 0$ instability which is known as a sausage mode. This mode occurs in the linear pinch where there is no B_z field. In this case, if part of the plasma moves in, as in the narrow regions shown in figure 1.6, then, since magnetic flux is convected with the plasma, the JxB term in the motion equation will increase and that element will move in

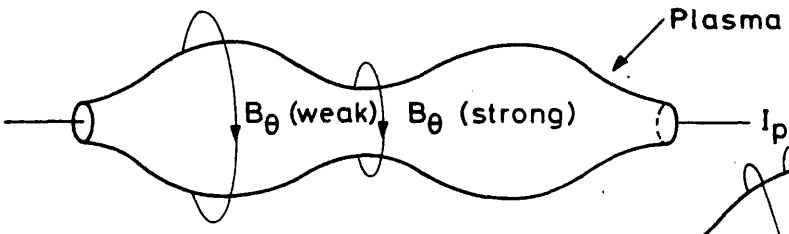

Figure 1.6 A Sausage mode (m = 0, n ≠ 0).

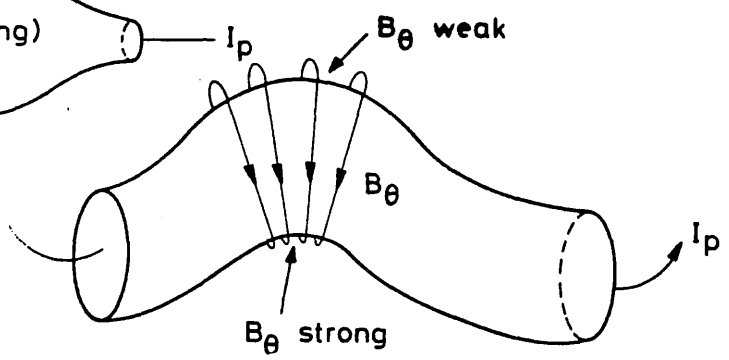

Figure 1.7 A kink mode (m = 1, n ≠ 0).

further. This process continues until the plasma 'necks off' at each narrow region. This mode may be stabilised by the application of a longitudinal field, B_z. In this case as each narrow region compresses, so B_z compresses producing a gradient in B_z which creates a force opposing the inward compression.

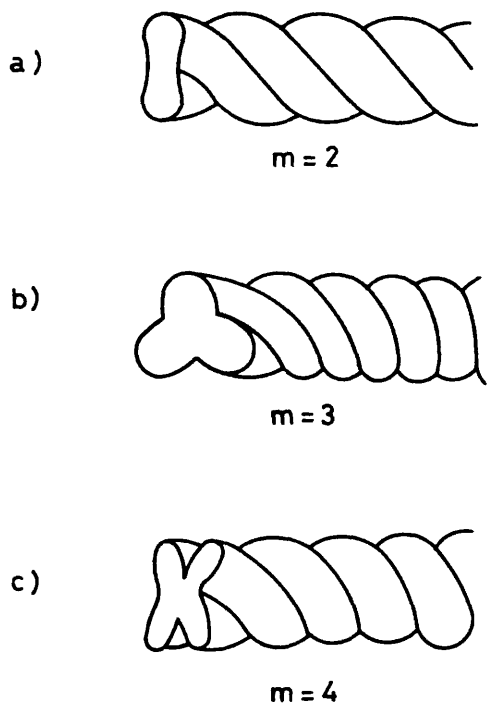

Figure 1.8 Examples of flute modes

Modes with m = 1 and n ≠ 0 are known as kink modes. Figure 1.7 shows an example. These modes are unstable in the linear pinch since the magnetic pressure on the concave side of the kink is higher than on the convex side. Again, the introduction of a longitudinal field serves to stabilise the modes because in this case field lines are under greater tension on the convex side of the kink. Stabilisation may also be obtained by the proximity of a conducting wall where image currents oppose the plasma motion.

Modes with m > 2, n ≠ 0 correspond to a longitudinal 'fluting' of the plasma column (figure 1.8). These higher mode deformations are theoretically less dangerous than the m = 0 and m = 1 modes because they tend to be localised in the radial direction and so do not cause such large

scale motion at the plasma edge. Also these instabilities may be shown to have lower growth rates.

1.3.2.3 Summary Of Ideal Stability

We have now discussed most of the general stability criteria applying to pinches. In particular we have seen that there exist basically two stable regimes. The first is the Tokamak regime where topology and toroidicity dictate stabilisation and the second is the RFP where the reversed toroidal field allows stability. The reversed field acts in two ways. First it allows the presence of a vacuum field outside the plasma without the consequence of a pitch minimum which is always destabilising and second, it dictates high shear and so allows, via the Suydam criterion, stability with large plasma pressure. In fact ideally stable RFP configurations with $\beta_o \equiv \beta_\theta B_\theta^2/B_o^2 = 31\%$ are possible under the ideal MHD theory.

1.3.3 Resistive Instabilities

As we discussed in section 1.1.2.2 the inclusion of resistivity, even if vanishingly small, allows fundamentally different types of plasma motions to occur. Specifically, in the Ideal MHD model the magnetic field topology is fixed, whereas with the inclusion of resistivity this constraint is relaxed and field-lines may break and reconnect.

1.3.3.1 Magnetic Islands

In order to elucidate the phenomena which may occur only when resistivity is added to the Ideal MHD description let us consider the linearised ideal Ohms law:

$$\underset{\sim}{E} + \underset{\sim}{v} \times \underline{B} = 0 \quad . \qquad - (1.45)$$

Dotting with $\underline{k}^*$, this yields for the r-component:

$$(\underline{k}.\underline{B})\ \xi_r = \tilde{B}_r, \qquad - (1.46)$$

which states that at the resonant surface where $\underline{k}.\underline{B} = 0$ ($r = r_s$), the radial magnetic field component is constrained to be zero. If we now introduce resistivity, equation 1.45 will be supplemented by an $\eta\underline{J}$ term and $\tilde{B}_r$ will in general be non-zero at $r = r_s$.

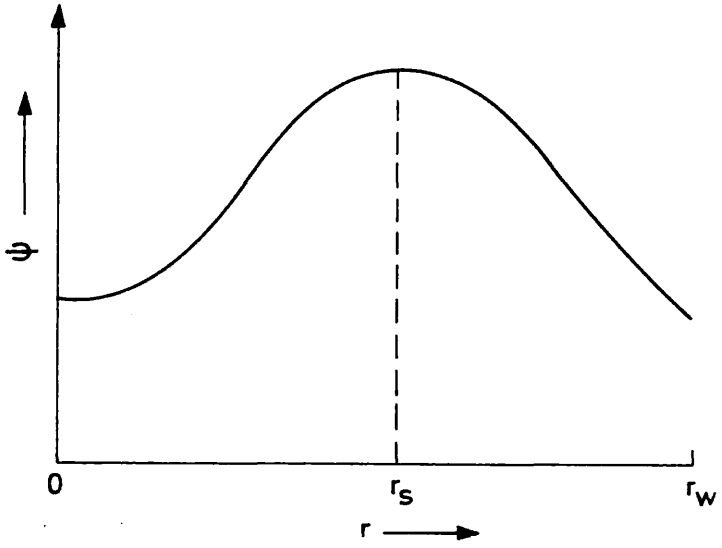

Figure 1.9
Example of $\Psi(r)$ for an equilibrium situation (for any τ).

For simplicity let us consider a single instability of helicity $\underline{k} = (0, m/r, k_z)$. Then we may define a flux function as follows:

$$B_r = -\frac{1}{r}\frac{\partial \Psi}{\partial \tau}\ ,\ \underline{k}.\underline{B} = \frac{1}{r}\frac{\partial \Psi}{\partial r}\ , \qquad - (1.47)$$

where $\tau \equiv m\theta + k_z z$. Ψ has the property that $\underline{B}.\nabla\Psi = 0$ and hence field lines are constrained to lie on the surfaces of Ψ = constant. By forming contours in the (r,τ) plane we may thus trace out the intersection of field-lines with this plane. For an equilibrium situation Ψ has the form shown in figure 1.9. In this case there is no variation with τ and so a contour plot in (r,τ) space reveals parallel flux-surfaces. This is shown in figure 1.10. If we now consider a non-equilibrium case but constrain $\tilde{B}_r$ to be zero at r_s (an ideal

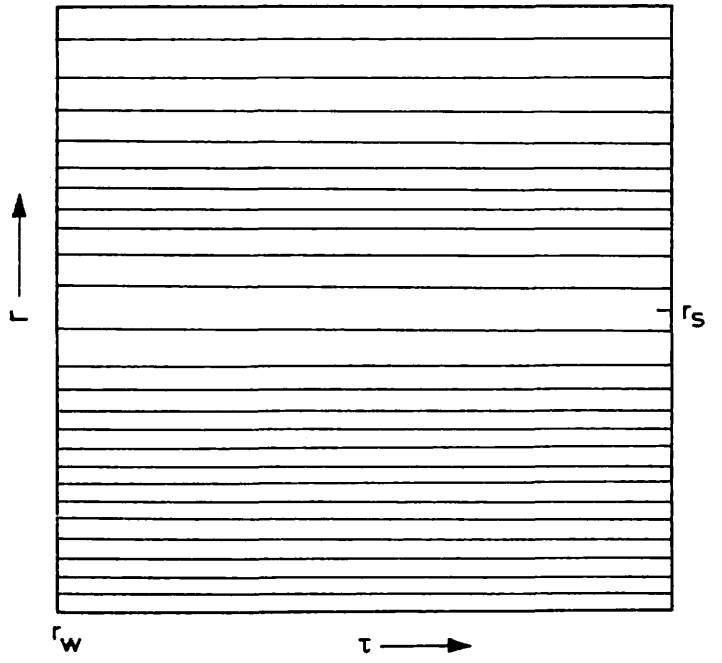

Figure 1.10
Contour plot of figure 1.9 showing parallel flux surfaces.

* $\underline{k}$ is the wavevector.

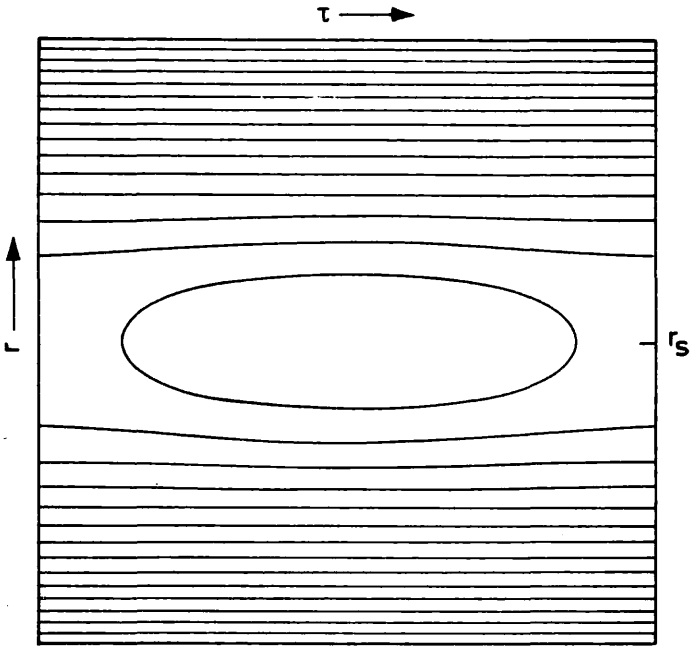

Figure 1.11 Contour plot of $\Psi(r,\tau)$ for the case of a resistive instability where $B_r(r_s) \neq 0$.

mode) then we have a similar situation but now with the flux surfaces being only strictly parallel in (r,τ) at $r = r_s$ and $r = 0$. However, if we relax the constraint that $B_r = 0$ at $r = r_s$ then $\Psi(r_s)$ may vary with τ and the flux surfaces will now take on an 'island' structure as shown in figure 1.11. The outermost flux-surface of the island is known as the separatrix, the point where it crosses the resonant surface as the X-point and the point at the centre of the island as the O-point.

The importance of island structures is that a given field line is no longer confined to a given radius as in figure 1.10 but now fills a region in r. Since parallel transport along field lines is very much larger than cross-field transport this amounts to a degradation of the confinement and insulation properties of the magnetic field. This aspect is accentuated when islands are nested side by side. Furthermore, when any two islands overlap significantly, the field lines take on random trajectories leading to even worse confinement. This particular problem will be discussed further in section 1.5.

1.3.3.2 Overview Of The Analytic Theory

Resistive instablities were first considered by Furth, Killeen and Rosenbluth in 1963 [33] for a slab geometry and subsequently by Coppi, Greene and Johnson in 1966 [34] for a linear pinch. The fundamental idea used in these papers is that since resistivity is small it may be disregarded in all but a small region centred around the singular surface. The analysis of resistive modes is thus a boundary layer problem: most of the plasma may be approximated by an Ideal MHD description, but in the layer around the singular surface the full resistive MHD equations must be solved. The matching of the solutions for these two regions together with appropriate boundary conditions essentially gives the dispersion relation for the relevant instabilities.

In both papers use is made of various orderings which determine which terms in the governing equations are dominant. The two most important orderings are the 'slow-interchange' and 'tearing'. Under the approximation of these orderings the growth rate of resistive modes is much smaller than the Alfven frequency and so the ideal outer region (away from the singular surface) is simply described by the marginal Euler-Lagrange equation of 1.40 which is a second order ODE. The inner solution (at the resonance region) depends on the growth rate and in general is a fourth order ODE. In the approximation of infinite Lundquist number ($S \equiv \tau_R/\tau_H$) the resistive layer thickness tends to zero and then this equation may be solved in terms of Hermite polynomials under the so-called constant-Ψ approximation [33].

Three important new instabilities arise from the inclusion of resistivity, all with growth rates intermediate between the resistive diffusion time $\tau_R \equiv 4\pi\sigma a^2$ and the hydromagnetic transit time $\tau_H \equiv a(4\pi\rho)^{1/2}/|\underline{B}|$. First there is the tearing mode, corresponding to the breakup of the resistive layer along current flow lines. This mode is driven by the parallel current gradient and is the resistive equivalent of the kink

mode of ideal hydrodynamics. Then there is the rippling mode which is caused by the flow of current across resistivity gradients in the resistive layer and finally the g-mode, which is due to the interaction of pressure and curvature and is the resistive counterpart to the ideal interchange mode. Of these the most dangerous for the RFP appears to be the g and tearing modes, the rippling modes being heavily damped by thermal conduction even at quite low electron temperatures.

As we noted above, inertia only becomes important for resistive instabilities in the region directly surrounding the singular surface. This means that the fluid motions associated with these instabilities will be localised to this layer. However, in general, the field eigenfunctions will not possess this local character. To clarify this, figure 1.12 shows the field and velocity eigenfunctions of an $m = 0$ resistive g-mode and figure 1.13 shows similar graphs for an ideal Suydam mode. Note that the resistive mode has $\tilde{B}_r \neq 0$ at $r = r_s$ whereas the ideal mode, as we discussed above, is constrained to have $\tilde{B}_r = 0$ at $r = r_s$.

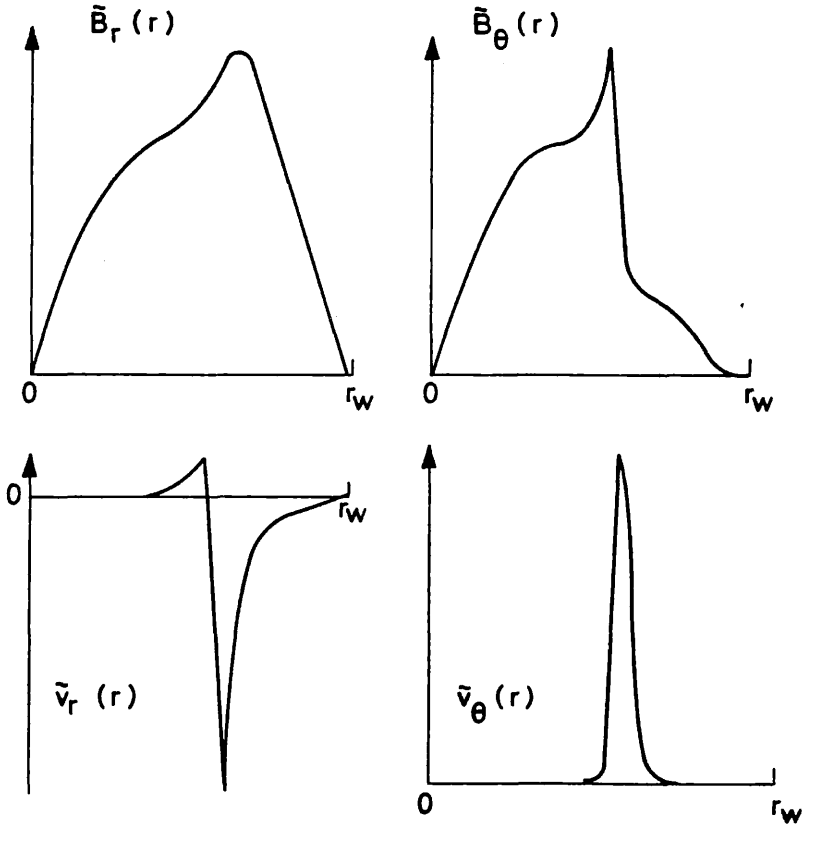

Figure 1.12 Field and velocity eigenfunctions for an m = 0 resistive g-mode. ($S=10^3$)

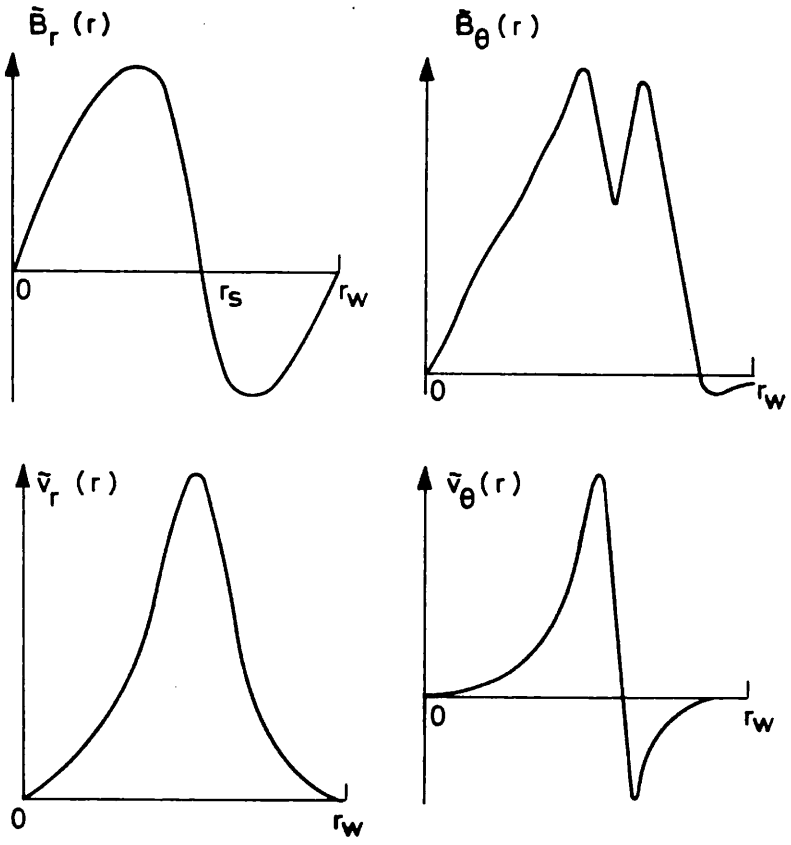

Figure 1.13 Field and velocity eigenfunctions for an ideal Suydam mode (same helicity as figure 1.12).

1.3.3.3 Δ' Stability Tests : The Tearing Mode

It has been shown in the two papers referenced above [33,34] that for the tearing mode there exists a very simple form for the dispersion relation in the limit of infinite Lundquist number. This may be written in the form:

$$\Gamma = f^+(\Delta'), \qquad - (1.48)$$

where $\Delta' \equiv (\delta\psi')/\psi(r_s)$,

and $$\psi \equiv \frac{r^{3/2}\,\tilde{B}_r(r)}{(m^2 + k_z^2 r^2)^{1/2}}.$$

Here $\delta\psi'$ is the jump of ψ' in the marginal ideal Euler-Lagrange equation across the singular surface and f^+ indicates a positive function. Thus the sufficient and necessary condition for stability to tearing modes (with $S\to\infty$) is $\Delta' < 0$. It is thus possible to test an arbitrary equilibrium field

configuration for the stability to tearing modes by simply integrating the marginal ideal Euler-Lagrange equation from the axis to the resonance and then from the wall to the resonance to compute Δ'. Such a procedure has been used by Robinson [35] (in a slightly different form) to investigate the marginal stability points of various equilibria. In chapter 6 we will use this technique to analyse experimentally measured field configurations.

1.3.3.4 General Stability To Resistive Modes

In general, realistic resistive stability calculations must be treated numerically. However, for the tearing mode an on-axis analytic criterion can be derived [35] in the limit of $S \to \infty$. This states that for stability:

$$\frac{4}{\gamma} > 2m - 7, \text{ where } \gamma \equiv \frac{P}{2}\frac{d^2P}{dr^2} \qquad - (1.49)$$

and P is the field line pitch. Combined with the ideal stability criterion on-axis for m = 1 modes this dictates that:

$$-\frac{4}{9} > \gamma > -\frac{4}{5}\,. \qquad - (1.50)$$

To satisfy this condition the current distribution must be peaked on axis; a flat distribution has $\gamma = -1$.

A range of field configurations have been tested for stability to tearing and g-modes using finite S computer codes such as RIPPLE 4A [36]. Perhaps the most important result for tearing modes is that a conducting wall is vital for stability to m = 1 perturbations which tend to have the largest growth rates. Indeed, the presence of even a small vacuum region can lead to instability. Despite this, tearing mode stable field distributions have been shown to exist with zero β and Θ up to 3.7. These configurations can be stable to Ideal MHD pressure driven modes with values of β on axis in the range 10-30% but are unstable to the resistive g-mode. In general the tearing mode is stabilised by shear.

Unlike the tearing mode, in the linear pinch the resistive g-mode is not stabilised by shear or a conducting wall. At low values of S ($<10^3$) resistive dissipation tends to stabilise these modes due to their local nature. For $S > 10^3$, ignoring viscosity, a general result appears to be that the poloidal mode number of the most unstable $m \neq 0$ g-mode increases with S as does the growth rate itself. So that at $S = 10^3$ the most unstable $m \neq 0$ mode is $m = 1$ whereas for $S = 10^4$ it is $m = 3$. At even higher values of S poloidal mode numbers as high as 11 have been seen (in codes) to be dominant. As it turns out the inclusion of anisotropic viscosity [37] prevents this cascade to higher m and current belief is that the $m = 1$ g-mode is generally the fastest growing $m \neq 0$ mode even at $S \approx 10^7$. In this case stability may be possible with $\beta < 10\%$ although here the pressure gradient at the reversal surface is very critical due to $m = 0$ modes being fairly immune to parallel viscosity.

1.4 QUASI-LINEAR EFFECTS

So far we have discussed only the linear theory of collective plasma instabilities. This theory holds when the perturbations of the various plasma parameters are small enough so that quadratic and higher order perturbation products are negligible compared to the linear terms. The theory thus comprises a set of linear differential equations which may be Fourier analysed in time and with suitable geometry, space; hence instabilities are characterised by independent modes of wavevector $\underline{k}$ and complex growth rate Γ. In both the ideal and resistive linear theories the instabilities of interest have real or complex growth rates and thus grow exponentially with time. The question then arises as to what happens when this exponential growth raises the level of perturbations to such a degree

that the linear theory no longer holds.

At this point there is an important distinction to be drawn. In general, when the perturbation amplitude is large, various non-linear effects can occur. In particular, different Fourier modes are no longer independent but are non-linearly coupled together, both in frequency and wavevector space. If the perturbations are large enough this can lead to a situation known as strong turbulence [38,39]. However, if the perturbation amplitude is relatively small then it is possible for this non-linear mode-mode coupling to be weak and its only effect is to modify the growth rate through quadratic terms coupling to the equilibrium. This situation is much more amenable to analytic and numerical treatment than the strong-turbulence case since the degrees of freedom are far more limited. We distingish the two cases by refering to those where instabilities act only on the equilibrium to modify the growth rate as quasi-linear and those in which strong mode-mode coupling occurs as fully non-linear. Since the typical level of fluctuations in the RFP is of the order of a percent or so, significant progress can be made by considering the quasi-linear theory. The importance of this and any more precise non-linear theory is that a method is provided for the saturation of instabilities at the finite amplitude observed in experiment.

Significant work has been done concerning the quasi-linear theory of the tearing and resistive g-modes and we shall now briefly review this topic. Notable contributions concerning the tearing mode have been made analytically by Rutherford [40] and both analytically and numerically by White et al [41]. Numerical studies of the g-mode have been carried out fairly recently by Hender and Robinson [42,43] in both the quasi-linear and more non-linear regimes.

Quasi-linear effects of both the tearing and g-modes first appear when the island size becomes comparable to the resistive layer thickness. In the case of the tearing mode the parallel current density is flattened at the

singular surface leading to a reduction in the growth rate. For the g-mode the equilibrium pressure is flattened. The tearing mode can actually saturate completely due to current flattening whereas, in the incompressible case, the g-mode growth rate can only be reduced. This is because of the 'overheating effect' where a g-mode quasi-linearly not only flattens the pressure at the singular surface but also raises the average pressure which acts to increase the growth rate. Numerical studies indicate that saturation can occur if a non-physical energy loss term is included in the model. Figure 1.14 shows a typical scenario of the quasi-linear evolution of the pressure profile for an m = 0 g-mode.

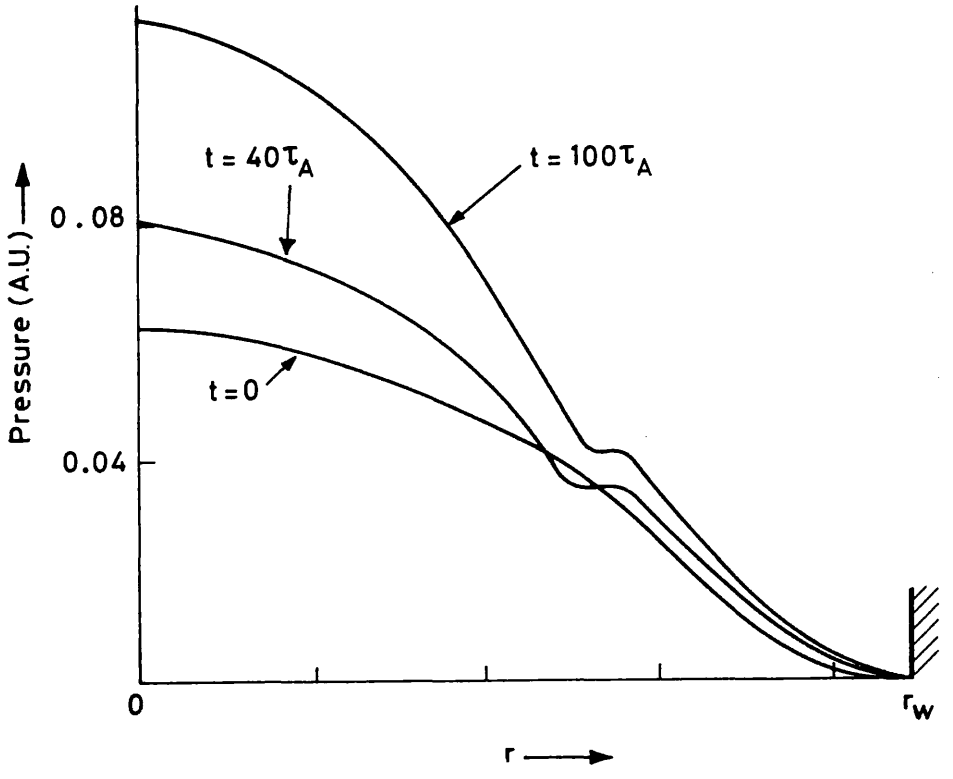

Figure 1.14 Quasi-linear evolution of the pressure profile during the growth of an m = 0 g-mode for S = 10^3.

Another important quasi-linear mechanism which affects the g-mode, but nevertheless has its analogue in tearing mode theory, is the destabilisation of modes by the pressure flattening of another mode. For instance an m = 0 mode in the RFP may grow and flatten the pressure at its singular surface. But this flattening of the pressure at the singular

surface must necessarily be accompanied by an increase in pressure either side of the surface which means that m = 1 modes, whose resonances are directly next to the reversal surface, are destabilised. Hender [43] has shown that the interaction of these two modes can give rise to ergodic field line behaviour (see next section) which may explain the inherently bad confinement properties of the RFP experimentally so far observed.

1.5 ERGODICITY AND STOCHASTIC TRANSPORT

The existence of magnetic surfaces in toroidal containment devices is a crucial ansatz for the high degree of thermal and particle insulation needed to contain a thermonuclear plasma. This is, of course, because transport along field lines is many orders of magnitude greater then across field lines. Perfect magnetic surfaces are known to exist rigorously in cases of special symmetry, but then only in the equilibrium situation. An important question thus arises as to the effect of magnetic perturbations on these surfaces. In answer to this question Rosenbluth, Sagdeev and Taylor [44] showed in 1966 that the overlap of magnetic islands within a region actually destroyed magnetic surfaces and that a Brownian motion of flux lines within that region ensued. The condition for this 'stochastic' or 'ergodic' behaviour of field lines may be expressed in terms of the stochasticity parameter:

$$s \equiv \frac{1}{2} (\Delta_{mn} + \Delta_{m'n'})/|r_{mn} - r_{m'n'}|, \qquad - (1.51)$$

where m,n and m',n' represent two resistive modes which have neighbouring resonant surfaces. If $s > 1$ then magnetic surfaces are destroyed in the region between r_{mn} and $r_{m'n'}$ and the field lines wander ergodically.

In 1977 Rechester and Rosenbluth [45] gave an expression for the electron thermal conductivity for ergodic plasmas in both the collisional and collisionless regimes. As can be appreciated, if the entire plasma is

ergodic a field line starting at the hot central core will eventually wander to the wall and thus the effective perpendicular heat transport will be much worse than classical. In the collisionless regime Rechester and Rosenbluth show that the radial thermal diffusion coefficient may be written:

$$\chi_r = D_{st} v_{eT}, \qquad - (1.52)$$

where $D_{st} \equiv \langle(\Delta r)^2\rangle/(2L)$,

and v_{eT} is the electron thermal speed. D_{st} is the spatial diffusion coefficient which describes the Brownian motion in radius of the field-lines; a given field line thus undergoes a random walk spreading in radius an amount $(\Delta r)^2$ in a (field-line) parallel distance L. For the collisional case a similar result applies but here heat transport is reduced somewhat by collisions.

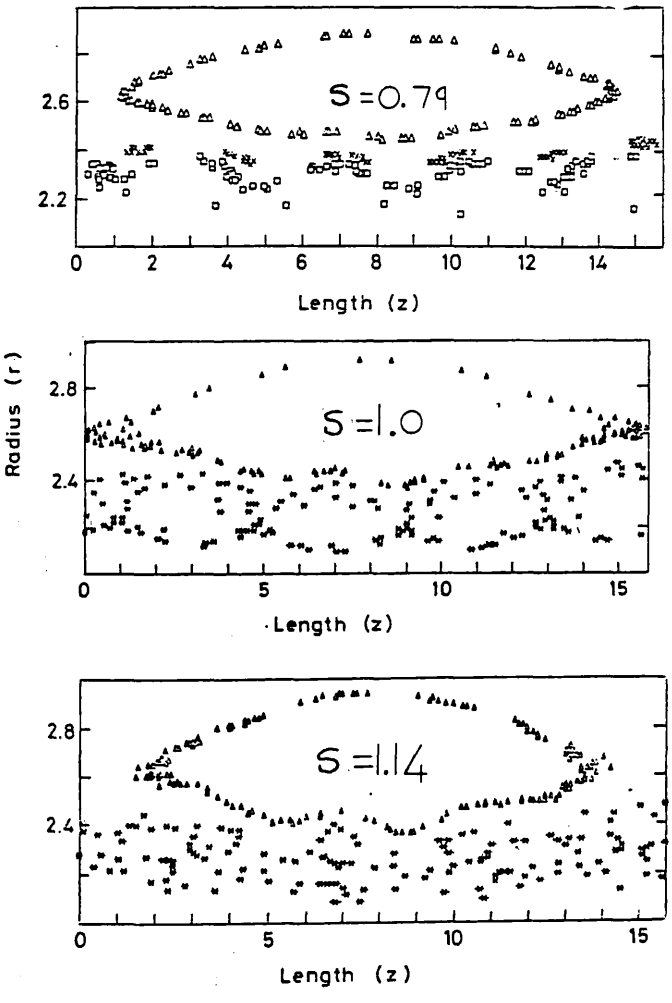

Figure 1.15

Interaction of two islands of differing helicity illustrating the onset of stochastic behaviour when s = 1.

To illustrate ergodic behaviour figure 1.15 shows a sequence of graphs depicting the interaction of an m = 0, n = 1 g-mode and an m = 1, n = -4 g-mode for three values of the stochasticity parameter. For s = 0.79 a closed flux surface is clearly visible (the x's) between the m = 0 and m = 1 islands. For the s = 1.0 case this flux surface has been destroyed, whilst for the s = 1.14 case all the m = 1 surfaces have been destroyed.

In chapter 5 we will see that there is strong evidence from the measurements reported in this thesis to believe that the observed

fluctuations act to create at least an inner ergodic region and may be responsible for the poor energy confinement observed in the RFP.

1.6 FIELD REVERSAL IN THE RFP

The observation that a reversed field configuration can be set-up and sustained in a steady state cannot be explained in terms of a simple equilibrium Ohm's law of the form $\underline{E} + \underline{v}\times\underline{B} = \eta\underline{J}$ in the context of the MHD theory [46]. This is because the sustainment or creation of reversed B_ϕ configurations requires J_θ currents to be driven at the reversal surface and a simple Ohm's contains no such prescription (with $E_\theta=0$). The resolution of this paradox may come from several effects. First, non-linear effects of instabilities may modify the equilibrium Ohm's law by coupling to the zeroth order harmonic (i.e. the equilibrium). In this way instabilities could be responsible for the generation of the required J_θ currents to sustain reversal. A second equally likely possibility is that stochasticity enforces a global Ohm's law rather than a local one. In this way J_θ currents at the reversal surface could be driven by emfs originating in the core of the plasma.

1.6.1 Taylor's Theory

Taylor [19] has considered the problem of reversal as an example of the more general process of relaxation to a minimum energy state. In his theory it is assumed that the plasma is a conducting viscous fluid enclosed in a perfectly conducting shell. The initial state of the plasma is arbitrary providing boundary conditions are satisfied. In general the plasma will move and in so doing will lose energy (e.g. due to turbulence) until it reaches a state in which its energy is a minimum. This final state will thus be the state of minimum

energy subject to a set of constraints determined by the fact that the plasma is only allowed certain types of motion described by its dynamical governing equations.

For a perfectly conducting plasma in the ideal MHD approximation the relevant constraints arise because the magnetic field topology is fixed and hence the helicity of the field configuration, which is a measure of the number of topological field-line knots, defined as:

$$K \equiv \int_V \underline{A}.\underline{B}\, d\tau \qquad - (1.53)$$

(where $\underline{A}$ is the magnetic vector potential defined through the relation $\nabla \times \underline{A} = \underline{B}$) is an invariant on every field line. Minimising the magnetic energy subject to these constraints yields the relations $\nabla \times \underline{B} = \lambda \underline{B}$ where λ is different for each field line. Under this picture the value of K on each field line in the final state is a direct mapping of its initial value. Experimentally, however, this is not observed to be the case. It is therefore necessary to consider the effect of including vanishingly small resistivity. As we have discussed above this allows the magnetic topology to change and so the constraint that K be invariant on each field line clearly no longer applies. However, since the resistivity is small, current redistribution will occur on a timescale short compared to the resistive diffusion time and so the integral of K over the entire plasma volume will still be approximately invariant. Mimimising the magnetic energy subject to this single constraint yields the equation $\nabla \times \underline{B} = \mu \underline{B}$ describing the relaxed state, where μ is now a single constant having the same value on all field lines.

The importance of Taylor's model is that it shows that, given any initial conditions, there exists just one final relaxed state depending only on μ. In a cylinder the solution of this relaxed state is the BFM of equations 1.25 and 1.26:

$$B_z = B_o J_o(\mu r) \ , \ B_\theta = B_o J_1(\mu r) \ , \ B_r = 0. \qquad - (1.54)$$

The parameter μ, being simply $|\underline{J}|/|\underline{B}|$, is related to the pinch parameter by the equation $\mu a = 2\Theta$. Hence the relaxed state depends crucially on Θ. In fact by plotting the field reversal parameter F against Θ a universal curve is seen to exist. If Taylor's theory is correct experimental measurements of F and Θ should lie near to this curve. Figure 1.16 shows an example where experimental points from ZETA, ALPHA and HBTXI have been overlaid on the theoretical curve. The agreement is certainly very good although the experimental points seem to be displaced slightly to the right of the diagram. Note that for $\Theta > 1.2$ the BFM possesses field reversal.

When $\Theta > 1.56$ the BFM is no longer the lowest energy solution of the equation $\nabla \times \underline{B} = \mu \underline{B}$ but rather a helical state which posseses field reversal is more energetically favourable. In this region Θ saturates with increasing applied volt-seconds and the amplitude of the helix grows. It is

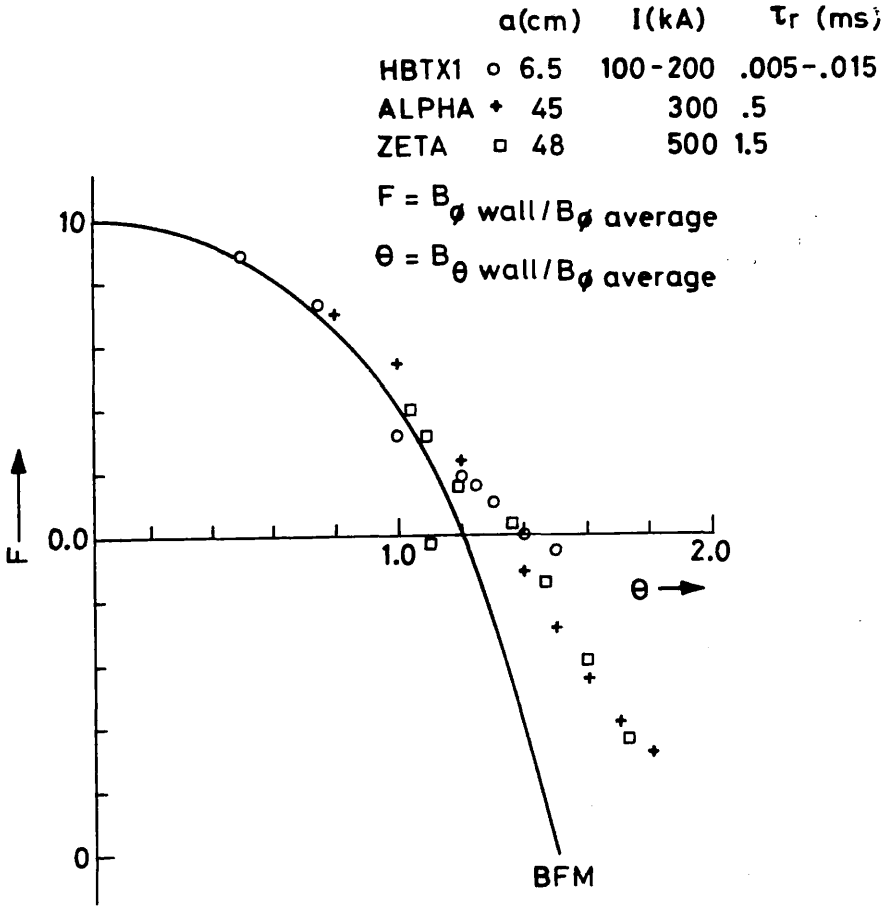

figure 1.16 F-Θ loci for the BFM and experimental points from ZETA, ALPHA and HBTXI.

perhaps an interesting coincidence that the condition $\theta = 1.56$ is both the point at which the Taylor relaxed state becomes helical and where resistive kink instabilities for the BFM are marginal.

1.6.2 Mechanisms Of The Reversal Process

Taylor's theory is a very general argument for the form of the basic RFP equilibrium. It poses the question as to how a reversed field configuration may arise in the context of the energy principle but it does not say anything concerning the dynamical route through which such a relaxation must travel. Indeed, feasible dynamical routes do not, a priori, have to exist as is the case in the Tokamak where (partial) relaxation only occurs very seldom in the form of disruptions. To elucidate possible dynamical routes for relaxation in the RFP much work has been performed both numerically and analytically.

1.6.2.1 Reversal By Direct Instability Action

Gimblett and Watkins have shown that if quadratic effects are included in the resistive MHD equations and suitable assumptions are made to remove turbulence terms (the assumption of so-called first order smoothing) then the equilibrium Ohm's law is effectively modified to the following form:

$$\eta \underline{J} = \underline{E} + \alpha \underline{B} - \beta \underline{J}. \qquad - (1.55)$$

This Ohm's law now caters for the J_θ currents required to sustain reversal through the α-effect. An additional effect is a turbulent resistivity, the β-effect.

Mathematically both the α and β-effects come from the cylindrically averaged component of the quadratic Lorentz perturbation term $\underline{\tilde{v}} \times \underline{\tilde{B}}$. Physically the α-effect may be explained with the aid of figure 1.17 which

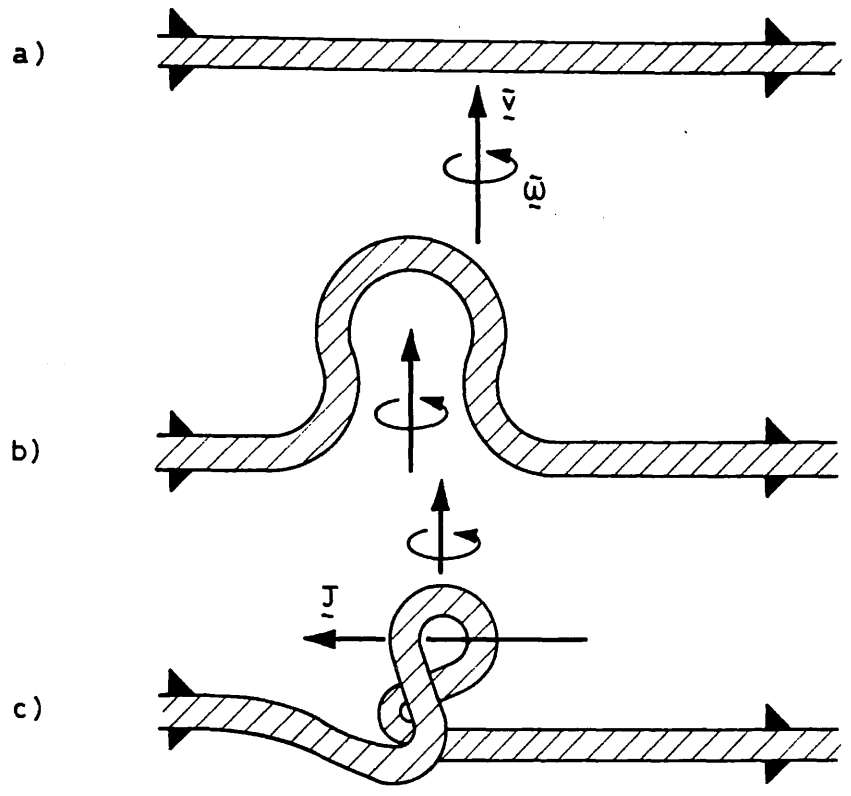

Figure 1.17 Diagram illustrating the α-effect.

shows the (non-linear) evolution of a flux-tube, initially in a plain slab, when the fluid motion possesses helicity. The upward linear motion combined with rotation forms a twisted loop giving rise to a current parallel to $\underline{B}$. By solving the appropriate dynamo equations in an infinite cylinder Gimblett and Watkins have shown that the fields are Bessel functions depending on Θ and a structural parameter $s = a\alpha/\eta_R$.

Similar quasi-linear scenarios such as the dynamo model above have been around for quite a long time. In fact the idea that a single large amplitude kink could amplify the flux in the plasma core and hence create reversal by flux-conservation was first proposed by Colgate [47] in 1958. Sykes and Wesson [48,49,50] studied this type of interaction numerically in 1976 and found clear evidence for such a process. In addition, in fast programmed experiments such as ETA BETA I [51,52], FRSX [53] and HBTXI [53,54] the actual magnitude of the reversed field could be explained using such a model.

Recently Hutchinson [55] has considered reconnection processes as in the Tokamak disruption scenario of Kadomtsev[56,57] but proceeding in an inverse direction appropriate to the energetics of the RFP. He shows that, providing islands from interior m = 1 type resistive instabilities overlap the reversal surface, then field reversal may be maintained. Evidence for these inverse reconnections has been seen in 2-D computer simulations [58] although in this case they do not directly sustain reversal.

1.6.2.2 The Tangled Discharge Model

We discussed in the introduction to this section that stochastic behaviour of the field lines can mean that a local Ohm's law is no longer valid and must be replaced by a global Ohm's law which specifies the local current density in terms of the electric field throughout the plasma. If this is the case reversed fields could in principle be created and sustained without direct effect from turbulence; this now being relegated to merely maintaining the stochastic behaviour by the overlap of adjacent islands. This is the basic theme of Rusbridge's Tangled Discharge Model (TDM) [59,60,61] which treats a plasma of a varying degree of 'ergodicity' under the assumption that current flows only along field-lines. Physical insight into this model may be gained by regarding the field lines or 'flux-tubes' as electrical wires, which due to ergodicity wander in radius. If one imagines one such wire which wanders from the centre of the plasma to the edge, then since the toroidal electric field will, in general, vary as a function of radius, there will exist a potential across the wire and hence a current will flow along it. The magnitude of this current will essentially be independent of the direction of the wire at any point in space, since when, the direction is not aligned with the driving potential, charges will accumulate in such a way as to make the current constant along the wire. Of course, this is the same reason why the current in a wire

connected to the two terminals of a battery is independent of the wire's topology. Clearly if our wire has a component of its direction vector in the θ direction at the reversal surface then a J_θ current will flow at this surface.

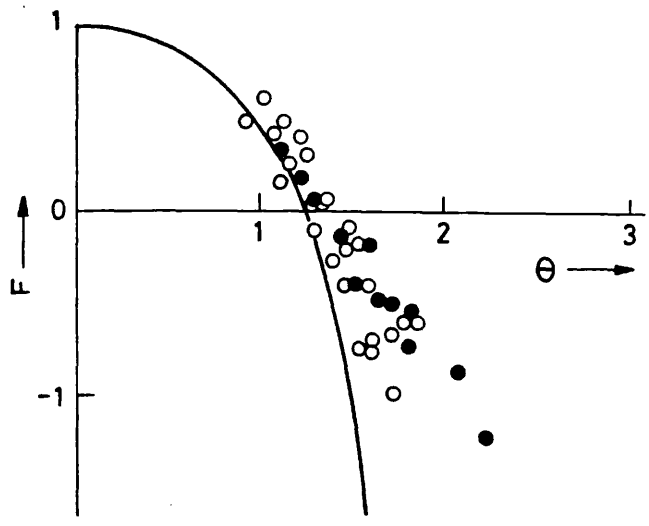

Figure 1.18
F-θ loci for the TDM and experimental points from ZETA.

As we outlined above the TDM treats plasmas of varying degrees of ergodicity. In the limit of good flux surfaces (zero ergodicity) the resulting global Ohm's law simply reduces to the Force-free Paramagnetic model (FFPM) whereas in the other limit, that of complete ergodicity, it gives a BFM. Figure 1.18 shows a comparison of the F-θ locus for an optimised TDM distribution and that of experimental points obtained from ZETA.

The importance of the Tangled discharge model and later non-local resistivity models [62] is to show that, on the basis of a physical picture involving the breaking and rejoining of flux lines, relaxation to a reversed field configuration similar to that experimentally observed can be explained.

1.6.3 Summary On Field Reversal

Relaxation to a reversed field configuration appears to be explicable from a number of different view-points and by quite a few different mechanisms. However, there do appear to be two distinct classes of mechanism; the first in which plasma instabilities directly create the reversed field, and the second, in which plasma instabilities act only to sustain stochasticity and reversal is caused by non-local effects. It may

well be that in different regimes different mechanisms occur. Indeed, as stated above, for low Lundquist number pinches, evidence seems to favour the direct dynamo mechanism (at least at high Θ). However for present day slow-pinch devices it may well be that the Tangled discharge approach is the more relevant mechanism. If this is so then stochastic transport could be an inherent property of the RFP at high values of the Lundquist number.

CHAPTER 2

REVIEW OF EXPERIMENT

2.1 INTRODUCTION

RFP experiments may be broadly divided into two categories. These are the 'fast pinch' experiments such as HBTXI, ZT1 and ETA-BETA and the slow pinch experiments such as ZETA, MkIV and most of the contemporary devices. The fast pinch is characterised by rapid field programming by which the reversed field configuration is set up on a timescale shorter than that required for profile relaxation. The slow pinch, on the other hand, uses the plasma's own self-reversal properties with optional slow-field control to set up the field configuration on a timescale longer than that required for profile relaxation. Of the two concepts there is little doubt that the slow pinch represents the best alternative for fusion. However, from a physics point of view, the fast pinch experiments were very productive.

2.2 SLOW PINCH EXPERIMENTS : ZETA AND THE MkIV

The main results concerning fluctuation studies in pre-contemporary slow pinch experiments came from the ZETA machine and to a lesser extent the MkIV both of which were operated at the AERE Harwell laboratory in England during the fifties and sixties. The ZETA machine was not specifically designed for reversed field operation as the RFP concept was essentially founded by the observation of improved discharge conditions in ZETA - 'quiescence' - when operating under this mode and within a specific parameter space. In fact, nearly all the fluctuation measurements on ZETA pertain to reversed discharges but quiescence was not attained. This fact should be kept in mind when comparing the fluctuations observed in ZETA with those observed in the reversed discharges of contemporary machines.

The ZETA experiment has been described in detail by Butt et al [1] and Burton et al [2]. The main parameters of the machine were minor radius 48 cm, aspect ratio 3:1, plasma current up to 1 MA, rise time to peak current ≥ 0.8 ms and pulse length up to 5 ms with passive crowbar and 20 ms with power crowbar. The measured values of the energy and particle confinement times were approximately 100 μs in the unreversed mode, increasing markedly in reversed (quiescent) mode.

The MkIV experiment was a much smaller toroidal pinch than ZETA. Its main parameters were minor radius 15 cm, aspect ratio 4:1, plasma current up to 50 kA, rise time 200-400 μs and pulse length 1 ms.

2.2.1 Observations Of Coherent Global Fluctuations

The first observations of regular fluctuations in a toroidal pinch were reported from the MkIV in 1961 by Rusbridge et al [3]. Langmuir and magnetic probes were used to measure the electric and magnetic fluctuations as a function of radius in partially ionised discharges. Figure 2.1 shows an example of the raw data. The oscillations are characterised by a frequency

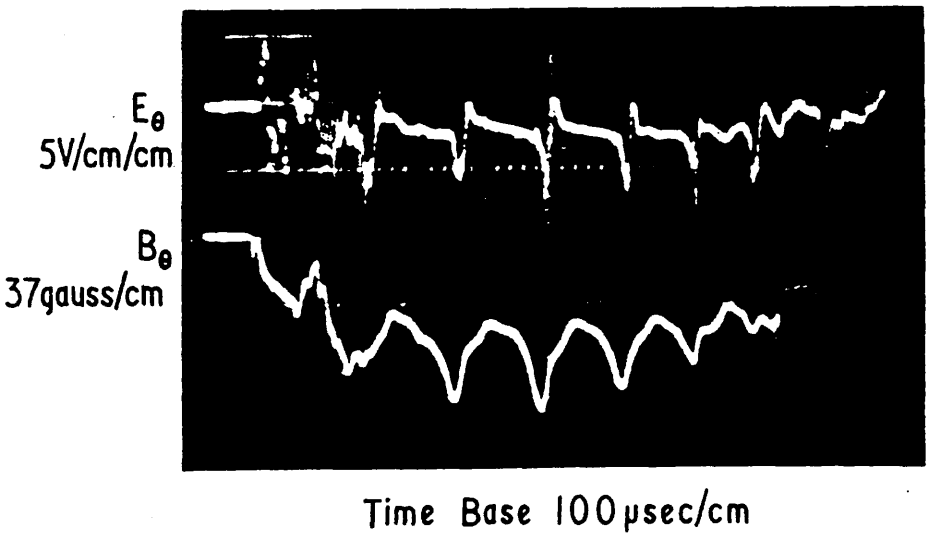

Figure 2.1 Correlation of electric and magnetic fields showing regular oscillations in the MkIV.

of 2-15 kHz dependent on the equilibrium. Measurements of the phase relation of the oscillations at different points along the discharge tube

were made with a T-shaped probe which measured the electric field at 4 toroidal locations. Results showed that the oscillations were to be associated with a wave propagating in the direction of conventional current at a uniform speed of $3.5 \times 10^3 ms^{-1}$

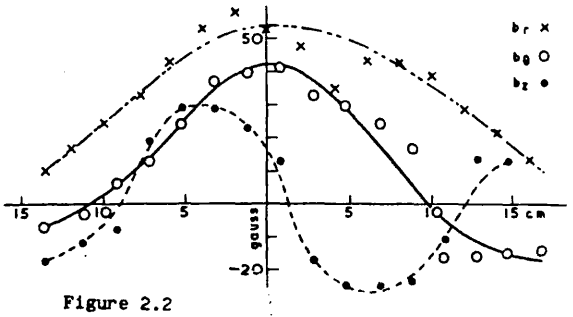

Figure 2.2
Amplitude of the fluctuating part of the magnetic field vs radius in the MkIV.

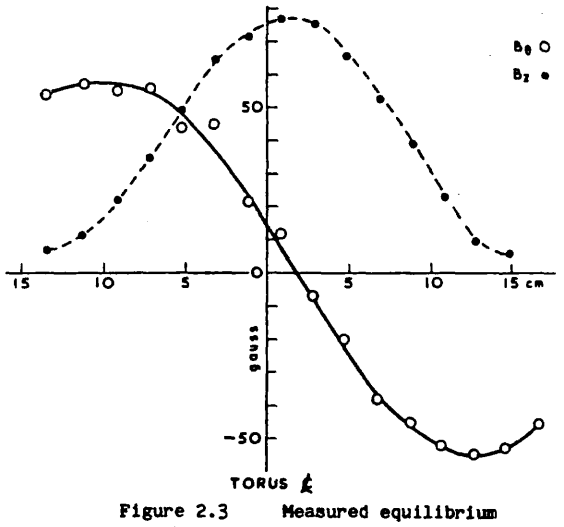

Figure 2.3 Measured equilibrium magnetic field profiles in the MkIV.

Figures 2.2 and 2.3 show respectively the measured fluctuating ($\underline{b}$) and mean ($\underline{B}$) magnetic fields as a function of radius. The fluctuating field amplitude was deduced by inspection. Clearly $|b_r| \approx |b_\theta| \neq 0$ on axis and so the oscillations must be associated with m = 1 (by single valuedness of the fields). This is also substantiated by the 'odd' form of b_z.

By using a special probe designed to measure the $\underline{E}x\underline{B}$ velocity it was shown that there existed a large inward velocity during the peak of the electric field fluctuation. Between peaks there also existed a small outward velocity. In addition to measuring the $\underline{E}x\underline{B}$ velocity the probe was used to measure density as a function of time and radius. Results indicated the presence of a helical notch of low density which propagated toroidally. These observations were interpreted at the time as the signature of a growing sound wave.

A similar analysis of magnetic and electric fluctuations was carried out on ZETA in 1962 by Rusbridge, Lees and Saunders [4]. The amplitudes and frequencies of the fluctuations were studied as a function of various equilibrium parameters. In addition a model configuration similar to the measured field profiles was tested for linear ideal stability to current

driven modes by the technique due to Newcomb (see chapter 1 sect 1.3.2.1). These calculations showed that only m = 1 modes were unstable and then only for a narrow band of k centred on -2.0. To compare the predictions of the linear theory with the measured radial variation of the magnetic fluctuations a simple analytic form for the radial displacement of the m = 1 modes was assumed:

$$\xi_r = \xi_o (1 - x^2) . \qquad - (2.1)$$

The ideal hydromagnetic equations (i.e. a small amplitude helical equilibrium) were then used to calculate the radial behaviour of the fluctuating field. Figures 2.4 and 2.5 show the comparison of these calculated variations with those measured for b_θ and b_z. Clearly the agreement is good indicating that the observed oscillations are attributable to m = 1, $|k|a \approx 0.4$ helical modes which are stable under the hydromagnetic approximation.

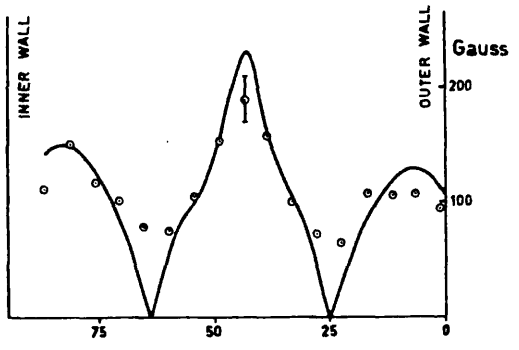

Figure 2.4 The measured amplitude of the fluctuating poloidal field in ZETA compared with a theoretical curve assuming an instability of ka = -0.4.

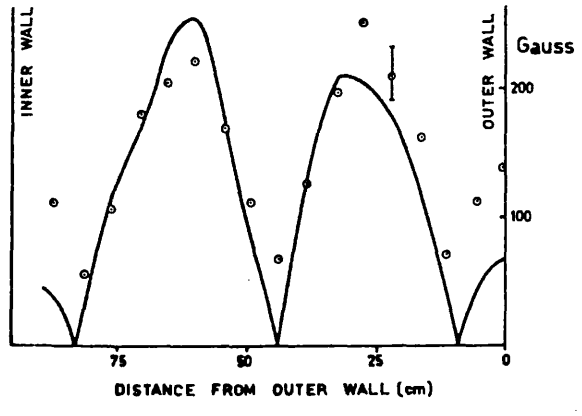

Figure 2.5 As for figure 2.4 but for the toroidal field component.

Electric field fluctuations were measured and compared with those predicted by the hydomagnetic theory in association with the magnetic fluctuations. Results indicated that only part of the electric fluctuations could be explained in this way. The origin of the dominant part of the electric fluctuations was not understood but it was hypothesised that they could be due to drift waves or an anomalous non-uniform resistivity.

2.2.2 Observation Of Localised Turbulence In The ZETA Discharge

So far we have addressed the observation and interpretation of large scale coherent modes. These appeared in ZETA and the MkIV as the dominant phenomena at low frequencies. At high frequencies, however, shorter scale length phenomena occurred. These fluctuations were addressed in three papers by Robinson, Rusbridge and Saunders [5] and by Robinson and Rusbridge [6,7], where interpretation concentrated on the theory of fluid turbulence developed by Edwards[8] in 1964 and extended to the presence of a magnetic field by Robinson [9] in 1966. In this theory turbulent eddies are envisaged to be produced of a scale length comparable to that of the mean flow. These eddies arise due to instabilities and, in the case of isotropic turbulence, non-linearly couple to eddies of a smaller scale. The energy flow is thus towards smaller scale lengths where dissipation eventually occurs due to viscosity. In the case of 2-dimensional turbulence the direction of the energy flow is actually reversed and the small scale lengths couple to the larger scale lengths, dissipation ultimately occurring due to effects such as eddie currents in the conducting shell.

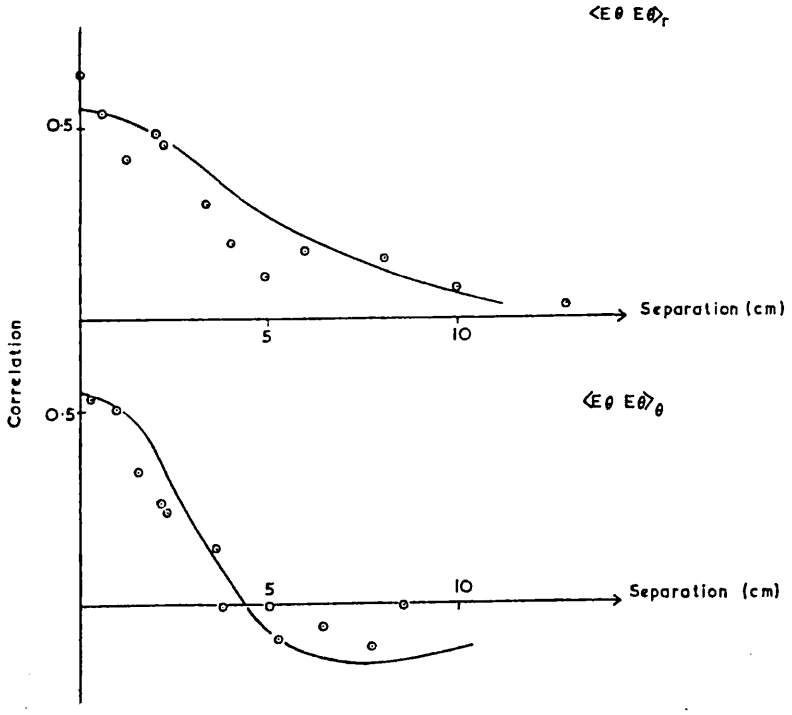

Figure 2.6 Electric field correlations $\langle e_\theta e_\theta \rangle_r$ and $\langle e_\theta e_\theta \rangle_\theta$ in ZETA (1/2 mTorr D_2 I=150 kA, applied axial field 0.37 T).

The first paper [5] reports results concerning the electric and magnetic fields as measured by insertable probes for frequencies greater than 10 kHz. The data were analysed using an analogue 'correlator' [10] which could form the correlation function between two time signals. Figure 2.6 shows the correlations $\langle e_\theta e_\theta \rangle_r$ and $\langle e_\theta e_\theta \rangle_\theta$, the curves being fitted under the assumption that the electric field is irrotational ('<>' indicates a time and ensemble average). Remembering that the ZETA machine had a minor radius of 48 cm it is clear that the observed electric field fluctuations are relatively localised in both radius and poloidal angle and that their form agrees well with the assumption of irrotationality. Figure 2.7 shows the correlation $\langle b_\theta b_\theta \rangle_r$ and for comparison that predicted by isotropic turbulence (upper) and 2-dimensional turbulence (lower). The form of the measured correlation is similar to that of the electric field, being localised in radius, and the best fit with theory is obtained for the two-dimensional case.

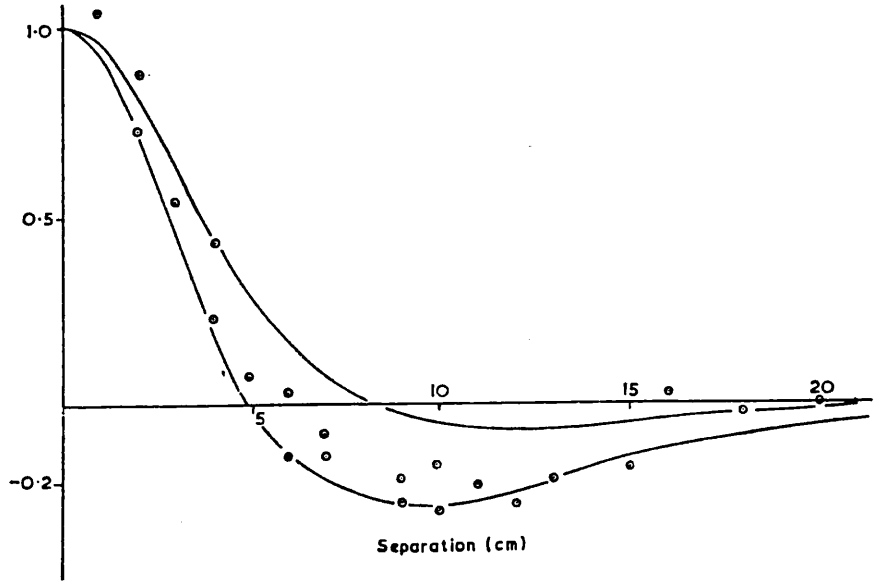

figure 2.7 Magnetic field correlation $\langle b_\theta b_\theta \rangle_r$ in ZETA. Fitted curves correspond to isotropic (upper) and 2-dimensional (lower) turbulence.

Further studies concentrated on determining a turbulent velocity which was used to calculate the Reynolds number. This was found to be large enough to be comparable with that obtained from laboratory fluid-flow experiments.

Estimates of the partition of energy between mechanical and magnetic modes revealed a value of about unity at high operating pressures consistent with theory. However, at low pressures this value increased to as much as six and for consistency with theory an anomalous resistivity had to be assumed.

The second paper concerning localised turbulence in ZETA [6] reported measurements from a double Langmuir probe. Again low frequencies (<10 kHz) were filtered out to exclude the global phenomena. Density fluctuations with an amplitude of up to 25% were observed. Figure 2.8 shows the density correlation function versus radius for two different filling pressures.

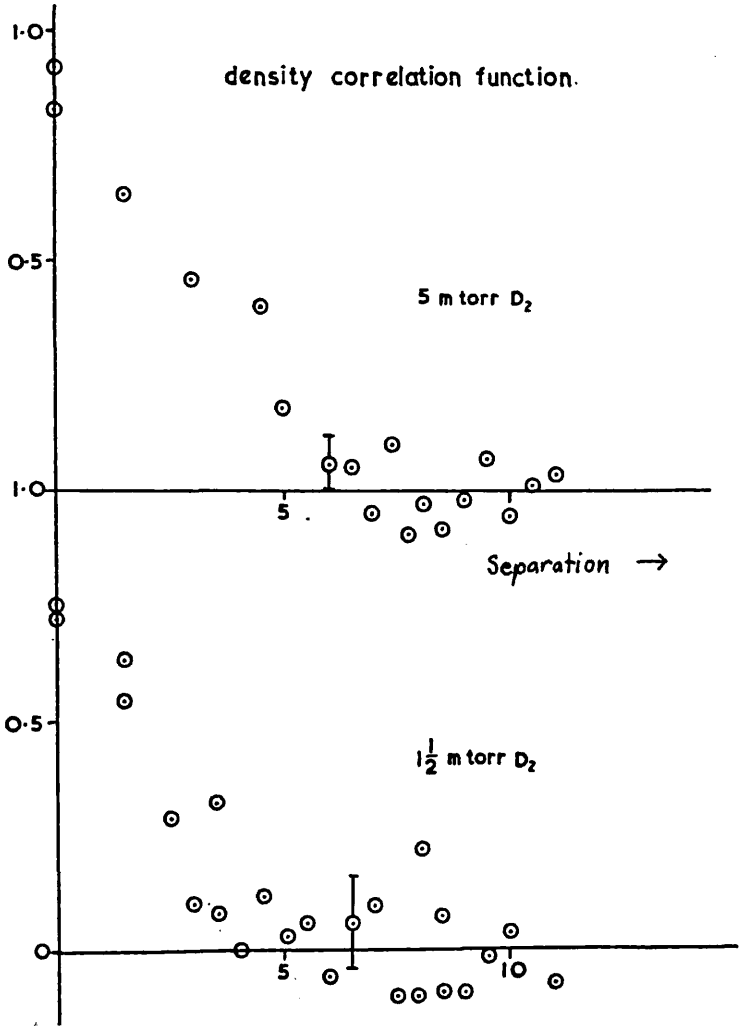

Figure 2.8 Density correlation functions in ZETA for two filling pressures.

These graphs show similar results to the electric fluctuations discussed above, being localised in radius. In particular the correlation function possesses no tail, negative or positive, but ends fairly abruptly at about

7 cm separation. Now it can be shown that this can only be consistent with density fluctuations arising from particle motions along the lines of force. This fact was substantiated by measurements made in the direction of the magnetic field which showed a correlation length of at least 30 cm.

Another check that density fluctuations arise from motions along the field lines is to compute the time delayed correlation $R(\delta,\tau) \equiv \langle n(r,t)n(r+\delta,t+\tau)\rangle$. If the density fluctuations arise from a diffusive process then the radial scale length of the delayed correlation should increase with time delay (τ). From the behaviour of this scale length with τ it is possible to derive a radial diffusion coefficient. Such a procedure was carried out for the ZETA data but no significant broadening was observed. This should be contrasted with earlier measurements by Robinson [9] and later measurements to be reviewed below where broadening was observed in the magnetic fluctuations and a diffusion coefficient calculated.

In addition to measuring the density fluctuations Robinson and Rusbridge also used their Langmuir probe to measure temperature fluctuations. Results indicated that, at high pressures, the fluctuations were adiabatic whereas at low pressures a negative correlation between temperature and density was observed. To explain this negative correlation it was hypothesised that a differential heating mechanism was operative.

Attempts to detect the presence of drift waves in the outer region of the discharge using a time delayed correlation for axially separated probes were not successful although a velocity was measured of about the right value. In order to see whether the confinement properties of the ZETA discharge were explicable by the density perturbations being in phase with the electric field perturbations the correlation function between these two variables was measured at the edge of the discharge. Results indicated that this effect could explain the observed confinement time.

The final paper concerning local turbulence in ZETA [7] returns to the

high frequency (> 10 kHz) magnetic and electric fluctuations. These were again measured by insertable probes. The paper concentrates on extending the previous work on the comparison with fluid-like turbulence.

Similar results to those reviewed above were found concerning the magnetic fluctuations; notably that they possessed a correlation scale length of about 5 cm. This scale length was found to be relatively unaffected by changes in pressure or indeed virtually any equilibrium parameter. Exceptions to this were found to be that the correlation length decreased slightly either towards the edge of the discharge or as θ was increased. This indicated that the correlation length depended weakly on the shear of the magnetic field.

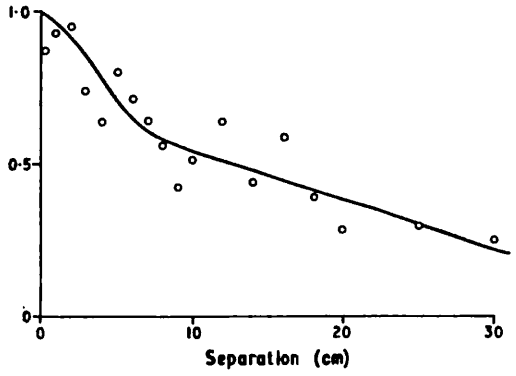

Figure 2.9

Magnetic field correlation function $\langle b_r b_r \rangle_r$ in ZETA at high θ showing large and small scale length components.

At high values of θ the correlation length was observed to increase markedly. This is shown in figure 2.9. It is clear, however, that the correlation function may be represented by two distinct scale lengths, one of about 4 cm which is consistent with the values at lower θ, and one of about 30 cm, comparable to the size of the discharge tube. Robinson and Rusbridge concluded that this phenemenon was indicative of the larger scale length motions of the lower frequencies extending to higher frequencies at larger θ.

Time delayed radial correlations were calculated to test the hypothesis that the magnetic fluctuations diffused radially outwards. Significant broadening was observed for a delayed correlation (figure 2.10) with respect to the undelayed correlation and it was thus concluded that the magnetic fluctuations did indeed diffuse radially. Note that the density fluctuations reviewed above did not share this behaviour.

There was some difficulty in measuring the correlation function in the

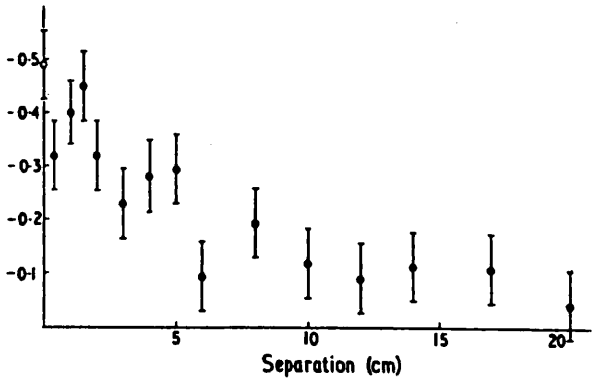

Figure 2.10
Magnetic field correlation function $\langle b_r b_r \rangle_r$ in ZETA with one signal delayed with respect to the other by 28 μs.

direction of the magnetic field. However a lower limit of 60 cm was measured which confirmed previous results (reviewed above) showing that the density fluctuations also had long parallel correlation lengths. It was thus concluded that the turbulent elements should be thought of as 'rolls' aligned along the magnetic field lines of length at least ten times their width.

Regarding the frequency dependence of the magnetic fluctuations it was shown that within the range 10-300 kHz $P(\nu) \propto \nu^{-n}$. The exponent n typically varied between 3 and 6 depending on the equilibrium pressure.

Electric fluctuations measured by a Langmuir probe were measured and a classical Ohm's law was used to predict a fluctuating fluid velocity of around 10^6 cms^{-1} in agreement with an extrapolation from doppler broadening measurements [11]. The actual correlation function appeared similar to that of the magnetic fluctuations being characterised by a correlation length of typically 5 cm. As with previous measurements reviewed above the form of the electric field correlation functions indicated that $\nabla \times \underline{e} = 0$. The frequency dependence was found to be adequately described by a power law of exponent $n = 2.8 \pm 0.3$.

Finally non-linear coupling was briefly studied by way of the triple correlation $\langle e_\theta e_\theta^2 \rangle_r$ which is a measure of the mode-mode energy transfer. A significant result is that such higher order correlations were found to exist within the statistical errors. A comparison was made between the measured triple correlation and the form of those deduced from isotropic and 2-dimensional turbulence. Results indicated that the measurements slightly favoured 2-dimensional turbulence but this was contradicted by

tentative measurements of the energy path which showed evidence of a cascade to small wavelengths, a characteristic of isotropic turbulence.

2.2.3 ZETA Quiescence

As we mentioned above, the ZETA device was not actually designed as an RFP but rather as an unreversed pinch. All the work reviewed above on the fluctuation activity was, in fact, performed in reversed conditions. However it was found that under the condition of reversed magnetic and electric toroidal fields the fluctuation activity quietened down considerably and the temperature and confinement time rose. This situation came to be known as quiescence [12,13,14,15,16] and effectively demonstrated the potential of the reversed pinch over the unreversed pinch. The requirement of a reversed electric field does not seem to apply to contemporary devices which experience quiescence simply by reversal of the toroidal magnetic field.

Unfortunately there are very little data on the structure of the fluctuations during quiescence in the ZETA machine, this being one of the major motivations for the topic of this thesis. However we will briefly review what information there is.

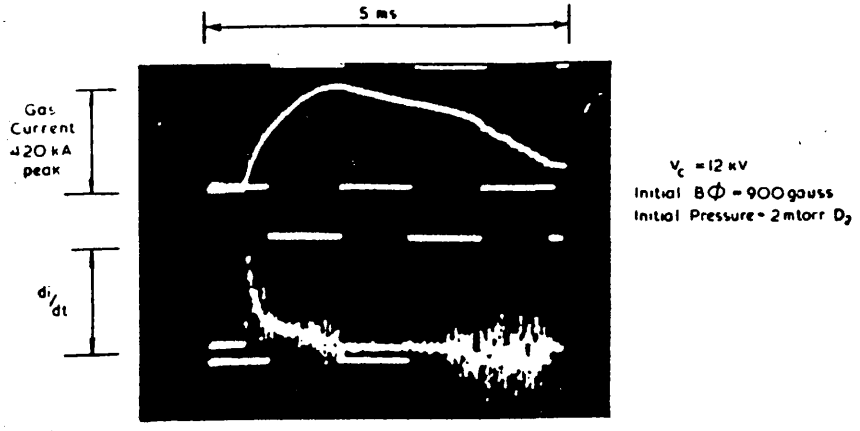

Figure 2.11 dI/dt trace from ZETA showing a marked reduction in amplitude in the quiescent period.

Figure 2.11 shows a graph of dI/dt for a typical discharge where a quiescent period is observed. Only in the middle portion of the graph are

the toroidal magnetic and electric fields reversed. It is clear that there is a significant difference between the unreversed and reversed time regions (a factor of 5-10). Semi-quiescent periods where the fluctuation reduced by 2 or 3 times were observed for small positive electric fields [16].

An important property of the quiescent condition was found to be that it was ideal MHD stable both at the edge of the discharge and near to the axis [13]. In non-quiescent conditions this was not found to be the case.

2.3 FAST PINCH EXPERIMENTS

The major results concerning fluctuations on fast pinch experiments came from the HBTXI machine at Culham, England. This device had minor radius 6 cm, major radius 100 cm, peak current of 30 - 300 kA and rise time 3 - 15 μs.

2.3.1 Observations Of The Relaxation To A Universal F-θ Curve

It had been found on the slow pinch experiments such as **ZETA** that the range of observed field configurations followed a universal F-θ curve. In 1974 Taylor [17] explained this phenomenon in terms of the relaxation to a minimum energy state (chapter 1 section 1.6.1). Experiments done on the HBTXI experiment were able to produce configurations away from this relaxed F-θ curve by programming the fields faster than the relaxation time. This allowed the experimenter to exite the relaxation mechanism at will and to study its dynamics. Studies were reported in a Culham report by Butt et al [18] in 1977 where data from FRSX, a 3.5 m linear pinch and HBTXI were analysed.

Figure 2.12 shows a diagram of the F-θ trajectory for an **FRSX** discharge where the current was sustained by a power crowbar. For reference the BFM

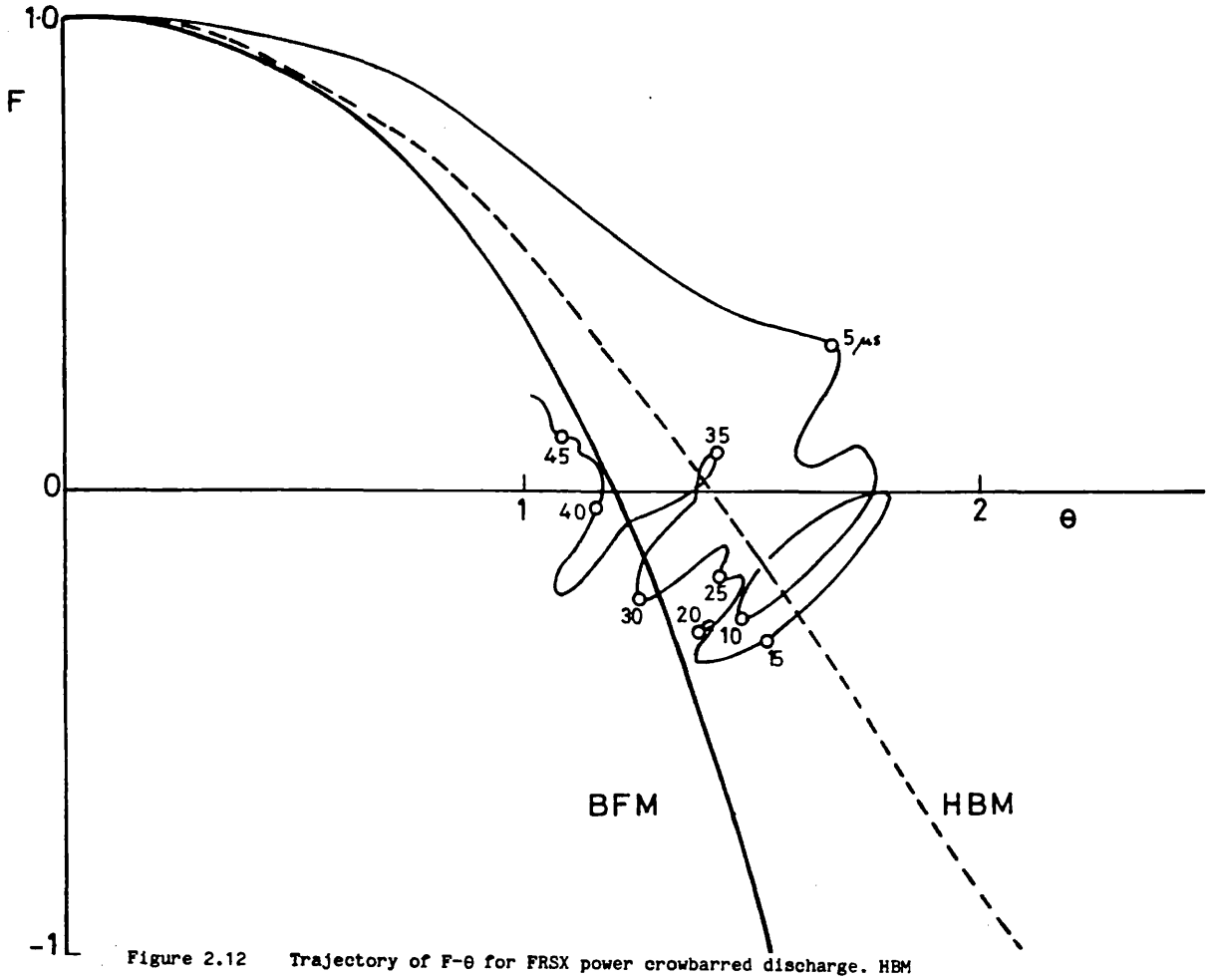

Figure 2.12 Trajectory of F-θ for FRSX power crowbarred discharge. HBM and BFM are shown for comparison.

locus and that of an inflated BFM, 'the HBM' are plotted. The configuration was programmed to the point at 5 μs. The plasma is then seen to relax by travelling back and forth roughly orthogonally to the BFM and HBM loci. These relaxation oscillations appeared to sustain the field reversal against diffusion. In order to study these oscillations further measurements were taken with a set of sine and cosine wound Rogowski coils to reveal the m = 1 activity at the plasma edge. At the onset of the discharge a toroidal drift motion outwards to 0.5 cm was clearly seen. During the growth of the self-reversal this drift was reversed and in this and subsequent phases irregular displacements of the plasma of about 0.5 cm were observed. When FRSX was operated without the power crowbar in what was termed 'overswing' mode the relaxation oscillations were not prominent and the F-θ trajectory was much smoother.

Figure 2.13 shows an example of the F—θ trajectory from HBTXI where the discharge is set up as a stabilised z-pinch (SZP). The plasma is formed by

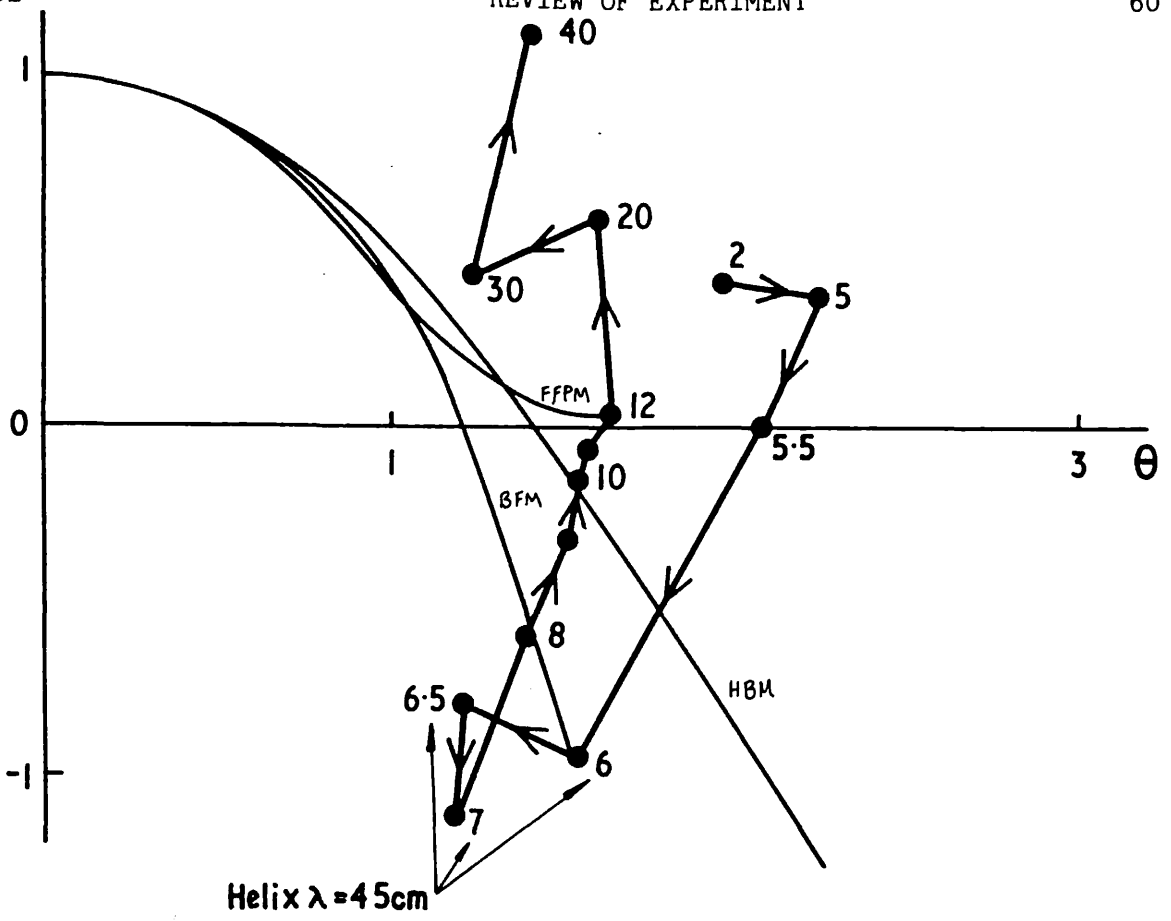

Figure 2.13 Trajectory of F-θ for HBTXI stabilised z-pinch showing rapid self-reversal and helix formation. Times are in μs. HBM, BFM and FFPM are shown for comparison.

4 μs with $\theta \approx 2.2$ and B_{zwall} positive. Then an instability occurs and the plasma relaxes within 1 μs to a helix with $\lambda \approx 45$ cm and a large self-reversal. The helix and reversal decay until 20μs when a second but weaker relaxation occurs. With differing currents a similar behaviour was observed but with different λ. After each relaxation significant m = 0 activity was observed.

Finally, to illustrate the very general nature of the relaxation process, data were analysed from a 3.5 m linear pinch. Figure 2.14 shows an F-θ curve for discharges similar to those of the FRSX device where it can be seen that similar relaxation oscillations are occurring. The fluctuations in B_{zwall} were seen to be larger in amplitude than in FRSX by a factor of 5 and were comparable to the initial equilibrium field. Investigations with search coils showed the reversal to be localised with a correlation length less than the tube diameter and to be transient in nature.

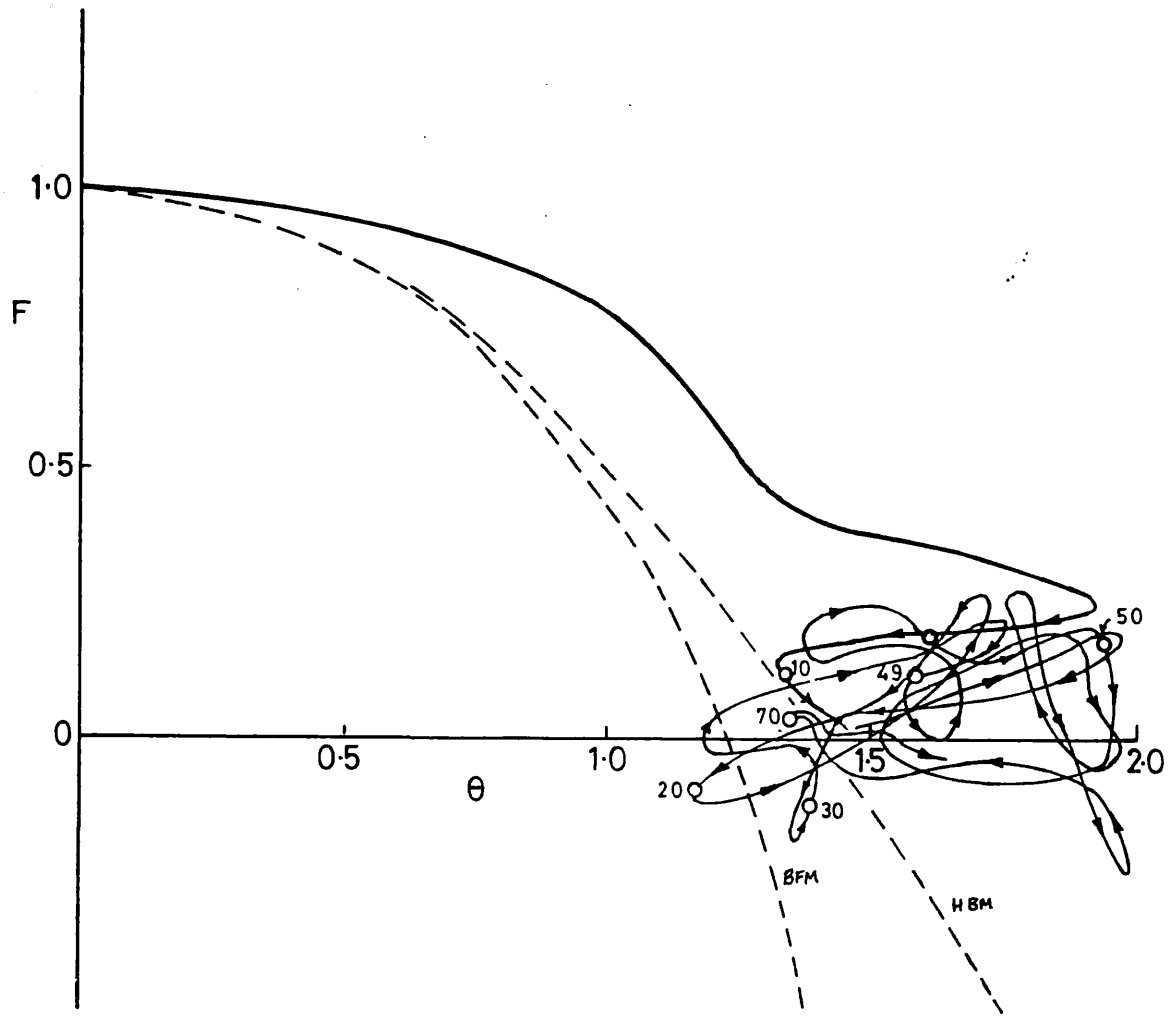

Figure 2.14 Trajectory of F-θ for the 3.5 m linear pinch. HBM and BFM are shown for comparison.

2.3.2 Large Amplitude Coherent Fluctuations in HBTXI

Results from the main fluctuation studies on the HBTXI machine were reported in a paper by Verhage, Furzer and Robinson in 1978 [19]. This paper concentrated on explaining the field-reversal observed in stabilised z-pinches in terms of MHD instabilities. Measurements were made using a poloidal array of magnetic edge coils, some edge integral coils and an insertable magnetic probe.

Verhage et al found that the appearance of field reversal was correlated to the presence of large amplitude m = 1 instabilities. This is shown in figure 2.15 where the toroidal field at the wall is plotted with signals representing the m = 1 and 2 activity. The growth and subsequent decay of such m = 1 instabilities was found to repeat several times during a typical

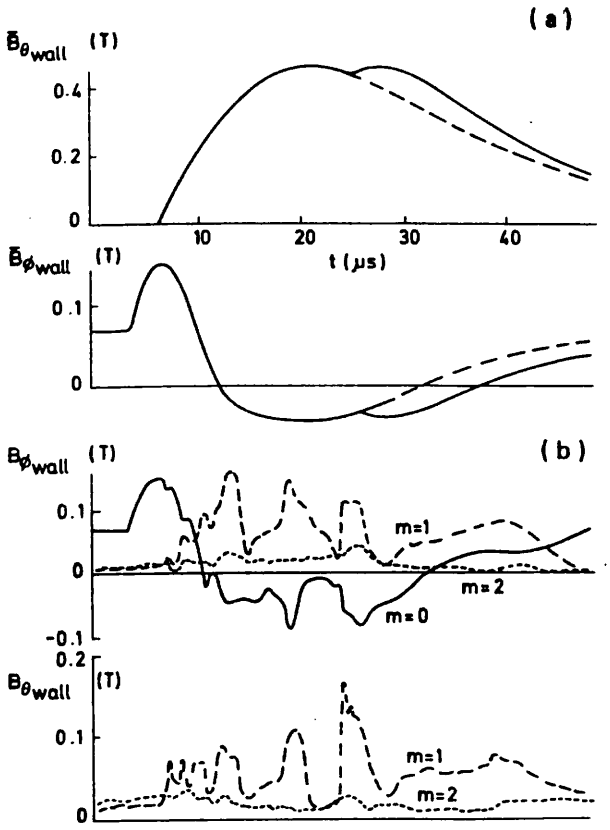

Figure 2.15

Diagram showing the correlation between the production of reversed toroidal field and m = 1 activity in HBTXI.

discharge, each time increasing the reversed field at the wall. The evolution of a typical cycle was investigated and it was found that during the initial phases of growth the dI/dt signal dropped. This was interpreted as an increase in the inductance of the plasma column corresponding to a transition from cylindrical to helical symmetry. The displacement of the plasma column was deduced during an instability from streak photographs and from sine and cosine coils. This indicated a marked outward motion during the final stages of a cycle with the plasma inevitably hitting the wall. Another effect that was observed was a systematic rotation. This was measured by plotting the phase angle between the m = 1 sine and cosine signals (figure 2.16).

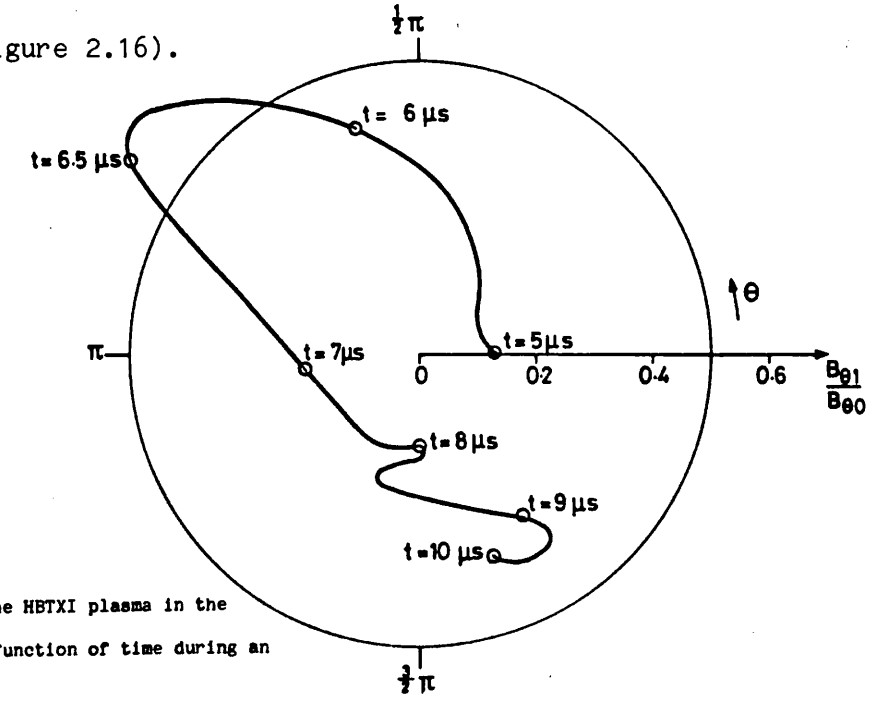

Figure 2.16

Position of the centre of the HBTXI plasma in the azimuthal plane (r,θ) as a function of time during an instability.

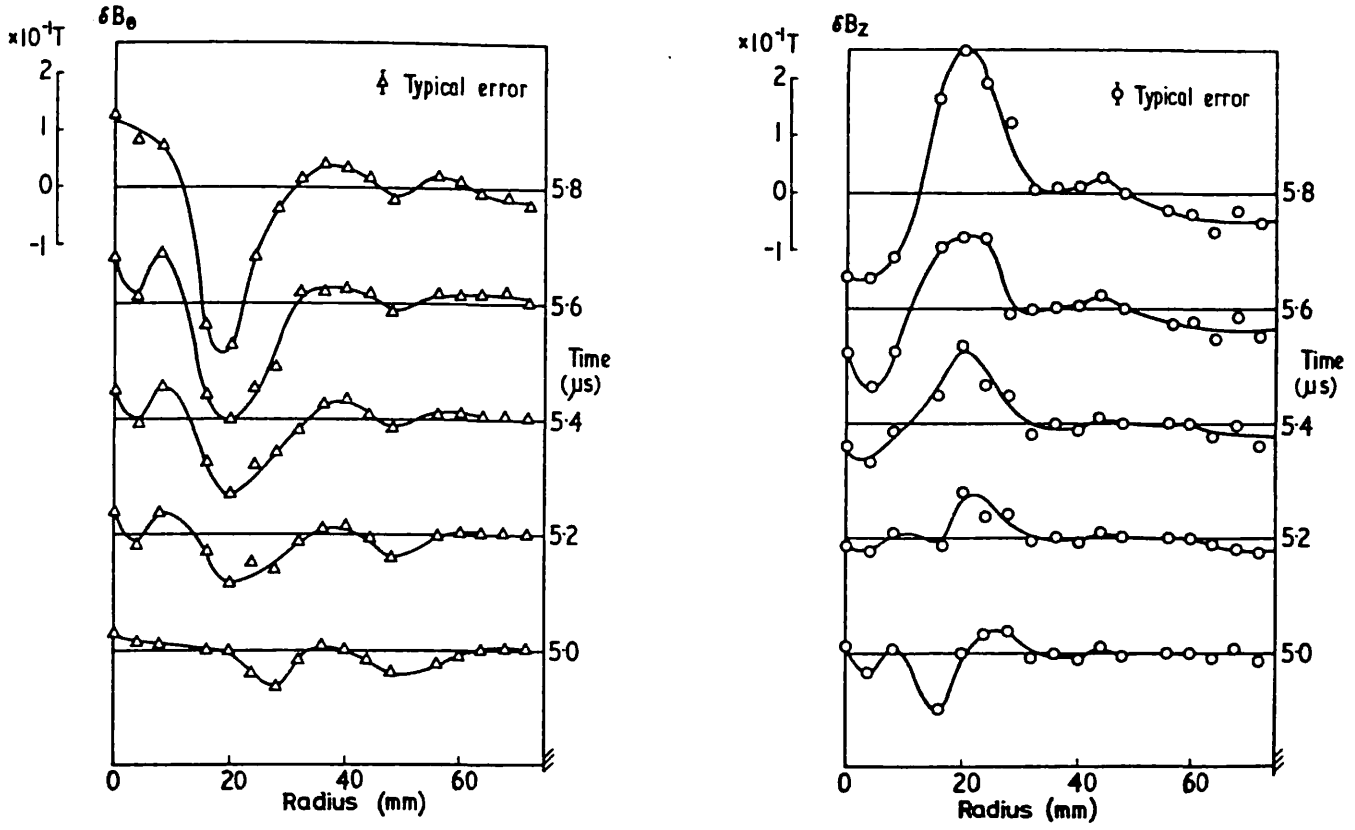

Figure 2.17 Radial dependence of the measured perturbations in B_θ and B_ϕ during the growth of an m = 1 helical instability in HBTXI.

In order to investigate the helical nature of the instabilities more thoroughly data were analysed from a poloidal array of edge coils. From such a study the poloidal fourier modes were separated and the equations $\nabla \times \underline{B} = 0$ and $\nabla . \underline{B} = 0$ were used to define the toroidal wavelengths for each m. Results indicated that the early stages of instability were entirely attributable to m = 1 and to a decreasing value of k which on average was 60 m^{-1} (this corresponds to a value of $|k|a$ of about 3.6). This m = 1 mode was found to be resonant at about r = 2 cm. By calculating the poloidal and toroidal fluxes it was shown that over a cycle of an instability the sum of the two was constant. This indicated that the helical flux was conserved.

By analysing data from an insertable magnetic probe radial distributions of the fluctuating magnetic field were obtained as a function of time. This is shown in figure 2.17 from which it was deduced that the perturbations grew exponentially with a growth time of 0.4 μs. Both the radial

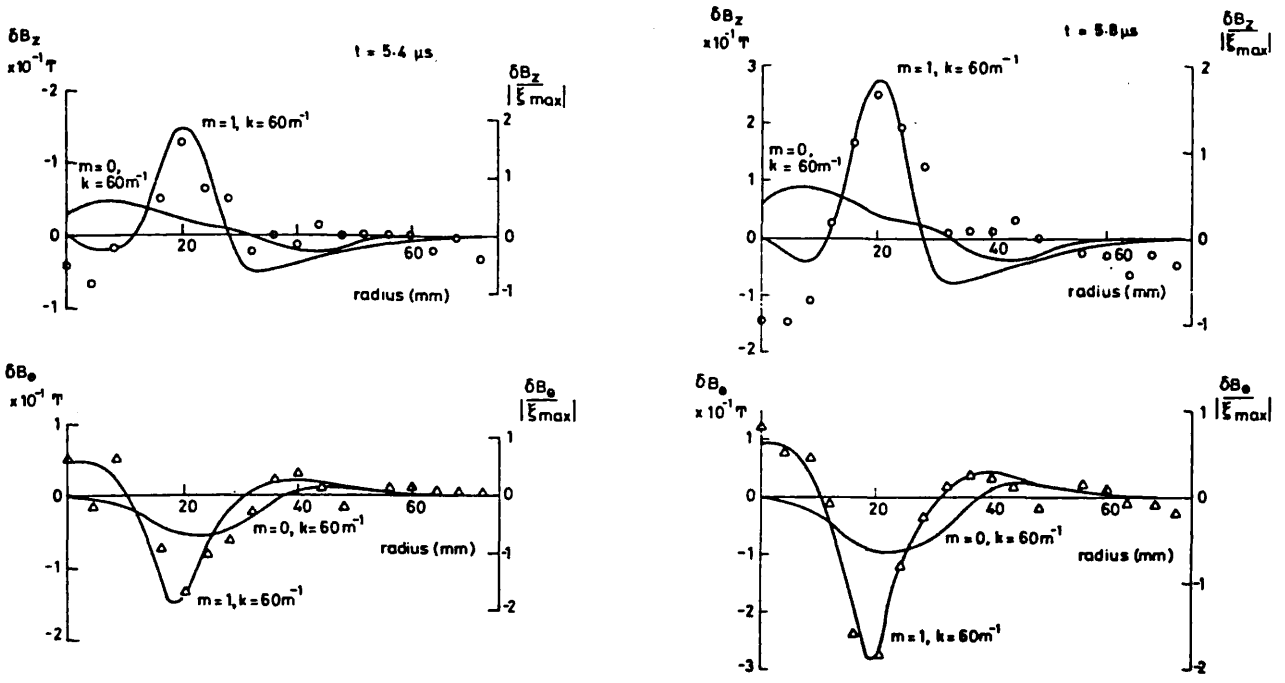

Figure 2.18 Comparison of the measured field perturbations in HBTXI with those predicted by the ideal MHD theory at two times.

dependences and this measured growth rate were compared with linear stability calculations using the measured equilibrium profiles. Results indicated that ideal MHD predicted the observed m, k and growth time provided dissipative effects were included. The field eigenfunctions for m = 1 predicted by ideal and resistive MHD showed good agreement with those measured (figure 2.18).

The interpretation of the various observations reviewed above was that an m = 1 ideal (or odd parity resistive) mode grew linearly due to the equilibrium being unstable to such a mode. The amplitude of this mode increased exponentially until it was about 30% of the mean field. At this high amplitude the linear approximation would not hold and quadratic terms in the governing dynamical equations were shown to give rise to the 'solenoidal effect' where helical currents associated with a gross kink act to increase the central axial flux. Due to flux conservation this would create a decrease and possible reversal of the axial field at the wall. Estimates of the magnitude of reversal produced by the m = 1 modes showed

very good agreement with this non-linear effect. In addition the non-linear field eigenfunctions were shown to be compatible with the probe measurements.

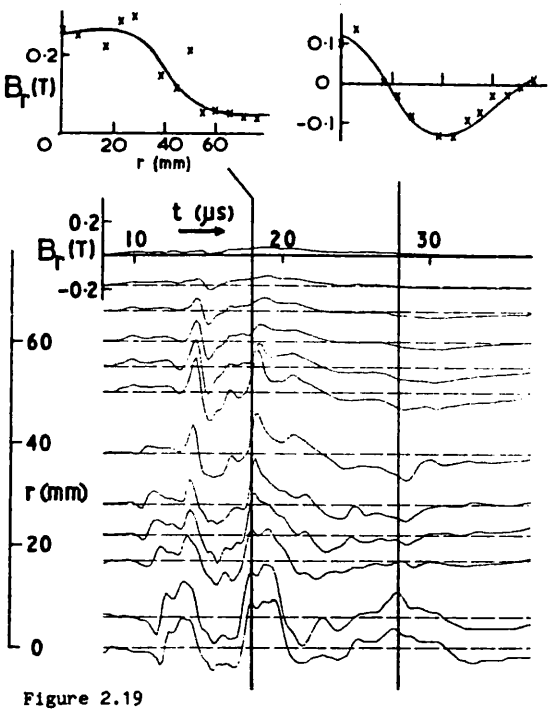

Figure 2.19

Evolution of the radial field at 12 radial positions during a sustained discharge set up by field reversal in HBTXI. The insets show the radial profile at t = 18μs and t = 28μs.

Subsequent to the paper by Verhage et al, in 1978 Carolan et al [20] reported some more fluctuation results from the HBTXI machine. The aim of these studies was to identify resistive interchange modes since before only ideal type instabilities had been observed. Measurements were again made with an insertable probe and various edge coils. In certain configurations it had been shown that the measured equilibrium field profiles were the most unstable to resistive g-modes. However these were low current discharges and the value of S was too low for the radial profiles of $\tilde{B}_r$ to be used to distinguish ideal from resistive modes. At higher currents a measured equilibrium was found which was unstable both to ideal and resistive modes and for these discharges the form of $\tilde{B}_r$ showed that a mixture of ideal and resistive modes were present. This is shown in figure 2.19 where the first inset shows a resistive type mode with even parity and the second shows a resistive mode of odd parity ($B_r(r_s) \equiv 0$).

2.4 CONTEMPORARY FLUCTUATION RESEARCH

During the past couple of years, contemporary to this thesis, there have been some interesting measurements regarding fluctuations in various slow

pinch devices. Notable contributions have been from OHTE [21], ηβ-II [22] and ZT-40 [23,24]. Results from the HBTX1A machine form the topic of this thesis and so will not be reviewed here.

In OHTE [21] results were reported from an insertable magnetic probe and various edge coils. The equilibrium and fluctuation magnetic profiles were measured (without recourse to statistical analysis). The edge coils showed that the dominant activity was m = 1. By the equation $\nabla \times \underline{\tilde{B}} = 0$ an n number of 19 was associated to this ($|k|a \approx 3$). The direction of the perturbed field at the wall showed that the mode was resonant inside the reversal surface. Stability calculations using the measured equilibrium field profiles indicated that the observed instability was predicted by the linear tearing mode theory. Figure 2.20 shows a graph of the measured fluctuating field profiles and figure 2.21 shows the calculated field eigenfunctions of the most unstable resistive tearing mode. Lastly, scaling of the measured fluctuating magnetic field was investigated and shown to be consistent with $|\underline{\tilde{B}}|/|\underline{B}| \propto S^{-1/2}$.

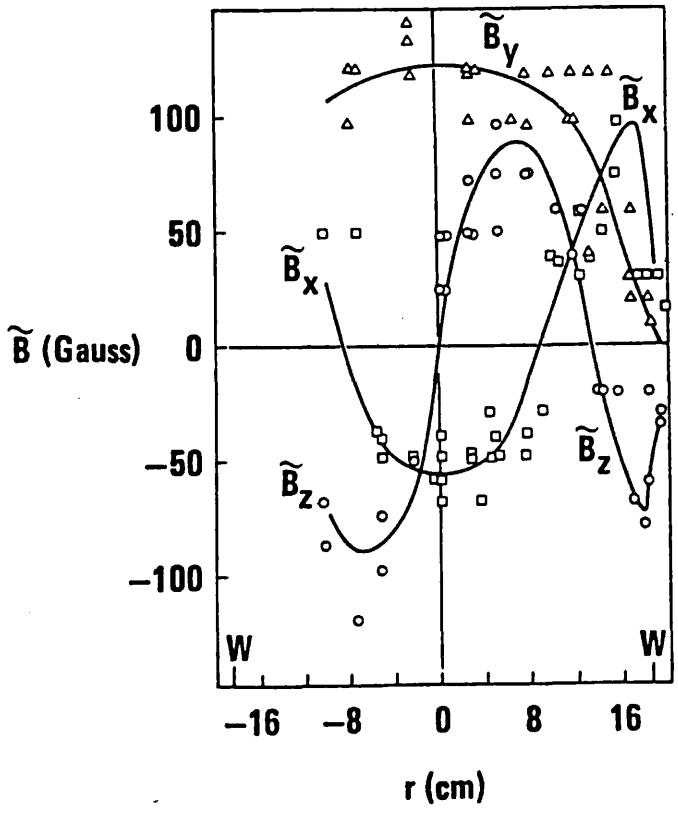

Figure 2.20 Measured profiles of the fluctuating magnetic field in OHTE.

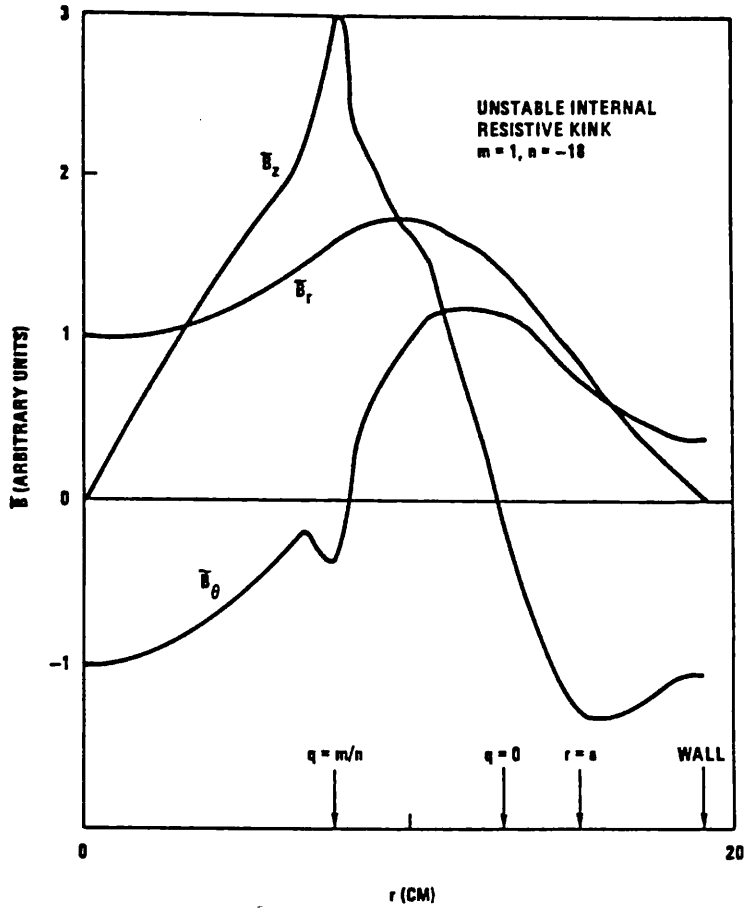

Figure 2.21 Theoretical profiles for the fluctuating magnetic field in OHTE.

Other investigations on the OHTE machine have concentrated on using the measured equilibrium magnetic fields to impose limits on the dynamo mechanism. These results are very tentative owing to the statistical errors of measurement and are also not directly connected with actual fluctuation measurements. For this reason they will not be reviewed. The same logic is applied to similar studies on the ETA-BETA-II machine.

In 1983 Antoni and Ortolani [22] reported results from an insertable magnetic probe on ηβ-II where a statistical analysis was employed similar to that used in the study of local turbulence by Robinson and Rusbridge (reviewed above). The theme of the paper was an investigation of magnetic field fluctuations as a function of density, time and radius. Measurements showed that the frequency behaviour of the fluctuations was in qualitative agreement with the ZETA behaviour, low frequencies being dominant and the power falling off with increasing frequency as about the second power.

Antoni and Ortolani studied fluctuations as a function of three

frequency bands. These were 5-15 kHz, 15-50 kHz and greater than 50 kHz. Figure 2.22 shows the correlation $\langle b_r b_r \rangle_r$ for these three frequency bands. It was deduced from this graph (and others similar) that there existed two characteristic regimes; one at low frequencies associated with long correlation lengths and one at high frequencies where activity was much more radially localised. Again this agreed qualitatively with the ZETA picture. Cross component correlations of the form $\langle b_\phi b_r \rangle_r$ were measured and these were found to be much smaller than the autocomponent correlations.

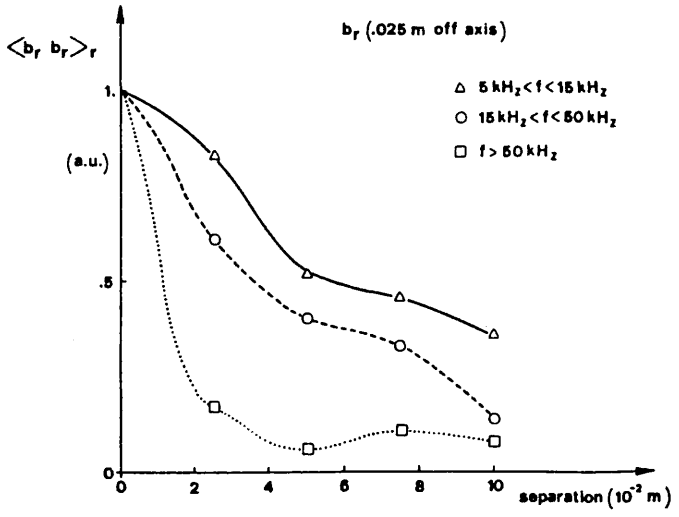

Figure 2.22 Magnetic field correlation function between the innermost insertable magnetic probe coil and the rest in ηß-II.

To investigate the temporal behaviour of the fluctuations a normalised rms level was defined. This was found to peak towards the end of a discharge and just inside the reversal surface. In addition scans over density indicated that the higher frequencies were strongly dependent on density and thus also on the streaming parameter. This was likewise found to be the case for stabilised z-pinch discharges.

For a comparison with theory the measured equilibrium field profiles were tested for linear stability to ideal and resistive modes. Results indicated that the low frequency large correlation length phenomena could be explained by the predicted m = 1 amd m = 0 instabilities. However no

detailed comparisons of the mode numbers, timescales or radial dependences were made to substantiate this. Estimates of island sizes from linear code predictions and the measured fluctuation amplitude suggested that island overlap should occcur. Stochastic diffusion estimates were in agreement with the observed energy confinement time.

Some interesting results concerning fluctuations have come from the ZT-40(M) machine in Los Alamos. This machine has the longest pulse lengths of any of the present RFPs mainly because field-errors are very small. As a result the fluctuations observed in this machine are sometimes fundamentally far more coherent than in usual RFPs, resembling, at times, Tokamak-like activity.

In 1982 Jacobson and Rusbridge reported some observations of the termination mechanism [23] concentrating on measurements from an array of interferometers and electrical diagnostics. Particularly interesting were the observations of precursor quasi-regular diamagnetic spikes and a toroidally propagating m = 0 annular density disturbance. Figure 2.23 shows the diamagnetic spikes seen on $E_{\theta wall}$. These spikes appeared only just

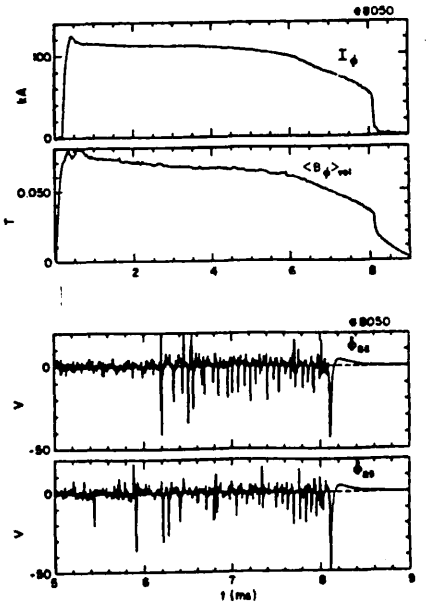

Figure 2.23 Current, toroidal field at wall and loop voltage traces in ZT-40(M) showing the occurrence of diamagnetic flux spikes just before termination.

before termination and were shown to be rotating in the $-I_\phi$ direction. The width of each spike appeared only to be about 10 μs in contrast to the more usual resistive timescale of about 100 μs.

The density disturbance appeared after a few milliseconds into the discharge and persisted thereafter, becoming more coherent and of larger amplitude at termination. By correlating the signals from an array of interferometers at one toroidal location with a single interferometer at another, it was found that the density disturbance had a good toroidal correlation length but was localised in an annular region near to the edge of the discharge. By forming similar correlations but with a time delay, a velocity of about 10^5 ms^{-1} was computed. This gave a repetition rate of about 80 μs which agreed with that obtained from the flux spikes. In fact, by cross correlating magnetic and density signals it was found that the two phenomena were phase locked such that negative voltage spikes coincided with density cavitations. This is shown for some 'raw' data in figure 2.24 where at least four narrow flux spikes can be seen to coincide with the broader troughs of the density disturbance.

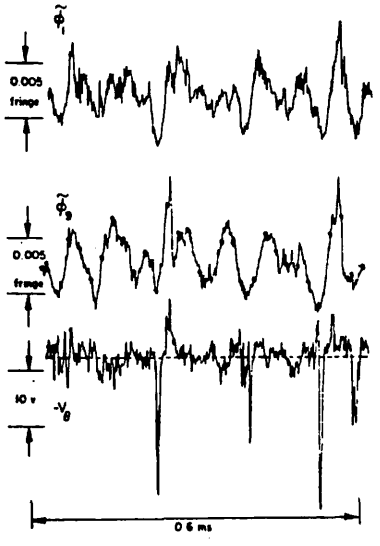

Figure 2.24

Correlation between density disturbance (top two traces) and the flux spikes (bottom) in ZT-40(M).

The correlation of the diamagnetic flux spikes with the travelling density disturbance was explained in terms of two-stream turbulence: when a density trough passes a certain toroidal location the drift parameter is increased (in the annular region) and two-stream turbulence excited causing the current to be locally suppressed and flux expelled.

To investigate the density disturbance more precisely a series of discharges were chosen where the

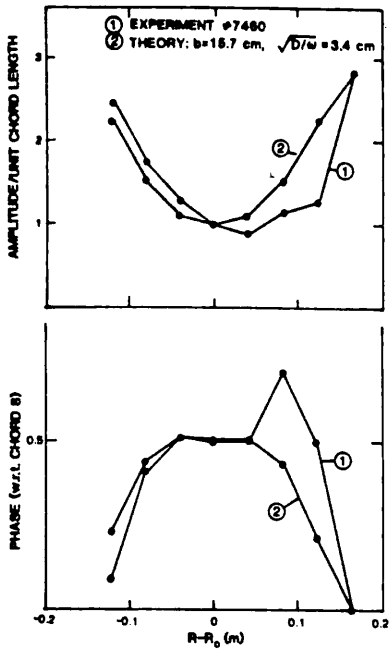

Figure 2.25
Normalised amplitude and phase of major-radial chord position (comparison of model with experiment) in ZT-40(M).

oscillation was very (temporally) coherent. The fourier amplitude and phase at the relevant frequency were then plotted. These measured profiles were compared with predictions from a diffusion model which assumed that the density fluctuations were concentrated in an annular region with a time dependence sin(ωt) and diffused out into the rest of the discharge. Figure 2.25 shows the results which yielded good agreement and predicted a particle loss rate of the same order of magnitude as the observed particle confinement time.

In addition to direct measurements of fluctuations Jacobson and Rusbridge also showed that there was significant evidence for termination being associated with a limit on I/n. This was interpreted as strong evidence that termination was directly caused by two-stream turbulence.

Another interesting publication concerning fluctuations in the ZT-40(M) RFP appeared in 1983 by Watt and Nebel [24]. Analysis concentrated mainly on high θ discharges where discrete toroidal flux increases were observable. Fluctuations were also observed in the ultrasoft X-ray flux (USXR), temperature, line density and C-V emission. Figure 2.26 shows a comparison of the USXR signal with $B_{\phi wall}$ and dB_{ϕ}/dt from which it was deduced that the USXR fluctuations were locked into the flux excursions. Similar results were reported to hold for the other measurements; notably that the density profile was flattened at the time of a flux increase and the central temperature fell. The interpretation given was similar to the mechanism for sawteeth in Tokamaks; overheating on axis would induce a corrective instability which would grow and then flatten the temperature

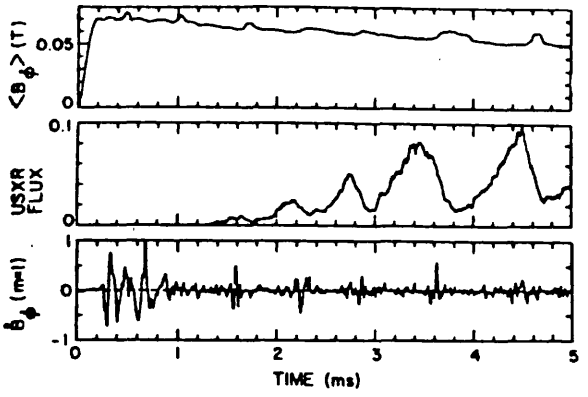

Figure 2.26

Sample waveforms showing the high degree of correlation between the USXR sawteeth and m = 1 activity at the wall in ZT-40(M).

and density profiles by a reconnection. This process appeared also to act as the 'dynamo'.

An analysis using edge coils revealed that the magnetic fluctuations during a flux spike were a combination of m = 0 and m = 1, the latter having $|n| \approx 12$ ($|k|a \approx 3$). Figure 2.27 shows a graph of the number of m = 0 and m = 1 events with respect to the time from a USXR burst. It was deduced that the m = 1 occurs before the USXR pulse and that the m = 0 pulse occurs at the same time as the USXR. This was interpreted as being consistent with 'sawtooth' explanation in that the m = 0 could be regarded as a non-linear consequence of the m = 1. This would not have been the case if the m = 0 preceeded the m = 1.

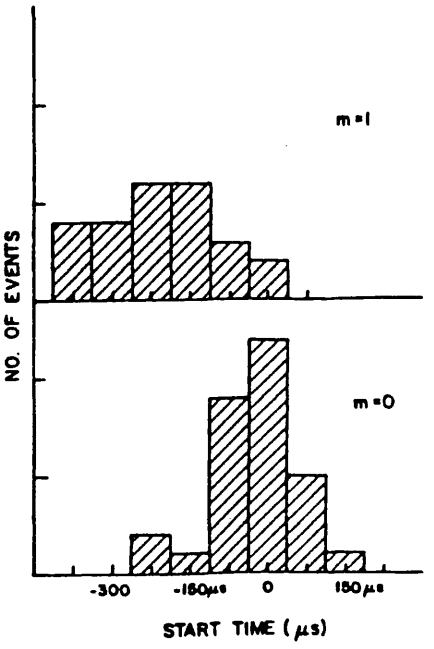

Figure 2.27 Histogram showing the time at which m = 0 and m = 1 disturbances begin relative to the initiation of a USXR sawtooth.

An analysis was carried out similar to that reviewed above to discover the variation with θ. Results showed that below $\theta = 1.5$ no m = 0

disturbances were observed. However the m = 1 modes seemed roughly independent of θ. The USXR bursts increased in repetition with decreasing θ but decreased in amplitude. These observations were interpreted as implying that the same dynamo mechanism that was suggested for high θ should apply for low θ.

A fair number of other papers concerned with fluctuation activity in present day slow pinches have been very recently published in journals or as laboratory preprints. However, since these papers really do constitute work along side this thesis or even subsequent to it, they will not be reviewed here. Notable examples are given in refs 25 and 26.

CHAPTER 3

TECHNIQUES

This thesis is about the measurement and interpretation of fluctuations in an RFP. Unlike the Tokamak, where fluctuations in the magnetic field are of a fairly deterministic nature, the RFP is characterised by the presence of random fluctuations. It is therefore not possible to use simple deterministic methods of data analysis but rather statistical forms must be applied. In addition to reviewing the HBTX1A machine and the construction and experimental techniques concerning the two diagnostics employed in this thesis, this chapter is therefore also devoted to a review of current statistical methods and to a discussion of their application and extension.

3.1 THE HBTX1A MACHINE

HBTX1A is one of five large RFPs now operating. Table 3.1 specifies the main machine parameters, figure 3.1 shows a schematic diagram and plates 3.1 to 3.3 show photographs. The plasma is contained in a stainless

TEMPERATURE	UP TO 200 eV
ELECTRON DENSITY	$10^{19} - 10^{20}$ m^{-3}
MAJOR RADIUS	0.8 m
MINOR RADIUS	0.26 m
INITIAL TOROIDAL MAGNETIC FIELD	$\leq$ 0.32 T
PLASMA TOROIDAL CURRENT	0.1 - 0.5 MA
RISE TIME OF CURRENT	0.3 - 4.5 ms
DURATION OF CURRENT	UP TO 12 ms

Table 3.1

HBTX1A parameters

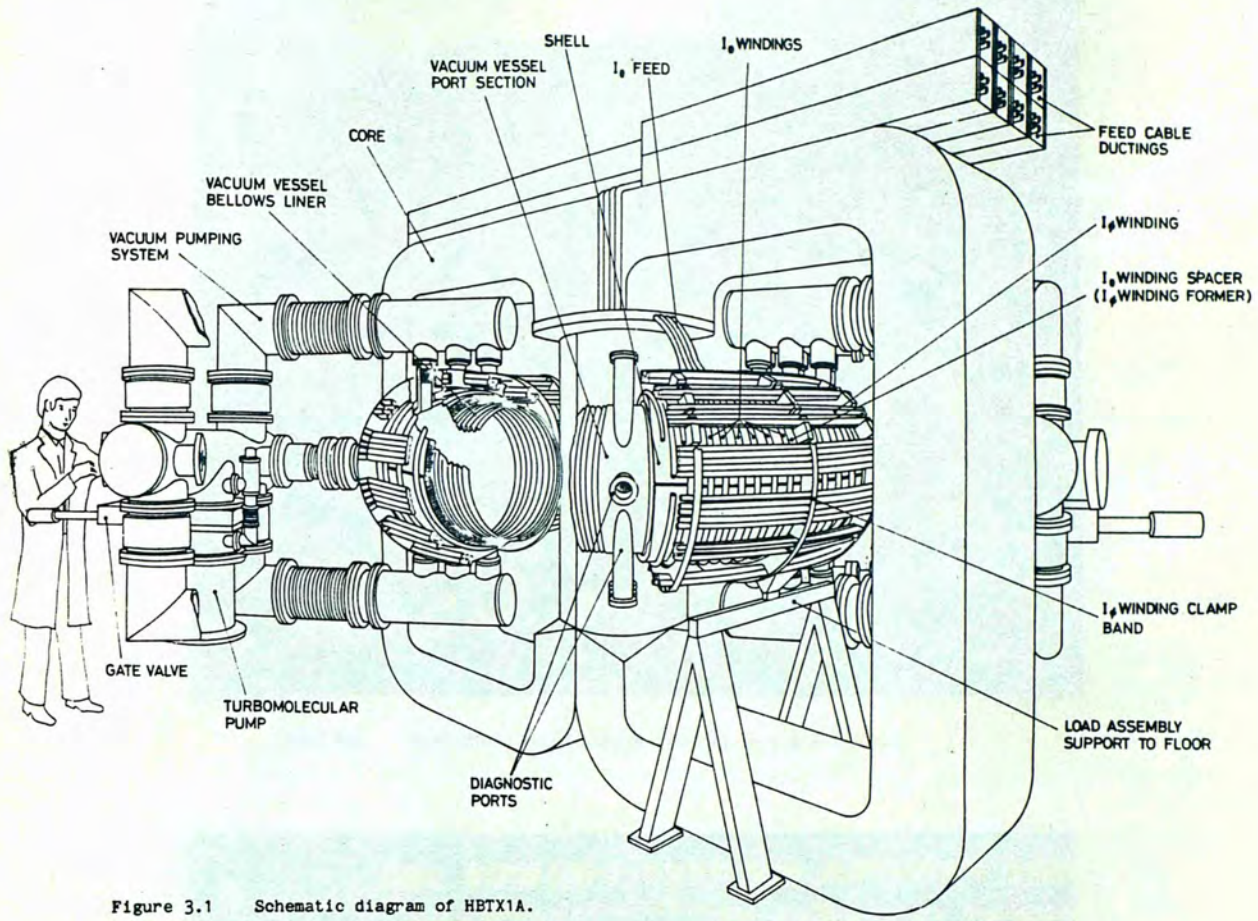

Figure 3.1 Schematic diagram of HBTX1A.

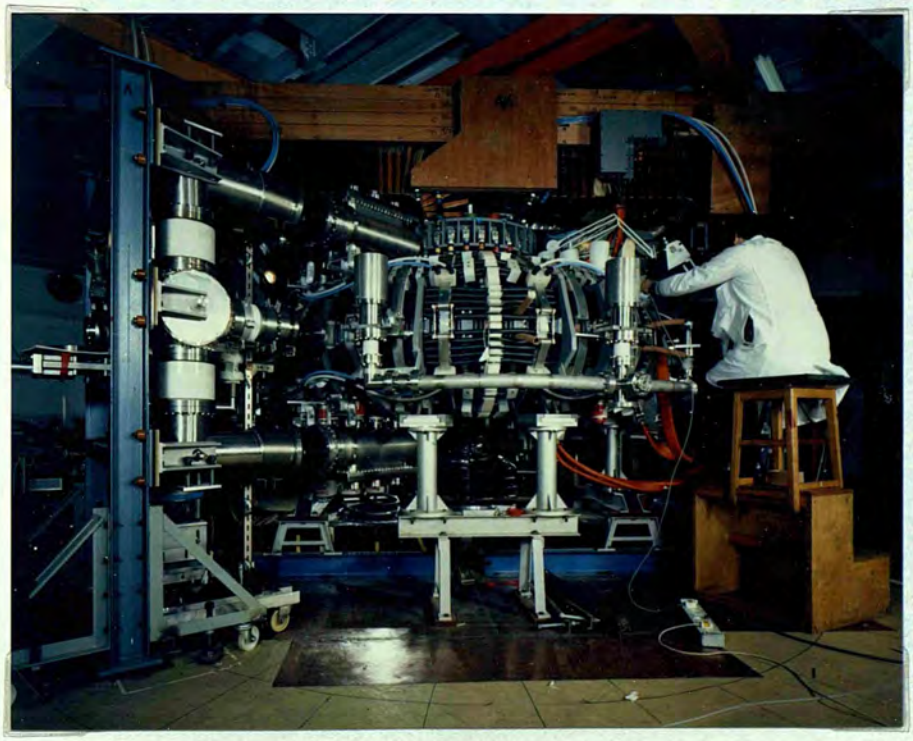

Plate 3.1 HBTX1A.

Plate 3.2 The HBTX1A torus before mounting on the iron core.

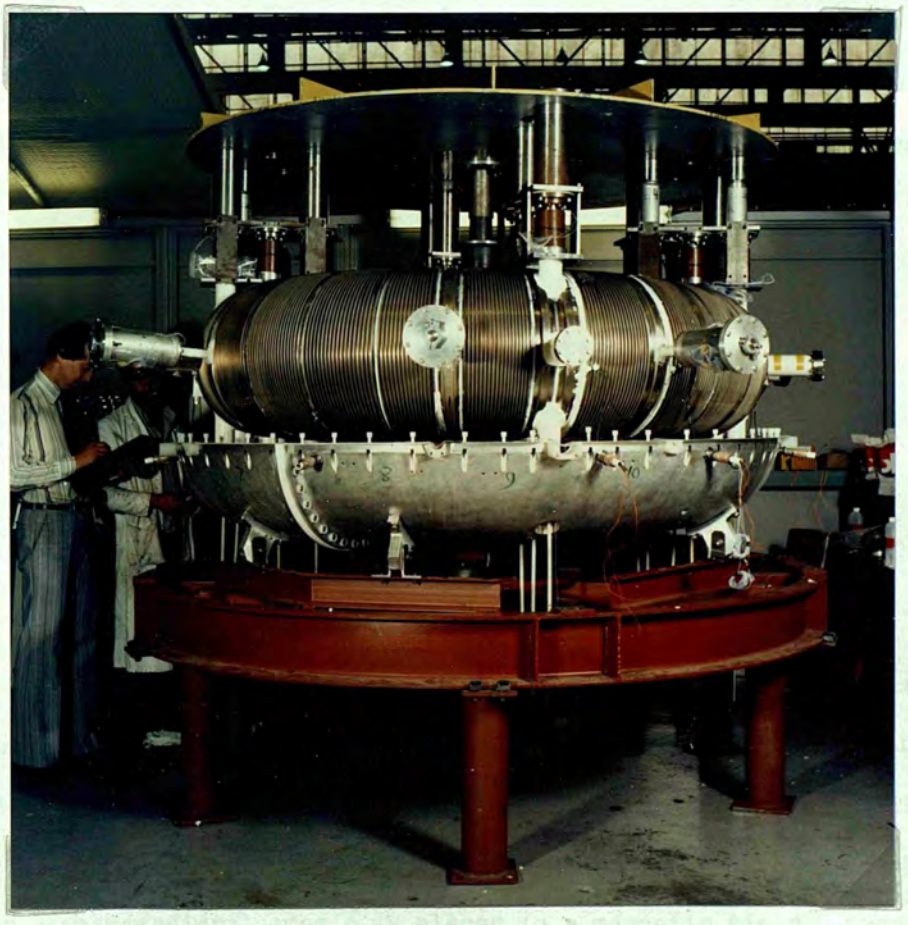

Plate 3.3 Photograph showing the HBTX1A torus disassembled to reveal the bellows vacuum liner.

steel toroidal vacuum vessel (the liner) which is surrounded by a thick aluminium shell required for the stability to MHD modes and the maintenance of plasma equilibrium. The vacuum vessel is pumped by two turbomolecular pumps to insure a UHV quality vacuum. In order to prevent plasma contact with the liner a band of graphite limiters dictates the plasma radius.

The two sets of windings on the machine are both made from standard cable. The I_θ windings for the toroidal field are closest to the shell to minimise stray inductance. Outside these are the I_ϕ windings which induce the toroidal plasma current; these are set on a displaced circle to reduce magnetic field errors at the insulated shell-gap (this allows penetration of the toroidal flux). The I_ϕ windings are coupled to the plasma by a 1 Vs iron core.

Capacitor banks located on the two floors above the experimental area are used to drive the I_θ and I_ϕ currents in the windings. The full value of current can be reached in less than a millisecond using 40 kV banks and then may either be maintained by an 8 kV power crowbar or by a passive clamp. The total energy available is 2 MJ.

3.2 EXPERIMENTAL TECHNIQUES

3.2.1 The Insertable probe

3.2.1.1 Introduction

An insertable magnetic probe is a device which will measure the rate of change of magnetic field as a function of both radius and time inside a plasma discharge. Usually it will consist of one or more very small coils mounted inside a protective silica-glass tube. In general, if a coil of n turns and cross-sectional area A is placed in a magnetic field B parallel to the coil axis, the induced electromotive force V is given by:

$$V = -nA \frac{dB}{dt} \quad . \qquad - (3.1)$$

Thus, according to the orientation of a given coil within the plasma discharge it is possible to obtain information about any component of the magnetic field. In general, insertable probes are really the only diagnostic that can provide detailed measurements of the internal magnetic structure. This is particularly true for the RFP where Faraday rotation effects [1] have not yet been used successfully. However probes have one serious drawback in that their insertion can lead to appreciable disturbance of the discharge. When this happens serious doubt must be cast on the relevance of the measurements since the internal structure of a seriously perturbed discharge may bear no resemblance to that of an unperturbed discharge. The aim is thus to make probes as small as possible to minimise their effect on the plasma. However, if one wants to keep a reasonable number of coils this becomes rapidly very difficult. In the end a compromise is sought where a certain amount of perturbation to the discharge is tolerated, but allowing a useful number of coils to be included. As will be seen later, the probe used in this study actually affects the discharge only very slightly and yet contains a very useful number of coils, thus permitting a detailed analysis of both the equilibrium and fluctuation magnetic structure of the plasma.

3.2.1.2 Construction

The magnetic probe used in this study is illustrated in figure 3.2 and in the photographs of plates 3.4 and 3.5. In all there are twenty-seven coils divided into nine sets of three. Each set of three comprises a radial, toroidal and poloidal coil thus defining the time varying magnetic field in nine equally spaced radial positions. The coils consist of 42 swg enamelled copper wire wound on alumina ceramic formers at fifty turns each, the mean coil radius being just over 1 mm. Each coil is set into a PTFE rod 33.5 cm

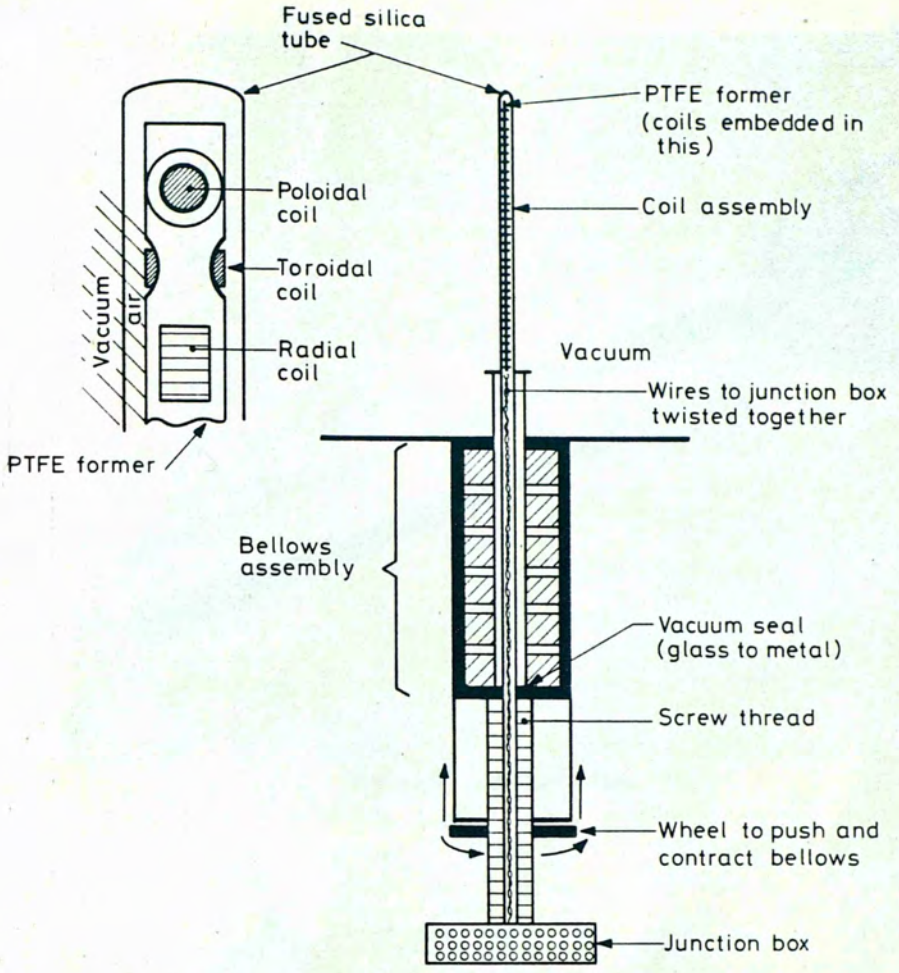

NOT TO SCALE

Figure 3.2 Schematic illustration of the insertable magnetic probe.

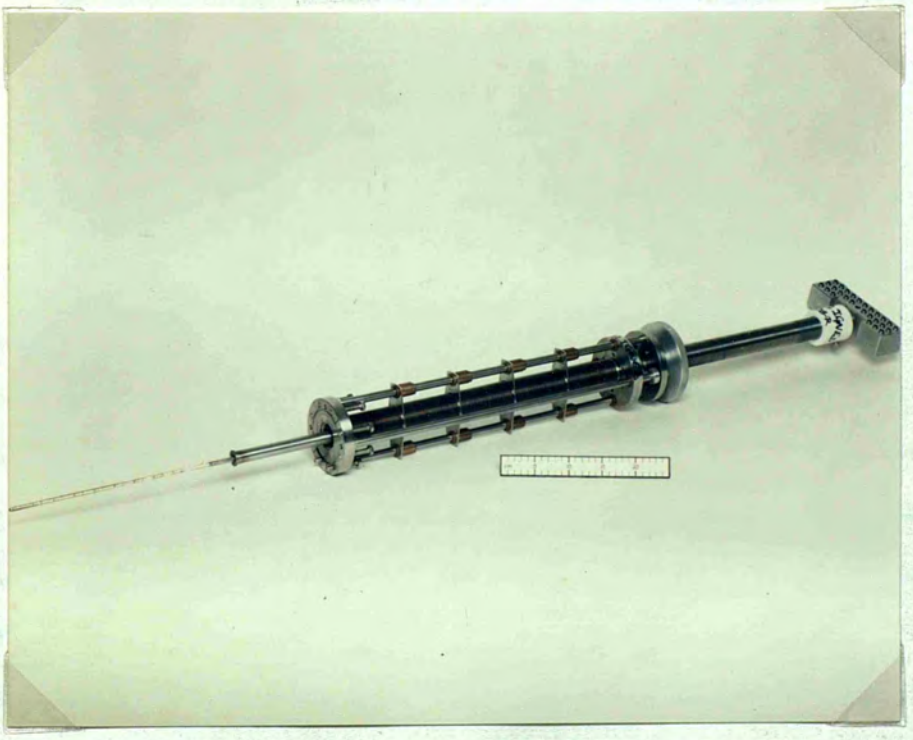

Plate 3.4 Photograph of the insertable magnetic probe.

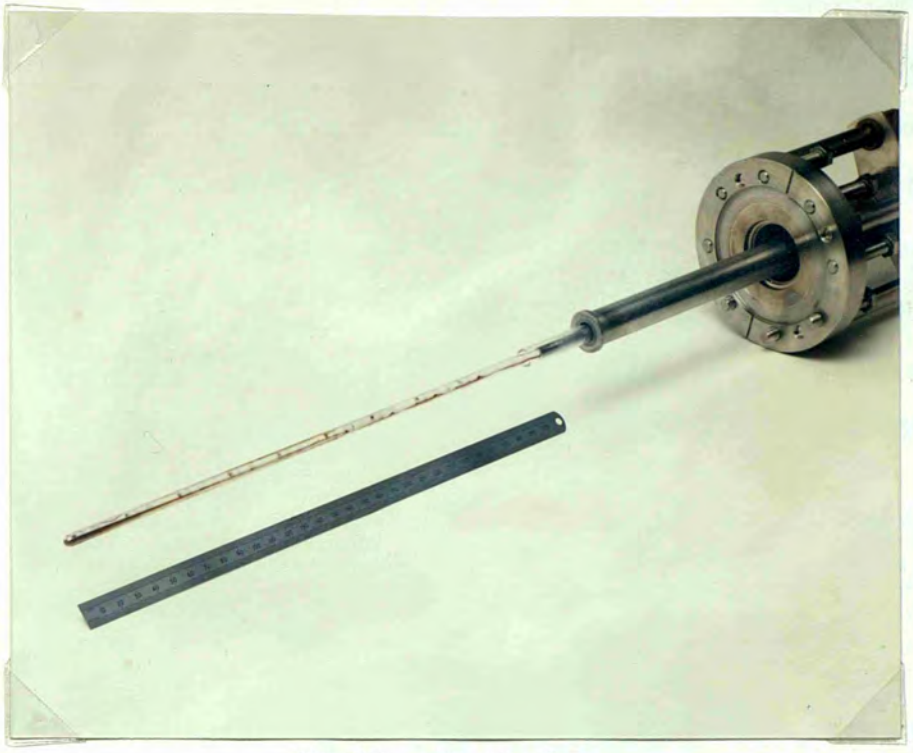

Plate 3.5 The probe tip.

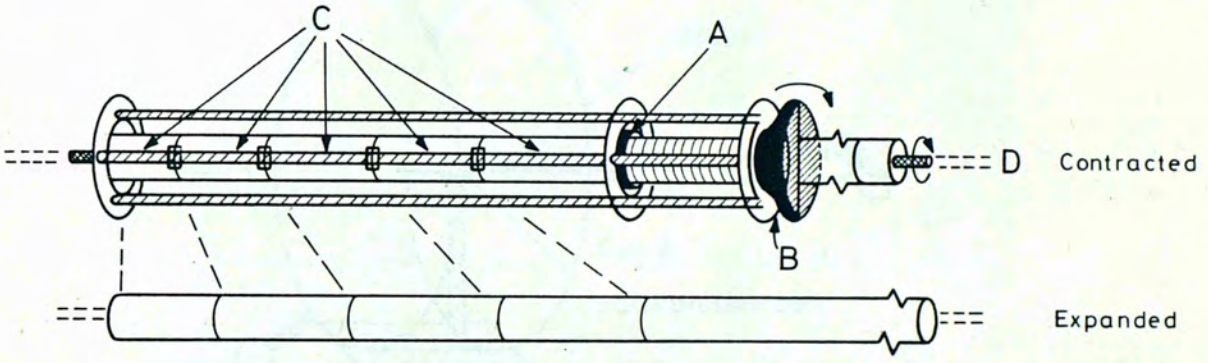

Figure 3.3 The probe bellows assembly.

long, machined with grooves along its length to allow for the passage of connecting wires. The inset of figure 3.2 shows the details of this assembly which is then inserted into a protective silica glass tube. This tube connects through a metal-to-glass seal to a bellows assembly which enables the probe to be inserted or retracted from the discharge vessel. Figure 3.3 details this assembly. Point A locates the metal-to-glass seal. By turning the wheel B, the bellows C expand and push the point A, together

with the entire coil assembly, into the discharge vessel. By turning this wheel from one extreme to the other, a coil-assembly movement of twenty-seven cm is obtained. Hence, in the retracted position, the probe does not penetrate the plasma at all whereas, in the other extreme, the tip of the probe extends all the way to the minor axis of the torus. In order to achieve the correct orientations of the toroidal and poloidal coils the junction box D in figure 3.3 is designed to turn, producing a rotation of the coil assembly inside the fused-silica tube.

3.2.1.3 Calibration

In order to calibrate the probe a Helmholtz coil assembly [2] was used. This is shown in figure 3.4. By driving this coil with a 300 Watt audio oscillator and comparing the output of the probe coils, situated in the

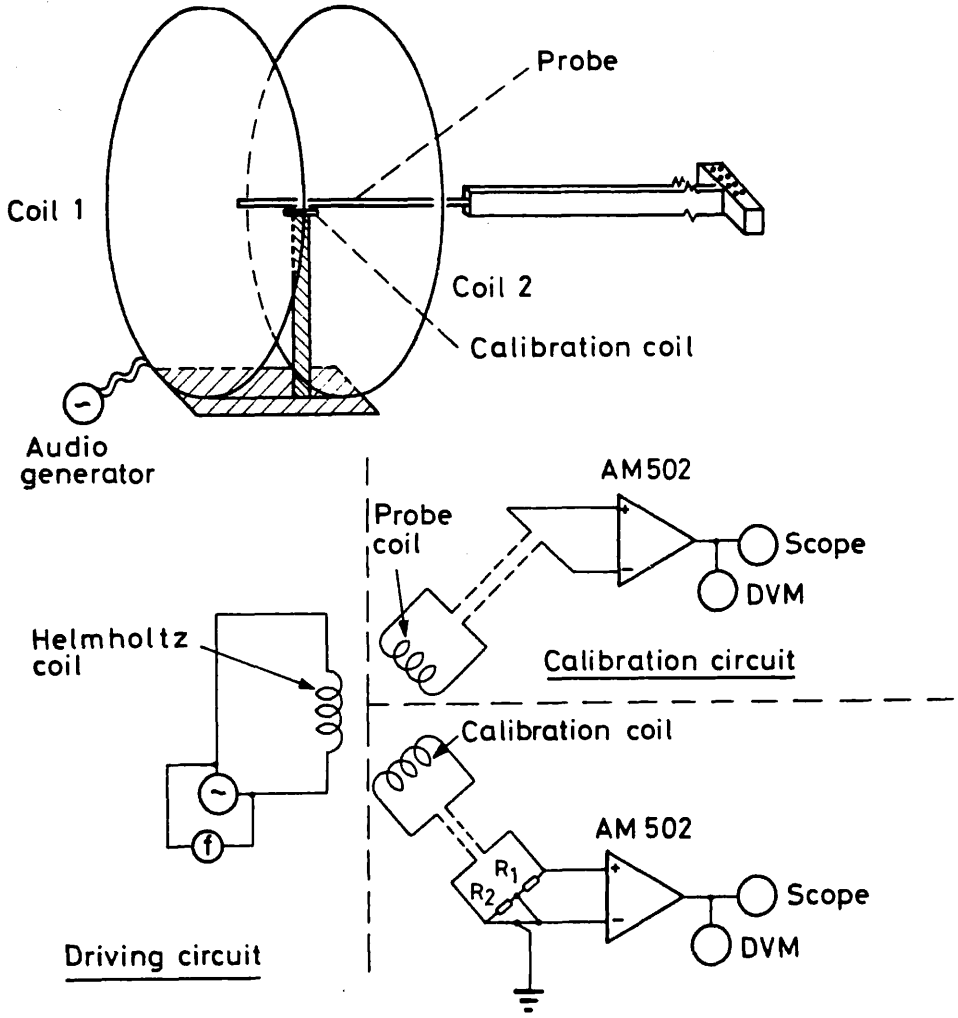

Figure 3.4 Calibration set-up for the probe

region of greatest field uniformity, with a calibration coil of known cross-sectional area and turns, we were able to calibrate the probe coils to an accuracy of better than 98%. Estimates as to the alignment accuracy of the various coils showed a standard error of ±1 degree.

By mounting a small coil on the silica glass envelope of the probe and by energising it with a high frequency oscillator we were able to calculate the frequency dependence of the probe coils. This is shown in figure 3.5 where it can clearly be seen that the coils have a fairly flat frequency response up to at least 1 MHz.

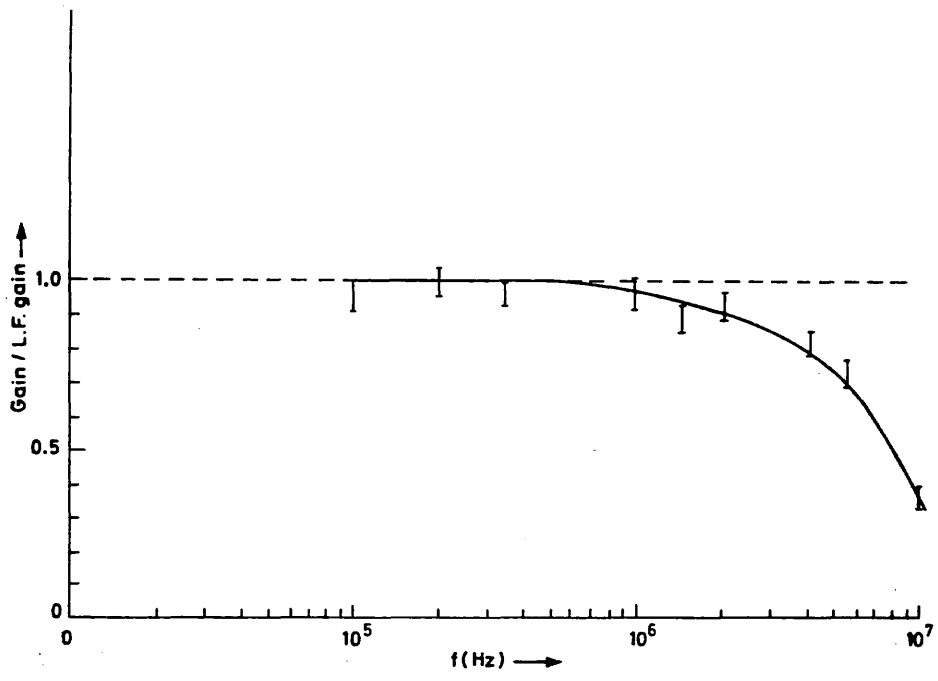

Figure 3.5 Frequency response for a typical probe coil.

3.2.2 EDGE COILS

Edge coils, as their name implies, are small coils mounted at the edge of the discharge vessel. HBTX1A, in its present form, possesses several hundred of these coils mostly grouped together into poloidal arrays encircling a minor cross-section of the torus. In addition to these poloidal arrays, HBTX1A also posseses a unique toroidal array spanning some sixty degrees around the length of the torus.

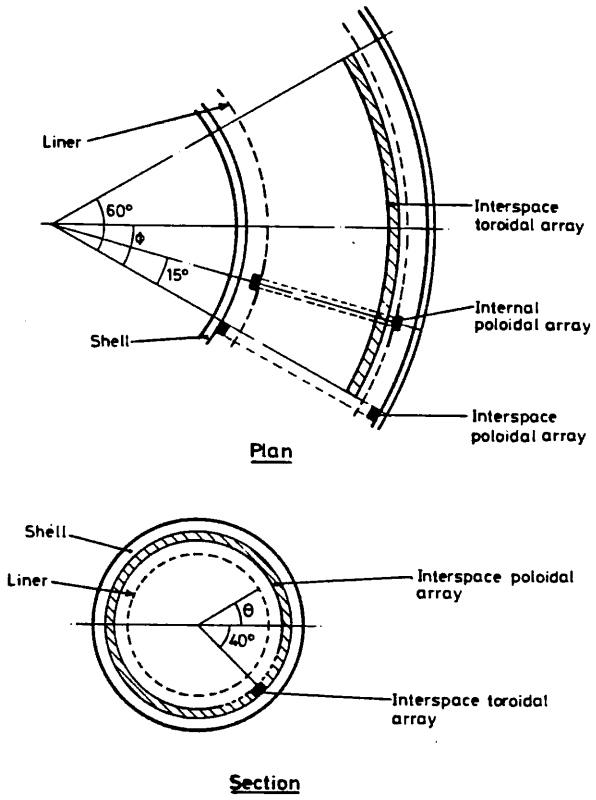

Figure 3.6 Edge-coil layout.

The magnetic coils used in this study consist primarily of three sets illustrated in figure 3.6. Outside the vacuum liner, in the 'interspace' between the liner and the conducting shell we use a poloidal array of coils measuring the toroidal and poloidal components of the field (B_ϕ,B_θ) at sixteen poloidal angles (θ). In addition, adjacent to this poloidal array, is the toroidal array which measures B_ϕ and B_θ at fourteen toroidal positions. This array is at a poloidal angle of -40 degrees. Inside the vacuum vessel are poloidal arrays similar to the interspace array but with the coils recessed into special sections of the bellows liner. These internal coils are more sensitive to higher frequency fluctuations because they do not require the fields to penetrate the liner.

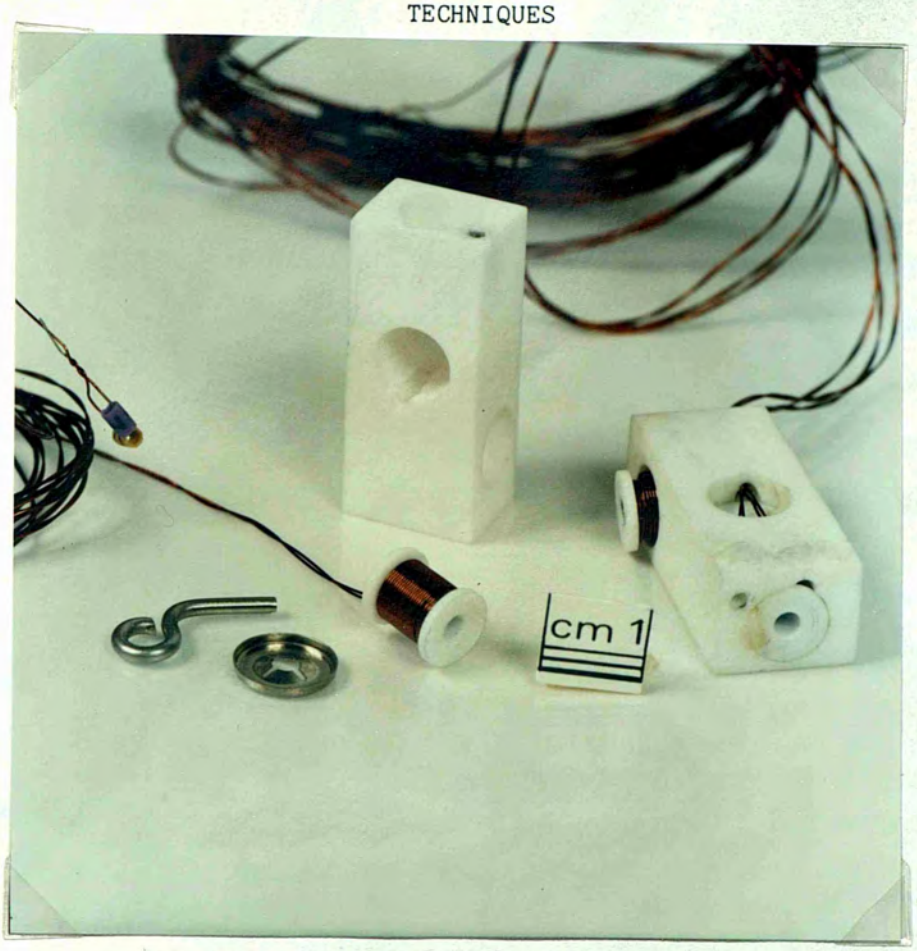

Plate 3.6 Individual edge coils and their mounts.

Plate 3.7 Photograph showing a poloidal array of edge coils. The curved metal band into which the coil formers are fixed fits into the inside of the bellows liner.

3.2.3 DATA ACQUISITION

The problem of acquiring data from diagnostics on a plasma discharge experiment is not trivial. The signals produced by a diagnostic may be very weak and these have to be detected in the presence of large rapidly varying magnetic fields. Consequently, much attention must be paid to screening and the proper matching of transmission cables to the loads presented by both the diagnostic and the electronic receivers.

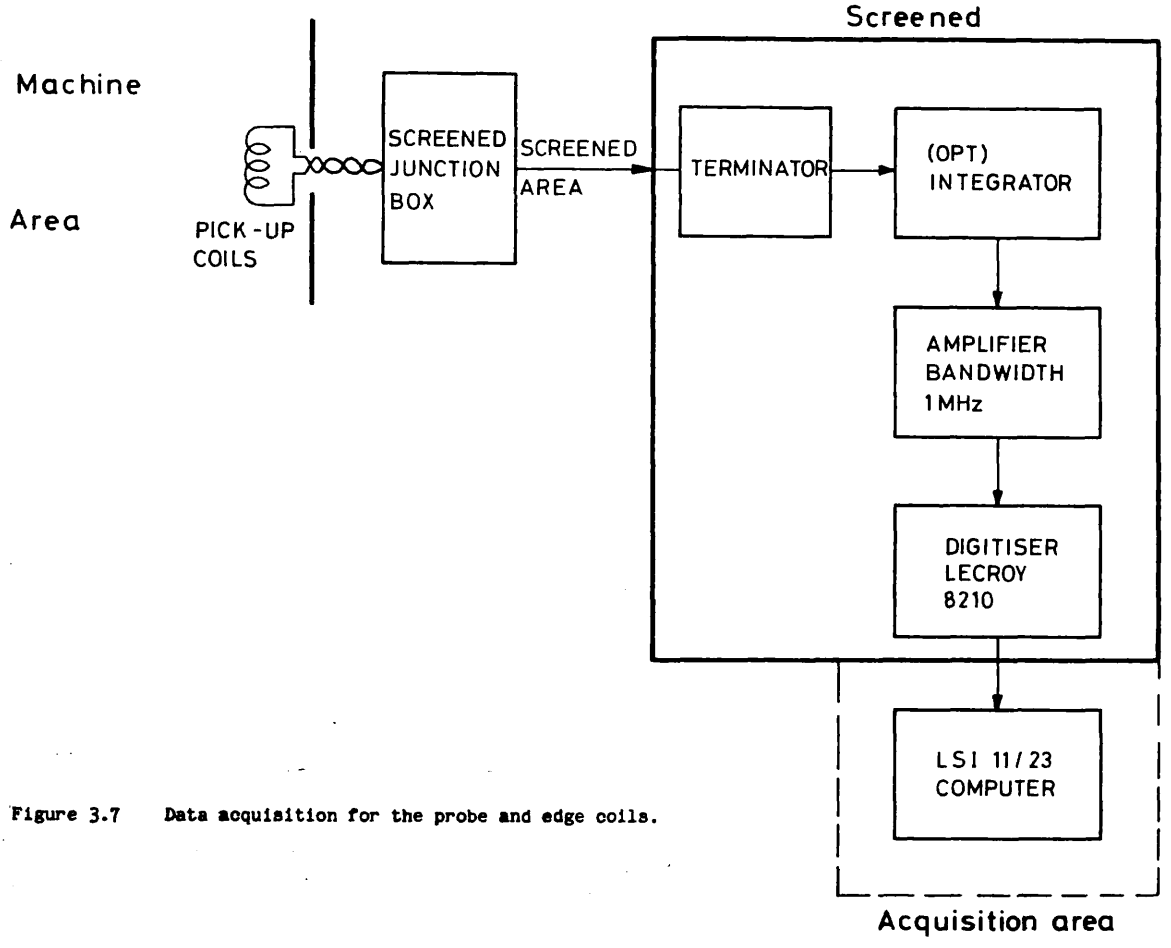

Figure 3.7 **Data acquisition for the probe and edge coils.**

The basic theme of data acquisition used for both edge coils and the insertable probe is depicted in figure 3.7. For each coil on the machine a twisted pair of wires connects to a screened junction box whose outer casing is earthed. From here every coil is connected to the outside world via a double core screened cable. To be effective the screening must be connected to the outer case of the junction box. The other end of each of these cables connects to an earthed metal box in which is contained the electronic

acquisition equipment. Each channel is fed into a differential amplifier which amplifies the signal between the two cores of cable, disregarding the common mode. The amplified signal is then either fed directly into a 10 bit analogue-to-digital converter or first into an analogue integrator with a 470 μs time constant.

When acquiring data from the insertable probe or from the internal poloidal arrays, both of which might, in fault conditions, connect to the plasma, we use shielded electronics in the vicinity of the machine to encode the signals onto fibre-optic transmission lines which may be fed out of the machine area with no danger of carrying high voltages. When using the interspace coils, however, no such precaution is needed and cables are run directly from the diagnostics to the acquisition area. In all cases the signals are digitised at a sampling rate of typically 2 μs for a period of 2 to 4 ms and encoded on RL01 digital equipment discs using LSI11/23 computers.

3.3 THEORETICAL TECHNIQUES

3.3.1 Correlation And Spectral Analysis

3.3.1.1 Introduction

Physical phenomena may be broadly divided into two classes; deterministic and random. Deterministic phenomena follow unique mathematical laws which describe their behaviour. As an example we may consider the motion of a simple pendulum. When the bob is raised to a certain height and then released, the pendulum oscillates. If we plot the amplitude of oscillation against time we obtain a graph describing the trajectory of the pendulum in phase space. If we were to repeat this experiment again, we would obtain exactly the same graph. In fact no matter where we performed the experiment (on the earth) and at what time, we would always get the same answer. This is a deterministic system. In contrast to this there are many systems where the same initial conditions do not lead to exactly the same behaviour. Such processes are termed random [3,4,5] and typify the class of fluctuating phenomena inherent to the RFP.

In order to investigate random processes we cannot simply apply the normal deterministic methods. Rather statistical quantities must be used to reveal the information contained within the data. A simple example would be the calculation of the mean value of wind velocity at a certain place and time of year calculated from many measurements made year after year (an ensemble). This quantity, which may be different from year to year, will allow a prediction of what on average the wind velocity at this location is. If this particular problem was tackled from the deterministic point of view, every time the wind velocity was measured a different value would be obtained. So the answer would depend on when the measurement was taken and would thus essentially contain no useful information.

3.3.1.2 Stationary And Ergodic Processes

The philosophy of random data analysis [3,4,5] is to describe the random process in terms of statistical quantities. The simplest example of such a quantity, as we have already discussed, is the mean value. This is defined for a random process {x(t)} as:

$$\bar{x}(t) = \lim_{N\to\infty} \frac{1}{N} \sum_{i=1}^{N} {}^{i}x(t) \quad , \qquad - (3.2)$$

where the index i sums over the members of an ensemble. In an exactly similar fashion we may define the mean square value, (which is defined for zero-mean processes as):

$$\sigma^2(t) = \lim_{N\to\infty} \frac{1}{N} \sum_{i=1}^{N} ({}^{i}x(t))^2 \quad , \qquad - (3.3)$$

and a quantity known as the autocorrelation at time delay, τ:

$$R_{xx}(t,\tau) = \lim_{N\to\infty} \frac{1}{N} \sum_{i=1}^{N} {}^{i}x(t)\,{}^{i}x(t+\tau). \qquad - (3.4)$$

All of these quantities are known as statistical moments of the random process {x(t)}. We may define any number of higher order moments in exactly the same fashion by simply including higher powers of x and different time delay parameters. In principle, a knowledge of all the moments of a given process will define the probability distribution function characteristic of that process.

If one or more of the moments defined in equations 3.2 to 3.4, or indeed a higher order moment, varies with time then the data is said to be nonstationary with respect to that moment. If, on the other hand, the

moments of interest are not functions of time, then the data is said to be stationary and in most cases the sums over an ensemble in equations 3.2 to 3.4 may be replaced by time averages:

$$\bar{x} = \lim_{T\to\infty} \frac{1}{T} \int_0^T x(t)dt \qquad - (3.5)$$

$$\sigma^2 = \lim_{T\to\infty} \frac{1}{T} \int_0^T x^2(t)dt \qquad - (3.6)$$

$$R_{xx}(\tau) = \lim_{T\to\infty} \frac{1}{T} \int_0^T x(t)x(t+\tau)dt \; . \qquad - (3.7)$$

In such cases the observed process is termed ergodic. This result, known as the ergodic theorem, is a very powerful tool, since in very many cases time histories of a given process are far more easily obtained than large ensembles.

3.3.1.3 Correlation Functions

In the previous section we introduced the time delayed autocorrelation function R_{xx} as an example of a statistical moment. This function, which will appear many times in this thesis, essentially tells you how 'linearly similar' a given process is at one time compared to a fixed time later. Hence if the time delayed autocorrelation function defined in equation 3.7 had the form of a gaussian of some suitably defined width W, then we would be able to infer that events happening at a time greater than (t+W) would be linearly independent of events happening at the time t. A useful qualitative way of understanding the implication of this is to think of the process having a finite (linear) memory. Events happening at a time greater than (t+W) have no memory of events happening at the time t or less. Hence

they behave linearly independent of these earlier events. On the other hand, if two events are separated by a time smaller than W, then the later event will have a memory of the prior event and will not be linearly independent.

Many situations arise in the study of random phenomena in which two measured time histories are required to be compared and a relationship established between them. In many cases this may have to be done in the presence of large amounts of uncorrelated noise. This may be formalised for a simple case by considering two random processes {x(t)} and {y(t)} and hypothesising that x(t) may be expressed as $\alpha y(t)+z(t)$, where z(t) and y(t) are linearly uncorrelated. The problem is now to find the constant α. By extending the definition of equation 3.7 it is easily seen that α is given by the following relation:

$$\alpha = \lim_{T\to\infty} \frac{1}{T} \int_0^T x(t)y(t)dt \quad / \quad \frac{1}{T} \int_0^T y^2(t)dt \ . \qquad - (3.8)$$

The numerator in this expression is termed the <u>cross-correlation</u> function at zero time delay between the processes {x(t)} and {y(t)}. A generalisation of this is the time delayed cross-correlation function defined (for ergodic processes) as:

$$R_{xy(\tau)} = \lim_{T\to\infty} \frac{1}{T} \int_0^T x(t)y(t+\tau)dt. \qquad - (3.9)$$

To see how this function arises we may consider the following rather deterministic problem. Suppose we have two closely spaced detectors measuring the level of water in a pond. Suppose further that a stone is dropped into the water near one of the detectors. A wave will propagate out past one detector and, shortly after, past the other. As this wave passes each detector in turn it will cause a signal to be emitted which is

proportional to the amplitude of the water disturbance. Now suppose that we want to find the velocity of propagation of the wave. If we denote the signal from one detector by x(t) and the other by y(t) then the time delayed cross-correlation function defined in equation 3.9 will peak at a certain time delay τ such that the velocity of propagation is simply the distance between the two detectors divided by this time delay. This is evident from the fact that the two signals will be the most 'linearly similar' when one is delayed by the time required for the wave to travel the intervening distance between the two detectors.

Until now we have only discussed linear relationships between two processes. We have used phrases such as 'linearly similar' and 'linearly correlated'. But suppose there exists a nonlinear relationship between two processes. In this case we must use higher order correlation functions to expose this relationship. For instance, if we have two ergodic processes {x(t)} and {y(t)}, then we might look for a relationship of the form $x(t)=y(t)^2$. This would be exposed by investigation of the Triple correlation function at zero time delay defined as:

$$T_{xy} = \frac{1}{T} \int_0^T x(t)\, y^2(t)\, dt. \qquad - (3.10)$$

However great care is required here since the theory of non-linear correlation functions is very complex. In this thesis we will only very rarely mention these higher order moments.

3.3.1.4 Spectrum Analysis

So far we have discussed methods for dealing with random processes in the time domain. Spectrum analysis [3,4,5], however, is a system of data analysis which operates in the frequency domain. As we will see, the functions defined in one field are related to similar functions in the other

field by Fourier transforms.

The theory of Fourier analysis tells us that a given periodic time series x(t) may be expressed in terms of the coefficients of a complete set of orthogonal harmonic functions (such as sine and cosine). This is known as a Fourier series. When the constraint of periodicity is relaxed the discrete coefficients map to a function and the series becomes an integral. In this case x(t) may be expressed as:

$$x(t) = \int_{-\infty}^{+\infty} X(\omega)\, e^{i\omega t} d\omega \,, \qquad - (3.11)$$

where $x(\omega)$ is given by:

$$X(\omega) = \frac{1}{2\pi} \int_{-\infty}^{+\infty} x(t)\, e^{-i\omega t} dt. \qquad - (3.12)$$

The function $X(\omega)$ is known as the Fourier transform of x(t). It essentially contains all the information that is inherent to the signal x(t) and, being a complex function, may be expressed in polar form as:

$$X(\omega) = |X(\omega)|\, e^{i\phi(\omega)} \qquad - (3.13)$$

The function $|X(\omega)|^2$ is known as the auto-power spectrum for the record x(t) and $\phi(\omega)$ as the auto-phase spectrum. These definitions may be extended for two signals x(t) and y(t) to the cross-power spectrum, defined as $X(\omega)Y^*(\omega)$ and the cross-phase spectrum, defined as $\phi_X(\omega)-\phi_Y(\omega)$. If we regard the signals, x(t) and y(t), as members of an ensemble of two ergodic random processes then we may also extend these definitions so as to define the spectral functions pertaining, not to a single record, but to the process itself. For instance, the cross power spectrum for the two processes {x(t)} and {y(t)} is defined as $|\langle X(\omega)Y^*(\omega)\rangle|$, where the triangular brackets indicate an ensemble average. similarly the cross-phase spectrum would be defined as $\arg\langle X(\omega)Y^*(\omega)\rangle$.

Spectral functions are very easily understood. The auto power spectrum, which is sometimes known as the auto-spectrum or just the power spectrum, is a measure of the power of the signal as a function of frequency. For instance, if the signal is a pure sine wave then the auto-spectrum would be a delta function at a value of ω corresponding to the frequency of the sine wave. The auto-phase spectrum gives the relative phase of each frequency component with respect to a common baseline.

The cross-spectrum between two signals x(t) and y(t) is simply the union of their individual auto-spectra. Hence if the two signals share a common peak in their auto-spectrum, then that peak will also enter in their cross-spectrum. To understand the cross-phase spectrum let us suppose that both signals were pure sine waves. Then the cross-phase, at the frequency of this sine wave, would be zero indicating that both signals were in phase. If, alternatively, one signal were a sine wave and the other a cosine wave the cross-phase would be $\pi/2$. So the cross-phase spectrum simply gives the phase difference between two signals as a function of frequency.

3.3.1.5 The Wiener-Kintchine Theorem

We have now introduced the two basic fields of random data analysis; correlation and spectrum analysis. As we hinted above, these two fields are, for ergodic processes, intimately related. In fact, if a process $\{x(t)\}$ is ergodic, then we may define the auto-spectrum $\Gamma(\omega)$ as the Fourier transform of the auto-correlation function $R(\tau)$:

$$\Gamma_{xx}(\omega) = \int_{-\infty}^{+\infty} R_{xx}(\tau)\, e^{-i\omega t} dt \ . \qquad - (3.14)$$

For two ergodic processes an exactly similar expression exists relating the cross-spectrum to the cross-correlation function. By inverting this and the above expression we can equally well express correlations in terms of

spectral functions. By extending this correspondence to higher order moments in the correlation field we may also define similar corresponding moments in the spectral field. Thus a two-dimensional Fourier transform relates the Triple correlation function to a higher order spectral function known as the Bispectrum [6]. A three-dimensional Fourier transform similarly defines the Trispectrum, and so on. Hence we see that the two fields of correlation and spectral analysis are indeed just two ways of looking at the same thing. However, as will become apparent in the course of this thesis, different problems are suited sometimes preferentially to one or other of these two fields.

3.3.2 Application Of Correlation And Spectral Analysis

In this section we will discuss the application of the techniques reviewed above to the analysis of data obtained from the insertable probe and edge coils. We start by summarising the statistical quantities used throughout this thesis, most of which have already been introduced above.

3.3.2.1 Definitions

Given ergodic processes $\{x(t)\}$ and $\{y(t)\}$ during a finite time period T with Fourier transforms $\{X(\nu)\}$, $\{Y(\nu)\}$, which we calculate numerically by FFT programs, we define the power spectrum (or auto-spectrum) of x by:

$$\Gamma_{xx}(\nu) = \frac{1}{T} < |X(\nu)|^2 > , \qquad - (3.15)$$

where triangular brackets indicate an average over ensembles (i.e distinct time periods or different shots) and the time T is short enough such that stationarity and hence, hopefully, ergodicity is ensured. The cross spectrum is likewise defined as:

$$\Gamma_{xy}(\nu) = \frac{1}{T} < X(\nu)\ Y^{*}(\nu) > \quad . \qquad - (3.16)$$

We define $|\Gamma_{xy}|$ to be the cross power spectrum and arg(Γ) to be the cross-phase spectrum. In addition to these we also define a normalised version of the cross-spectrum which we term the coherence:

$$\gamma = |\Gamma_{xy}| / [\ \Gamma_{xx}\Gamma_{yy}\ ]^{1/2}. \qquad - (3.17)$$

In the time domain we define the usual cross-correlation function:

$$R_{xy}(\tau) = < \frac{1}{T} \int_{0}^{T} x(t)y(t+\tau)dt > \qquad - (3.18)$$

Again, as with the cross-spectrum, we define a normalised version of this which we call the cross-correlation coefficient:

$$\rho(\tau) = R_{xy}(\tau) \ / \ [\ R_{xx}(0)\ R_{yy}(0)\ ]^{1/2}. \qquad - (3.19)$$

3.3.2.2 General Methods Of Data Analysis

Finite Data

Since the data which will be analysed in this thesis consist of finite-length time series, problems occur if the definition of the power spectrum, and indeed the cross spectrum, defined above is used directly. This is because a finite signal $x_f(t)$ may be regarded as the product of two signals; the real x(t) and a box function. This is illustrated in figure 3.8. On taking the Fourier transform of a finite signal, one is actually computing the Fourier transform of the product of the real signal with a box function. By the convolution theorem [7] this is equivalent to convolving the Fourier transform of the complete infinite signal x(t) with

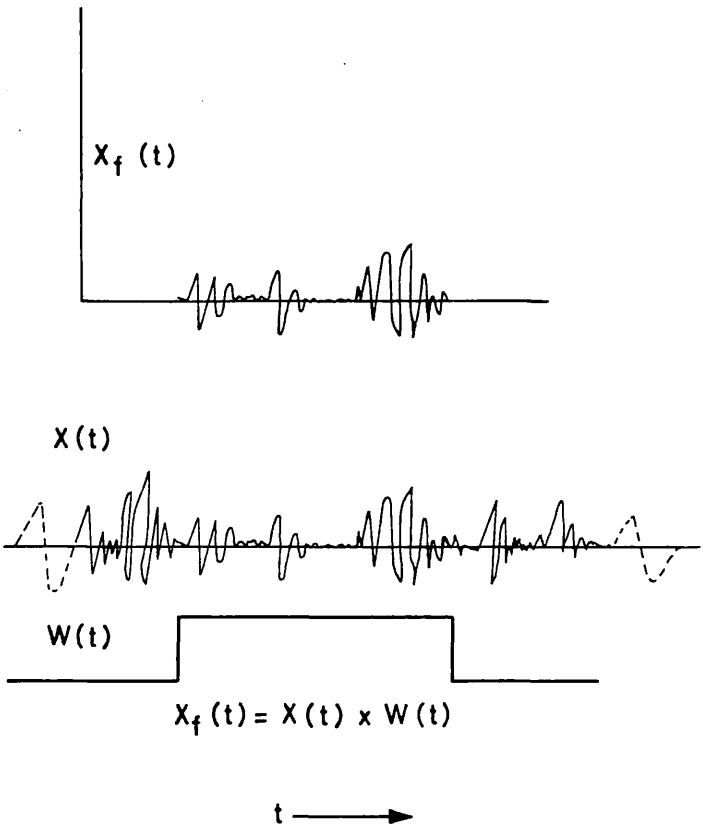

Figure 3.8 Illustration that a finite time series $x_f(t)$ may be ragarded as the product of the real infinite time series x(t) and a box function W(t).

the Fourier transform of a box function, which is a sinc function. It is clear that if we proceed to square the Fourier transform of such a finite signal then false features will appear in the power spectrum. This may be thought of as a leakage of power from a given frequency to surrounding frequencies. The problem is of course that of resolution. If you have information only about a certain time period then you cannot expect to have perfect knowledge of the power spectrum. Rather this dictates a finite resolution, given in the above case by the half-width-half-maximum of the sinc function.

This does not, however, mean that it is impossible to improve matters. For, in addition to the imposed box function apodisation due to the finite nature of the data, we are at liberty to impose, on top of this, our own apodisation. Hence we could, say, dictate a triangular apodisation by multiplying our finite time series with a triangular function. This would change the resolution by altering the convolving function. Information

theory will tell you that if you choose an instrumental function which gives poor resolution then the inherent errors in the derived power spectrum improve. If, on the other hand, you choose an apodising function which gives high resolution, the reverse will occur. Also, in general, apodising functions which give high resolution (such as a box) are associated with extensive side-lobes whereas poorer resolution apodisations (such as a gaussian) are not. If resolution is not a problem there is thus significant motivation for using a poor resolution apodisation.

In practice we don't actually use a gaussian but the function:

$$W(t) = \frac{1}{2} (1 - \cos(2\pi t/T)) , \qquad - (3.20)$$

which is known as a Hanning window. It is worth noting that the resolution given with a Hanning window is about twice as bad as a box function. However, since T is relatively long this small sacrifice is well worth it. We shall see later on in this chapter that a similar problem enters into the calculation of the toroidal mode spectra and in this case a similar sacrifice is most definitely unacceptable. In such cases there are deconvolution techniques which allow one to obtain the best resolution while also being free of side-lobe phenomena.

Filtering

It is most often essential to perform time domain correlation analysis on signals which have been filtered to exclude very low frequencies which correspond to an equilibrium evolution. It is also convenient at times to study specific frequency ranges. For this purpose we have developed a numerical bandpass filtering algorithm. This is depicted in flow-chart form in figure 3.9. For a given signal x(t) we form the Fourier transform X(ν), after weighting the signal with a Hanning window. This is then multiplied by

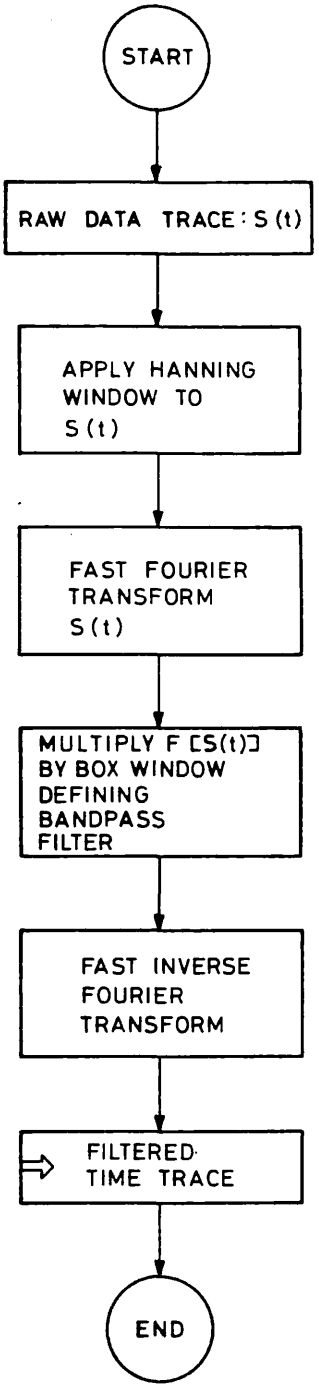

Figure 3.9 **Flow chart for the numerical filtering algorithm.**

a box window, thus defining the bandpass frequency range. We then inverse Fourier transform this to form the filtered time histories, from which it is possible to calculate the various correlation functions. This type of algorithm compares well with algorithms which operate in the time domain such as REMEZ.

3.3.2.3 Application To Edge Coils

We will now concentrate on the application of the correlation and spectral analysis techniques developed so far to data obtained from the various arrays of edge coils. In particular, emphasis will be placed on the calculation of the toroidal and poloidal spectra and the problems one encounters in their evaluation. The Helical Association spectrum will also be introduced and again the problems of evaluation discussed.

Poloidal Spectra

The poloidal arrays of edge coils provide information on the structure of fluctuations in the poloidal direction. One of the most useful ways of presenting this is to define the poloidal mode power spectrum. This is analogous to the power spectrum defined above for the time domain, except that since we are dealing with a periodic system, we must use a Fourier series. We therefore define the poloidal mode power spectrum as:

$$P_m = \frac{1}{2T} < \int_0^T | c_m^2(t) | + | s_m^2(t) | dt > \quad , \qquad - (3.21)$$

where $$c_m(t) = \frac{2}{N} \sum_{k=1}^{N} \tilde{B}_k(t) \cos (m\theta_k)$$

and $$s_m(t) = \frac{2}{N} \sum_{k=1}^{N} \tilde{B}_k(t) \sin (m\theta_k).$$

Here $\tilde{B}_k(t)$ represents the signal obtained from the k^{th} poloidal coil at poloidal angle θ_k. N is the total number of coils and m is the poloidal mode number, defined to be positive. As usual T defines the time interval over which data sampling occurs.

Since the poloidal arrays contain only a finite number of coils there

will exist a restriction on the highest mode number described by equation 3.21. In general, sampling theory will tell you that this mode number, termed the Nyquist frequency in relation to the time domain, is given by $m_{max} = N/2$. So if all of the coils in a poloidal array (16 for each field component) are used, it is possible to investigate mode numbers up to and including $m = 8$. In practice, however, we usually find that it is sufficient to use half the array, restricting attention to mode numbers less than $m = 5$.

It is worth noting that since each poloidal array covers the full 2π radians, the power spectrum, as defined above, has perfect resolution. As we shall see, this is definitely not the case with the toroidal array.

Toroidal Spectra

We define the toroidal mode power spectrum in an exactly analogous fashion to the poloidal mode power spectrum:

$$P_n = \frac{1}{2T} < \int_0^T | c_n^2(t) | + | s_n^2(t) | dt > \quad , \qquad - (3.22)$$

where $$c_n(t) = \frac{2}{N} \sum_{k=1}^{N} \tilde{B}_k(t) \cos (n\phi_k)$$

and $$s_n(t) = \frac{2}{N} \sum_{k=1}^{N} \tilde{B}_k(t) \sin (n\phi_k).$$

In this case, however, $\tilde{B}_k(t)$ represents the signal from the k^{th} toroidal array coil at the toroidal position defined by ϕ_K and n is the toroidal mode number.

Using this definition, it is possible to directly calculate the toroidal mode power spectrum. However, if one proceeds in this fashion, only very poor resolution is obtainable. This is, of course, due to the finite extent

of the toroidal array. As we discussed above, a finite signal may be described as the product of the true infinite signal with a suitable instrumental or apodisation function. On Fourier transforming this signal one thus obtains the true Fourier transform convolved with the Fourier transform of the apodising function. When this is squared to form the power spectrum this then determines the resolution by the width of the convolving function. If we apply this logic to the toroidal array which spans only sixty degrees, the best resolution we may obtain turns out to be about $\Delta n = \pm 6$ (choosing sensible well-behaved apodisations). However this is using a centred box window, whose Fourier transform has significant side-lobes (a sinc function). If we wish to get rid of this unpleasant feature then, by using a Hanning window, our resolution becomes about $\Delta n = \pm 12$. Clearly this is not acceptable given that the Nyquist frequency associated with the toroidal mode spectrum is only about four times this number.

There is therefore significant motivation for investigating other techniques of estimating the toroidal mode power spectrum. One particularly fruitful avenue is through the zero-time cross correlation function in toroidal angle. This may be defined as:

$$R(\phi,\delta\phi) = \frac{1}{T} < \int_0^T B(t,\phi)\, B(t,\phi+\delta\phi)\, dt >. \qquad - (3.23)$$

Now, following exactly the same reasoning as we applied to the time domain in section 3.3.1.5, if the process {B} is ergodic in ϕ, which amounts to different Fourier components having random phases, we may apply the Wiener-Kintchine theorem to show that the toroidal mode power spectrum is simply defined by the real part of the Fourier transform of $R(\delta\phi)$:

$$P_n = \frac{2}{\pi} \int_0^{\pi} R(\delta\phi) \cos(n\delta\phi)\, d(\delta\phi). \qquad - (3.24)$$

Note that we have used the fact that, since the process {B} is ergodic, the function R is independent of ϕ. That this is true is apparent from the ignorability of the coordinate ϕ (due to symmetry). As it turns out, however, the ergodic assumption is not fully born out due to the presence of portholes around the machine which lead to preferential phasing. As a result, the spatial correlation function $R(\delta\phi)$ appears slightly different when calculated using different reference coils. However, this effect is not very large and the approach we take is to symmetrise the spatial correlation by averaging $R(\delta\phi)$ as calculated by two extreme reference coils:

$$R(\delta\phi) = \frac{1}{2} \left(R(\phi_1, \delta\phi) + R(\phi_N, \delta\phi) \right) . \qquad - (3.25)$$

This method has one great advantage over the direct method. It allows twice the resolution with a simple sync convolving function. This is essentially because we have put in extra information in assuming that the underlying process is independent of ϕ, an assumption certainly warrented. To see this in terms of apodisation functions one must realise that equation 3.24 defines a shifted box function, the width of which is determined by the span of the toroidal array. However the integral is taken from 0 to π and so the resultant convolving function is equivalent to that obtained from a centred box of twice the width in the case of the integral ranging from $-\pi$ to $+\pi$. This latter case is of course analogous to the case arising in the direct computation of the toroidal mode power spectrum, except that there the box width was the array span. So it's simple to see that the resolution is doubled.

This method is also advantageous for the reason that it predicts a mode power spectrum which is linearly convolved with a simple sync function. This should be contrasted with the direct method where the power spectrum is predicted as the square of two functions, both of which are linearly convolved with a sync function.

Deconvolution

For many cases the fact that the toroidal mode power spectrum is convolved with a known apodisation function is of little consequence. However, when one wishes to interpret the finer structure in the spectrum, this can become a large problem. In such cases deconvolution techniques are available.

Deconvolution is the process whereby, given a convolved spectrum and the convolving function, one is able to predict the true (un-convolved) spectrum. The simplest method of deconvolution is known as 'linear deconvolution'. To understand this let us denote the convolved power spectrum by P_n and the true spectrum by X_n. Then, further denoting the convolving function by C_n, we may express mathematically what we mean by a convolution:

$$P_n = \sum_{\delta=-\infty}^{\infty} (X_{(n+\delta)} \cdot \quad C_{(\delta)}) \ . \qquad - (3.26)$$

If one now assumes that X_n tends to zero as n gets large, it is reasonable to truncate the sum to a finite length. On doing this we may rewrite the above equation in vector form as follows:

$$\underline{P} = \underline{\underline{A}} \ . \ \underline{X} \ , \qquad - (3.27)$$

where $\underline{\underline{A}}$ is a matrix whose elements are defined by C_n. Clearly the true spectrum is now obtainable by inverting this equation:

$$\underline{X} = \underline{\underline{A}}^{-1} . \ \underline{P} \ . \qquad - (3.28)$$

This is essentially the method of linear deconvolution. Given that we know exactly the convolved spectrum and the convolving function, this is what one wants. However one very rarely has an exact knowledge of the spectrum.

Rather, the spectrum is known to some finite accuracy. This then casts a slightly different tune; for in this case the method of linear deconvolution will generate false features on the deconvolved spectrum due to even very slight errors on the convolved spectrum. For this reason linear deconvolution is regarded as being notoriously unsafe.

A solution to this dilemma is provided by the increasingly popular non-linear technique known as Maximum Entropy [8,9,10,11]. Owing to the complicated nature of this technique we will only discuss here the rudimentary theory. Since, however, it is a technique which will be used in this thesis to calculate the toroidal mode power spectrum when increased resolution is required, appendix A discusses the subject at greater length, giving details of various algorithms used.

The technique of Maximum Entropy, in relation to spectral estimation, can be broadly explained as follows. The algorithm is iterative. An initial spectrum is chosen and then transformed to calculate the correlation function. By comparing this correlation function with the true function, a new spectrum is predicted which is closer to the real spectrum than the previous estimate. If this process is continued indefinitely it would converge to the same estimate as that predicted by a linear deconvolution. However there are certain constraints imposed. The algorithm, which chooses a better estimate of the spectrum each time around, is conditioned so as to choose the smoothest possible positive function. In addition, the iteration is stopped before complete convergence is reached by an error test which senses when the noise level is being fitted. The outcome is that the Maximum Entropy spectrum is the smoothest possible positive definite deconvolved spectrum which is consistent with errors. It is thus uniquely safe as it contains the least information possible. In practice this is a very useful technique in the estimation of the toroidal mode power spectrum when increased resolution is required.

Helical Association Spectrum

The poloidal and toroidal mode power spectra provide information as to the power contained by given n and m modes. However, these spectra do not tell us what the association is between a given n and m number. For instance, if the poloidal mode power spectrum had two peaks, one at m = 1 and one at m = 3, and the toroidal spectrum had similarly two peaks, the first at n = 7 and the second at n = 16, how can we relate these? Is the m = 1 to be associated with the n = 7 or the n = 16? And so on. What is required is a two-dimensional power spectrum which would give information as to the power contained by a given (m,n) pair. Such a spectrum, following our definitions of the individual spectra, would be defined as:

$$P_{mn} = \frac{1}{2T} < \int_0^T | c_{mn}^2(t) | + | s_{mn}^2(t) | dt > \quad , \qquad - (3.29)$$

where $$c_{mn}(t) \propto \sum_{k=1}^{N'} \sum_{j=1}^{N} \tilde{B}_{kj}(t) \cos (m\theta_k + n\phi_j)$$

and $$s_{mn}(t) \propto \sum_{k=1}^{N'} \sum_{j=1}^{N} \tilde{B}_{kj}(t) \sin (m\theta_k + n\phi_j).$$

However, to calculate this spectrum, information is needed about the field $\tilde{B}(t)$ at all poloidal and toroidal angles, which in turn requires a matrix of edge coils covering a large proportion of the torus. At least, this is the case when one performs the calculation in a direct manner. In fact it can be shown that, adopting a similar stategy to the correlation function approach to calculating the toroidal mode power spectrum, one can prove the following theorem:

'If the coordinates θ and ϕ are ignorable, then the two dimensional power spectrum is given by:

$$P_{mn} = \mathrm{Re}\left(\frac{1}{(2\pi)^2} \int\int Q(\theta,\phi) \exp(-i(m\theta + n\phi))\, d\theta d\phi \right), \quad (3.30)$$

where $Q(\theta,\phi)$, the poloidal-toroidal correlation matrix, is defined as:

$$Q(\theta,\phi) = \frac{1}{T} < \int_0^T B(\theta,\phi_0,t)\, B^*(\theta_0,\phi,t)\, dt >.$$

Further, P_{mn} is always positive definite and the imaginary part of equation 3.30 is identically zero.'

By using this theorem, it is possible to determine the two-dimensional power spectrum without having a complete matrix of edge coils. We will refer to this spectrum, when calculated in this fashion, as the 'Association spectrum'. There are, however, several problems, some of which are quite severe. The first and most obvious of these is the fact that the θ direction in a torus is not ignorable and hence different m numbers will not be linearly independent. This will cause spurious features to arise in the Association spectrum some of which may be negative. It will also cause the imaginary part of the spectrum to be non-zero.

Another severe problem is that of finite data which we encountered in the calculation of the toroidal mode power spectrum. However, here the problem can be much worse. The reason for this is that the poloidal and toroidal arrays do not intersect at their midpoints. This means that the Fourier transform of the apodisation function has both real and imaginary components which couple the real and imaginary parts of the power spectrum together. Denoting the Association spectrum by A_{mn} and the true two dimensional power spectrum by P_{mn}, this may be expressed:

$$\mathrm{Re}(A_{mn}) = \alpha_{mn} \otimes \mathrm{Re}(P_{mn}) + \beta_{mn} \otimes \mathrm{Im}(P_{mn}) \quad - (3.31)$$

$$\mathrm{Im}(A_{mn}) = -\beta_{mn} \otimes \mathrm{Re}(P_{mn}) + \alpha_{mn} \otimes \mathrm{Im}(P_{mn}),$$

where the operator $\otimes$ indicates convolution and the matrices $\underline{\underline{\alpha}}$ and $\underline{\underline{\beta}}$ are

determined by the apodisation function. Now clearly, if θ and ϕ were ignorable, we would not have a problem, since in this case $Im(P_{mn})=0$ and so the real part of the Association spectrum would simply define the convolved two dimensional power spectrum. But this is not the case and in fact the imaginary part generated through the non-ignorability of θ couples into the equation relating A_{mn} to P_{mn}. Hence what one really needs to do is to solve equation 3.31 for P_{mn}. However this amounts to a linear deconvolution and owing to the inherently large errors involved, would not work as such. Rather a Maximum Entropy approach would be more fruitful. In this thesis, however, we do not use this approach. Instead, by realising that mode-mode linear coupling induced by the non-ignorability of θ is relatively small, we simply take the real part of the Association spectrum as an estimate for the true two dimensional power spectrum. This does lead to spurious features though, and as a consequence one has to be careful in the interpretation.

The resolution obtainable in the Association spectrum is determined in part by the intersection point of the two arrays. The best resolution is found when the intersection is located at the end of the toroidal array. This corresponds to $\delta n = \pm 3$. With the intersection at the half way mark, this resolution is halved. The intersection point is, of course, fixed by the physical location of the various edge coil arrays which dictates two possible intersections, one near the end of the toroidal array and one fairly near the centre. The central intersection has the further problem, however, that the poloidal array is internal to the liner and the toroidal array is external. This means that data must be corrected for penetration effects through the liner (see appendix B), which can themselves depend on helicity.

3.3.2.4 Insertable Probe Techniques

: Determination Of The Radial Structure Of Instabilities

An insertable magnetic probe provides information on the time-history of the magnetic field at a finite number of radial locations. In the case of the fluctuations being due to just one instability, this information can easily be translated into the radial amplitude distribution of that instability. For instance, this may be accomplished by taking the square-root of the radial power distribution. However, when there is more than one instability present the problem of determining the various radial amplitude distributions becomes non-trivial. Since this case typifies the RFP it is of considerable importance to formulate algorithms which solve this problem to some extent. In this section we will thus develop an effective solution which will then be used extensively in interpreting probe data in chapter 6.

Introduction To Correlation Matrix Fitting (CMF)

To a certain approximation the fluctuating magnetic field may be regarded as the sum of several (linearly) independent gaussian processes of zero mean. In such a case the first order statistical moments completely define the combined probability distribution function and hence the correlation matrix, defined as:

$$R_{ij} = \frac{1}{T} < \int_0^T b_i(t) b_j(t) dt > , \qquad - (3.32)$$

represents the totality of information obtainable from the probe data. In this definition $b_i(t)$ is the fluctuating magnetic field at the radial position dictated by the suffix i. The integral is a time integral and should be taken over a statistically stationary region of the time history

described by the region (0,T). Triangular brackets indicate an ensemble average over many statistically similar shots.

The approach we take is thus to assume a finite number of linearly independent processes, global or local modes, and then to use the correlation matrix to define the various radial amplitude distributions characteristic of each process. On a physical basis we use the linear independence or random phasing of different modes to descriminate them. In this way we sacrifice information about the time variation to gain more information concerning radial structure.

2-Process Model

To begin with we will assume that the fluctuating magnetic field may be decomposed into just two components; a global mode with a radial correlation length of the order of the minor radius and a local component defined in terms of the correlation matrix:

$$R_{ij} \propto \delta_{ij} \equiv \begin{matrix} 1 & i = j \\ 0 & i \neq j. \end{matrix} \qquad - (3.33)$$

We denote the time dependence of the local contribution by $l_i(t)$ and that of the global contribution by $g_i(t)$. Then, further assuming that there is no radial propagation associated with the global mode, by using equation 3.32 we may calculate the correlation matrix:

$$\begin{aligned} R_{ij} &= \frac{1}{T} < \int_0^T (l_i(t)+g_i(t))(l_j(t)+g_j(t))dt> \\ &= \frac{1}{T} < \int_0^T l_i(t)g_j(t)dt> \qquad -(i) \\ &+ \frac{1}{T} < \int_0^T l_i(t)l_j(t)dt> \qquad -(ii) \\ &+ \frac{1}{T} < \int_0^T g_i(t)g_j(t)dt> \qquad -(iii) \\ &+ \frac{1}{T} < \int_0^T g_i(t)l_j(t)dt> \qquad -(iv). \end{aligned} \qquad - (3.34)$$

Terms (i) and (iv) vanish since we assume that the local turbulence is not linearly correlated to the global instability (this essentially defines what we mean by linearly independent). Term (ii) will also vanish when $i \neq j$ since this was our definition of local turbulence. Hence we may rewrite equation 3 as follows:

$$R_{ij} = \frac{1}{T} < \int_0^T l_i(t) l_j(t) dt + \int_0^T g_i(t) g_j(t) dt >$$

$$= \bar{l}_i \bar{l}_j \delta_{ij} + \bar{g}_i \bar{g}_j \ , \qquad - (3.35)$$

where the operator '$\bar{}$' denotes a signed root-mean square over the interval (0,T), the sign depending on whether g_i and g_j are in or out of phase. Given the measured correlation matrix this equation may now be solved for the g_i by minimisation of the quantity,

$$Q = \sum_{i \neq j} \sum (R_{ij} - \bar{g}_i \bar{g}_j)^2, \qquad - (3.36)$$

which is essentially a non-linear optimisation problem and may be solved numerically by the method of steepest descents [eg 12]. Denoting the n^{th} successive estimate of $\bar{g}_i$ by $\bar{g}_i^{(n)}$ we use the following algorithm:

$$\bar{g}_i^{(n+1)} = \bar{g}_i^{(n)} + \beta \frac{\partial Q}{\partial g_i}$$

where $$\frac{\partial Q}{\partial g_i} = -4 \sum_{j \neq i} \bar{g}_j (R_{ij} - \bar{g}_i \bar{g}_j) \qquad - (3.37)$$

and β is a small positive constant. If desired this procedure can be much improved for speed by the use of conjugate gradients [12]. However we find that with LSI 11/23 computers and $N \leq 10$ this is unnecessary. Note that when the $\bar{g}_i$'s are known, the profile of local turbulence may easily be calculated:

$$\bar{l}_i = \sqrt{\{ R_{ii} - \bar{g}_i \bar{g}_i \}}. \qquad - (3.38)$$

This follows directly from equation 3.35.

In the above model we have made several very particular assumptions. Notably that the fluctuation activity is due only to two components: A global instability and a local contribution. In equation 3.36, where we eliminate the local turbulence by not summing with i=j, we are thus fitting the correlation matrix with an N-parameter family. However the correlation matrix itself (ignoring diagonals) is a function of N(N-1)/2 independent parameters. Hence the value of Q is a strong indication of whether or not the initial assumptions were correct. In fact a better indication is furnished by a chi-squared parameter:

$$\chi^2/N = \frac{1}{N(N-1)} \sum_{i \neq j} \sum \{ R_{ij} - \bar{g}_i \bar{g}_j \}^2 / \sigma_{ij}^2 \quad , \qquad - (3.39)$$

where σ_{ij} is the error (stm) associated with the measured R_{ij}. If χ^2/N is approximately unity then the fit is good and we will have confidence in the initial assumptions. If, on the other hand, χ^2/N is much greater than one, the fit is not consistent with errors and we must adopt another model.

Many Process Model

The fact that Q depends on many more variables than the number of signals, N allows us to consider more complicated cases than that of just one global mode and local turbulence. In fact we may generalise our model to the case of there being p linearly independent global modes present in addition to the local turbulence. Extending our previous notation, we denote the time history of the global mode,i by ${}^i g_j$, where j ,as usual, indicates radial position. Then in the same fashion as we derived equation 3.35 we may write:

$$R_{ij} = \bar{l}_i \bar{l}_j \delta_{ij} + \sum_{s=1}^{p} ({}^{s}\bar{g}_i {}^{s}\bar{g}_j) , \qquad - (3.40)$$

where quadratic terms involving different modes cancel due to the linear independence of each global mode. Again we may now solve this equation for the ${}^{s}\bar{g}_i$'s by the minimisation of a modified Q function:

$$Q = \sum_{i \neq j} \sum (R_{ij} - \sum_{s=1}^{p} ({}^{s}\bar{g}_i {}^{s}\bar{g}_j))^2 , \qquad - (3.41)$$

which leads to a similar algorithm as that in equation 3.37. The limitation as to the number of modes that it is possible to include must come from two factors: firstly the size of the error bars so that one does not fit the noise level and secondly from the criterion:

$$p << (N-1)/2 , \qquad - (3.42)$$

which corresponds to there being a lesser number of parameters to fit the correlation matrix than the matrix itself depends on.

Propagation Effects

We have assumed above that the temporal phase of each $g_i(t)$ is the same so that no propagation effects occur. We will now look briefly at the effects of relaxing this assumption. To start, let us Fourier decompose ${}^{k}g_i(t)$:

$${}^{k}g_i(t) \propto \sum_{m} {}^{k}g_i(\omega) \cos (\omega_m t + {}^{k}\phi_i) , \qquad - (3.43)$$

where ${}^{k}\phi_i$ is the phase of the i^{th} element of the k^{th} global process. By substitution in equation 3.32 this yields the following form for Q:

$$Q = \sum_{i \neq j} \sum \{ R_{ij} - \alpha \sum_{k} {}^{k}g_j {}^{k}g_i \cos({}^{k}\phi_j - {}^{k}\phi_i) \}^2 , \qquad - (3.44)$$

where α is a constant. Now this equation may also be written as follows:

$$Q = \sum_{i\neq j}\sum \{ R_{ij} - \alpha \sum_k [{}^k g_j \cos(\phi_j)][{}^k g_i \cos(\phi_i)] \quad - (3.45)$$
$$- \alpha \sum_k [{}^k g_j \sin(\phi_j)][{}^k g_i \sin(\phi_i)]\}^2.$$

And so we see immediately that the effect of propagation is to create two processes for every k; a 'sine' process and a 'cosine' process. Hence if we know that there is just one global mode and we find two statistically significant processes then we may infer the module and phase distributions of the real process. However, if there are more than a single global process there is in general no way of labeling different processes as sine or cosine components of a single propagating real process. In this case outside information must be used to match the sine and cosine processes correctly to obtain the various module and phase distributions.

Non-Gaussian Signals

Finally we come to an interesting point which will not be used in this thesis but nevertheless should be mentioned. The motivation for the above model is that the magnetic coil signals from an RFP have an approximately gaussian nature. This means that essentially all the information about spatial structure contained in the signals from the magnetic probe may be extracted by fitting the first order correlation matrix, R_{ij}. Suppose now, however, that the signals have an appreciable, although small, non-gaussian component. Then higher order correlations such as the triple correlation defined as:

$$T_{ij} = \frac{1}{T} < \int_0^T b_i^2(t) b_j(t) dt > \quad - (3.46)$$

now contain information. If we first fit R_{ij} to obtain the linearly independent processes ${}^k g_i$ and then use these in 3.46 we may calculate the quadratic inter-process coupling coefficients. Similarly, by fitting higher

order correlations, we may hope to estimate an expansion for the full non-linear coupling between linearly independent processes. The method outlined in this section thus presents an avenue to the possible elucidation of non-linear coupling measurement.

CHAPTER 4

EQUILIBRIUM STUDIES

We now turn to the results and interpretation of measurements made with the insertable probe and arrays of edge coils. In this chapter, probe measurements will be discussed in the context of evaluating the magnetic equilibrium. In particular, emphasis will be placed on determining the equilibrium magnetic field profiles. Once these have been evaluated, other profiles such as those of current density, safety factor and pressure may be derived. The importance of such an equilibrium study to the topic of this thesis is to form a background in which the fluctuation measurements of chapters 5 and 6 may be interpreted.

4.1 TECHNIQUES

In order to obtain the best estimate of the equilibrium magnetic field profiles, the signals from the insertable probe are averaged over both a limited time window and many discharges. In this way a set of average field profiles for a specific time range are produced which are not affected by random fluctuations. The probe insertion is varied slightly between consecutive discharges so that small misalignments of the individual coils tend to cancel out. The profiles obtained are then fed into a least-squares algorithm to fit even and odd polynomials to B_ϕ and B_θ respectively. The coefficients of these polynomials are altered in such a way as to correct for the horizontal plasma displacement characteristic of toroidal devices.

In the sustainment phase of discharges, where liner currents are dominated by easily calculated resistive effects, the edge-field polynomial fit is improved by including points from hairpin coils at the shell and a toroidal current Rogowski. A vacuum field configuration is also strongly

weighted from the limiters to the shell by including calculated points with a '1/r' dependence for B_θ and a constant dependence for B_ϕ. Once the final polynomial expressions for the field profiles have been obtained it is a simple matter to calculate the various derivable quantities by simple algebraic manipulation of the polynomial coefficients.

4.2 RESULTS

4.2.1 General

The evolution of the main discharge parameters and various probe signals for typical discharges discussed in this chapter are shown in figure 4.1.

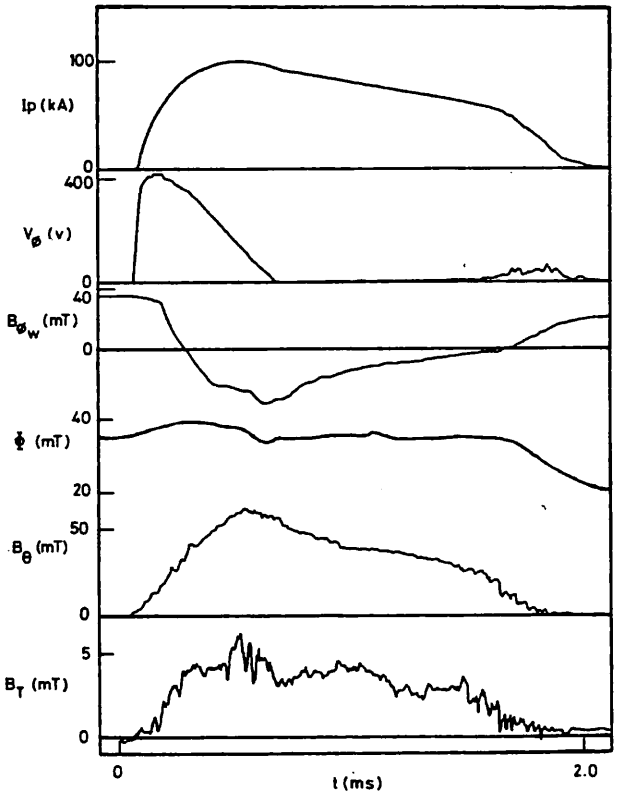

Figure 4.1
Typical parameter traces: toroidal current (I_p), loop voltage (V_ϕ), toroidal field at wall ($B_{\phi w}$), toroidal flux (ϕ), B_θ probe trace ($B_\theta{}^p$)and B_r probe trace ($B_r{}^p$).

These shots are short (2 ms) decaying current discharges (100 kA) suitable for probe insertion. We present here results only from these type of discharges, although comparisons with discharges where the current is sustained reveal no obvious qualitative differences.

In figure 4.2 we plot the plasma current with the probe (a) retracted and (b) fully inserted. The main differences are that termination occurs about 7% earlier with the probe inserted and that the current decay rate is slightly increased. The effect of the probe on this plasma is thus rather small, an increase in resistivity of only about 20%, so we anticipate that the magnetic fields measured are representative of such discharges even without the probe inserted.

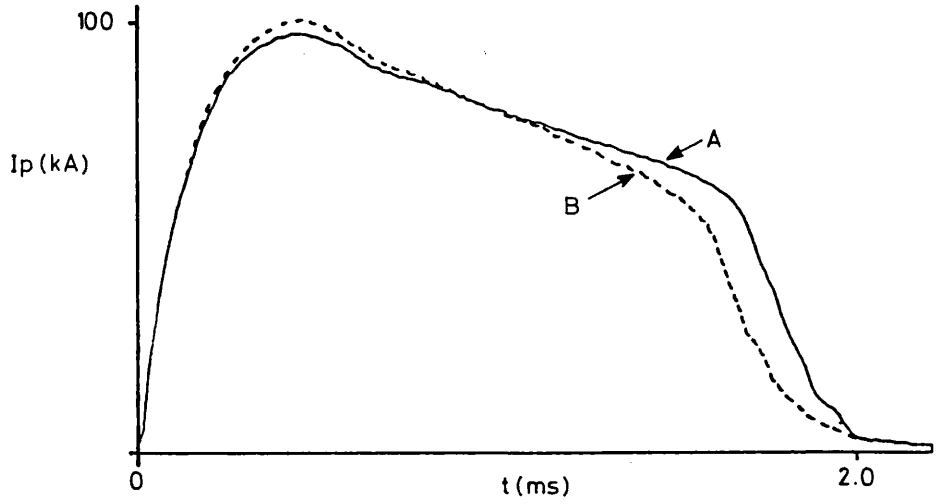

Figure 4.2 Toriodal plasma current with probe retracted (a) and probe inserted (b).

4.2.2 Magnetic Field And Current

Figure 4.3(a) shows 'raw' data from the probe plotted in profile form for a 0.2 ms time-slot in the middle of the sustainment phase (1.0-1.2 ms in figure 4.1) utilising a data-base of around 20 shots. The radial coordinate in this diagram refers to a vertical minor radius as the probe was inserted vertically. The scatter in points is due to shot to shot variation. The curve fitted to B_θ in this case includes a constant term as well as the odd powers of r in the polynomial expansion. However the least-squares fit is found to make this term very small so that the curve essentially intersects the origin. This shows that there is no vertical plasma shift.

In a toroidal system the plasma column will experience a horizontal shift due to curvature in the toroidal direction. Any radial field, which we measure with the probe, will give us information about this shift. Specifically, the shift, δ of the centre of the flux surface (assumed circular) passing through r, in relation to the geometrical axis is given by:

$$\delta = r\, B_r/B_\theta \ , \qquad - (4.1)$$

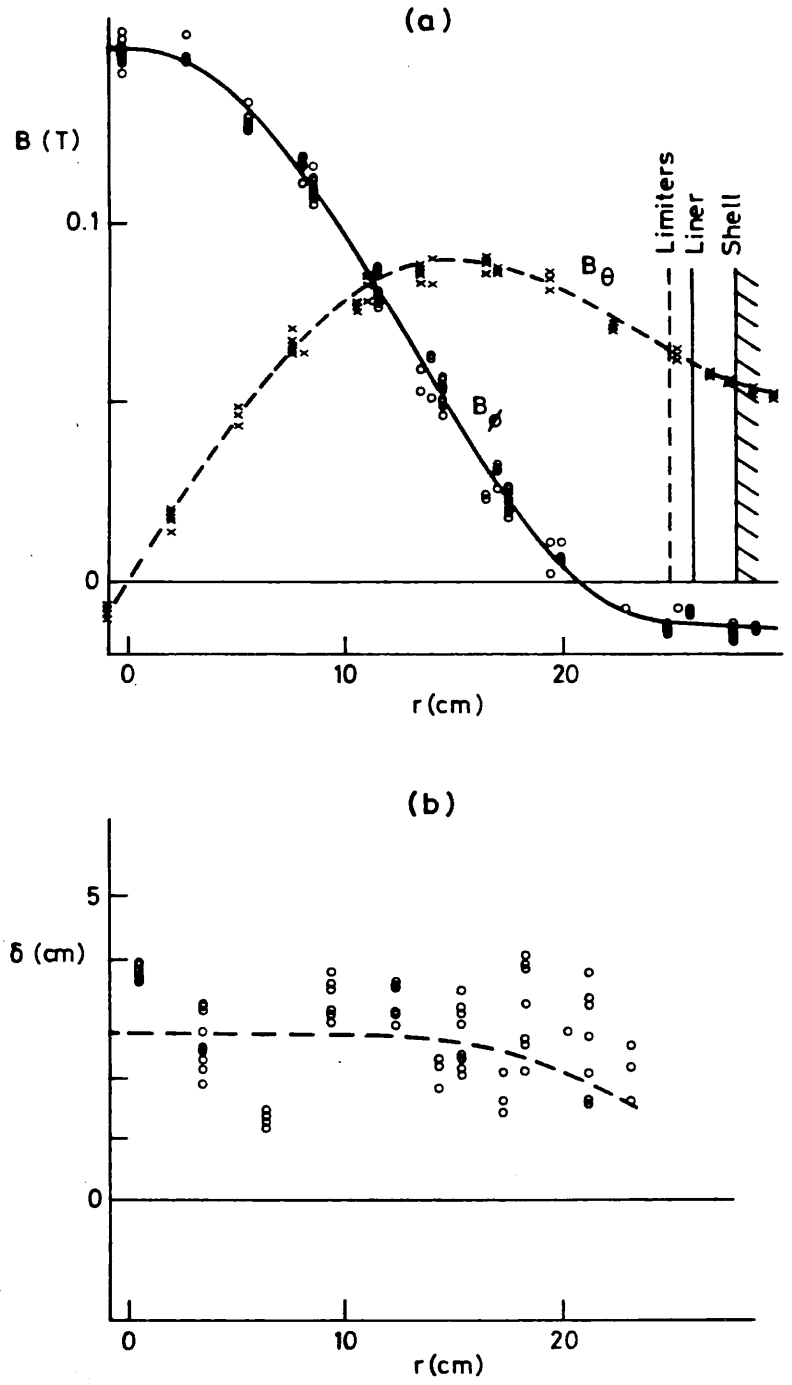

Figure 4.3 (a) 'Raw' Magnetic field profiles and (b) measured plasma displacement vs radius compared with theoretical displacement calculated from the field profiles.

where r is the geometrical minor radius. We may compare this measured displacement with that predicted by formulae given by Shafranov for toroidal equilibrium [1]. In particular, the displacement of the flux surfaces Δ, as a function of radius r, is given by the following formula if we neglect plasma pressure (justified for this purpose since $\beta \ll 1$) and assume $a \ll R_o$:

$$\Delta(r) = \frac{1}{2R_o} \int_r^a \ell_i(r')r'\,dr' + \Delta_w(a) \qquad - (4.2)$$

where $$\Delta_w(a) = \frac{b^2}{2R_o} \{ \ln \left|\frac{b}{a}\right| + (1 - a^2/b^2)(\ell_i(a) - 1) \} \qquad - (4.3)$$

and $$\ell_i(r') = 2 \int_0^{r'} B_\theta^2(r)\, r\, dr \,/\, (r'\, B_\theta^2(r')). \qquad - (4.4)$$

Here a is the plasma minor radius, R_o the major radius of the torus and b, the minor radius of the shell. ℓ_i is the internal plasma inductance.

Figure 4.3(b) shows a comparison between this predicted displacement using the measured B_θ profile and that obtained from equation 4.1. The scatter in the displacement calculated by the latter method is rather large. This is mostly due to small alignment errors in the radial coils which then pick up the much stronger B_θ or B_ϕ fields. However, agreement is certainly reasonable showing that in the central region of the plasma the displacement is about 2.8 cm falling to around 1.7 cm at the limiters. The value of central displacement agrees well with that measured by X-ray emission profiles (see appendix of published papers - paper 2).

We may deduce from figure 4.3(b) that the plasma takes on the form of a uniformly shifted equilibrium in the central region of the discharge, since in this region the displacement appears approximately flat. Accordingly we may correct the field profiles so that we plot them, not as a function of the geometrical minor radius, but as a function of the radial coordinate whose origin is the shifted axis of the displaced flux-surfaces. Denoting the polynomial expansions of the two uncorrected field components as:

$$B_\theta(x) = \sum_{j=0}^{n} a_j\, x^{(2j+1)}; \quad B_\phi(x) = \sum_{j=0}^{n'} b_j\, x^{2j} \quad , \qquad - (4.5)$$

where x now represents the geometrical minor radius, the corrected field

profiles may, in fact, be written (see appendix C):

$$B_\theta(r) = \sum_{j=0}^{n} a_j\left(1 - \frac{j\Delta^2}{r^2}\right) r^{2j+1} \qquad - (4.6)$$

$$B_\phi(r) = \sum_{j=0}^{n'} b_j\left(1 - \frac{j\Delta^2}{r^2}\right) r^{2j} \ ,$$

where Δ represents the central plasma displacement. These corrected profiles are shown in figure 4.4. In the outer regions, of course, they are

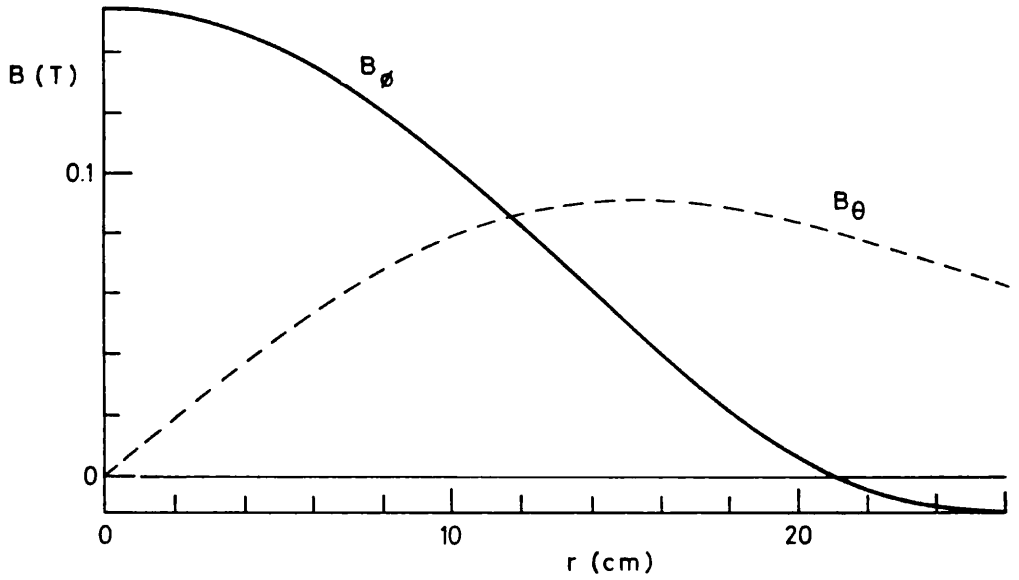

Figure 4.4 Shift-corrected magnetic field profiles.

virtually indistinguishable from the uncorrected ones, as expected. However, near the axis there are substantial differences. In particular, inspection of figures 4.3(a) and 4.4 show that B_ϕ on axis is about 7 mT higher once the profiles have been corrected. While this may not be an enormous effect on the field profiles themselves, when estimating the pressure profile, this correction is very important.

Since we now have the field profiles as a function of the radial coordinate whose axis is the plasma axis, we may assume cylindrical symmetry in the derivation of quantities which depend on the fields. As we have noted above, this is due to the very constant form of the displacement as a function of radius in the inner region of the

discharge (figure 4.3(b)). Hence, by differentiating the corrected field profiles according to the equation:

$$\underline{\text{Curl}}\ (\underline{B}) = \mu_0 \underline{J}\ , \qquad - (4.7)$$

written in cylindrical coordinates, we may calculate the current density profiles. These are shown in figure 4.5. The accuracy in the outer regions of the discharge is not sufficient to distinguish whether the toroidal current density reverses as expected from certain force-free models.

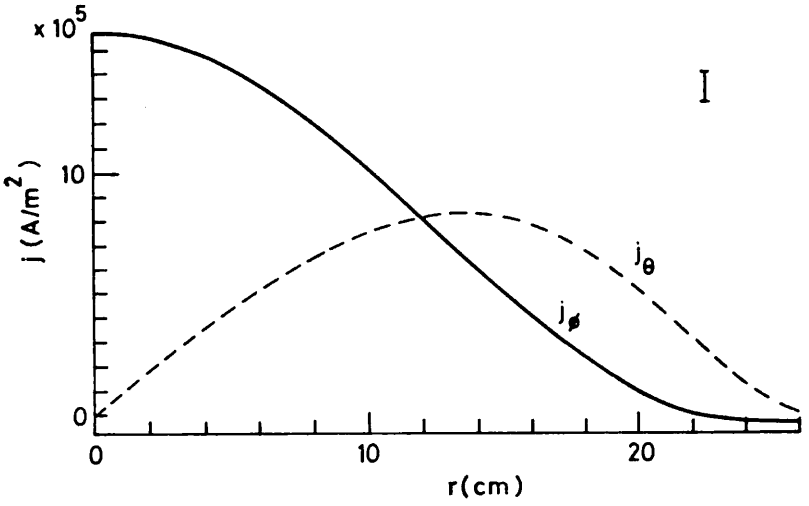

Figure 4.5 Current profiles J_θ and J_ϕ.

Figure 4.6 shows profiles of the parallel and perpendicular current densities $\underline{J}.\underline{B}/B^2$ and $\underline{J}\times\underline{B}/B^2$. To a good approximation we see that the discharge is force-free. In fact, by inspection of this figure, the ratio

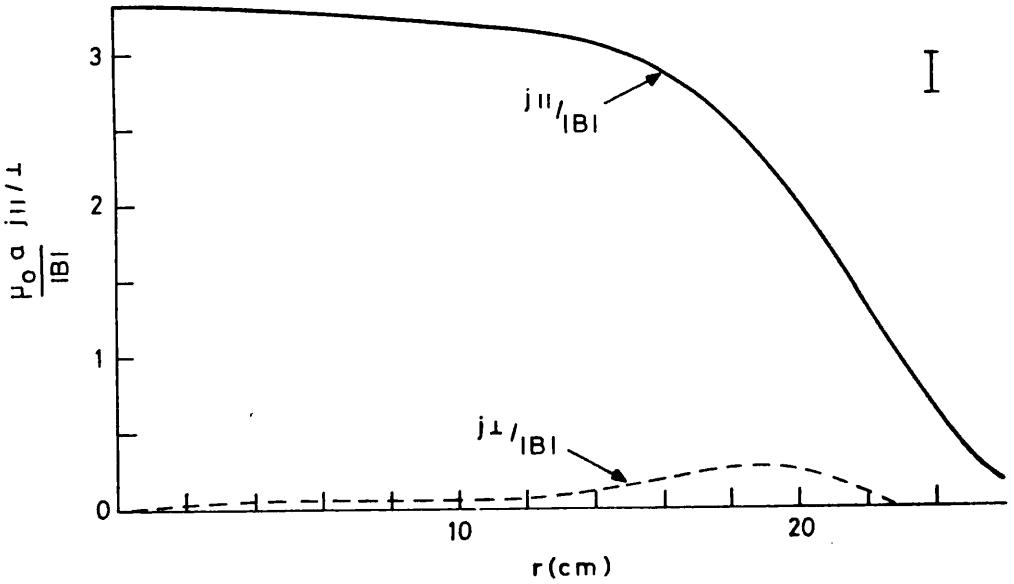

Figure 4.6 Profiles of parallel and perpendicular current densities, $\underline{J}.\underline{B}/B^2$ and $|\underline{J}\times\underline{B}|/B^2$

$J_{//}/J_{\perp}$ may be seen never to be less than about 10 and in the central region of the discharge around 50. Within errors the μ (= $\underline{J}.\underline{B}/B^2$) profile is flat from the axis out to about 15 cm where it falls monotically to zero at the wall. Accordingly we can deduce that the profiles which we observe are in good agreement with a modified Bessel description (MBFM) [2].

Figure 4.7 shows a profile of the safety factor $q = rB_\phi/RB_\theta$ which appears monotonic. This observation excludes the presence of instabilities driven by 'pitch minima'. The value of q on axis is about 0.2, signifying that resonant m = 1 instabilities in the inner region of the plasma must have a toroidal mode number greater than $|n| \approx 5$. Lastly the value of q at the limiters is about -0.04. In a similar fashion this imposes a lower limit on the toroidal mode number of $|n| \approx 25$ for m = 1 modes to be resonant outside the reversal surface.

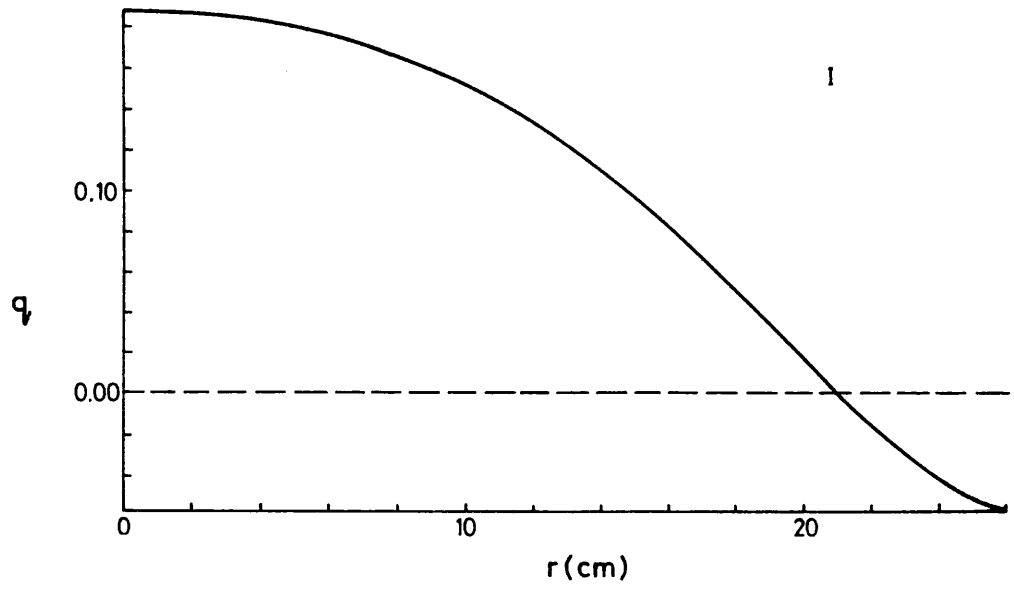

Figure 4.7 Profile of the safety factor $q = rB_\phi/RB_\theta$.

4.2.3 Estimation Of The Pressure Profile

By integrating the equilibrium pressure balance equation:

$$\underline{\text{Grad}}\ (p) = \underline{J} \times \underline{B} \qquad - (4.8)$$

in cylindrical form from the limiters inwards it is possible to obtain the pressure profile. It must be stressed that the computation of this profile is extremely sensitive to experimental errors and is thus very uncertain with low β values. This is because the pressure profile is directly related to the perpendicular current density which in our case is very small. However, with the type of corrections we have applied to our estimates of the field profiles, we find that we can estimate the pressure profile with useful accuracy in the sustainment phase of the discharge. In particular, this is because we can improve the edge-field fit in this period by using external coils to weight a vacuum-field configuration from the limiters outwards. This is accomplished by including extra points, calculated from the external coils, with a '1/r' dependence for B_θ and a constant value for B_ϕ. This process improves not only the edge-field fit, but also the central region fit as it allows higher order polynomials to be fitted to the data without introducing spurious oscillations at the edge. In addition to this, an equally important factor is the correction we have made to the field profiles to take into account plasma displacement. Without this, we would expect false features to appear on the pressure profile near the axis. Lastly, and not by any means least important, is the fact that our probe perturbs the plasma only very slightly.

Figure 4.8 shows a best estimate of the pressure profile obtained by averaging over several polynomial fits for each of many different random realisations of the initial data. The error bar shown in this graph pertains to the on-axis pressure and is calculated as the standard deviation over the many polynomial fits and random realisations and decreases monotonically to zero at the limiters, where we assume that the wall pressure is zero. The profile may be characterised by the following values of the various β parameters:

$$\beta_\theta = \frac{2\mu_0\langle p\rangle}{B_\theta(a)^2} \approx 14\% \pm 5\% \qquad - (4.9)$$

$$\langle\beta\rangle = \frac{2\mu_0\langle p\rangle}{\langle B^2\rangle} \approx 5\% \pm 2\% \qquad - (4.10)$$

$$\beta_0 = \frac{2\mu_0 p(0)}{B(0)^2} \approx 9\% \pm 3\% , \qquad - (4.11)$$

where here a represents the plasma radius.

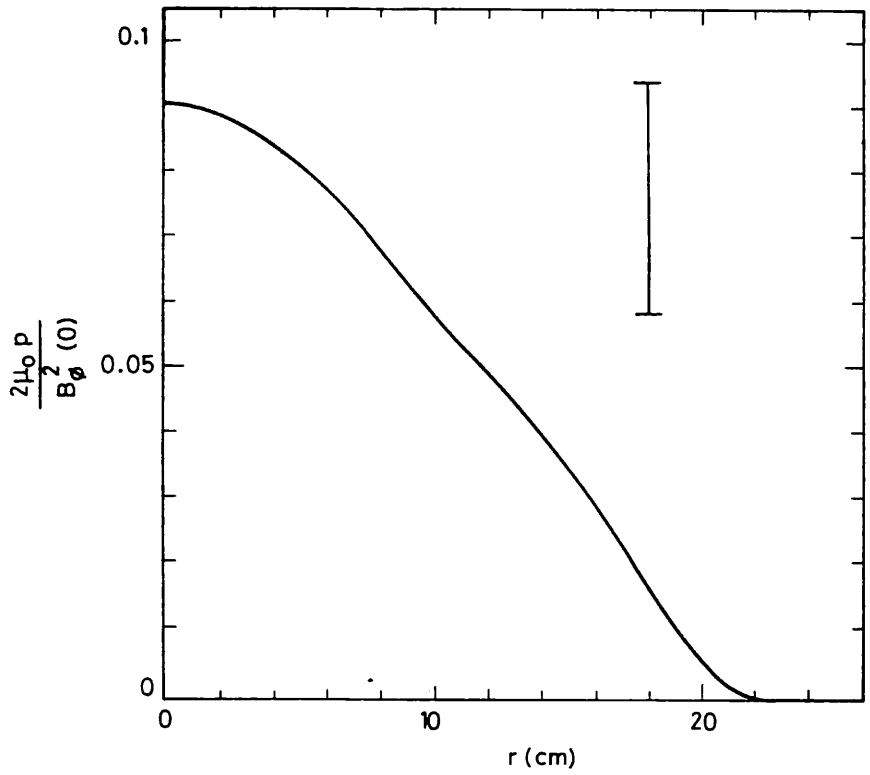

Figure 4.8 Profile of kinetic pressure normalised to the on-axis magnetic pressure.

The overall shape of the best estimate pressure profile is peaked on axis. At the extreme of the error estimate the profile could be flat (or slightly hollow) out to about 8 cm but not beyond.

In the sustainment phase of the discharge we find that the pressure profile is essentially constant in shape and evolves in magnitude so as to keep β approximately constant. During periods of the discharge when the plasma current varies very quickly, the termination and set-up phases, it is not generally possible to use edge coil measurements to improve the fitting procedure owing to inductive effects in the liner. So any study of the evolution of the pressure profile will inherently be subject to much greater inaccuracy. Despite this, however, we are able to say that in the

time-interval just before termination the pressure peaks on axis (increasing by a factor of about 1.5 in absolute magnitude) indicating that the plasma undergoes a sharp compression before extinction.

4.2.4 Electric Field and Energy Confinement

In the approximation of cylindrical symmetry the Faraday equation:

$$\underline{\text{Curl}}\ (\underline{E}) = -d\underline{B}/dt \qquad - (4.12)$$

defines the toroidal and poloidal electric field distributions as a function of minor radius given suitable boundary conditions at the wall, which are provided by loop voltage measurements. Typical profiles, obtained by subtracting successive estimates of the field profiles, are shown in figure 4.9.

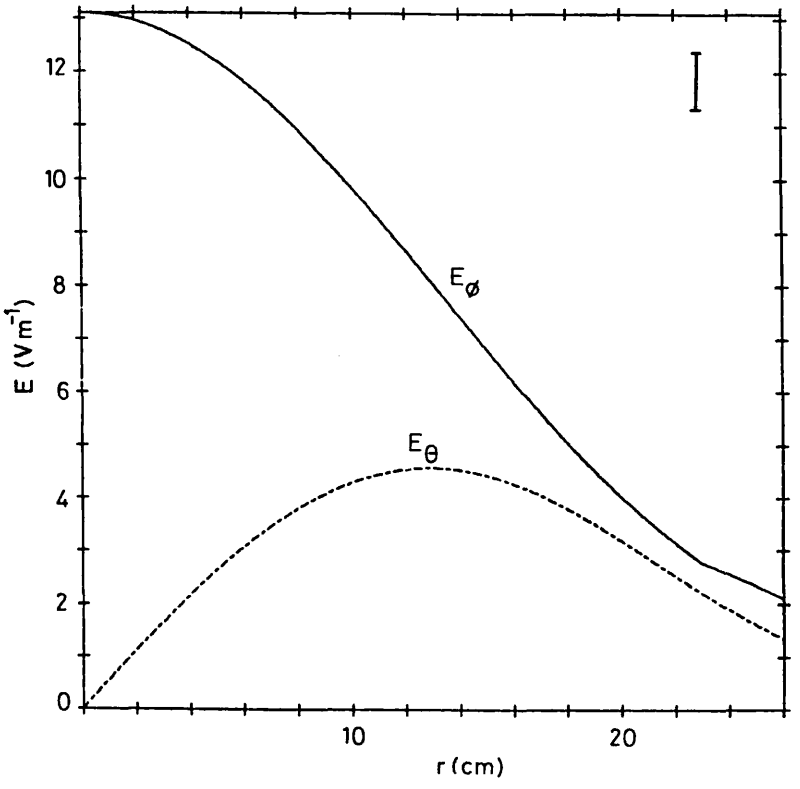

Figure 4.9 Electric field profiles E_θ and E_ϕ.

Since we have the plasma kinetic energy from our pressure measurements and the ohmic dissipation power from $\underline{E}$ and $\underline{J}$ we may obtain the energy

confinement time as:

$$\tau_E = \iiint_{V_{plasma}} \frac{3}{2} p \, dV \Big/ \iiint_{V_{tot}} \underline{E}.\underline{J} \, dV \, , \qquad - (4.13)$$

where we have ignored dp/dt since it is small in our case compared to $\underline{E}.\underline{J}$. Our measurements yield a value of $\tau_E = 70\mu s$ in which the uncertainty is virtually all in the pressure and so is about 30% as with $\langle\beta\rangle$.

4.2.5 Conductivity

Since we have profiles of $\underline{E}$ and $\underline{J}$ we can obtain profiles of an effective parallel conductivity defined as:

$$\sigma_{eff} \equiv (\underline{J}.\underline{B})/(\underline{E}.\underline{B}). \qquad - (4.14)$$

This is shown in figure 4.10. Now if the plasma obeyed a simple Ohm's law of the form:

$$\underline{\sigma}.(\underline{E} + \underline{v}x\underline{B}) = \underline{J} \qquad - (4.15)$$

(which it does not) then naturally σ_{eff} would be equal to the actual (Spitzer) conductivity σ.

The true conductivity σ may be obtained directly from an estimate of the electron temperature profile. We may derive this crudely by assuming that the electron and ion temperatures are equal and that the shape of the density profile is the same as the electron temperature so that $T_e \propto p^{1/2}$. Then, using the Spitzer formula [3] for the conductivity with an assumed constant resistivity anomaly Z, we can find the conductivity σ_T corresponding to the electron temperature profile deduced. This is shown in figure 4.10 for Z = 2 and 4.

The current-to-field ratio σ_{eff} has a clearly hollow profile even in these decaying-current discharges whereas the Spitzer estimate, σ_T, is naturally peaked on axis because the temperature profile we deduce is

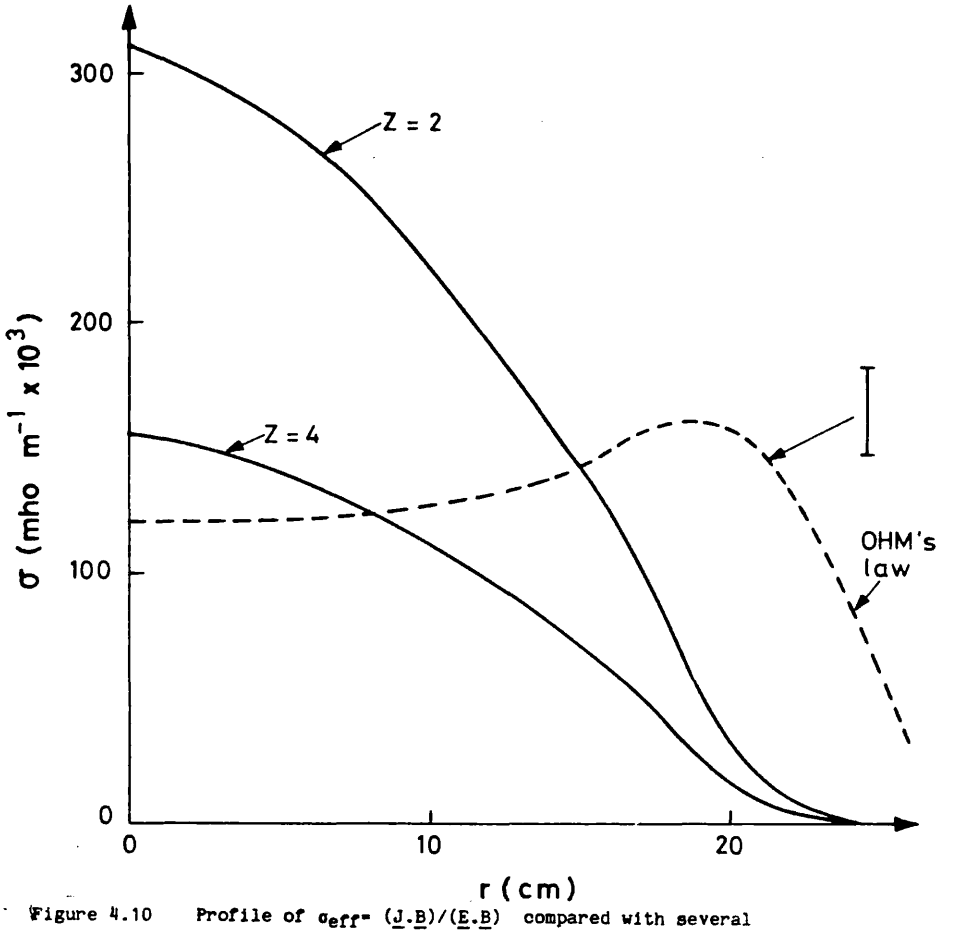

Figure 4.10 Profile of σ_{eff}= $(\underline{J}.\underline{B})/(\underline{E}.\underline{B})$ compared with several profiles estimated from the pressure for Z = 2,4.

monotonically decreasing. Plausibly, one could argue that virtually any T_e profile would become monotonic because of thermal deposition and the transport equations regardless of our somewhat cavalier assumptions about the density profiles.

It seems most unlikely that the discrepancy between σ_{eff} and σ_T could be explained by spatial variations of Z since this would require $Z < 1$ at the edge. We conclude, as noted above, that the plasma does not satisfy the simple ohm's law of equation 4.15 but experiences some type of 'dynamo effect' sustaining the reversal [4].

4.3 DISCUSSION

That the flux-surface shift deduced from B_r is consistent with the Shafranov value is, of course, no surprise, although it is reassuring. Perhaps the most important point is that, once measured, the shift can be properly corrected for in further analysis of the measurements from the

viewpoint of the cylindrical approximation. Without proper correction serious errors might occur.

The μ profile of parallel current confirms the observations elsewhere [5,6] and also the theoretical expectation that the central regions of the RFP relax to the minimum energy, μ = constant, state but that $\mu \to 0$ at the wall. It thus supports descriptions such as the modified Bessel function and Bessel vacuum models as a reasonable approximation to RFP profiles.

The absence of a 'pitch minimum' in the outer regions of the discharge is an important result. As well as excluding instabilities driven by such a configuration it also confirms the rationale for choosing the RFP over 'unreversed' pinches.

The deduction of pressure profiles from magnetic probe measurements is, as we have seen, subject to considerable uncertainty owing to the accumulation of calibration, alignment and other errors. Nevertheless it is believed that the profile presented represents a reasonable approximation to the actual profile. In confirmation of this we note that, at this time in the discharge, interferometer measurements show that the chord averaged electron density is about 2.7×10^{19} m^{-3}. Assuming a parabolic distribution for which $n_{eo} = 3\langle n_e \rangle/2$, taking the central electron temperature to be twice the mean conductivity temperature (as indicated by Thompson scattering for different discharges [7]), T_e = 50 eV, and taking $T_e = T_i$ and $n_e = n_i$ gives an independent rough estimate of the central beta of 0.07. This then agrees quite well with the value 0.09 in figure 8, considering the uncertainties of the assumed n_o and T_{eo} as well as p_o.

The accuracy we estimate for p(r) enables us to rule out the possibility that the pressure profile is rather flat out to a radius close to the reversal surface and then steeply falling from there to the wall. The importance of this observation is in excluding certain radial dependences of the transport coefficients. In chapter 5 we will see that there is

considerable evidence that the magnetic field lines inside the reversal surface are stochastic and that the transport associated with such stochasticity is sufficient to explain the observed energy losses. However these measurements are not able to establish whether or not the field is stochastic at the reversal surface and beyond. This is an important point since recent 3D-MHD simulations [8] seem to indicate that even if the centre of the RFP is stochastic, the edge region, from about the reversal surface outward, may have well defined magnetic flux surfaces and hence much smaller electron diffusivity.

If such a situation of good 'edge confinement' were to occur then the temperature would, in order to satisfy the diffusion equations, adopt a profile flat in the centre, where the electron diffusivity is large, and steep at the reversal surface and beyond, where it is small. Less obviously the density profile might also be expected to take on this form and and in this case the pressure profile would follow suite. However this is precisely the profile shape which is ruled out by our measurements.

Of course, in the absence of actual ambipolar stochastic transport calculations, the assumption that the density profile must follow the temperature is weak and thus, within errors, our measurements cannot rule out the existence of a stochastic interior and non-stochastic edge. However, if we do assume that the plasma is only stochastic inside the reversal surface, then the density profile consistent with our measurements will have to be very peaked.

Our measurements of σ_{eff} and their deviation from the expected profile shape of the ohmic conductivity are a rather direct observation of the 'dynamo mechanism' at work, even in decaying discharges. Of course, in steady state discharges the persistence of magnetic field reversal is itself a manifestation of this reversal sustaining mechanism. Unfortunately, the measurements do not presently enable us to distinguish between the various possible detailed mechanisms which may be responsible

for the 'dynamo' effect (for example, the mean-field electrodynamics approach [9,10], the tangled discharge model [11] or some form of non-local resistivity due to stochasticity). Further theoretical refinement of these models in the future may reveal characteristics which are sufficiently well defined as to be testable against our present results.

4.4 CONCLUSIONS

Equilibrium results from the insertable probe have been presented. The effect of the probe on the plasma is to increase the resistance by only about 20% and therefore it is assumed that the measurements have a direct relevance to discharges where the probe is not inserted. The magnetic field profiles obtained agree well with an MBFM description. Measurements of horizontal plasma displacement as a function of radius agree, within uncertainty, with the predicted theoretical variation according to Shafranov. In particular the value of displacement in the centre of the discharge is 2.8 cm falling to about 1.7 cm at the limiters. No vertical plasma shift is observed.

Examination of the pitch profile reveals that there are no pitch minima and that $m = 1$ modes with $|n| < 5$ in the core or $|n| < 25$ at the edge, if present, would be non-resonant.

The pressure profile has been calculated which appears consistent with independent values of the temperature and electron density and is peaked on axis. Typically $\beta_\theta \approx 14\%$, $\langle\beta\rangle \approx 5\%$ and $\beta_0 \approx 9\%$. Electric field profiles have also been obtained. These have been used to calculate an effective parallel conductivity which has been compared to that calculated from the pressure profile, assuming a suitable density profile. The very great difference between these two estimates requires the presence of some kind of a dynamo mechanism acting in such a way as to sustain field reversal.

CHAPTER 5

EDGE COIL MEASUREMENTS

In this chapter measurements obtained from the various arrays of edge coils are presented and discussed in terms of fluctuation activity. Extensive use will be made, both in this chapter and in chapter 6, of the techniques reviewed and developed in chapter 3. The reader may thus find it convenient to flick back occasionally to recap on some of the definitions.

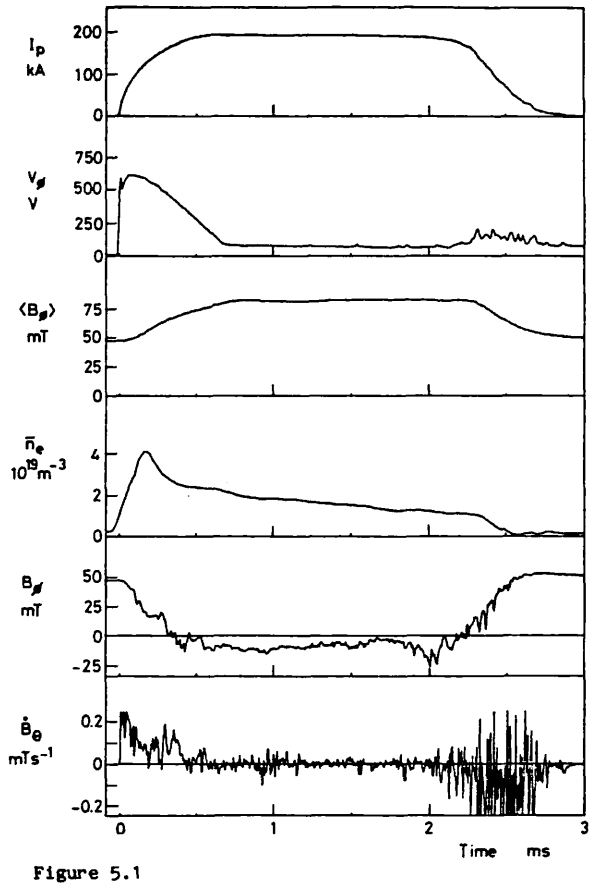

Figure 5.1
Time history of a typical discharge used for edge coil measurements: Plasma current (I_p); toroidal loop voltage (V_ϕ); average toroiodal magnetic field ($\langle B_\phi \rangle$); average line of sight electron density (n_e); toroidal magnetic field at the liner (B_ϕ); time rate of change of the poloidal magnetic field at the liner (dB_θ/dt).

The majority of this chapter is devoted to the analysis of the sustainment phase of optimal 'power crowbar' discharges. Figure 5.1 shows the evolution of the main discharge parameters for this type of shot. Towards the end of section 5.1, however, results from extensive scans over a relevant parameter space and an investigation of the termination and set-up phases is presented.

5.1 RESULTS

5.1.1 General

To achieve an understanding of why the relatively complicated techniques of random data analysis have to be used in the investigation of fluctuations

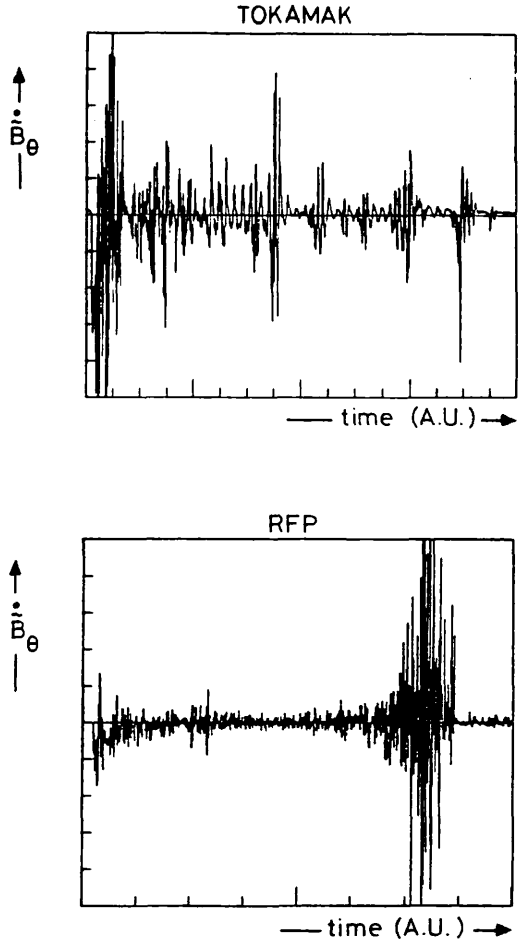

Figure 5.2 Raw data traces from a B_θ edge coil for HBTX1A running as (a) a Tokamak and (b) an RFP.

in the RFP, it is instructive to compare typical raw-data traces from HBTX1A running as a Tokamak and as an RFP. Figure 5.2 shows such a comparison. The top graph in this diagram is clearly quite periodic, discrete events being observable. This is an edge coil signal for a Tokamak discharge. The bottom graph, however, shows no such signs of periodicity. This is the RFP discharge.

To reveal the dependence of the fluctuations on the frequency ν, we may calculate the power spectrum $\Gamma_{xx}(\nu)$ as defined in equation 3.15. This is shown in figure 5.3 for two internal edge coils, one measuring B_θ and one B_ϕ. The spectra are averaged over five shots so as to illustrate the trends, although substantial variation in the detail occurs from shot to shot. It is

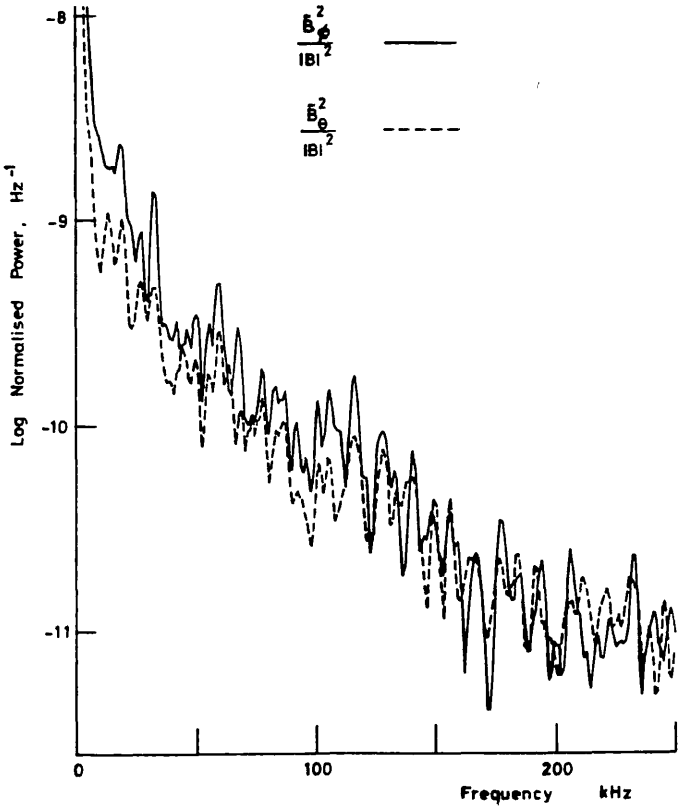

Figure 5.3 Power spectrum of $(B_\phi/|B|)^2$ and $(B_\theta/|B|)^2$ during the sustainment phase obtained from the internal coils.

clear that the dominant power is at low frequencies and that above about 40 kHz the spectra fall off approximately as ν^{-2}. It is also apparent that there is little difference between the spectral shape of the two field components, although below about 40 kHz B_ϕ is systematically slightly stronger than B_θ.

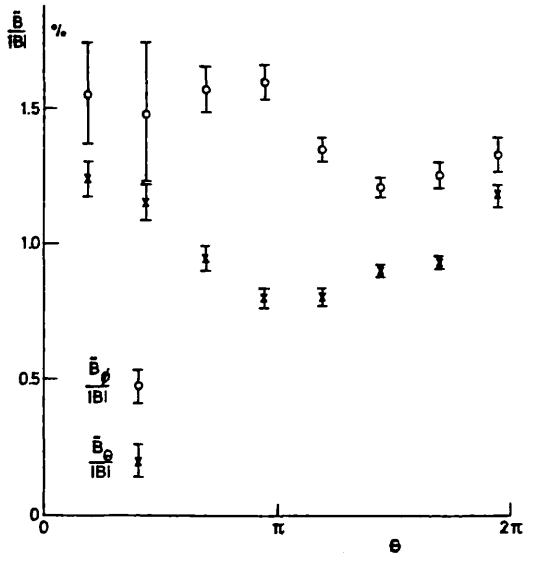

Figure 5.4
Ensemble averaged amplitude of $\tilde{B}_\phi/|B|$ and $\tilde{B}_\theta/|B|$ as a function of poloidal angle during the sustainment phase in the frequency band 5-250 kHz.

Another basic measurement is the rms fluctuation level. This is plotted in figure 5.4 as a fraction of the total poloidally averaged magnetic field, $(B_\phi^2+B_\theta^2)^{1/2}$, and as a function of the poloidal angle θ. The mean value for $\tilde{B}_\theta$ is typically 1% and for $\tilde{B}_\phi$, 1.5%. In the set-up and termination phases of the discharge this rises considerably for both components to 6-10%. Also apparent from figure 5.4 is the significant variation of the rms level with θ. This effect, being particularly obvious for $\tilde{B}_\theta$, is indicative of the importance of toroidicity in the RFP.

5.1.2 Poloidal mode structure

As we discussed in chapter 3, to determine the poloidal structure of the fluctuations we may evaluate the poloidal mode power spectrum (equation 3.21). Figure 5.5 shows an example of this spectrum, pertaining to an internal poloidal array, for the two field components. Clearly the $\tilde{B}_\phi$ spectrum is dominated by mode numbers m = 0,1 with negligible contribution at higher m. The $\tilde{B}_\theta$ spectrum relates a similar story, except that there appears to be relatively less m = 0 and more m = 2.

An alternative approach to determining the poloidal mode structure is to

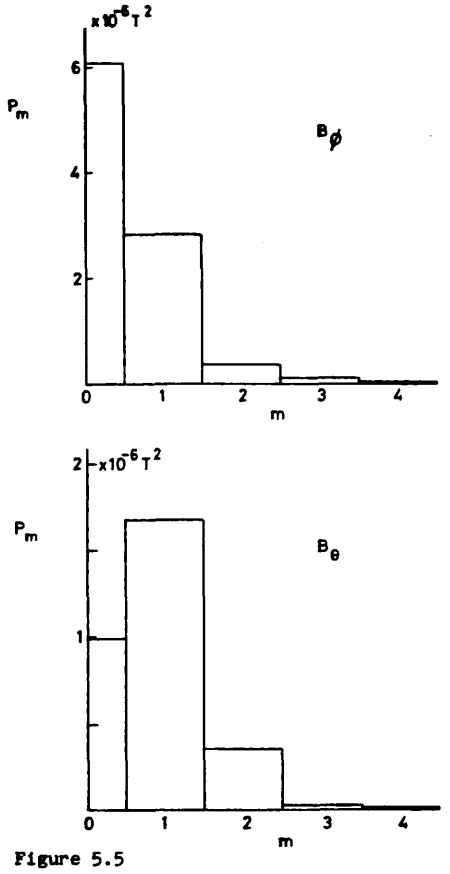

Figure 5.5

Poloidal mode power spectrum for $\tilde{B}_\phi$ and $\tilde{B}_\theta$ during the sustainment phase in the frequency band 5-250 kHz.

use correlation analysis. For instance, we may calculate the spatial autocorrelation by forming the cross correlation coefficient (equation 3.19) between the various coil signals in a poloidal array. Figure 5.6 shows examples of this for $\tilde{B}_\theta$ using coils on the inner (a) and outer (b) equator as reference. Clearly the choice of reference makes a great deal of difference. This reflects the fact that θ is not an ignorable coordinate, and hence the fluctuations do not possess rotational symmetry in their statistics. However, in principle, this does not alter the fact that inspection of such autocorrelations will allow the nature of the fluctuations to be deduced. In fact, to lowest order,

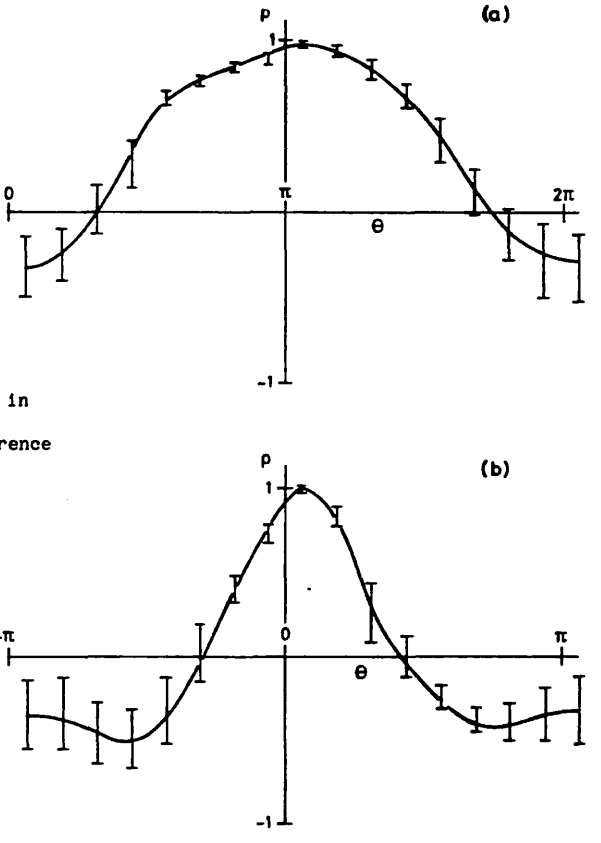

Figure 5.6

Equal time cross-correlation coefficient (spatial autocorrelation) for $\tilde{B}_\theta$ as a function of displacement in poloidal angle; (a) reference coil at $\theta = \pi$; (b) reference coil at $\theta = 0$. Sustainment phase: filter 5-50 kHz.

disregarding the lack of rotational symmetry, the shape of the autocorrelation is that which would be expected from similar proportions of linearly independent m = 1 and m = 0. In other words it is the sum of a constant plus a cos(θ) dependent part. The lack of symmetry and hence the non-ignorability of θ indicates that 'm = 1' component is distorted due to toroidicity so that its phase varies more rapidly at the outer equator (θ ≈ 0) than the inner (θ ≈ π).

An equivalent picture to this is that each independent mode is not simply a fourier mode but a combination of fourier modes linearly coupled together. Hence the independent 'm = 1' mode is actually expressible as:

$$M_1 = \cos(\theta - \alpha_1) + \varepsilon_2 \cos(2\theta - \alpha_2) + \ldots, \qquad - (5.1)$$

where α_1 and α_2 are arbitrary phases and ε_2 is a coupling coefficient. The equation $(\underline{\text{curl}}\ \tilde{\underline{B}})_r = 0$, written in toroidal geometry, in principle determines this expansion. To see this we write this equation:

$$\frac{-\sin(\theta)}{R_0 + r\cos(\theta)} \cdot \tilde{B}_\phi + \frac{1}{r}\frac{\partial \tilde{B}_\phi}{\partial \theta} - \frac{1}{R_0 + r\cos(\theta)} \cdot \frac{\partial \tilde{B}_\theta}{\partial \phi} = 0. \qquad - (5.2)$$

Here R_0 represents the major radius of the torus and r the minor radius. If we now Fourier expand the toroidal field component in the following fashion:

$$\tilde{B}_\phi = \sum_m a_m e^{i(m\theta + n\phi)}, \qquad - (5.3)$$

where, as usual, the coefficients a_m are complex and the real part is taken implicitly, then on substitution into equation 5.2 we are led to a similar expansion for $\tilde{B}_\theta$:

$$\tilde{B}_\theta = \sum_m \left\{ \frac{m+1}{2n} e^{i\theta} + \frac{mR_0}{nr} + \frac{m-1}{2n} e^{-i\theta} \right\} a_m e^{i(m\theta + n\phi)}. \qquad - (5.4)$$

Now, from the poloidal mode power spectrum we have observed that there is

virtually no m = 2 toroidal component. Also the spatial autocorrelations show much less distortion for this component. So that to a good approximation:

$$\tilde{B}_{\phi}^{M1} = a_1 e^{i(\theta+n\phi)} \qquad - (5.5)$$

And so equation 5.4 tells us that

$$\tilde{B}_{\theta}^{M1} = \frac{a_1}{n} \cdot \left[\frac{R_0}{r} + e^{i\theta} \right] e^{i(\theta+n\phi)} \qquad - (5.6)$$

$$= a_1 \{ \left[\frac{R_0}{nr}\cos(\theta) + \frac{1}{n}\cos(2\theta) \right] + i\left[\frac{R_0}{nr}\sin(\theta) + \frac{1}{n}\sin(2\theta) \right] \} e^{in\phi}.$$

And hence the signature of the toroidal distortion is that the cos(θ) and cos(2θ) components (and similarly the sin(θ) and sin(2θ)) are always in phase with each other. This is readily confirmed by figure 5.7 which shows the cross-spectrum between the cos(θ) and cos(2θ) signals (formed as weighted sums of the various poloidal array signals). At low frequencies the coherence is very high(>0.8) indicating that about 60% of the power is linearly coupled. In addition the phase is zero showing that the cos(θ) and cos(2θ) components are in phase at the outer equator (θ=0); a result expected from the autocorrelation data. The fact that the level of coherence tends to drop at high frequencies, accompanied by a randomisation of the phase, is indicative of the increasing importance of electronic system noise owing to the decrease of absolute

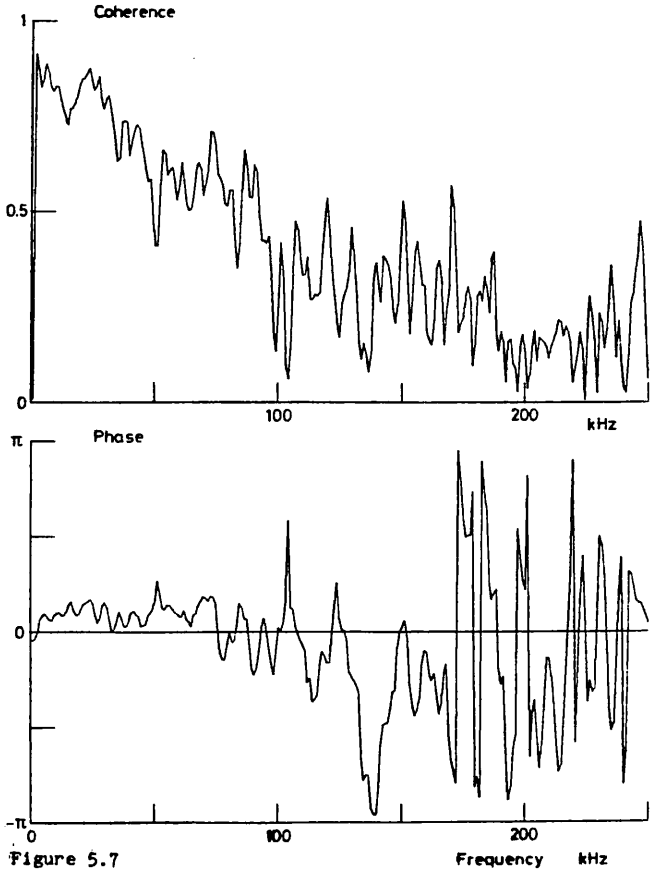

Figure 5.7

Coherence and cross-phase spectrum between the m = 1 and the m = 2 cosine modes for B_θ (ensemble average over 10 shots, sliding averaged over 3 frequency points during the sustainment phase).

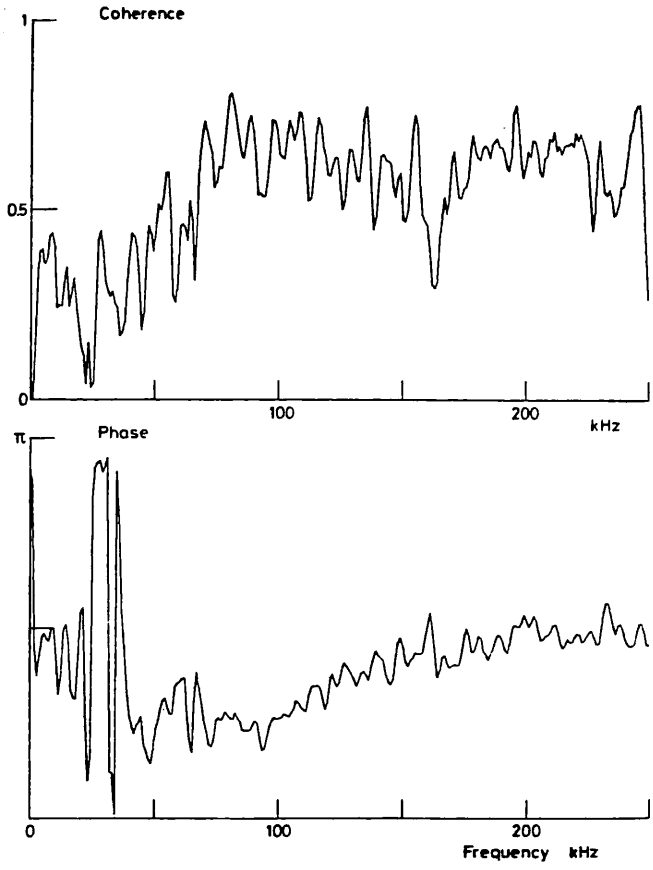

Figure 5.8

Coherence and cross-phase spectrum between the m = 0 and m = 1 cosine modes for B_ϕ (averaged as in figure 5.7).

power with frequency. Coherence spectra obtained by using unintegrated signals do not suffer from this problem and possess high values of coherence right out to the Nyquist frequency.

Another type of linear coupling is illustrated in figure 5.8. This shows the cross-spectrum for B_ϕ between m=0 and m=1 (cos(θ)). At high frequencies the cross phase can be seen to be π, showing that the modes add constructively at the inner equator. This may be thought of most simply as the toroidal distortion of the m=0 mode due to the fact that $B_\phi \propto 1/R \approx 1-(a/R_0)\cos(\theta)$. The lower coherence at low frequencies may be interpreted as indicating that the major parts of the m=0 and m=1 are independent.

So the poloidal structure is very simple. There are basically just two types of statistically independent modes present. We may label these as M_0 and M_1. These modes correspond to the fourier modes 'm=0' and 'm=1' along with their concomitant toroidal distortions. The fact that these toroidal distortions are greater for the θ component is not a priori explicable in any simple fashion. However, knowing this fact the equation $(\underline{\text{curl}}\ \tilde{\underline{B}})_r=0$, written in toroidal geometry, dictates the nature of the toroidal distortion on $\tilde{B}_\phi$. In fact it is possible to extend this type of argument to establishing a general algorithm capable of completely determining the eigenmodes of the system in terms of the fourier modes. However a discussion of this topic is not within the scope of this thesis. The presence of higher poloidal mode numbers than m = 1 is not established. If they do exist,

however, their power is certainly less than 3% of that contained in the M_0 and M_1 modes.

5.1.3 Toroidal mode structure

In chapter 3 we discussed a variety of different methods for estimating the toroidal mode spectrum. The two most favourable methods relied on calculating the toroidal autocorrelation in space. Figure 5.9 shows an example of this for $\tilde{B}_\phi$. The left hand side of this diagram is computed by using a reference coil at one end of the array and the right hand side using a reference coil at the other end. As is apparent, the diagram is not completely symmetric, indicating that portholes, shell gaps, etc tend to introduce asymmetries which distort the ignorability of ϕ. However, by using the prescription of equations 3.25 and 3.24, we may use this graph to estimate the toroidal mode power spectrum. This is shown in figure 5.10 for a variety of different frequency ranges. It is apparent that, irrespective of the frequency range, the spectrum shows a broad band of n numbers centred on $|n| \approx 8$ with some evidence of a higher harmonic at $|n| \approx 16$. It is important to remember that, due to the finite extent of the toroidal array, the

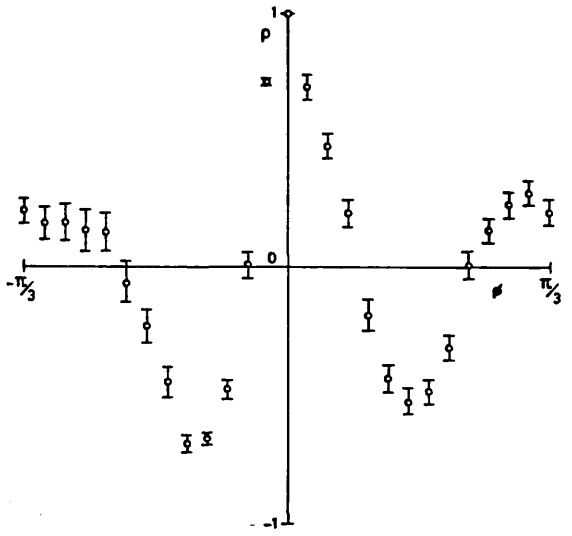

Figure 5.9 Autocorrelation in space, $\rho(\phi)$ for $\tilde{B}_\phi$ (frequency band 5-15 kHz).

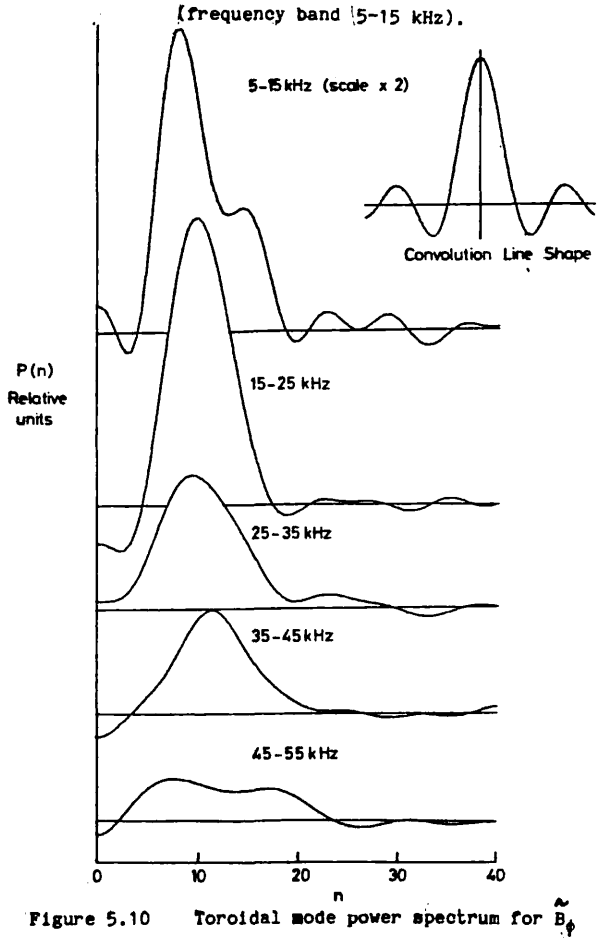

Figure 5.10 Toroidal mode power spectrum for $\tilde{B}_\phi$ for various frequency bands.

plotted spectra are in fact the 'real' spectra convolved with an instrumental function (shown in the inset). However it is clear that the width of the convolving function is less than the width of the spectrum, indicating that the real spectrum is truly broad and not simply a delta function. This is also easily seen direct from the spatial autocorrelation function since this has the form of an exponential cosine which, by definition, fourier transforms to a broad spectrum. Other features to note are the relatively higher importance of the higher harmonic at high frequencies and the near absence of any power below about $|n| = 5$. This last feature corresponds to the statement that all modes are resonant inside the plasma, given that we only have $m = 0,1$, since the q profile as measured by the probe in chapter 4 peaks at 0.2 on axis.

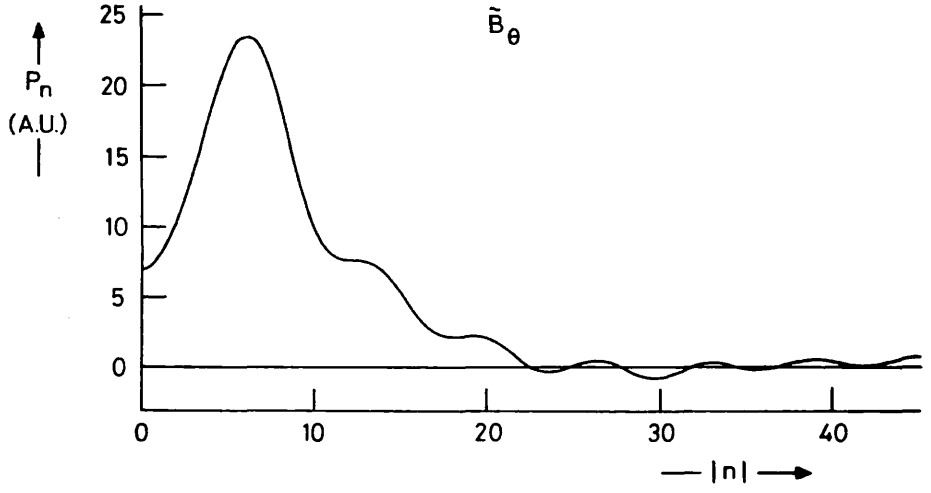

Figure 5.11 Toroidal mode power spectrum for $\tilde{B}_\theta$ for the frequency band 5-15 kHz.

Figure 5.11 shows a similar toroidal mode spectrum for $\tilde{B}_\theta$. Broadly, the characteristics are the same, although there seems to be, in addition, a very low n feature. There are two possible explanations for this. Firstly the mode could be an $m = 0$. However, if this was true, the equation $(\underline{\text{curl}}\ \underline{\tilde{B}})_r = 0$, written in cylindrical geometry, would tell us that the associated n number must also be zero. So it could be an $m = 0, n = 0$ mode,

which amounts to an oscillation of the toroidal current. The second possibility is that it is an m = 1 mode. If this was the case, the fact that this feature only appears on the poloidal component of the spectrum would naturally be explained by the low n number. Again this is simply due to the equation $(\underline{\text{curl}}\ \underline{\tilde{B}})_r=0$ which may, in fact, be written:

$$\tilde{B}_\phi = \frac{rn}{mR_o}\tilde{B}_\theta. \qquad - (5.7)$$

So we can see that for a given kink mode the power in $\tilde{B}_\phi$ is about $0.1n^2$ times the power in $\tilde{B}_\theta$, which if $|n| = 1$ would amount to a tenth. So either of these two mechanisms could account for the low n feature on $\tilde{B}_\theta$. However, as we have discussed before, the poloidal mode spectrum for $\tilde{B}_\theta$ reveals significant power in the m = 0. But by equation 5.7 we know that any m = 0 power in B_θ must also be n = 0. So given information on the poloidal mode spectra we would expect a low n feature on the $\tilde{B}_\theta$ toroidal mode spectrum due to this effect. Whether or not, however, this is augmented by a low n kink mode is not clear. We will return to this question in sections 5.1.7.1 and 5.1.8.2.

5.1.4 Helical mode structure

Although the results presented so far give a general description of the individual poloidal and toroidal structure, they do not in themselves allow us to unequivocally determine the helical mode structure and to associate given m's with given n's. As we discussed in chapter 3 this requires, in principle, a two dimensional array of measurements which can then be decomposed in helical Fourier components of the form $\exp i(m\theta+n\phi)$. Since we don't have such an array the best we can do is to calculate the Association spectrum as defined in equation 3.30 by computing the double Fourier transform of the θ-ϕ correlation matrix.

Figure 5.12 shows an example of a typical correlation matrix for $\tilde{B}_\theta$

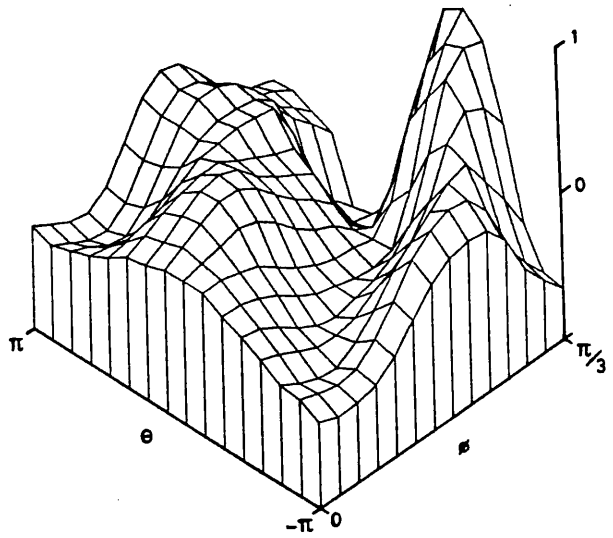

Figure 5.12

Correlation matrix for $\tilde{B}_\theta$ between the poloidal and toroidal arrays (frequency band 5-50 kHz) indicating a dominantly helical structure.

obtained from the toroidal array and an interspace poloidal array, whose cross-over point is $(\theta,\phi)=(-40°,60°)$. Clearly the diagram peaks, as expected, at the intersection point. In addition the correlation appears dominantly diagonal indicating that the structure is indeed helical.

By transforming figure 5.12 according equation 3.30 we may derive the Association spectrum. This is shown in figure 5.13. Since we have seen from the poloidal mode spectra that there is negligible power at mode numbers greater than m = 1 we adopt the policy of displaying this spectrum as several toroidal mode spectra, each pertaining to a given m number. Owing to the the fact that the correlation matrix has no imaginary part the Association spectrum respects the symmetry $A_{mn} = A^*_{-mn}$. This allows us to

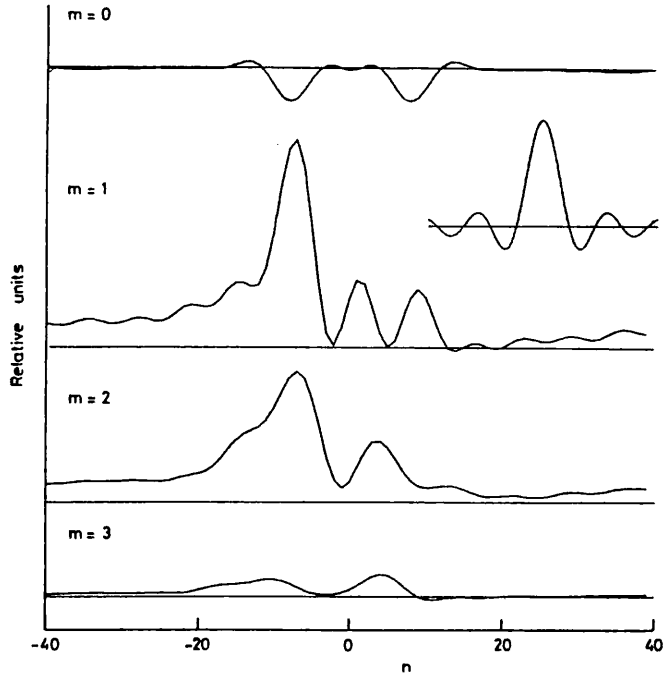

Figure 5.13 Association spectrum for $\tilde{B}_\theta$. Inset shows convolution line function (frequency band 5-50 kHz).

adopt the convention of m always being positive definite and n ranging from $-\infty$ to $+\infty$, negative n values refering to modes resonant inside the reversal surface.

It can be seen from figure 5.13 that the dominant feature is a kink mode at $n \approx -7$. As in the complete toroidal spectrum, this should not be thought of as representing one mode, but rather a broad band of instabilities, as the width of this feature is greater than the convolution function width. Indeed this feature appears to have a tail which extends out to $n \approx -20$. In addition there are also peaks near $n = 0$ and $n = +9$ on the $m = 1$ spectrum and a negative feature on the $m = 0$ spectrum coinciding with the main $m = 1$ peak. Further, the $m = 2$ spectrum appears to be a reflection of the $m = 1$.

We discussed at length in chapter 3 the various short-comings of the Association spectrum. In particular we showed that the non-ignorability of the θ coordinate, combined with the finite toroidal array length, would generate spurious features. It would thus be a mistake to interpret all the features, visible on the Association spectrum of figure 5.13, as representing independent modes with a physical existence. Indeed, we would interpret virtually all the $m = 2$ features as arising from linear coupling effects due to toroidal distortion. Also we must interpret the $m = 0$ feature as likewise spurious since, by definition, power is positive definite, and second by equation 5.7 we know that there can be no poloidal field component for a true $m = 0$, $n \neq 0$ perturbation.

The $m = 1$ features near $n = 0$ and $n = +9$ are less easily disposed of. Inspection of the correlation matrix reveals little evidence of opposite helicity modes which would be resonant outside the reversal surface. We should also note, from our studies of the equilibrium q-profile in chapter 4, that an $m = 1$ mode resonant in this region must have $n > 20$. And so, if we are to regard the $m = 1, n = +9$ feature as representing an independent mode, we must realise that it will be non-resonant. It is thus likely that this feature is an artifact arising from linear coupling

although we cannot fully rule out the possibility of it representing an independent mode. The m = 1, n ≈ 0 may well indicate a true mode, in which case it represents an oscillation of the equilibrium shift. However, again this could be explained, at least in part, by sidelobes arising from the dominant m = 1, n ≈ -7 modes.

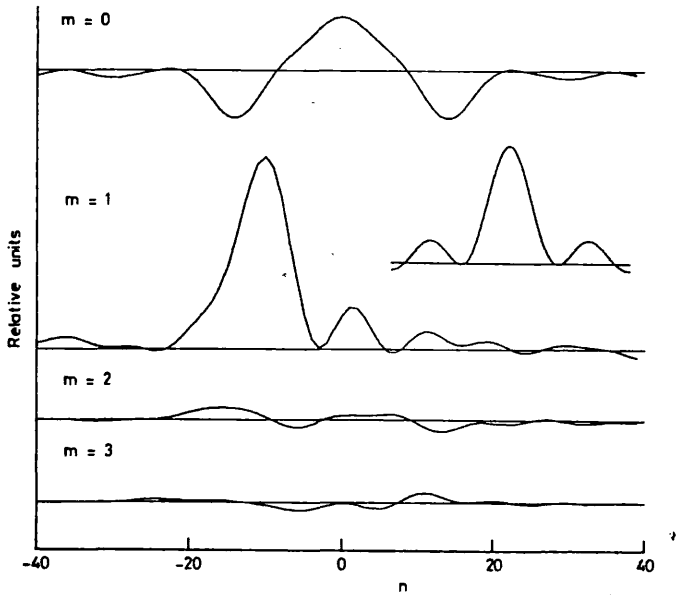

Figure 5.14 Association spectrum for B_ϕ. Inset shows convolution line function (frequency band 5-50 kHz).

Figure 5.14 shows the Association spectrum for $\tilde{B}_\phi$ obtained from an internal poloidal array and the (interspace) toroidal array. Since these two arrays are separated by the liner, we correct the resulting Association spectrum assuming a single 10 μs penetration time. The m = 1 component looks similar to the $\tilde{B}_\theta$ spectrum although the peak is shifted to n ≈ -10. This effect may be explained by $\tilde{B}_\phi$ being more sensitive to high n numbers than $\tilde{B}_\theta$ because of the direction of the perturbed field at the wall (equation 5.7). As expected from our identification of the $\tilde{B}_\theta$ m = 2 spectrum as being due to linear coupling, the $\tilde{B}_\phi$ m = 2 is much smaller, consistent with weaker toroidal distortion. There is still a negative feature on the m = 0 spectrum, slightly shifted with respect to the m = 1, n = -10 peak, the shift being explicable in terms of incomplete correction

for liner induced phase shifts. The m = 1, n = +10 peak is much less significant than with $\tilde{B}_\theta$, consistent with its interpretation as a toroidal distortion artifact. There then remains the m = 0, n ≈ 0 component which we take as real and indicating a definite contribution from those modes; and m = 1, n ≈ 0 which most probably can be attributed to toroidal distortion of the m = 0, n ≈ 0.

As we have mentioned above, these Association spectra are corrected for liner penetration effects only by assuming a single 10 μs penetration time, whereas the theoretical liner penetration time is different for different modes (see appendix B). In particular, for m = 0, n = 0 the penetration time for $\tilde{B}_\phi$ is about ten times longer, causing attenuation by a factor of ten. If this effect is allowed for, the m = 0, n ≈ 0 feature on $\tilde{B}_\phi$ is significantly enhanced over that shown.

5.1.5 Propagation

5.1.5.1 Poloidal

In order to determine propagation and rotation effects we must examine the time delayed correlation (defined in equation 3.18-3.19) between different coils in either the toroidal or poloidal arrays. Figure 5.15(a) shows the result for $\tilde{B}_\theta$ in the poloidal array for which clear evidence of rotation is found. The direction of rotation is with the electron poloidal current flow and so is in the ion diamagnetic drift direction inside the reversal surface. The rapid fall-off with time or distance of the peak value of the correlation coefficient is indicative of the relative incoherence of the modes due either to a broad spread of rotation rates or to growth and decay rates of the same order of magnitude as the rotation.

That there are different rotation rates is emphatically confirmed by figure 5.15(b) in which the time-delayed correlation for $\tilde{B}_\phi$ shows rotation

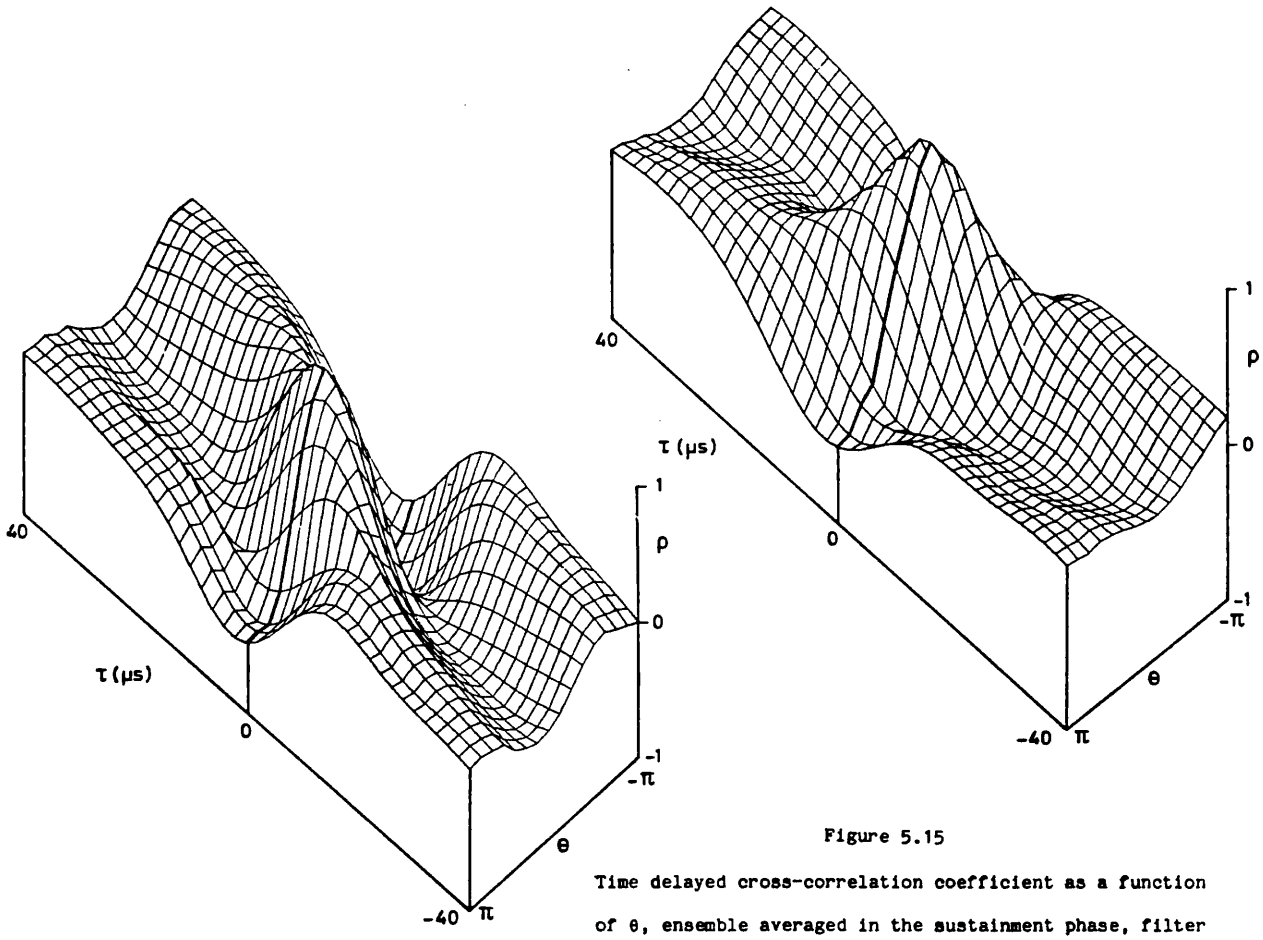

Figure 5.15

Time delayed cross-correlation coefficient as a function of θ, ensemble averaged in the sustainment phase, filter 5-50 kHz: (a) $\tilde{B}_\theta$ (b) $\tilde{B}_\phi$; showing evidence for rotation.

for nominally identical shots in the opposite direction to the $\tilde{B}_\theta$ rotation. This cannot be explained by shot-to-shot variation since this phenomenon is observed on single shots. Hence the explanation must presumably lie in the fact that $\tilde{B}_\theta$ and $\tilde{B}_\phi$ have different sensitivities to different helicities determined by the direction of the perturbed field at the wall. So we must imagine that the fluctuations to which $\tilde{B}_\phi$ is most sensitive rotate in the opposite direction to those which $\tilde{B}_\theta$ is most sensitive. Other sets of discharges of nominally similar parameters sometimes show almost no significant rotation. The reasons for this are unclear.

5.1.5.2 Toroidal

As with the poloidal array, to investigate toroidal propagation we must calculate the time delayed correlation between various coils in the

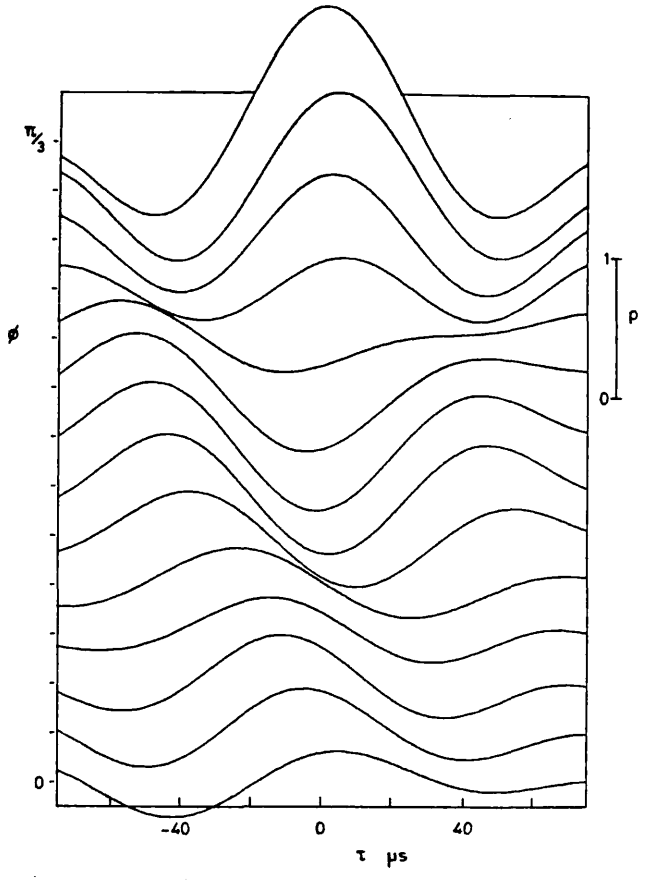

Figure 5.16

Correlation function ρ vs time delay, τ and toroidal angle, φ for $\tilde{B}_\phi$ (frequency band 5-15 kHz) showing evidence of toroidal rotation.

toroidal array. Figure 5.16 shows an example. The propagation is generally even less pronounced than that observed in the poloidal direction indicating the incoherence of the modes. At low frequencies (5-15kHz) the rotation is generally least ambiguous and the observed direction of preferred rotation is in the direction of (conventional) toroidal plasma current. The velocity is essentially given by the phase velocity of the dominant modes, consistent with the perturbations being of the form $\sin(\omega t+n\phi+m\theta)$, and is typically 10^4 ms^{-1}.

5.1.6 Evolutionary phenomena

So far we have restricted our observations to frequencies greater than about 5 kHz. This enables us to exclude the evolution of the equilibrium fields. However, on a large proportion of the discharges there exist evolutionary phenomena at frequencies as low as 1 kHz which justify the designation 'perturbation' since they are not, as such, simply evolutions of a quasi-cylindrical equilibrium.

Because these features turn out to be spatially fairly coherent, even though they exist for no more than typically one time cycle, we can illustrate their characteristics by plotting directly the temporal evolution of the edge field profiles. Figure 5.17 shows a particular clear example of polar plots from a single discharge of the toroidal field

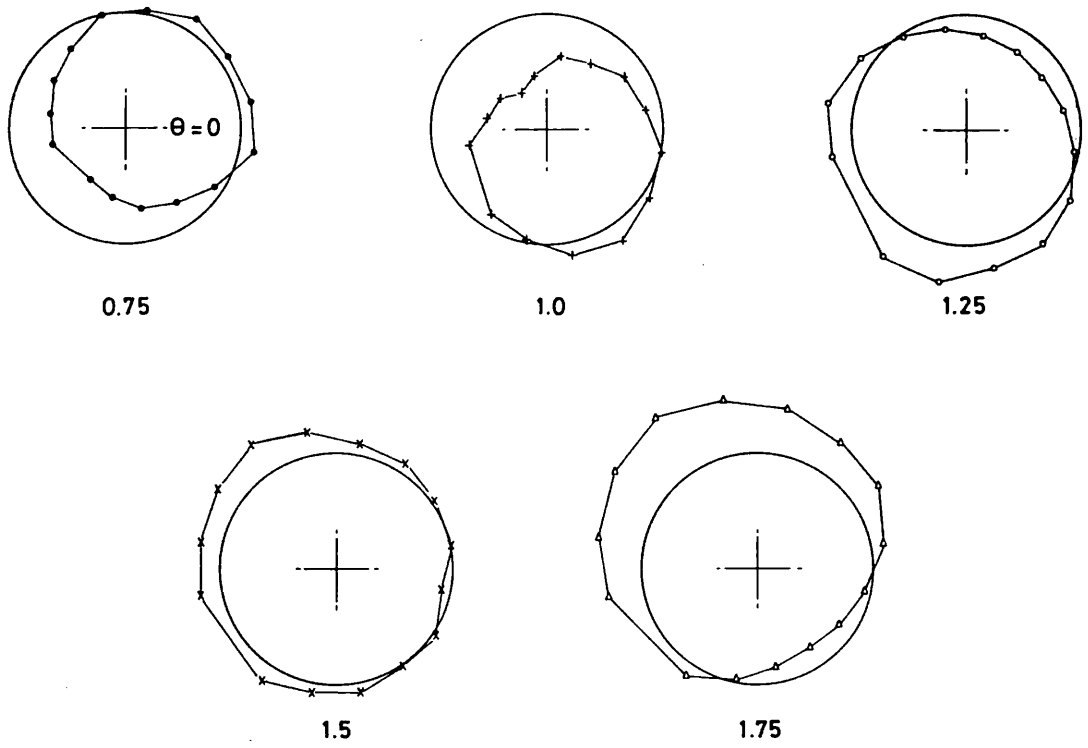

Figure 5.17 Polar plots of B_ϕ: evolution in time (ms) showing low frequency m = 1 rotation.

amplitude as a function of θ referred to the mean B_ϕ at each θ (over the time plotted) as zero. The clear m = 1 character slowly rotating in azimuth is evident from inspection. By a similar analysis using the toroidal array we are able to identify the associated n number as being n ≈ -8. Hence we should regard this evolutionary structure as an m = 1, n ≈ -8 helical mode resonant inside the reversal surface. The (peak) amplitude of this mode is sometimes as great as $\tilde{B}_\phi/|B| \approx 5\%$ which, for typical reversal levels, is $\tilde{B}_\phi/|B_\phi|_a \approx 50\%$. These perturbations tend to be present only during the first msec or so of the sustainment phase, their amplitude decaying with time.

A second point which must be emphasised under the heading of evolutionary phenomena concerns the various spectra presented earlier. These are time and shot averages over typically 1 ms and 5 - 10 shots. However, we find that the characteristics of the fluctuations vary with time in a systematic though not reproducable manner. Indeed the

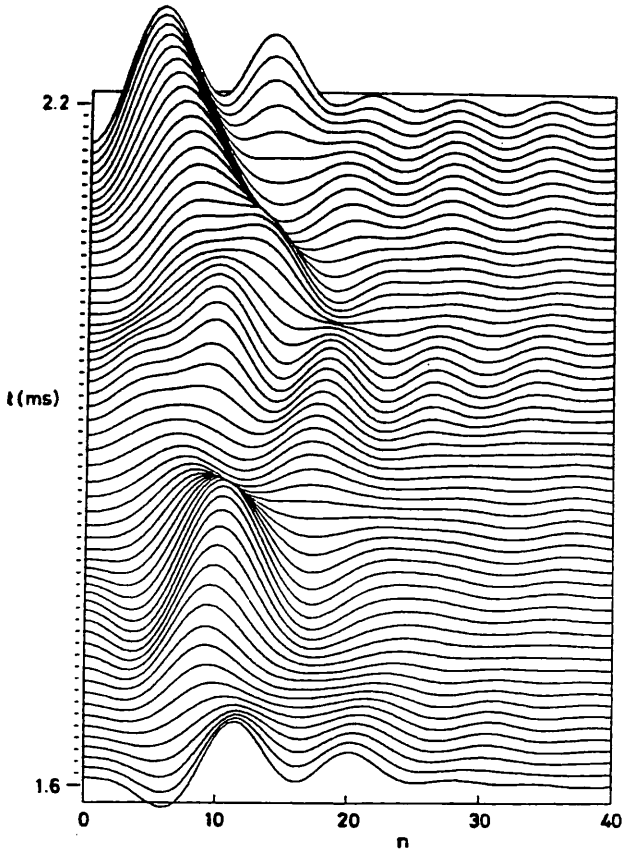

Figure 5.18
Time evolution of the n-spectrum for B_ϕ (frequency band 5-50 kHz).

fluctuations occur in bursts separated by quieter periods and are not in the statistical sense stationary random signals. One striking observation is a form of cyclic behaviour in the evolution of the n-spectrum. Figure 5.18 shows this evolution, the individual n-spectra being calculated by a sliding average over 128 μs during a period of 0.6 ms in the sustainment phase. During this period the spectrum evolves from single-peaked high power to double-peaked lower power and back again, going through about two cycles in 0.6 ms. The average spectra of figure 5.10 are dominated at lower frequencies by the higher power single peaked type of spectrum but it is evident that at other times, other wave-numbers are dominant.

5.1.7 Fluctuations In Different Discharges

Up until now we have only discussed 'optimal' discharges characterised by a toroidal plasma current of 200 kA and a value of the pinch parameter, Θ, of about 1.8. In this section we will discuss the differences observed in the structure of the fluctuations in different discharges. In particular we will present the results from a series of scans carried out by varying the pinch parameter, plasma current and filling pressure.

5.1.7.1 Variation of θ

Figure 5.19 shows the variation with θ of the rms fluctuation level (filtered in the band 3 - 250 kHz). Clearly the optimum value of θ is about 1.7 - 1.8, corresponding to a minimum in the fluctuation activity. Thus, as we decrease or increase θ away from this optimum value the level of fluctuations begins to rise. To see if this increase in the absolute level of fluctuations corresponds simply to an increase in the amplitude of the mode structure we have previously discussed, or whether it signifies the onset of fundamentally new phenomena, we may plot the m and n spectra for a variety of θ values. This is shown in figure 5.20 for $\tilde{B}_\theta$ and figure 5.21 for $\tilde{B}_\phi$.

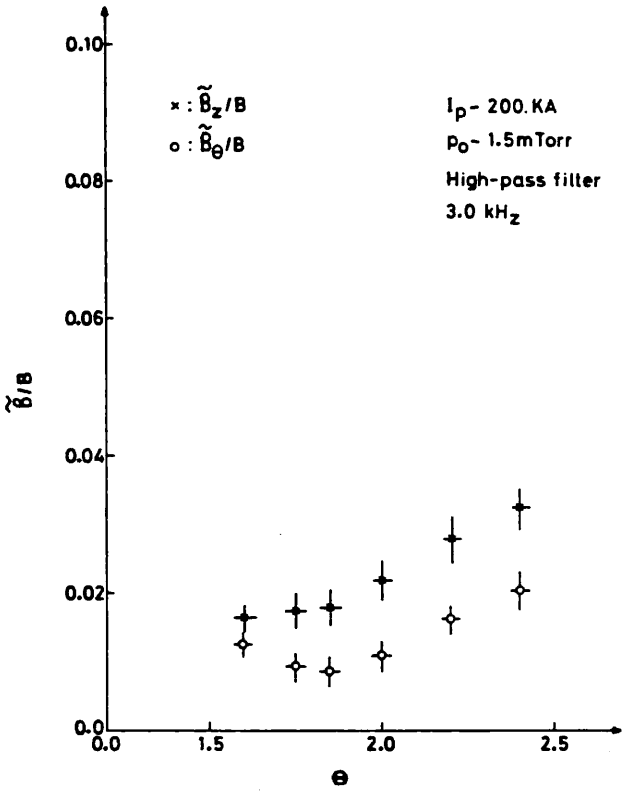

Figure 5.19
Variation of $\tilde{B}/|B|$ with θ (p_o = 1.5 mTorr, I_p = 200 kA).

Clearly the main m = 1, n = -8 mode remains broadly the same with variation in θ. However, as θ increases the n ≈ 0 feature on the $\tilde{B}_\theta$ spectrum grows, until at θ = 2.4 it is of the same amplitude as the n ≈ -8. The $\tilde{B}_\phi$ n-spectrum does not show this feature indicating that the responsible mode is either an m = 0, n = 0 or a low n m = 1 mode. However, since the m = 0 component of the $\tilde{B}_\theta$ m-spectrum does not increase appreciably with θ, we must favour the m = 1, n ≈ 0 explanation. The exact n number we should associate with this mode is unclear. Maximum Entropy spectra indicate |n| ≈ 3. In order to substantiate this, however, we may plot a complete toroidal spatial autocorrelation function by correlating coils in the toroidal array with other coils from various arrays at the same poloidal angle around the

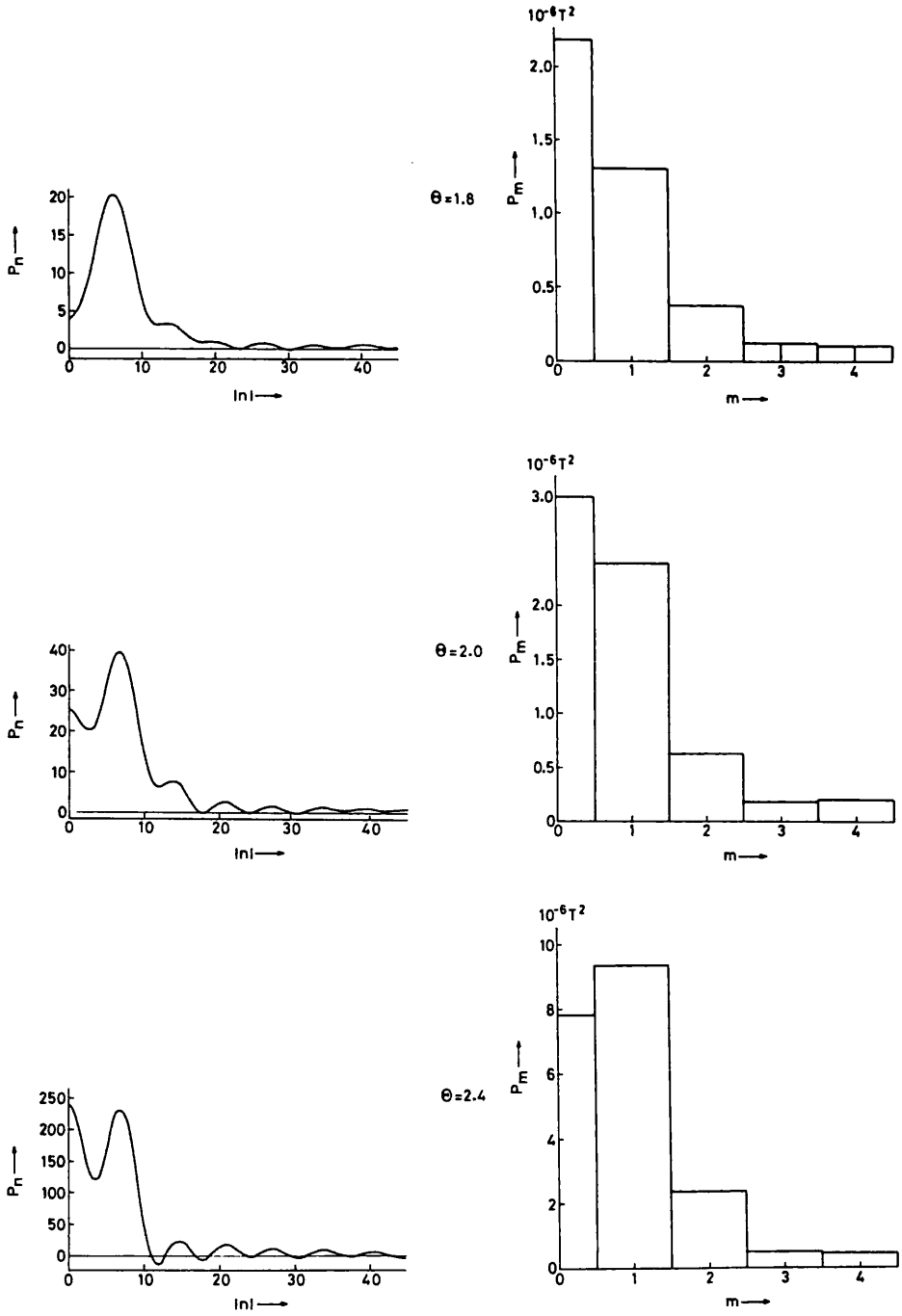

Figure 5.20 Toroidal and poloidal mode spectra for $\tilde{B}_\theta$ (frequency band 5-50 kHz) in the sustainment phase for several different values of θ (p_o = 1.5 mTorr, I_p = 200 kA).

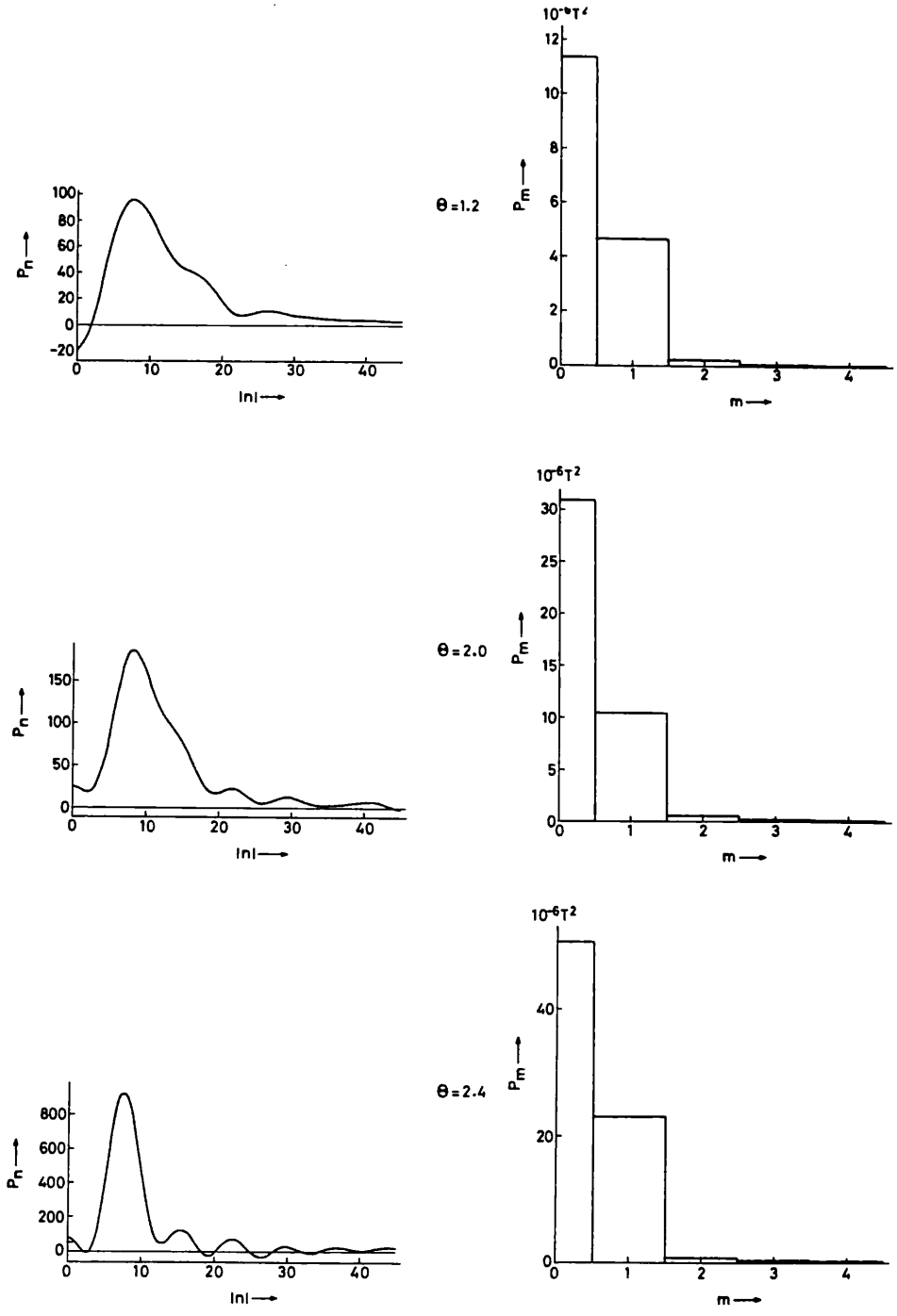

Figure 5.21 Toroidal and poloidal mode spectra for $\tilde{B}_\phi$ (frequency band 5-50 kHz) in the sustainment phase for several different values of θ (p_o = 1.5 mTorr, I_p = 200 kA).

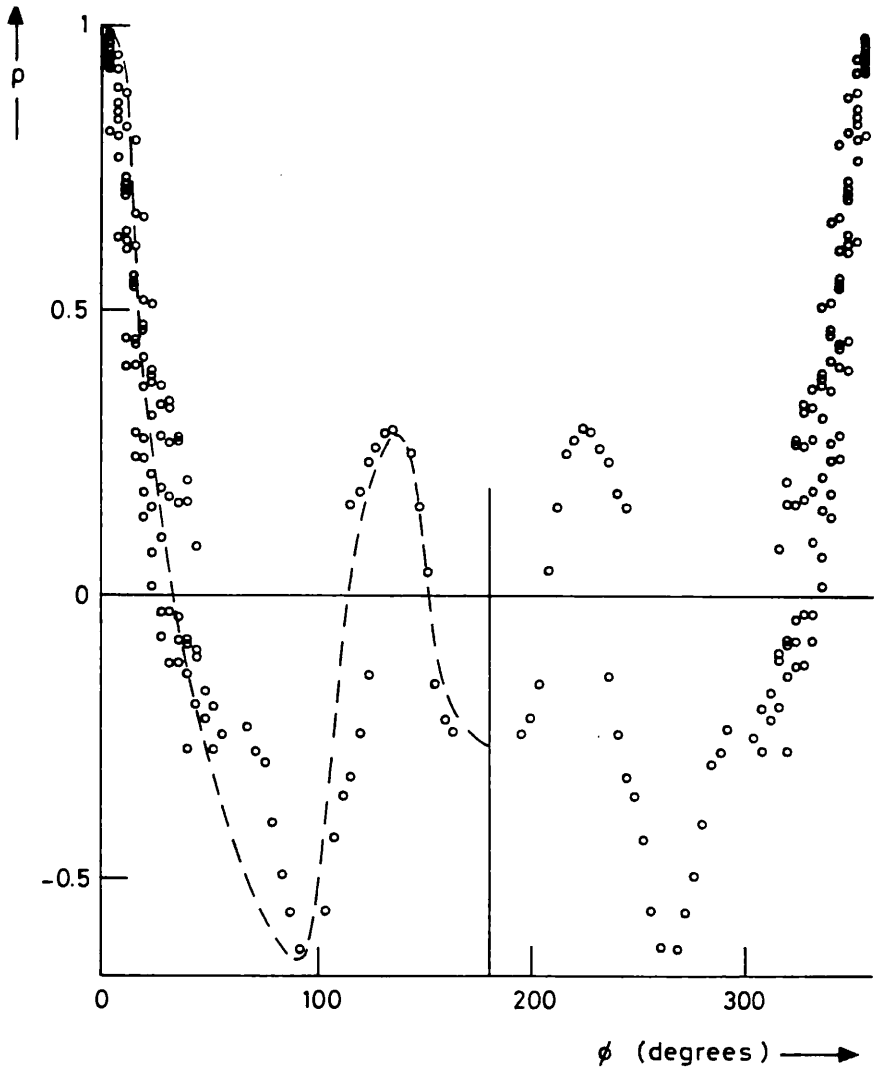

Figure 5.22 Complete toroidal autocorrelation for $\tilde{B}_\theta$ in the sustainment phase (frequency band 5-50 kHz). Each point represents a correlation between two coils displaced toroidally.

machine. In principle we could then fourier transform this to provide the exact (perfect resolution) n-spectrum. Figure 5.22 shows an example of this for $\Theta = 2.4$. Clearly there are large errors due to port holes and shell-gaps distorting the ignorability of ϕ. However, by inspection of this spatial correlation we can see that the dominant long wavelength mode is an $|n| \simeq 2\text{-}3$.

By forming the Association spectra for these high Θ discharges we are able to show that this mode has the same sign of helicity as the previous $m = 1$ modes. From calculations of the safety factor, q, on axis using the Bessel Vacuum Model (BVM) we may deduce that this mode is non-resonant.

Another feature of interest is that as Θ is increased, the width of both the $\tilde{B}_\theta$ and the $\tilde{B}_\phi$ $|n| \approx 8$ features decrease. Thus, as the absolute amplitude of these modes increases, so the actual number of modes seems to decrease.

5.1.7.2 Variation Of Plasma Current And Filling Pressure

Figure 5.23 shows the variation of the rms fluctuation level with plasma current, I_p. The variation is consistent with previous measurements [1] which showed two regimes, one at low current where $\tilde{B}/|B|$ scales approximately as I_p^{-1}, and another at high current where the scaling is much weaker. By calculating the various mode spectra for different values of I_p we find that there is no significant variation in the actual structure of the fluctuations.

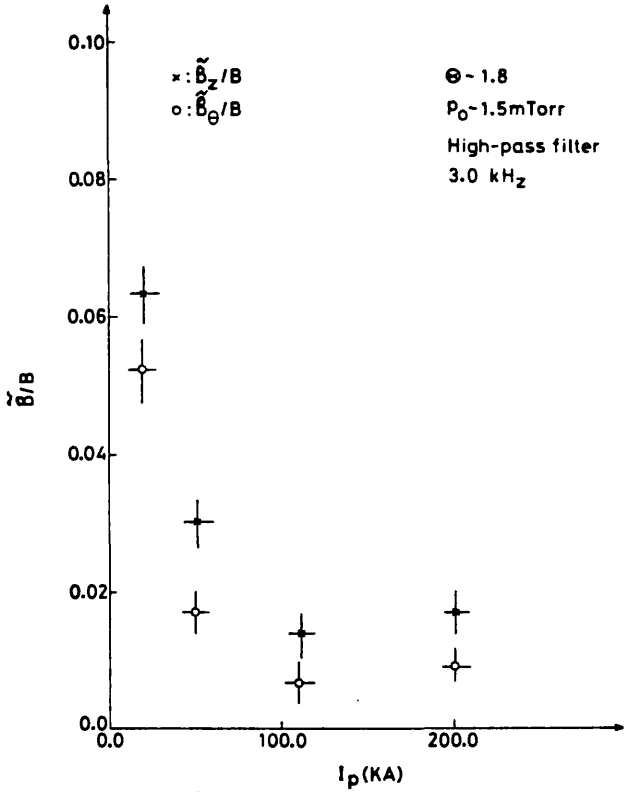

Figure 5.23

Variation of $\tilde{B}/|B|$ with plasma current I_p (filter: 3-250 kHz, θ = 1.8, p_o = 1.5 mTorr).

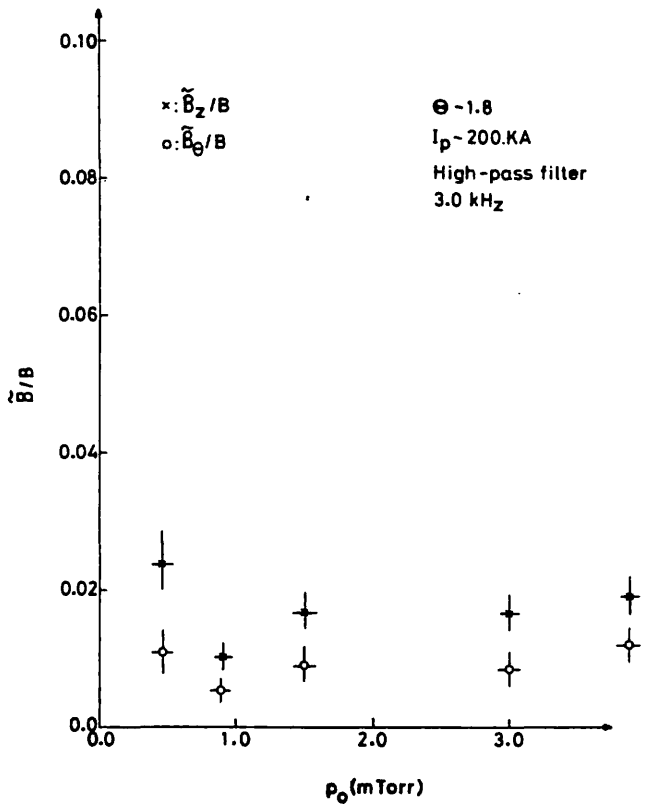

Figure 5.24

Variation of $\tilde{B}/|B|$ with filling pressure p_o (filter: 3-250 kHz. θ = 1.8, I_p = 200 kA).

Figure 5.24 shows the rms fluctuation level as a function of filling pressure. Unfortunately, at the time of the scan, there was no independent measurement of the electron density and so the relatively flat nature of this graph could be explained by differing amounts of pumpout. Again, a full calculation of the various mode spectra at different filling pressures reveals no significant changes in the fluctuation structure.

5.1.8 Termination And Set-up Phases

So far we have been concerned only with the sustainment phase of the discharge. In this section we turn to the more turbulent phases of the discharge where the reversed field configuration is first set up (the set-up phase) and when the discharge violently ends (the termination phase). In both these regions of the discharge the rms value of the fluctuation level is about 5 to 10 times higher than in the sustainment phase. However, as we shall see, different processes appear to be occurring in each phase.

5.1.8.1 Set-up Phase

Figures 5.25 and 5.26 show examples of the n amd m spectra for B_θ and B_ϕ respectively in the set-up phase. It is clear that the general picture is

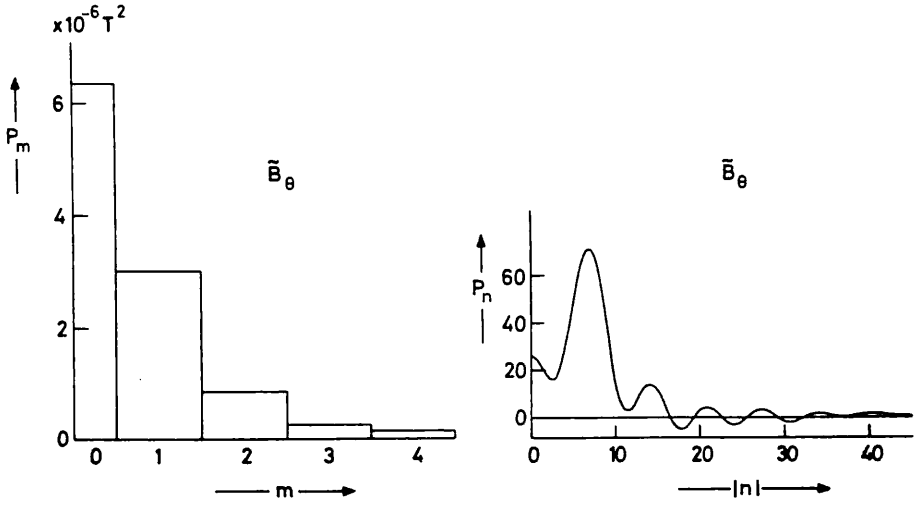

Figure 5.25 Poloidal and toroidal mode power spectra for $\tilde{B}_\theta$ in the set-up phase (frequency band 5-50 kHz).

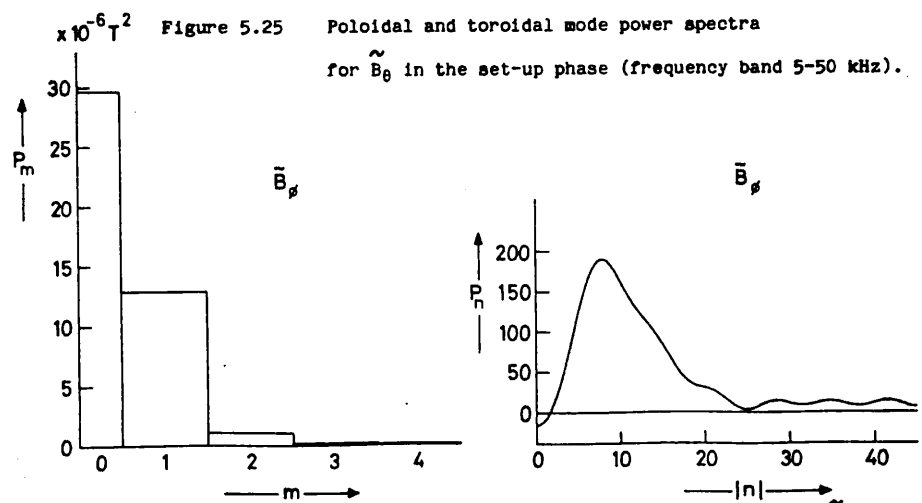

Figure 5.26 Poloidal and toroidal mode power spectra for $\tilde{B}_\phi$ in the set-up phase (frequency band 5-50 kHz).

fairly similar to the sustainment phase but with a higher amplitude of fluctuations. In particular there do not seem to be any low n kinks as observed above at high values of the pinch parameter. A power spectrum analysis also reveals no qualitative change in frequencies from sustainment.

5.1.8.2 Termination Phase

In figure 5.27 we plot on a relative scale, power spectra for the termination and sustainment phases. Clearly, for termination, the shape is significantly altered, showing a rise up to about 50 kHz; thus high frequencies become more important. Another characteristic of the termination phase is that the rotation is much more coherent. This is shown clearly on the time delayed cross-correlations illustrated in figure 5.28. The rotations are always in the same direction during termination, being toroidally in the direction of electron current flow and poloidally in the electron diamagnetic drift direction.

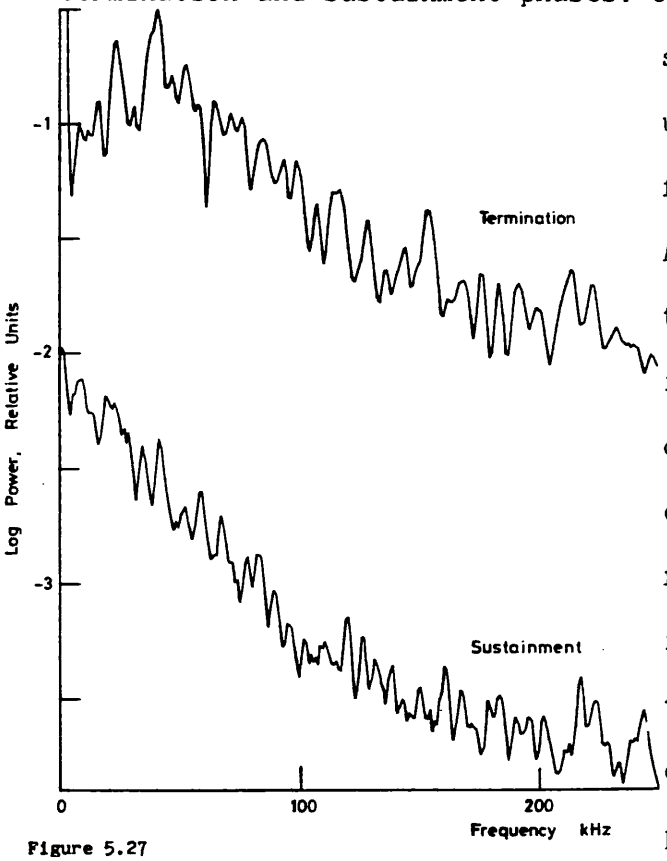

Figure 5.27
Relative power spectra for B_θ during the sustainment phase and termination.

Another effect which shows clearly in figure 5.28 is that the toroidal wavelength and coherence length increase. This is a progressive effect but of course our figure captures only one period during the current decay. At the time of figure 5.28 θ is about 1.0. The poloidal structure is always dominantly $m = 1$ and the helicity corresponds to negative n; For figure 5.28 $n \approx -3$ to -4 for $\tilde{B}_\phi$ and ≈ -1 to -2 for $\tilde{B}_\theta$.

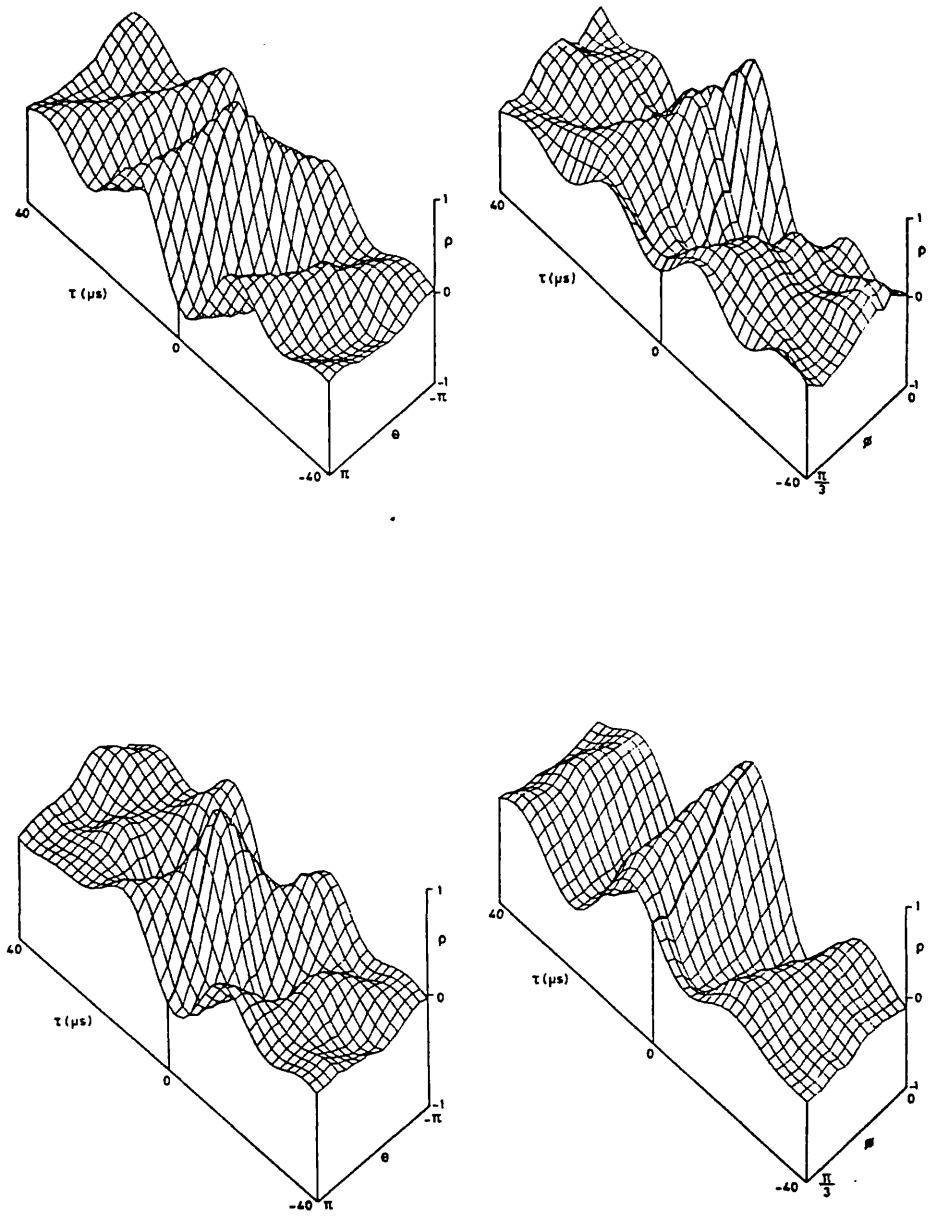

Figure 5.28 Time delayed cross-correlation coefficient for $\tilde{B}_\phi$ (top) and $\tilde{B}_\theta$ (bottom) as a function of θ (left) and φ (right) during the termination phase (filter: 5-50 kHz).

In order to investigate more thoroughly the spatial and temporal structure of the fluctuations in the termination phase of the discharge we adopt the policy of defining three time regions of equal length, measured from the time at which reversal is lost. In general each shot in an ensemble will then have different times associated with each such region since reversal is lost at slightly different times for each discharge. This enables us to distinguish phenomena which occur before and after the loss of

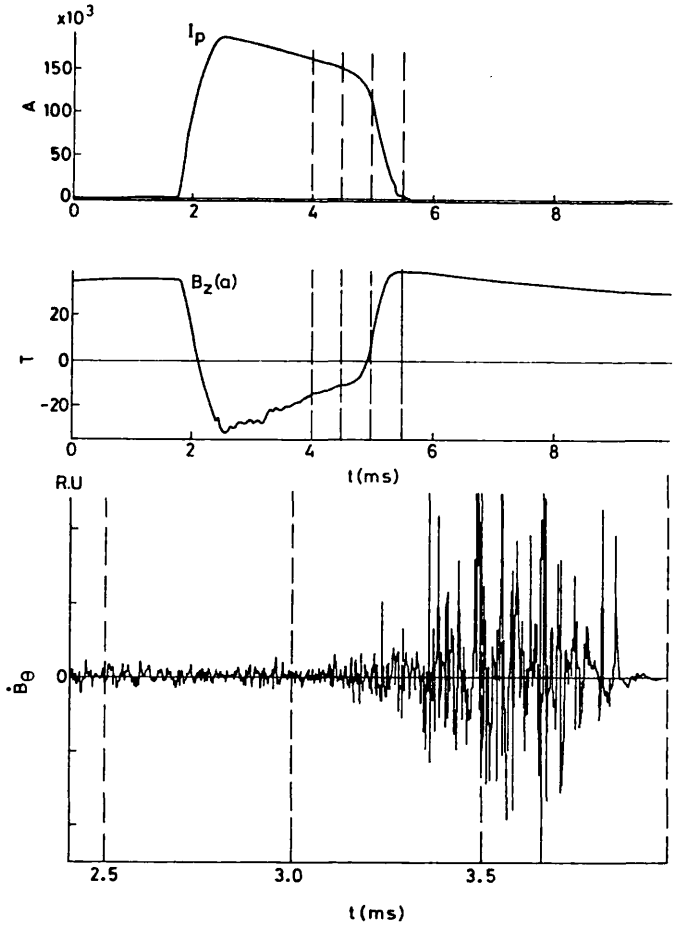

Figure 5.29 Magnetic fluctuations in termination.

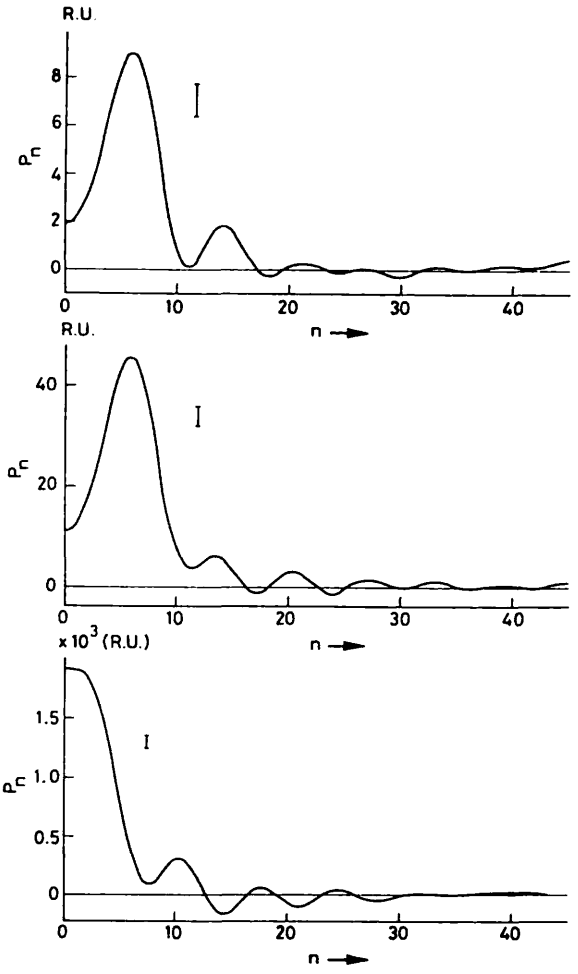

Figure 5.30
Evolution of toroidal mode spectrum for $\tilde{B}_\theta$
(time slots shown in 5.29, filter: 5-50 kHz).

field-reversal. Figure 5.29 shows these time regions in relation to the traces of $B_{\phi w}$ and I_p for a typical shot. Figure 5.30 shows the evolution of the $\tilde{B}_\theta$ n-spectrum. In the first time region (end of sustainment) the dominant activity is the usual $|n| \approx 7$, $m = 1$. This remains the same until the third time region, after the loss of reversal. Here the n-spectrum shows the presence of low n features; Maximum Entropy and total toroidal autocorrelation studies indicate $|n| = 2\text{-}3$ and Association spectrum studies indicate $m = 1$.

By performing a similar 'relative time slot' analysis for the power spectrum we are able to associate the appearance of high frequencies (as in figure 5.27) with solely the second time interval.

5.2 DISCUSSION

The measurements reported in this chapter show that the fluctuation activity is attributable to low poloidal mode numbers M_0 and M_1 corresponding to the fourier modes m = 0 and m = 1 along with their concomitant toroidal distortions. Of course, the nature of our measurements naturally favour large scale perturbations such as these, since fine scale perturbations originating well inside the plasma will generally fall off more rapidly with radius and would therefore be proportionately smaller at the edge. In chapter 6 we will see that these internal fluctuations are indeed present and that they are in fact negligible at the wall.

We have seen that the difference between the poloidal mode spectra for $\tilde{B}_\theta$ and $\tilde{B}_\phi$ for m > 1 is explicable by consideration of the details of the toroidal distortion effects. In particular we have shown that writing the condition $(\underline{\text{Curl}}\ \underline{\tilde{B}})_r = 0$ in toroidal geometry provides a relationship between the fields outside the plasma for a given helical mode. Hence, if we assume that $\tilde{B}_\phi$ is purely m = 1 then $\tilde{B}_\theta$ will have an m = 2 component of amplitude a/R_o. That the toroidal distortion of $\tilde{B}_\theta$ is stronger than $\tilde{B}_\phi$ cannot, a priori, be explained by this simple relation, but rather must be determined by a full set of equations describing the behaviour of the plasma. The outward (Shafranov) shift of the plasma in the shell is at least partly responsible for these toroidal distortions but this cannot be easily distinguished from the departure of the internal mode structure from the quasi cylindrical approximation. Experiments conducted with a vertical field to centre the plasma and hence remove any shift should be able to shed light on this area.

Perhaps the major advance of this work is the detailed information we have obtained on the toroidal mode structure. In order to see the significance of this we need to consider the radial profile of the safety factor,q. Now it is well known that the RFP relaxes to a configuration which

may be satisfactorally described by various quasi-cylindrical models such as the MBFM [2] or the BVM. For discharges of interest calculations using these models indicate that the on-axis q is about 0.2 and that the reversal surface where q = 0 is at about r/a = 0.75. At the liner q ≈ -0.04. In chapter 4 we measured the q-profile for low-current passive decay discharges where very similar results were obtained.

Helical perturbations are resonant at a radius where the equilibrium field-line pitch matches the pitch of the perturbation. This means that a mode characterised by poloidal and toroidal mode numbers m and n will be resonant at a radius where q = -m/n. At this radius non-zero radial magnetic field perturbations will lead to the formation of magnetic islands by the 'tearing' of magnetic field lines. Our main peak in the n spectrum at n ≈ -10 is a mode which is resonant at r/a ≈ 0.5 and the broad spectrum which we see extending from n ≈ -5 to -20 indicates modes which are resonant at radii from r ≈ 0 out to quite close to the reversal surface. We cannot exclude, with our modest resolution, modes which are non-resonant (i.e. $|n| < 5$) but their contribution in the sustainment phase and at optimum values of Θ is at any rate small. However, in the termination phase of the discharge and at high values of Θ m = 1 modes of n ≈ -3 are found which may well be non-resonant although there is significant doubt concerning the estimates of q. Nevertheless these modes appear to share the same timescales as the other resonant modes. In addition to the m = 1 modes the m = 0 perturbations are always resonant at the reversal surface.

The perturbations we see seem to correspond qualitatively quite well with the expectations of resistive instability theory [3] in that we see m = 1 perturbations resonant from the origin out to near the reversal surface and also m = 0 perturbations of long toroidal wavelength. For the wide range of discharges studied here we have not observed perturbations resonant outside the reversal surface although the statistical accuracy of our measurements only allows us to put an upper bound of 5% of the fluctuation

power in such modes. This corresponds to an rms amplitude of $\tilde{B}/|B| < 0.2\%$. In chapter 6 we will return to the problem of comparing the observed fluctuations with that predicted by a linear stability analysis of the measured equilibrium.

It is possible to obtain an estimate of the growth (and decay) times for the dominant fluctuations by inspection of the frequency spectra presented. Taking the overall width of the spectrum as the relevant frequency spread (30 kHz) this gives a growth time of about 5 μs. Alternatively, taking the individual features to define the spread yields 30 μs. This should be compared with the poloidal Alfven transit time of about 0.5 μs and Lundquist number $S \approx 10^5$ (valid for the 'optimal' discharges). Taking our second estimate of the growth time as being the more relevant this corresponds a value of $S^{-1/3}$ in resistive units. This suggests, although it is admittedly only a single point, that we should take the perturbations as being 'resistive' rather than ideal MHD in character. Of course, the states we are observing are non-linear and so this distinction is of debatable significance except that we may assume that changes in magnetic topology occur. In chapter 6 we shall see that this resistive character is confirmed for the dominant instabilities although evidence will also be presented to show that there is an 'ideal' type component at lower powers.

The present analysis does not allow us to distinguish whether the $m = 0$ perturbations arise independently from the $m = 1$ or as a non-linear consequence. Preliminary studies employing toroidal mode bispectra and triple correlations, although not reported here, have shown disappointing results. Much further study is needed in this area. In addition we are not able, as such, to distinguish the driving energy sources for any of the perturbations which provide the usual theoretical distinction between tearing and pressure driven g-modes.

Given that we believe that the dominant perturbations are of a resistive nature it is interesting to estimate the island size. In principle we could

integrate the linearised forms of Curl (JxB) =0 and Div (B) = 0 from the wall to the resonance to find $\tilde{B}_r(r_s)$. However, as we shall see in chapter 6 and as tearing mode studies [3] have shown in the past, the radial derivative of $\tilde{B}_r$ is approximately constant outside the resonant surface for modes whose resonance is not too close to the axis. Hence given that we measure our fluctuating fields near to the shell where $\tilde{B}_r = 0$, the equation Div $(\tilde{B}) = 0$ alone allows us to estimate $\tilde{B}_r(r_s)$ by linear interpolation. Thus:

$$\tilde{B}_r(r_s) = (a-r_s)\left| \frac{m}{r} \tilde{B}_\theta + \frac{n}{R_o} \tilde{B}_\phi \right|_a \quad . \qquad - (5.8)$$

The island width, W, is then given by the standard linear formula [4]:

$$W = 4 \left| \frac{\tilde{B}_r r_s q}{m \tilde{B}_\theta q'} \right|^{1/2} \quad . \qquad - (5.9)$$

For m = 1, n ≈ -10, typically $|r_s q/q'| \approx 1$ and $\tilde{B}_\theta(r_s) \approx 1.5|B(a)|$ so:

$$W/r_s \approx 4\left|\tilde{B}/B\right|_a^{1/2} \quad . \qquad - (5.10)$$

In order to determine the amplitude $|\tilde{B}|$ to be ascribed to each mode we may assume that 1/2 of the 2% rms fluctuation level is attributable to m = 1 and take this as being spread over about six toroidal modes as indicated by the n-spectrum. This then indicates a single mode rms level of $2/\sqrt{12} \approx 0.5\%$ which gives an island size of $W/r_s \approx 0.3$.

The separation, δ, of (m = 1) resonant surfaces in this region of the plasma is given by:

$$\delta = q^2/q' \approx 0.1 r_s \quad . \qquad - (5.11)$$

Thus the island overlap condition [5] $W > \delta$ is easily satisfied, corresponding to a value of the stochasticity parameter of ≈ 3. If the

different helicities are simultaneously present with this typical amplitude we would thus expect the magnetic field lines to be stochastic throughout the region occupied by the m = 1 resonances and that magnetic surfaces should no longer exist. That the different helicities are simultaneously present is not immediately obvious in view of the 'bursting nature' revealed by the evolutionary n-spectrum. However, it seems most improbable that the different modes would be sufficiently separated in time for stochasticity to be avoided. Estimates of the m = 0 island sizes give similar values for W, though in this case we are less certain of the resistive MHD character. Indeed, much of the M_0 power may arise non-linearly from the M_1.

So we have shown that, assuming simultaneity of the various m = 1 helicities, the central region of the plasma is expected to be stochastic and hence a field line passing through the centre of the discharge will eventually pass through all other points in the stochastic region. Further assuming that this stochastic region extends to the edge of the plasma enables us to calculate an energy confinement time determined by stochastic diffusion. Of course, if only the central region of the plasma is stochastic, this being surrounded by an insulating non-stochastic layer, then our estimate will not apply. However, adopting this assumption we may express the field-line diffusion coefficient quite generally as (see appendix D):

$$\langle \Delta r^2/L \rangle = \left\langle \left| \frac{\tilde{B}_r}{B} \right|^2_{r_s} \right\rangle \Lambda_{,,} \quad , \qquad - (5.12)$$

where $\Lambda_{,,}$ is the parallel coherence length. Now since $\Lambda_{,,} = \Lambda_\phi B/B_\phi$, where Λ_ϕ is the toroidal correlation length,

$$\langle \Delta r^2/L \rangle = \left\langle \left| \frac{\tilde{B}_r}{BB_\phi}^2 \right| \right\rangle \Lambda_\phi \quad . \qquad - (5.13)$$

Taking $r_s = a/2$, $\Lambda_\phi = 2a$ and using our previous arguments to relate the values of $\tilde{B}$ at r_s to those at the wall this becomes:

$$\langle \Delta r^2/L \rangle \approx a \left| \frac{\tilde{B}}{B} \right|_a^2 \quad . \qquad - (5.14)$$

From this we may calculate the effective perpendicular energy diffusivity [6] $\chi_{eff} \approx v_{eT} \langle \Delta r^2/L \rangle$ (assuming a collisionless regime) where v_{eT} is the electron thermal speed. For $|\tilde{B}/B|_a = 0.01$ and $T_e = 100$ eV this leads to an estimate of the energy confinement time,

$$\tau_E = a^2/(8\chi_{eff}) \approx 50 \ \mu s \ . \qquad - (5.15)$$

This value, while being consistent with experimentally observed parameters, should be regarded as an order of magnitude estimate only because of the sensitive (squared) dependence on $\tilde{B}_r$ which has been estimated somewhat crudely. Nevertheless it should be pointed out that this is a direct estimate based on the measured longitudinal correlation lengths and not, like earlier stochastic transport estimates[7,8], on theoretical estimates of longitudinal correlation.

Given that the m = 1 modes observed above 5 kHz lead to stochastic behaviour, it is of interest to estimate the island size for the larger slowly rotating perturbations that we discussed under 'evolutionary phenomena'. The linearised estimates are somewhat questionable for such large perturbations but nevertheless, taking the peak perturbation amplitude we obtain $W/r_s \approx 1$. This is about 3 times the size of our smaller scale m = 1 islands and as such this island would not quite overlap the reversal surface.

The poloidal and toroidal propagation effects that we have observed seem to be consistent with the magnitude expected from estimates of the diamagnetic drifts. However the ambiguity of direction observed indicates that a simple interpretation in terms of these drifts is hardly adequate. It should be noted that the magnitude of plasma rotation can also be explained as being due to an electrostatic potential of about 100 V.

Results from a systematic scan over different discharges have shown the mode numbers and frequencies of the dominant fluctuations to be relatively invariant with respect to changes in plasma parameters. This emphasises the fundamental nature of these instabilities. The observation at high values of Θ of a low-n non-resonant kink mode is interesting as the characteristic frequencies associated with this mode are resistive rather tham ideal.

Investigations into the set-up and termination phases of discharges indicate that the structure of the global fluctuations in the set-up and sustainment phases is very similar whereas fundamentally different processes appear to be occuring in the termination phase. If we thus assume that the observed global modes are indeed a vital ingredient to the reversal process, this indicates that the production and sustainment of reversal rely on the same mechanism.

Finally the apparently cyclic behaviour observed in the evolution of the n-spectrum leads to a rather persuasive picture of the overall behaviour. Suppose that the evolution of the field profiles leads to a situation in which resistive $m = 1$ modes at $r/a \approx 0.5$ are preferentially destabilised. These modes will then grow for a time (the linear phase) after which quasi-linear effects dominate and the modes stabilise themselves via non-linear modifications to the profiles. Their amplitude then decreases. However the profile changes tend to destabilise other modes (with n greater and smaller). These other modes then grow and, in a similar fashion, enforce profile changes which compete with those of the first modes. This competition continues, establishing a quasi-equilibrium in which cyclic variations of mode-amplitude maintain the mean profile such that no set of modes achieves complete dominance. The quasi-linear tearing [9] and g-mode [10] effects discussed in chapter 1 would certainly substantiate this type of picture and indeed theoretical ideas of such cyclic processes have been proposed [11] in the context of the Tokamak disruptive instability. However, here we seem to have direct experimental evidence in

the RFP for the importance of this MHD mode competition.

5.3 CONCLUSIONS

Results from an extensive analysis of edge coil measurements have been reported. In the sustainment phase of the discharge it has been shown that the superficially random fluctuations are attributable to global modes of poloidal mode number $m = 0$ and $m = 1$ provided account is taken of the toroidal distortion. A toroidal array of edge coils shows a broad spectrum of toroidal mode numbers with a peak at $|n| \approx 10$ and significant variation with time and frequency. Cross correlation establishes that the $|n| \approx 10$ is $m = 1$, a set of helical modes resonant inside the reversal surface and also shows the presence of $m = 0$, $|n| \approx 0$. Further studies indicate that the $m = 0$ feature is composed of two linearly independent modes, the first being an $n = 0$ $\tilde{B}_\theta$ oscillation and the second an $|n| \approx 0$ $\tilde{B}_\phi$. Timescales of the measured fluctuations indicate that the instabilities are probably resistive in character and mode amplitudes are such that island overlap and magnetic field ergodization should occur. The energy confinement time due to stochastic transport, estimated directly from the measured fluctuations, is consistent with that experimentally observed.

Studies of edge magnetic fluctuations have been applied to discharges of differing conditions and in the termination and current set-up phases. With respect to change in I_p and p_o, the mode numbers and frequencies of the fluctuations appear invariant. At high values of Θ, however, an $m = 1$, $n \approx -3$ mode becomes of equal significance to the more usual $m = 1$, $n \approx -10$ activity. Although the observed timescale of this mode appears 'resistive' estimates of the safety factor indicate that these modes are not resonant. The mode numbers and frequencies of the global fluctuations in the current set-up phase appears very similar to those during sustainment although the amplitude is higher. However, in the termination phase the observed

fluctuations show several differences. Nevertheless, after reversal is lost the observed frequencies correspond to resitive timescales rather than the Alfven timescales expected for ideal modes.

CHAPTER 6

INSERTABLE PROBE MEASUREMENTS

We now turn to an investigation of the radial structure of the magnetic fluctuations by an analysis of data from the insertable probe. This is principally accomplished by the technique of correlation matrix fitting (CMF) developed in chapter 3. The problem of the linear stability of the equilibrium configuration measured in chapter 4 is also addressed. The results presented in this chapter pertain to the same type of low current discharges discussed in chapter 4.

6.1 RESULTS

6.1.1 Time History Analysis

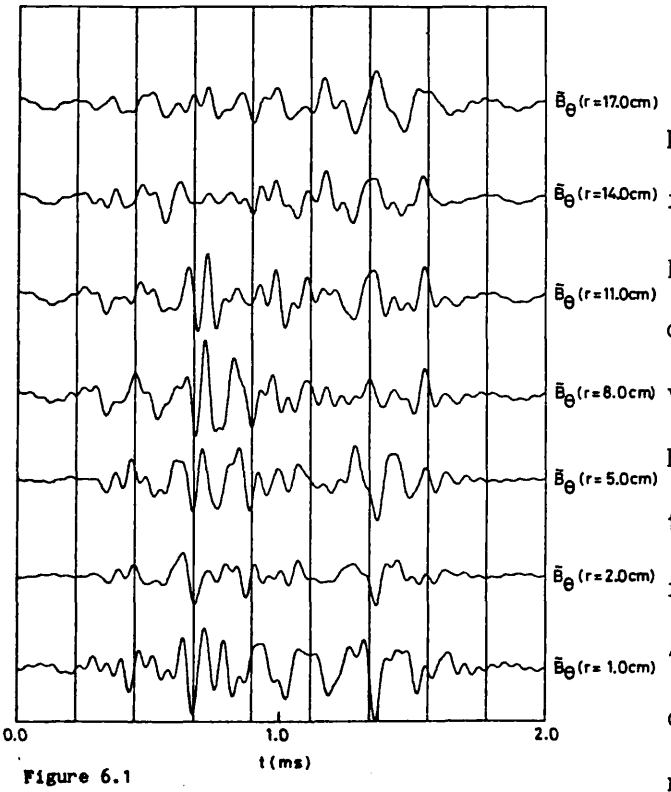

Figure 6.1

Filtered time histories (frequency band 4-20 kHz) of 7 $\tilde{B}_\theta$ probe traces from the probe.

The most obvious way of analysing probe data is to look for similarities in the individual time histories pertaining to a single shot. This type of analysis has, for instance, been very successful in Tokamaks. Figure 6.1 shows an example of this technique for the $\tilde{B}_\theta$ signals obtained from the probe in the frequency range 4-20 kHz. It is clear from this diagram that there is no unique relationship between the various signals at different radial locations. Rather, on close inspection, it is

apparent that many features appearing on one trace do not seem to relate to features on the other traces. Some features, however, can be related and for these it is apparent that maxima on traces of large radial position seem to associated with minima on traces of small radial position. This is shown rather well in figure 6.2 where a least squares linear fit has been computed for each time-step and plotted in a 3-D format. By doing this, features peculiar only to one trace are heavily damped whereas the global traits are accentuated.

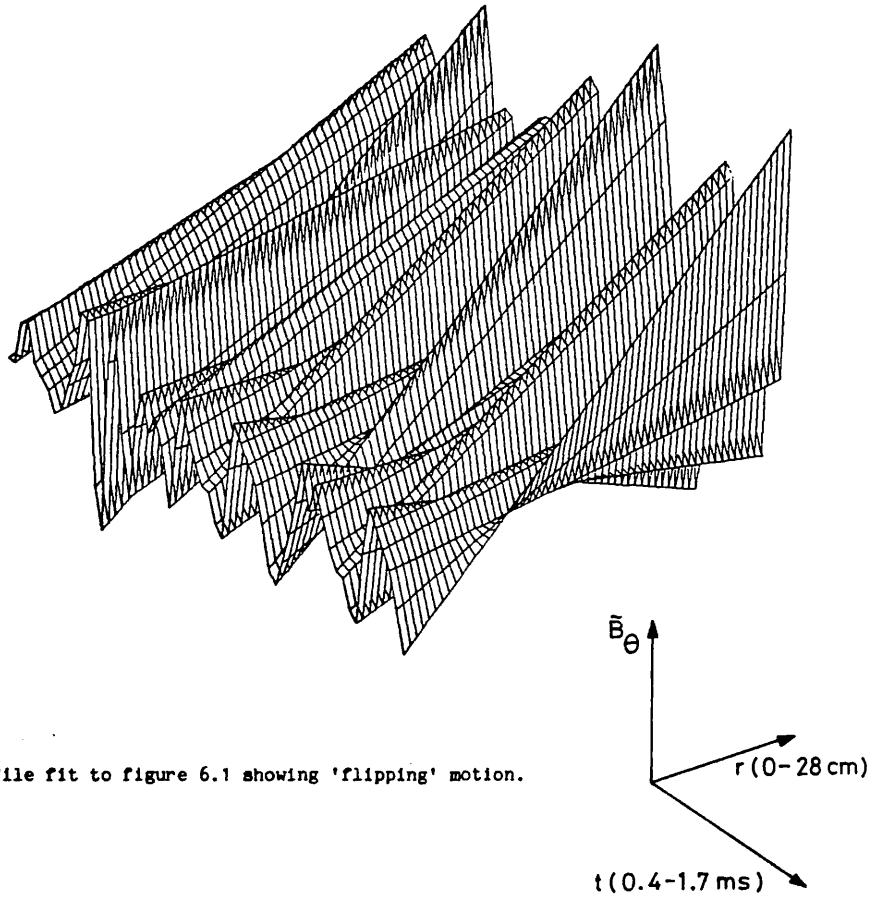

Figure 6.2 **Linear profile fit to figure 6.1 showing 'flipping' motion.**

So the picture we have is that many of the features visible on the individual time-histories of the probe data are peculiar to just one coil. These are then local fluctuations. In addition to this, however, we also see the presence of common features to all traces, which represent global fluctuations. For $\tilde{B}_\theta$ these global fluctuations are characterised by the outer and inner regions of the discharge being 180° out of phase. The null point of this 'flipping' motion is at about 10 cm. With a similar analysis $\tilde{B}_\phi$ is found to behave in the same fashion but with a null point near the

reversal surface. $\tilde{B}_r$, on the other hand, seems to be in phase throughout the discharge radius. The absolute magnitude of the combined fluctuations is typically about 2 to 3% of the spatially averaged equilibrium field at low frequencies and falls off inversely with increasing frequency as $1/\nu$.

6.1.2 Radial Propagation And Perturbation Phasing

To gain more information about the character of both these local and global fluctuations we must resort to a statistical analysis. One very important question concerning the global modes of a system is the existence of radial propagation. Such propagation, if it occurs, will be accompanied by a concomitant energy transport which might explain the bad confinement properties inherent to the RFP. In order to investigate propagation effects we define the normalised time-delayed cross correlation matrix as:

$$R_{ij}(\tau) = \frac{\left\langle \int_0^T \tilde{b}_i(t)\, \tilde{b}_j(t+\tau)\, dt \right\rangle}{\left\{ \left\langle \int_0^T \tilde{b}_i^2(t) dt \right\rangle \right\}^{1/2} \left\{ \left\langle \int_0^T \tilde{b}_j^2(t+\tau) dt \right\rangle \right\}^{1/2}}, \qquad - (6.1)$$

where $\tilde{b}_i(t)$, as usual, represents the fluctuating magnetic field at the radial location dictated by the suffix i and τ is a time delay parameter. Figure 6.3 shows an example of this matrix for $\tilde{B}_\phi$ in the sustainment phase of the discharge, where it is clearly apparent that $R_{ij}(\tau)$ has its greatest value at zero time delay for each i and j. In fact, from an estimation of the associated errors we may say that the greatest phase difference between any two coils is at most $\pi/10$. Exactly similar results are found to hold for $\tilde{B}_r$ and $\tilde{B}_\theta$ and so we may conclude that there is no evidence for global propagation within the statistical accuracy and therefore an explanation for the poor energy confinement must be sought in other areas.

In order to investigate the phasing between the various fluctuating field components it is useful to define the phase spectrum between two

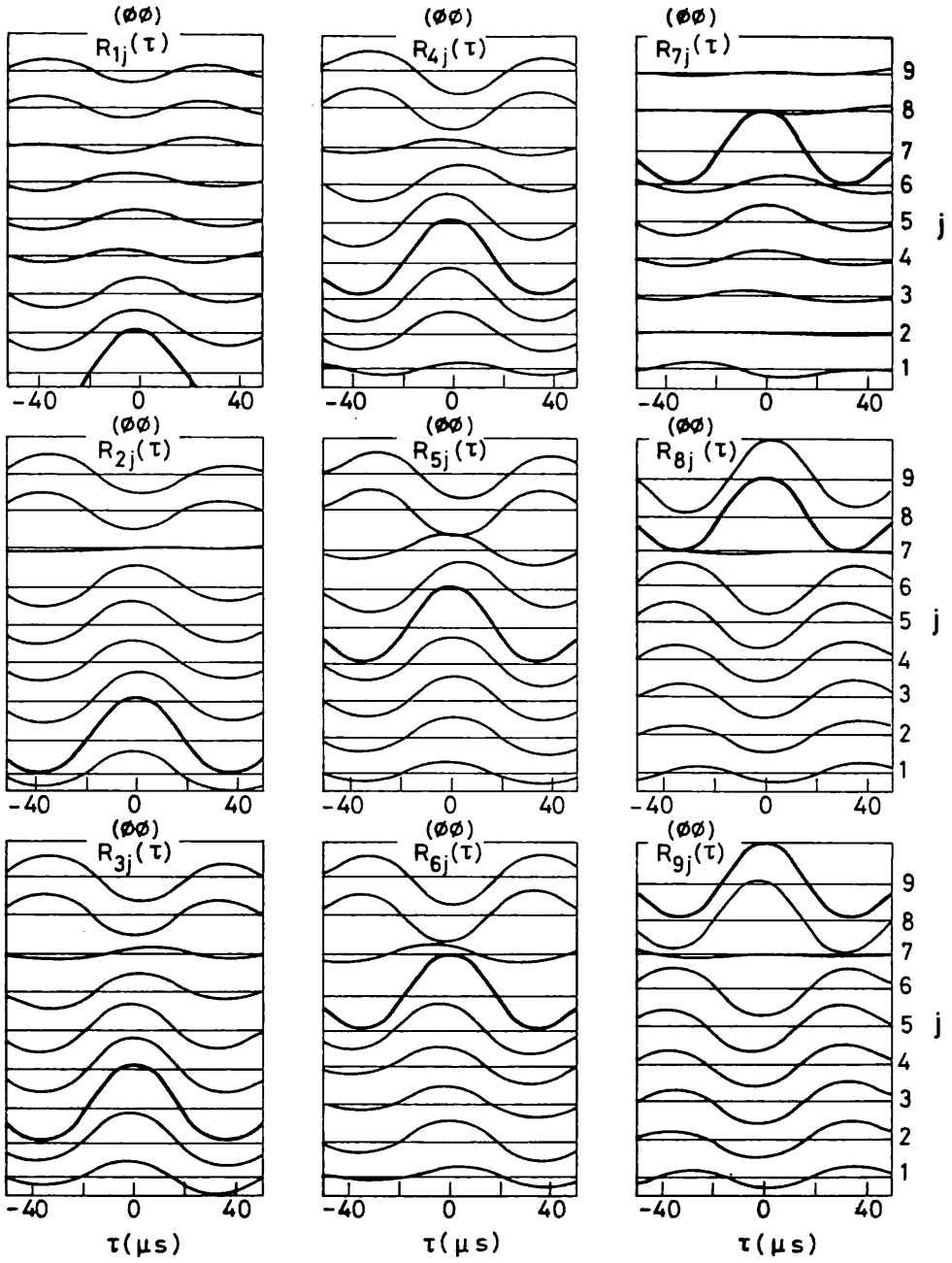

Figure 6.3 Time-delayed correlation matrix for B_ϕ probe signals in the sustainment phase (frequency band 4-20 kHz) showing that there is no observable radial propagation.

signals x(t) and y(t) :

$$\phi_{xy}(\nu) = \text{Arg} < x^*(\nu)\ y\ (\nu) >. \qquad - (6.2)$$

'$\phi_{xy}(\nu)$' represents the average phase difference, as a function of the frequency ν, between the two signals. '*' denotes complex congugate. Essentially, computing all possible phase spectra between the probe signals amounts to the same information as computing all possible time delayed correlations. However, the phase technique has the advantage of being able

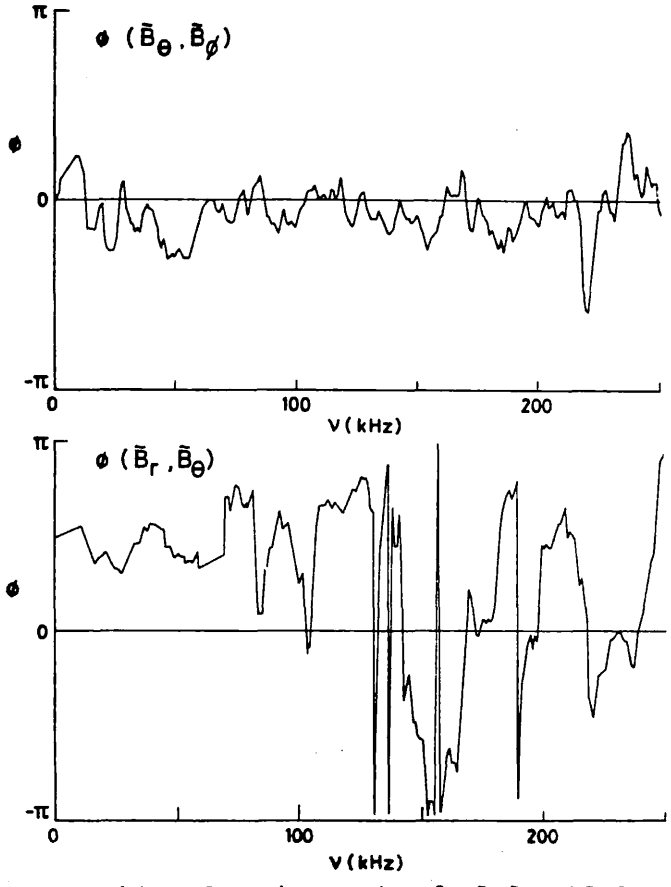

Figure 6.4 Cross-phase spectrum for B_θ, B_ϕ and B_r, B_θ.

to discriminate different phases at different frequencies. Figure 6.4 shows the two examples of $\phi(B_\phi, B_\theta)$ and $\phi(B_\phi, B_r)$ computed at $r \approx 14$cm. Clearly, in the region of 4-20 kHz $\tilde{B}_\phi$ and $\tilde{B}_\theta$ are in phase whereas $\tilde{B}_\phi$ and $\tilde{B}_r$ are about $\pi/2$ out of phase. At higher frequencies, particularly for $\phi(B_\phi, B_r)$ the phase becomes randomised largely due to a rapid decrease in absolute power. In some discharges $\phi(B_\phi, B_\theta)$ appears to be a little less than $\pi/2$. However $\phi(B_\phi, B_\theta)$ tends always to remain at zero.

By considering the equation $\nabla.\underline{\tilde{B}} = 0$ in cylindrical geometry one can show that the spatial phasings are such that $\tilde{B}_\phi$ and $\tilde{B}_\theta$ are an integer multiple of π out of phase. Further $\tilde{B}_r$ must be an odd multiple of $\pi/2$ out of phase with $\tilde{B}_\theta$ and $\tilde{B}_\phi$. This phasing is what we see except that we are looking at the temporal and not the spatial phasing. This means that we must regard the global perturbations as being of the form $\sin(\omega t + k_z z + m\theta + \phi)$ which is a travelling wave. The fact that in some discharges $\phi(B_\phi, B_r) < \pi/2$ is indicative of the presence of a standing wave component in addition to the travelling waves. This picture is closely substantiated by the observations of poloidal and toroidal rotations discussed in chapter 5.

6.1.3 Radial Structure

Now that we understand some of the basic properties of these fluctuations, we would like to have a more detailed knowledge of their radial structure. Since we have already discovered from a cursory inspection of the individual time histories that there is more than one process at work we must rely on the CMF analysis model developed in chapter 3. Indeed, because there is no evidence for propagation this model is very appropriate. It is worth noting that it is possible to formulate similar models which account for propagation effects although they all suffer from non-uniqueness problems in the predicted radial structures. This was emphasised in chapter 3.

6.1.3.1 2-process CMF Model

As a first approximation we will thus regard the fluctuations as being composed of two linearly independent processes; a global component and a local component. As we have seen above this would represent our best guess at the simplest possible structure. With this approximation we can use the zero-time delay correlation matrix defined in equation 3.32 to choose the most likely radial distributions of the local and global modes by using the iterative algorithm outlined in equation 3.37. As it turns out, however, it is better to use a quasi-normalised version of the correlation matrix defined as:

$$R_{ij} = \left\langle \frac{\int_0^T \tilde{\beta}_i(t)\,\tilde{\beta}_j(t)\,dt}{\frac{1}{N}\sum_{k=1}^{N}\left\{\int_0^T \tilde{\beta}_k^2(t)dt\right\}} \right\rangle , \qquad (6.3)$$

but otherwise to proceed as we have outlined above. The reason for adopting this stategy is that for each discharge the fluctuation structure appears to remain roughly the same but at widely varying amplitudes. Hence, if we

were to use the definition given in equation 3.32, the error bars which we would calculate, a standard error in the mean over many shots, would be largely linearly dependent. By using this quasi-normalised form what we are essentially doing is restricting errors so that they pertain to the structure of the fluctuations and not to the absolute amplitude. Using this method we are thus able to predict accurate relative amplitude distributions for the assumed component processes. These may then be translated into absolute estimates by means of multiplication by a spatially averaged fluctuation amplitude.

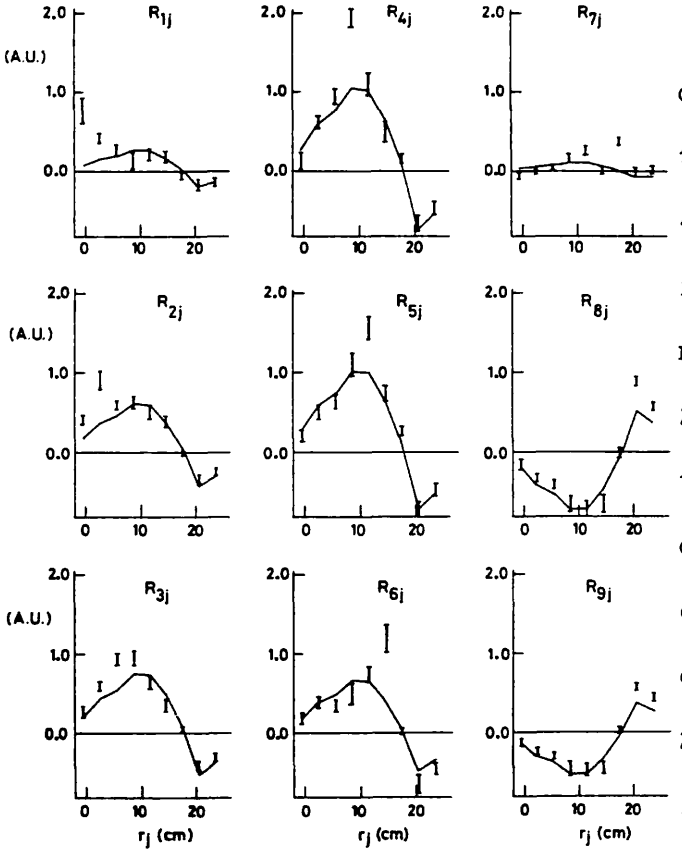

Figure 6.5
Correlation matrix for $\tilde{B}_\phi$ (frequency band 4-20 kHz) in the sustainment phase and best fit assuming a two-process model.

Figure 6.5 shows the measured correlation matrix for $\tilde{B}_\phi$ taken for twelve shots in the frequency band 4-20 kHz. Also shown in this diagram is the computed correlation matrix representing the best fit for a 2-process CMF model. It is clear that the fit is quite good on all off-diagonal components. In fact the chi-squared parameter defined in equation 3.39 has a value of about 2.5 and so we may express confidence in our initial assumptions. Figure 6.6 shows the predicted global-mode radial amplitude distribution for this fit and also for $\tilde{B}_\theta$ and $\tilde{B}_r$ obtained from similar fits. Now, in principle, the local turbulence profile is defined by the mismatch between the measured and fitted correlations (e.g. equation 3.38). However it would be a mistake to interpret all the mismatch on diagonal elements in figure 6.5 as being due to local turbulence. In particular we will see that by assuming more than

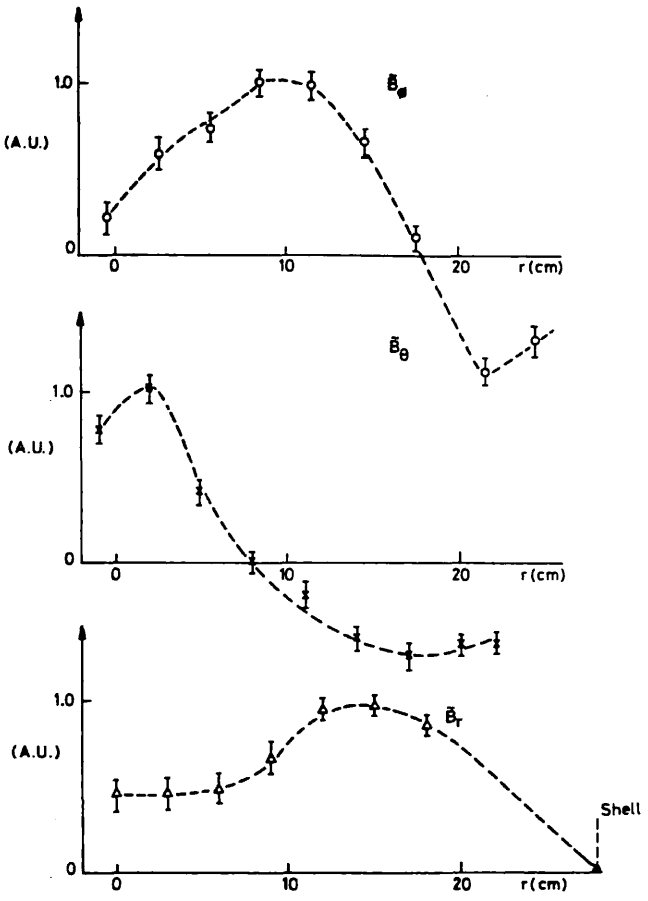

Figure 6.6
Best fit normalised global radial amplitude distributions for $\tilde{B}_\phi, \tilde{B}_\theta, \tilde{B}_r$ via two-process fit as in figure 6.5.

one global mode it is possible to obtain better diagonal fits. At this point we should also mention that there are problems associated with the fact that the probe extends to the geometrical minor axis rather than the plasma axis, which is 3 cm shifted due to toroidal equilibrium (see chapter 4). This essentially means that the central B_r coil actually measures B_θ and vice-versa. However, it turns out that these effects largely cancel for the global modes due to their 'm = 1' symmetry and the fact that $\tilde{B}_r$ is $\pi/2$ out of phase with B_θ (appendix E).

So far then we have been able to elucidate the relative radial structure of the three field components of the dominant global instabilities. However, since we have calculated these stuctures separately, how do we know that they are all associated? For instance, suppose there were actually several global modes present in the plasma, of which the dominant instability had virtually no field component in one direction. In such a case our algorithm would choose, for this field component, the next most dominant mode. And so we would obtain a set of three radial amplitude distributions which were not all associated. To confirm that our above radial estimates, given in figure 6.6, are in fact associated we can fit the cross-component correlation matrix. For instance, to obtain the associated radial structures for B_ϕ and B_θ we simply minimise:

$$Q = \sum_{i \neq j} \sum \{ R_{ij}^{\theta\phi} - \bar{g}_{\theta i} \, \bar{g}_{\phi j} \}^2, \qquad - (6.4)$$

where $\bar{g}_{\theta i}$ and $\bar{g}_{\phi i}$ are the θ and ϕ-components of the global radial amplitude vector and $R_{ij}^{\theta\phi}$ is the quasi-normalised theta-phi cross-component correlation matrix defined as:

$$R_{ij}^{\theta\phi} = < \frac{\int_0^T \tilde{B}_{\theta_i}(t)\, \tilde{B}_{\phi_j}(t)\, dt}{\frac{1}{N}\{\sum_{k=1}^{N} \int_0^T \tilde{B}^2_{\theta_k}(t)dt\}^{1/2} . \{\sum_{k=1}^{N} \int_0^T \tilde{B}^2_{\phi_k}(t)dt\}^{1/2}} > \quad .-(6.5)$$

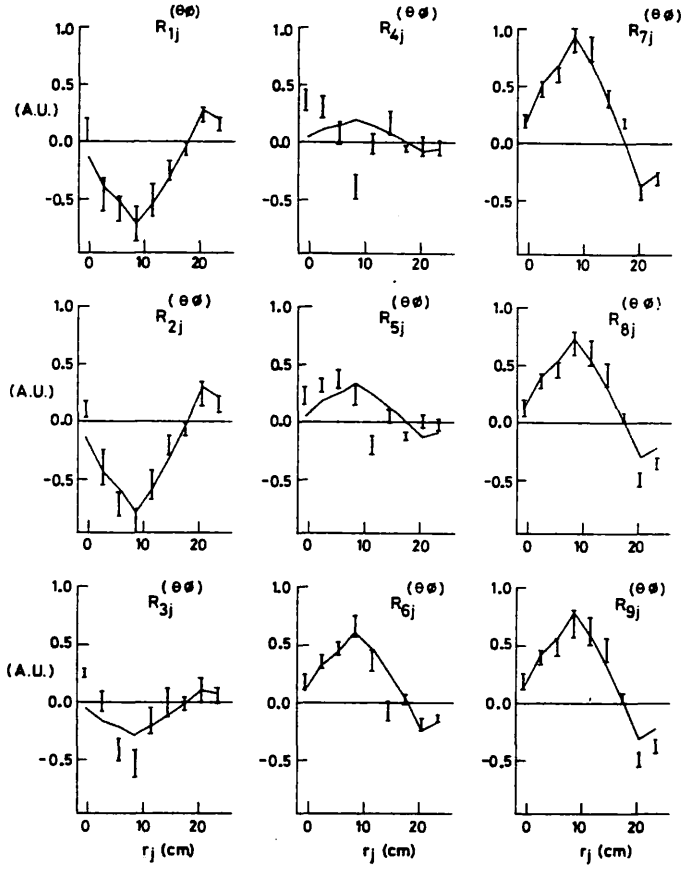

Figure 6.7
$\tilde{B}_\theta$-$\tilde{B}_\phi$ cross-component correlation matrix (frequency band 4-20 kHz) in the sustainment phase and best fit assuming a two process model.

The fit to this matrix is shown in figure 6.7 where it is apparent that we have good agreement corresponding to a chi-squared parameter of around three. Figure 6.8 shows the two associated radial amplitude distributions for $\tilde{B}_\theta$ and $\tilde{B}_\phi$ which appear fairly identical to our previous estimates. So we can be sure that these θ and ϕ radial amplitudes are to be associated with the same mode. In addition figure 6.8 tells us that $\tilde{B}_\theta$ is in (temporal) antiphase with $\tilde{B}_\phi$ in both the inner and outer regions of the discharge but is in phase in the central region - i.e. it gives us the relative phasing. This agrees well with phase spectral estimates.

It is worth noting that the cross-component matrix contains twice the information as the auto-component matrix since it is not Hermitian. This allowed us in equation 6.4 to fit twice as many parameters as usual but with

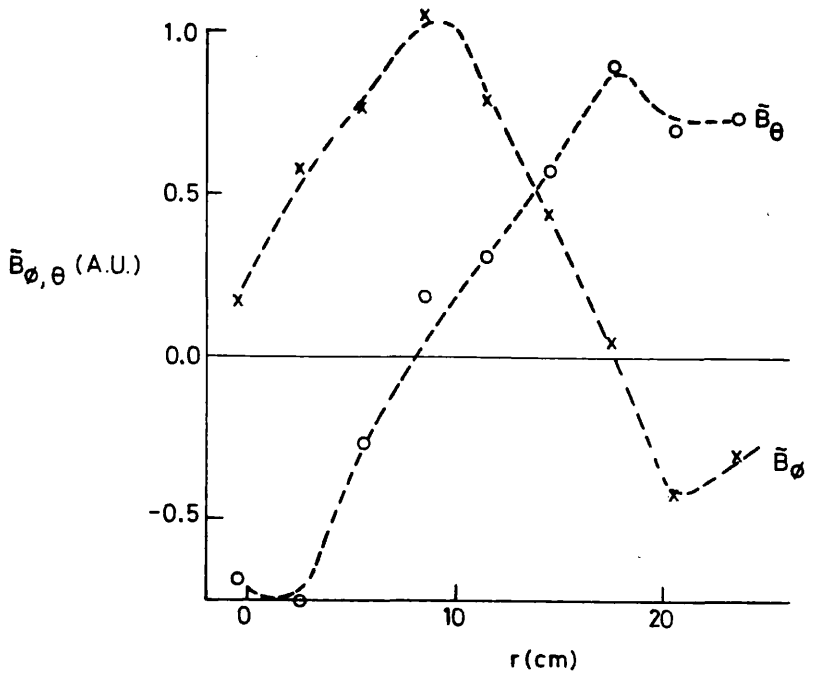

Figure 6.8 Best fit (individually) normalised global radial amplitude distributions for $\tilde{B}_\theta, \tilde{B}_\phi$ for figure 6.7.

the same accuracy. So one could envisage the possibility of using both auto and cross matrices to predict all three field components by minimising a combined Q function defined as:

$$Q = \sum_{i \neq j} \sum \{ \alpha[R_{ij}^{\theta\theta} - \bar{g}_{\theta i} \bar{g}_{\theta j}]^2 + \beta[R_{ij}^{\phi\phi} - \bar{g}_{\phi i} \bar{g}_{\phi j}]^2 + \gamma[R_{ij}^{rr} - \bar{g}_{ri} \bar{g}_{rj}]^2 + \delta[R_{ij}^{\theta\phi} - \bar{g}_{\theta i} \bar{g}_{\phi j}]^2 + \varepsilon[R_{ij}^{\theta r} - \bar{g}_{\theta i} \bar{g}_{rj}]^2 + \zeta[R_{ij}^{\phi r} - \bar{g}_{\phi i} \bar{g}_{rj}]^2 \}, \quad - (6.6)$$

where the constants α to ζ should be suitable chosen so as to weight the fit to each correlation matrix according to its statistical errors. In principle this would let us estimate the amplitude vector associated with a given mode at three times our normal accuracy. Further, this method defines the relative phasings between the field components and of course there is no association problem. However there is one problem in that we already know that $\tilde{B}_r$ is about $\pi/2$ out of phase with $\tilde{B}_\theta$ and $\tilde{B}_\phi$ and so $R_{ij}^{\theta r}$ and $R_{ij}^{\phi r}$ are

by definition very small (and hence prone to large errors). This can be resolved by forming a new $\tilde{B}_r(t)$ time-history by taking the fourier transform of the initial $\tilde{B}_r(t)$, shifting the phase by $\pi/2$ and then inverse fourier transforming. By renormalising the resultant radial amplitudes we are then able to plot our best possible estimate of the amplitude vector associated with the dominant global instability. This is shown in figure 6.9.

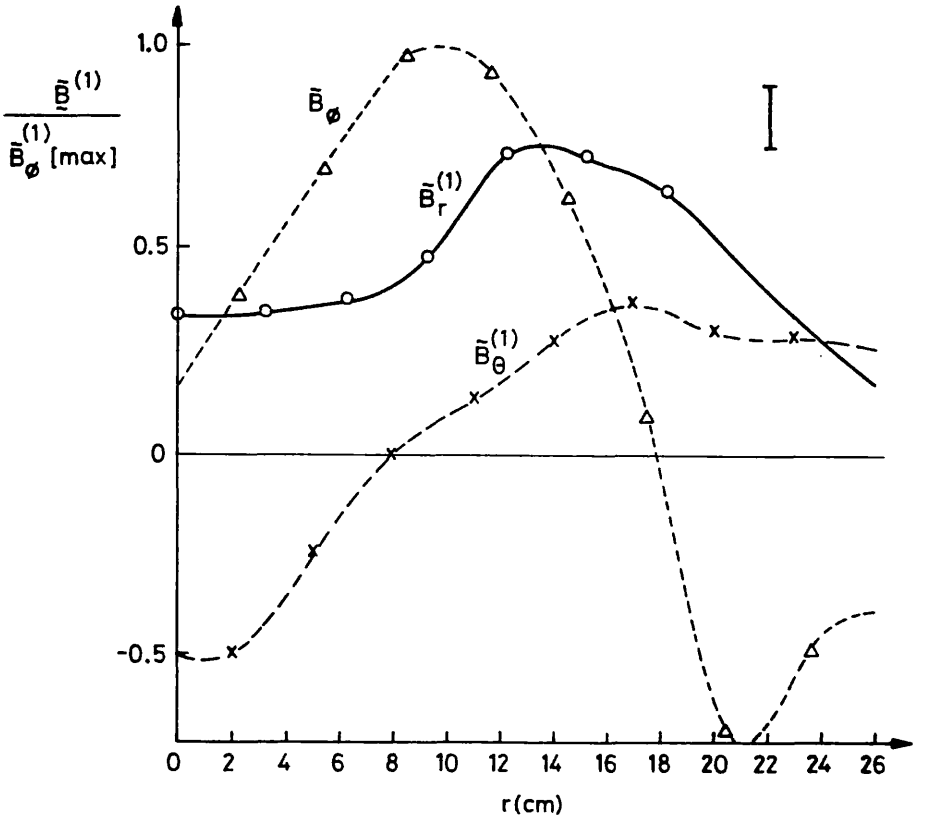

Figure 6.9 Best fit global radial amplitude vector using 2-process multi-component fit.

There are a number of points we may extract from this graph. Firstly the $\tilde{B}_{\phi}$ trace appears to almost intersect the minor axis with a positive gradient. This tells us that the instability must be associated with an odd m number. The fact that there is a small discrepancy here may be explained by linear coupling effects due to toroidicity. Secondly we see that on axis $\tilde{B}_r \approx -\tilde{B}_{\theta}$. By considering the single valuedness of the fields at the origin in a cylindrical geometry this restricts the value of m to one. Hence we may deduce that the dominant instability is m = 1. Further, by the fact that at

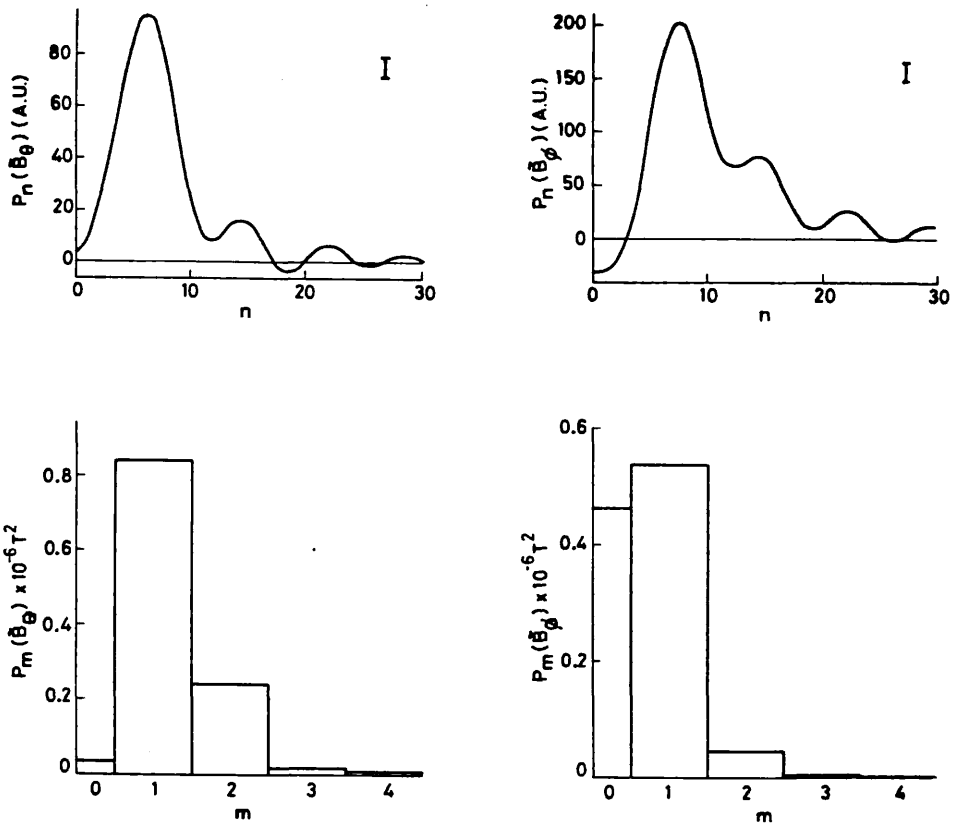

Figure 6.10 Poloidal and toroidal mode power spectra for $\tilde{B}_\theta$ and $\tilde{B}_\phi$ in the sustainment phase (filter: 4-20 kHz).

the wall $\tilde{B}_\phi \approx 2\tilde{B}_\theta$ and using $(\nabla \times \underline{\tilde{B}})_r = 0$ we may calculate the n-number to be (very) approximately six and by the fact that $\tilde{B}_r$ does not cross zero at any point in the discharge radius we may identify the mode as resistive.

In order to relate this picture to other measurements we may use arrays of edge coils to plot the poloidal and toroidal mode spectra. The details of this type of analysis has been discussed in chapter 5. Figure 6.10 shows these spectra plotted for both the θ and ϕ-field components. From this diagram we see that the dominant feature on the n-spectrum is a band of instabilities centred around $|n| = 8$. Likewise the m-spectrum shows dominantly $m = 1$. By forming the 'Association spectrum', we may link these two features and show that the dominant modes are a band of resistive $m = 1$ kinks of $n \approx 8$ resonant inside the reversal surface. In addition to this, however, there also appears to be some $m = 0$ on $\tilde{B}_\phi$ and some $m = 2$ and low n-numbers on $\tilde{B}_\theta$. Virtually all the $m = 2$ may be explained by linear coupling due to toroidicity. The low n-number features on $\tilde{B}_\theta$ are indicative either of

m = 0, n = 0 modes or low n m = 1 modes.

So the picture related by the edge coil measurements is in good agreement with the CMF model predictions for the dominant global instability. However, as we have seen, the edge coils also predict other less powerful modes such the m = 0.

6.1.3.2 3-process CMF Model

By assuming a two-process fit we have seen that it is possible to obtain fits to the various correlation matrices with a chi-squared parameter of around three. There is thus information to be gained by including another process. Indeed, as we have discussed above, this may lead to identifying other modes predicted by the edge-coils. Therefore we will now assume two linearly independent global modes and a local component. As before we start by fitting the auto-component matrices. These are shown for $\tilde{B}_\theta$ and $\tilde{B}_\phi$ in figures 6.11 and 6.12 and figure 6.13 shows the two radial amplitude distributions obtained for all three field components. The fits are typically much better now, being characterised by a chi-squared value of about unity.

There are several points we may obtain from figure 6.13. It is clear that the first process obtained with this model is almost exactly the same as our previous results. So including another process has not altered in any way the previous one. The second process however does not appear to be an m = 0 mode. Rather the $\tilde{B}_r$ trace indicates an ideal type kink similar to the resistive modes already discussed. A question which now arises is whether this mode might be explained by phase distortions or a plasma shift phenomenon. In chapter 3 we showed that propagation effects, which lead to different phasing of different coils, act to create spurious processes. However, taking the $\tilde{B}_\phi$ component as an example, if one regards the second process as a phase distortion of the first, one is led to the belief that

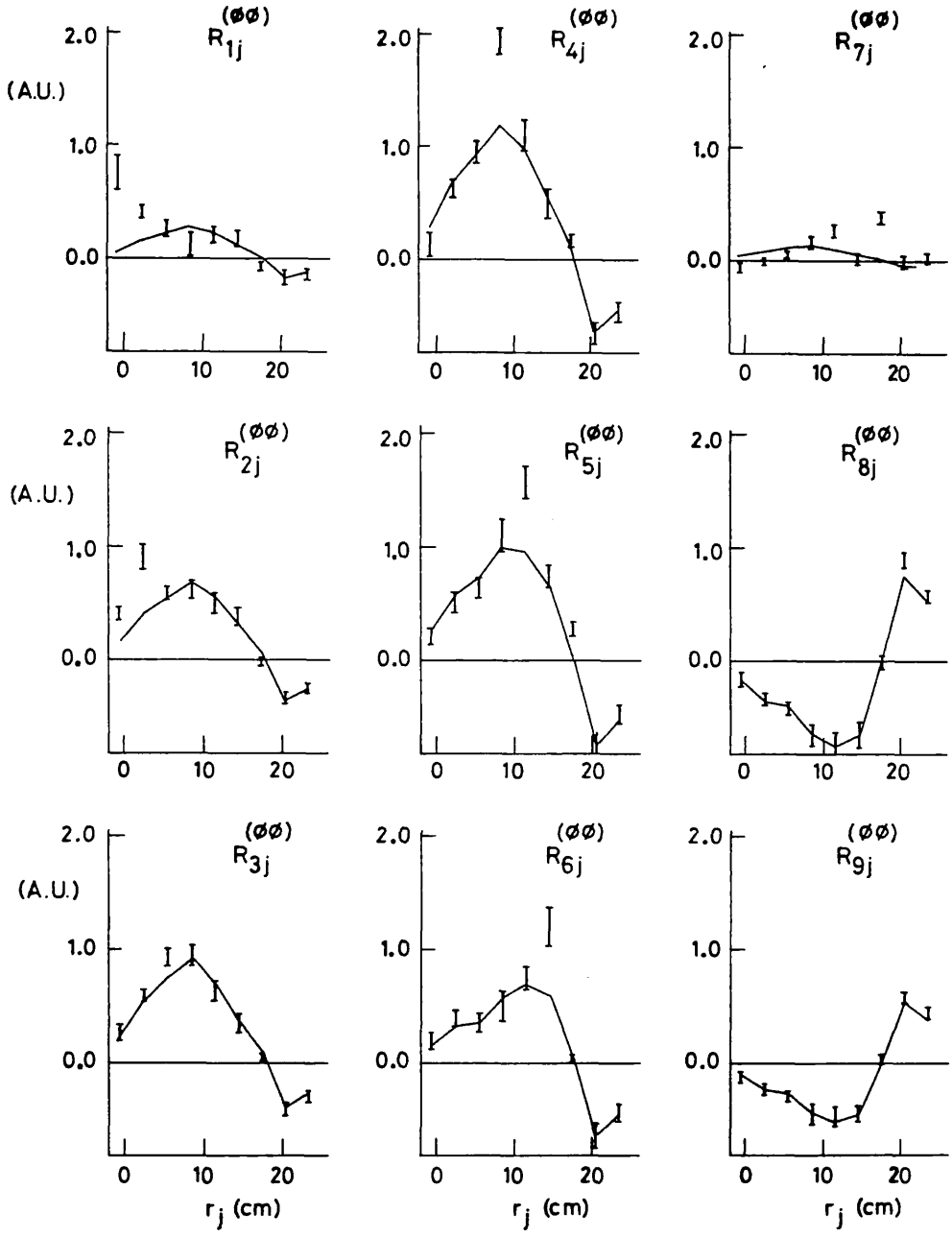

Figure 6.11 Correlation matrix for $\tilde{B}_\phi$ in the sustainment phase (frequency band 4-20 kHz) and best fit assuming a 3-process model.

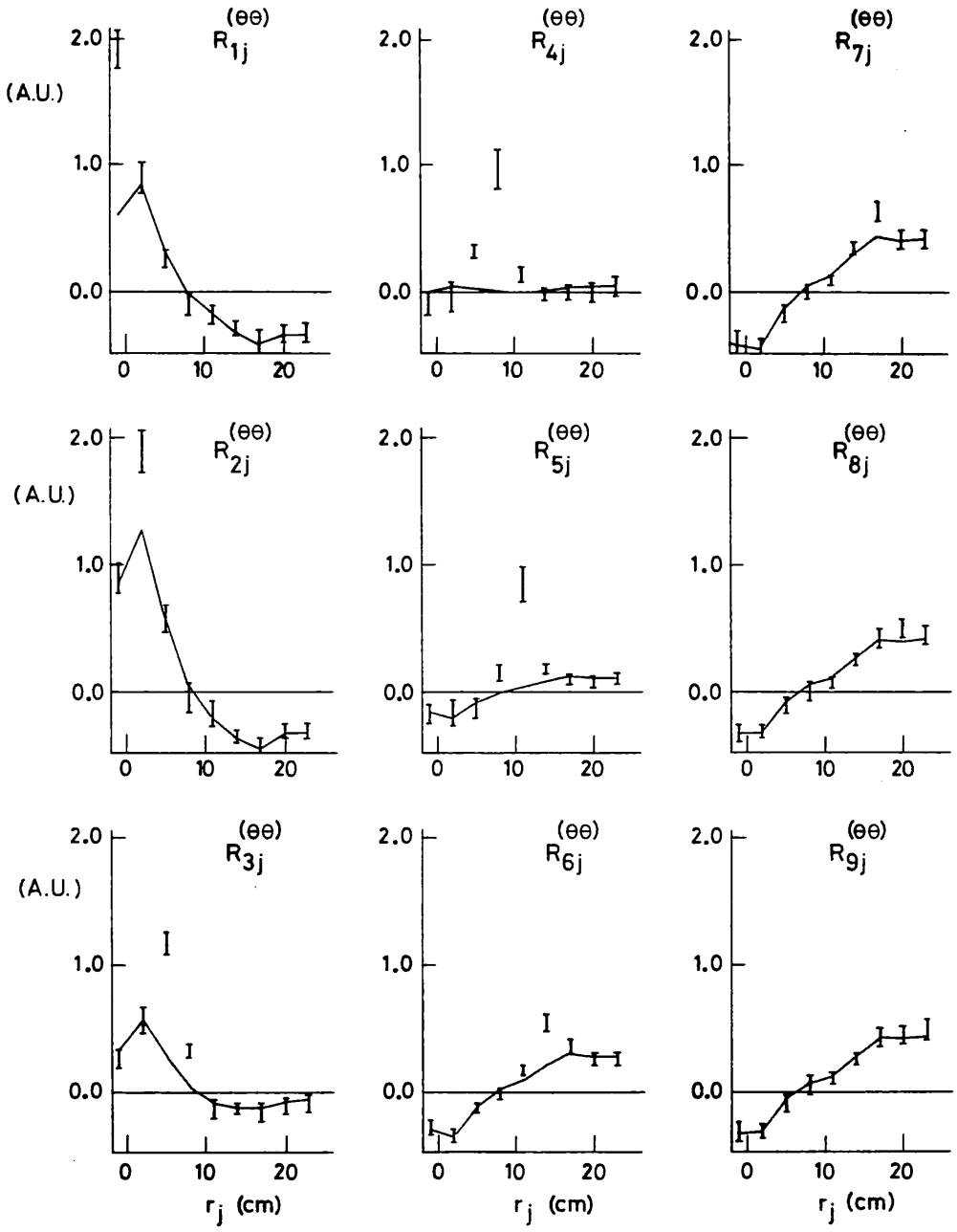

Figure 6.12 Correlation matrix for $\tilde{B}_\theta$ in the sustainment phase (frequency band 4-20 kHz) and best fit assuming a 3-process model.

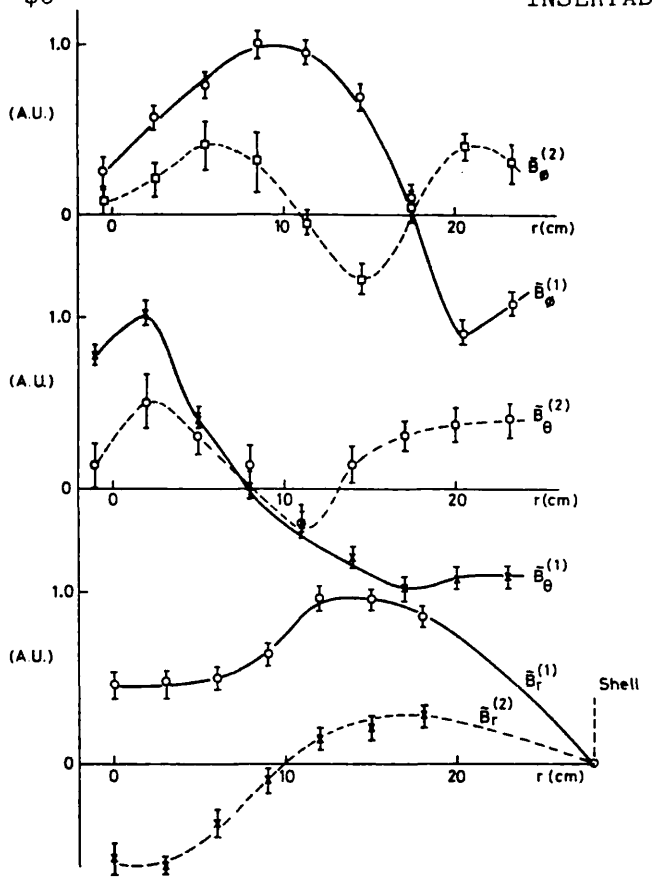

Figure 6.13
The two global radial amplitude distributions for the fits of figures 6.11 ($\tilde{B}_\phi$), 6.12 ($\tilde{B}_\theta$) and not shown $\tilde{B}_r$.

phase distortions of $\pi/2$ exist. But as we have seen in section 2.2, we know that the phase of $\tilde{B}_\phi$ is the same on all coils to within about $\pi/10$. So we cannot explain the second process in terms of a phase distortion. So what about a plasma shift? Again the answer is negative since excluding the first two coils, which are the ones effected by this shift, does not alter the results. Also a theoretical analysis of the expected effects of such a shift do not explain the observed form of the radial distributions of the second process.

So we must conclude that the second process is a real effect. But, having established this, we are faced with our old association problem. Are all three components of this second process to be associated with one mode? To answer this we must proceed by the prescription of equation 6.6. In this way we find that again all three components are indeed associated and as before we may plot the combined renormalised second-process vector. This is shown in figure 6.14. As before, since $\tilde{B}_r = -\tilde{B}_\theta$ on axis and $\tilde{B}_\phi$ approximately intersects the origin with a positive gradient we may conclude that $m = 1$. This is substantiated by the edge coil measurements which do not detect the relevant amount of power in $m > 1$. In addition, we may strongly disfavour an $m = 0$ explanation by, for instance, the fact that $\tilde{B}_\theta$ does not go to zero at the wall and that $\tilde{B}_r$ does not go through zero at the reversal surface.

Returning to figures 6.11 and 6.12, which show the fits to the θ and ϕ auto-component correlation matrices, we can now use the type of

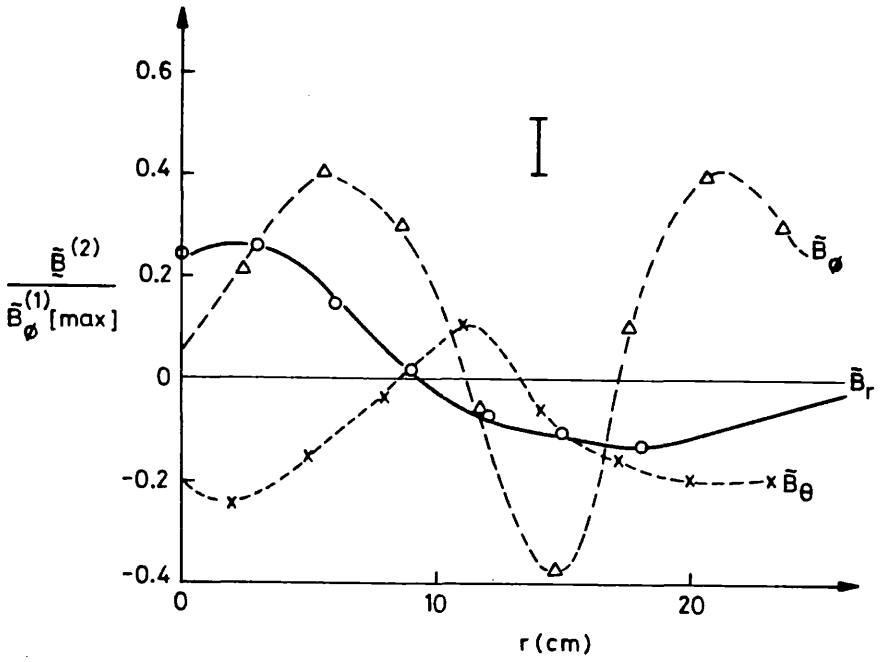

Figure 6.14 Best fit for the second global radial amplitude vector using a 3-process multi-component fit.

prescription outlined in equation 3.38 to calculate the profile of local turbulence. We must be careful however, since the probe is inserted to the geometrical minor axis and not to the plasma axis, the two being separated by the Shafranov shift. As we discussed briefly before this means that the first $\tilde{B}_\theta$ coil actually measures $\tilde{B}_r$ and vice-versa. Nevertheless it can be shown (appendix E) that the Shafranov shift does not affect the local turbulence profiles for $\tilde{B}_\theta$ and $\tilde{B}_r$ deduced from the diagonal element mismatch apart from interchanging the two components on axis. For $\tilde{B}_\phi$, however, the Shafranov shift acts to create a spurious quasi-local process producing anomalous diagonal and next-to-diagonal mismatch on the first two coils. With this in mind it is apparent that the $\tilde{B}_\theta$ local turbulence is peaked on axis falling, within errors, to zero at the edge of the discharge. For $\tilde{B}_\phi$ much of the diagonal mismatch on the first two coils is explicable in terms of the Shafranov shift and hence for this component the local turbulence appears to peak a little further out but nevertheless falls, within errors, to zero at the edge of the discharge. For both $\tilde{B}_\phi$ and $\tilde{B}_\theta$ the peak amplitude of the local turbulence is seen to be roughly equal to that of the global modes. For $\tilde{B}_r$, the local activity is subject to some

uncertainty due to a lack of coils at large radial positions. However evidence suggests that it follows the $\tilde{B}_\theta$ behaviour but at a lower amplitude.

6.1.3.3 High Frequency And Set-up/Termination Results

Up until now we have only discussed the sustainment phase of the discharge for the frequency band 4-20 kHz. A similar analysis has however been applied to both the set-up and termination phases and to higher frequencies. A very striking feature which appears is that, as one increases the frequency, the local turbulence becomes dominant over the global instabilities. In fact in the range 50-100 kHz the global modes are barely visible. This is shown for $\tilde{B}_\phi$ in figure 6.15, where we plot a normalised cross correlation matrix. This observation agrees well with measurements performed on the ETA-BETA-II machine at Padova [1].

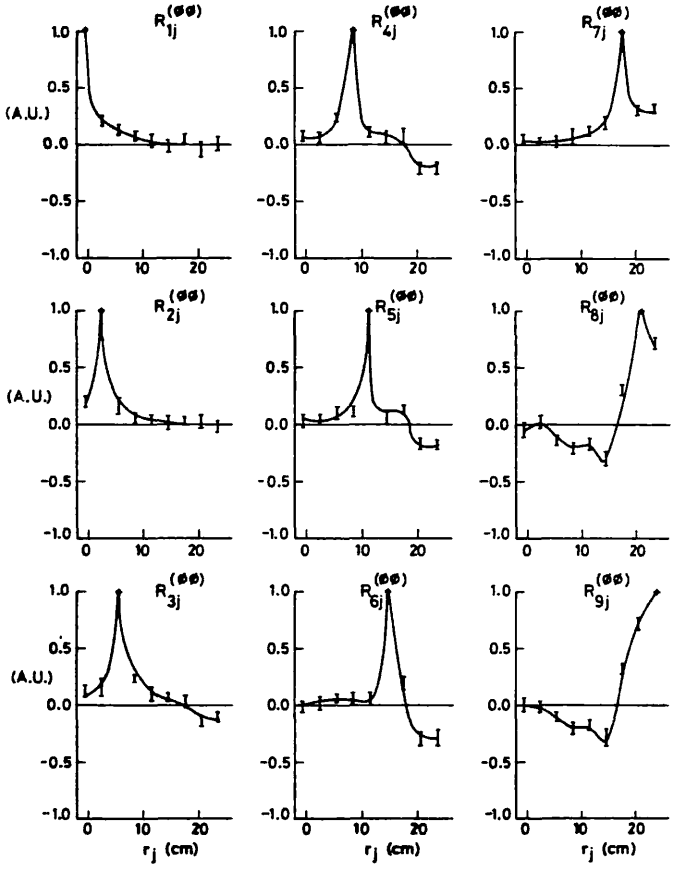

Figure 6.15
Correlation matrix for $\tilde{B}_\phi$ in the sustainment phase (frequency band 50-100 kHz).

Regarding the set-up and termination phases of the discharge, our study again reveals the same qualitative picture for the global and local modes. However there are two effects of interest concerning the local turbulence profile. In the set-up phase, while the $\tilde{B}_\phi$ local component remains at the same amplitude in relation to the global component, the $\tilde{B}_\theta$ term becomes much stronger. In the termination phase both the $\tilde{B}_\theta$ and the $\tilde{B}_\phi$ components become stronger in relation to the global modes.

6.2 LINEAR STABILITY OF THE EQUILIBRIUM FIELDS

6.2.1 Introduction

In this section we will report results obtained from testing the equilibrium field profiles measured in chapter 4 for linear stability to ideal current and pressure driven modes and, in the limit of infinite Lundquist number, to tearing modes. By means of this analysis we will compare our detailed observations of the actual fluctuation structure with the predictions of the linear theory.

6.2.2 Ideal Stability

A good algebraic guide to the stability to ideal pressure driven instabilities is furnished by the Mercier criterion (for stability) (see chapter 1):

$$\left\{\frac{B_\phi^2}{B^2}\right\}\left\{\frac{r}{q}\frac{dq}{dr}\right\}^2 + 8\mu_0 r \frac{dP}{dr}\frac{(1-q^2)}{B^2} > 0 . \qquad - (6.7)$$

As we discussed in chapter 1 the first term in this criterion, which represents the shear of the magnetic field lines, is positive definite and hence always represents a stabilising influence. However the second term is generally negative for typical RFP configurations and is accordingly destabilising. Both terms are plotted separately in figure 6.16. It is apparent that the shear term is, within errors, dominant at all Radii and there is thus no evidence for pressure driven ideal instabilities.

In order to test the ideal linear stability to current driven modes we use the testing procedure introduced by Newcomb applied to deflated field profiles which possess no pressure. The algorithm used for the deflation

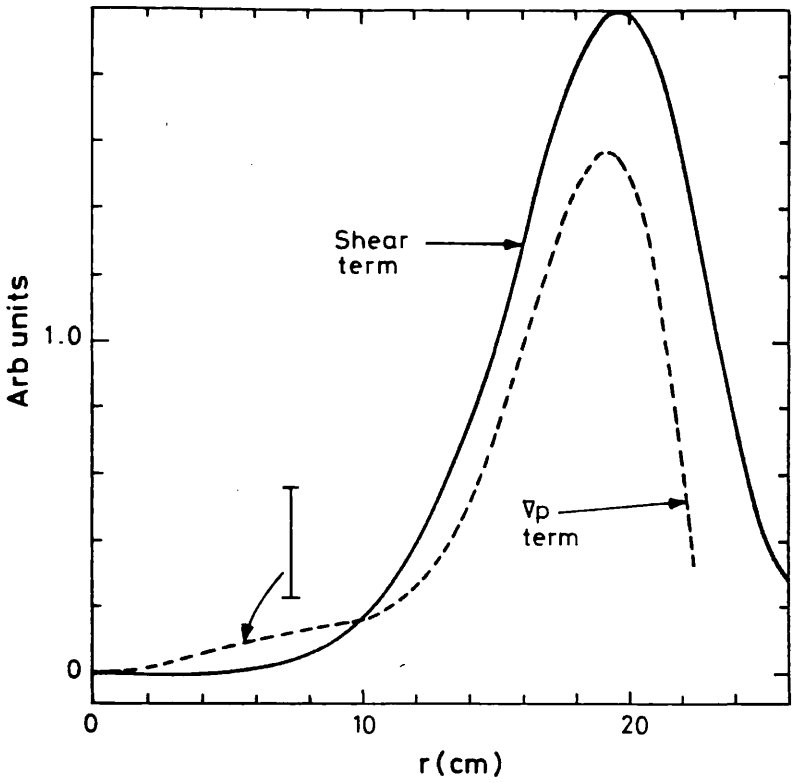

Figure 6.16 Variation with radius of the two terms in the Mercier criterion.

process is to calculate the μ profile, defined as $\underline{j}.\underline{B}/B^2$, and to then solve the force-free relation $\nabla \times \underline{B} = \mu \underline{B}$ for the fields. In practice we find complete stability to all current driven ideal modes when the liner is regarded as an infinitely conducting wall. However, if we disregard the liner and take the shell as being the relevant infinitely conducting wall, at near-extreme values of our error estimates, we find marginal ideal instability for on-axis m = 1 current driven modes.

6.2.3 Resistive Tearing Mode Stability

Δ' tests offer a very simple solution to investigating the linear stability properties of tearing modes in the limit of infinite Lundquist number. These were briefly reviewed in chapter 1. It has been shown that these tests agree well on the prediction of marginal stability points with finite Lundquist number codes as long as $S > 10^3$ [2]. Since estimates of the Lundquist number in HBTX1A range from about 10^4 to 10^5 we can accordingly express confidence in this method.

To recap, the basic element involved in a Δ' test is to calculate, for

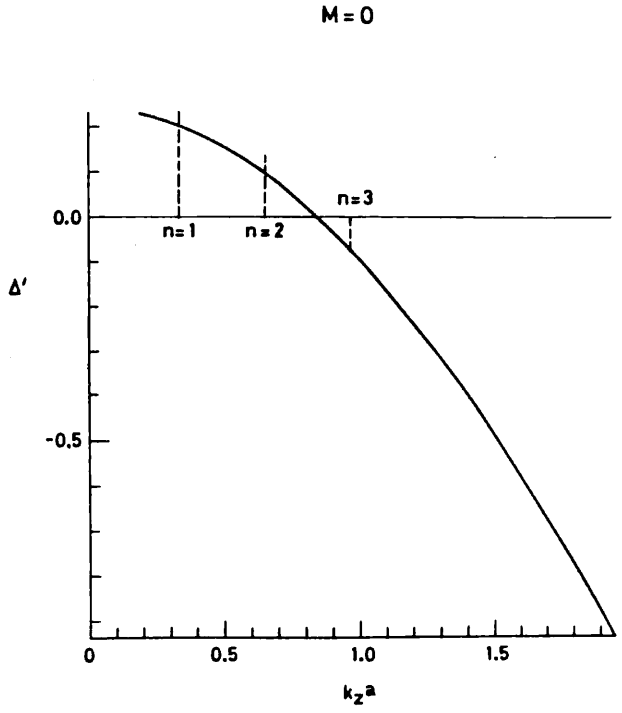

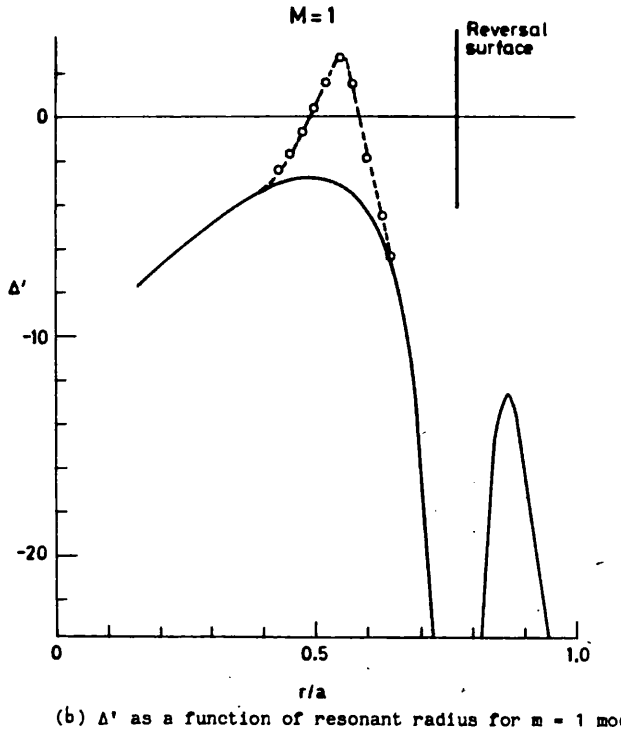

Figure 6.17

(a) Δ' as a function of $k_z a$ for m = 0 modes using the unperturbed equilibrium of figure 6.18(a).

(b) Δ' as a function of resonant radius for m = 1 modes. Full line refers to the unperturbed equilibrium of figure 6.18(a) and dotted line refers to adjusted equilibrium of figure 6.18(b).

given m and n numbers, a parameter Δ' such that if $\Delta' > 0$ there is instability and if $\Delta' < 0$ then there is stability [3,4,5]. In the case of $\Delta' > 0$ the value of Δ' is directly related to the growth rate of the particular mode pertaining to that Δ'. As for ideal current driven instability tests, for consistency, we eliminate pressure from the field profiles by the deflation process described above.

Figure 6.17(a) shows Δ' as a function of the parameter $k_z a$ (a is the liner radius) for poloidal mode number, m = 0. In this case the liner has been taken as the relevant infinitely conducting wall. Clearly for low k_z, corresponding to $n \leq 2$, there is instability whereas for high k_z there is stability. Similar m = 0 stability calculations where a vacuum region is included, the liner conductance assumed negligible and the shell taken as the relevant infinitely conducting wall indicate slightly higher Δ' but otherwise very similar results. The m = 0, $|n| \approx 0$ activity observed by the edge coils (figure 6.10) would thus seem to be explicable in terms of the linear theory.

The picture for the m = 1 instabilities is not quite so simple. Figure 6.17(b) (trace 1) shows Δ' plotted as a function of the resonant

radius. As with the m = 0 case the relevant infinitely conducting wall has been taken as the liner. It is clear that Δ' certainly peaks at about r=0.4a, where edge coils predict a dominant instability, but it never actually goes positive. By ignoring the liner conductance and taking the shell as the infinitely conducting wall this picture does not qualitatively change although Δ' does increase. However, by perturbing the input field profiles to the edge of the estimated error bars (figure 6.18) an instability can be generated. This is shown in trace 2 of figure 6.17(b). The overall impression acquired is thus that the m = 1 linear tearing mode stability is about marginal.

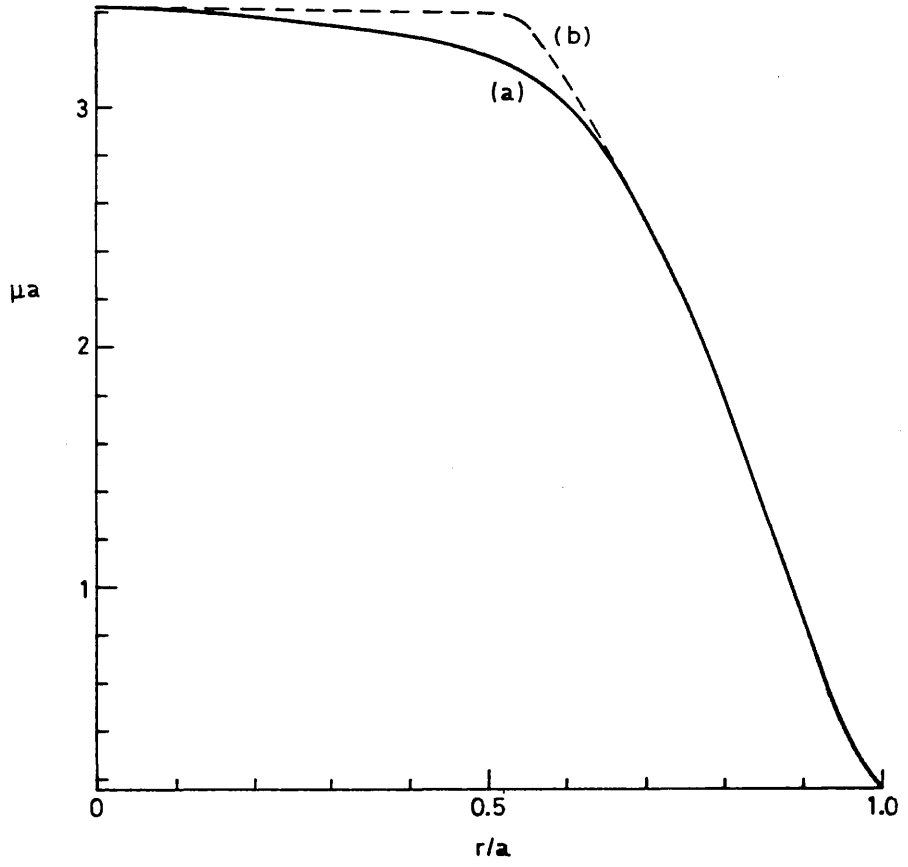

Figure 6.18 (a) Equilibrium μ profile calculated from probe measurements and (b) adjusted μ profile on the limits of experimental error.

In order to further pursue the question concerning the origin of the dominant kink instabilities it is possible, for the 'perturbed' equilibrium μ profile of figure 6.18 to compare the eigenfunctions associated with the consequent instability with the radial amplitude distributions reported in

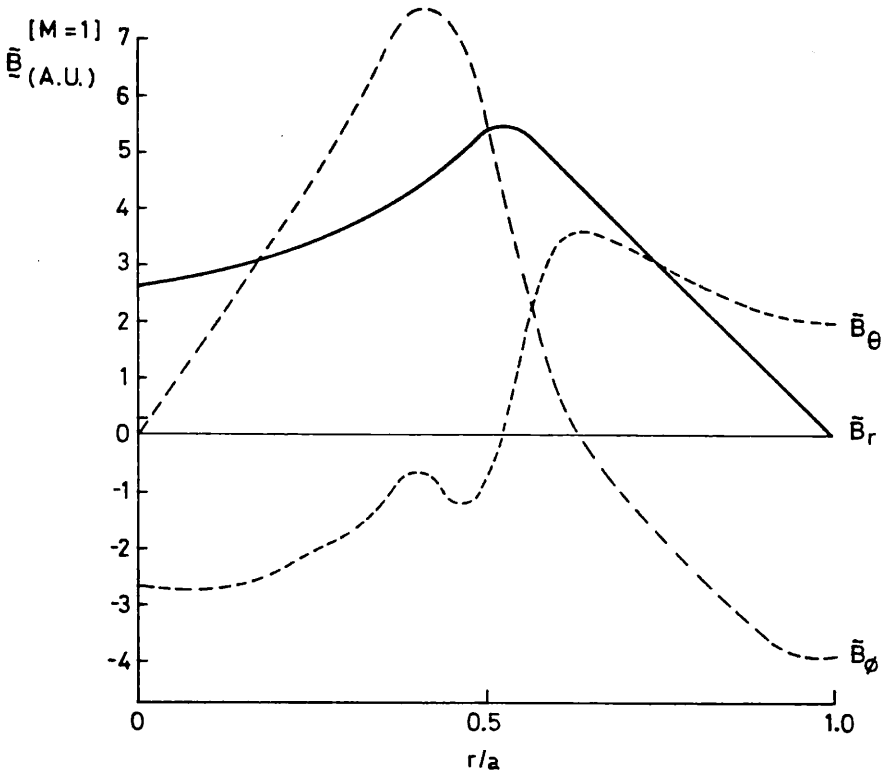

Figure 6.19 Calculated linear m = 1 eigenfunctions corresponding to the largest value of Δ' in figure 6.17(a).

section 6.1 of this chapter. Figure 6.19 shows these eigenfunctions. Comparing them with the measured 'first process' eigenfunctions shown in figure 6.9 it is apparent that there is good agreement. It should be noted that calculating the stable eigenfunctions using the non-perturbed μ profile yields very similar results.

Stability calculations for $m \geq 2$ show $\Delta' << 0$ indicating complete stability.

6.3 DISCUSSION

In this chapter an analysis of the internal structure of magnetic fluctuations has been presented. To distinguish linearly independent processes the technique of correlation matrix fitting (CMF, chapter 3) has been applied to the probe data. As a result, in the sustainment phase of the discharge, it has been possible to distinguish three linearly independent processes simultaneously and to obtain, to a good accuracy, their radial distributions. Previously this type of discrimination has not been

possible. Hence the advantage of applying the relatively sophisticated technique of CMF has been demonstrated.

The largest process distinguished by CMF at low frequencies (4-20 kHz) possesses a radial structure which identifies it with the global m = 1, $|n| \approx 8$ instabilities seen by the edge coils. The fact that $B_r \neq 0$ for any $r < r_{wall}$ is consistent with the timescale arguments of chapter 5 showing that these modes are resistive. In addition, the close agreement of the radial amplitude distributions predicted by CMF with the field-eigenfunctions of most unstable tearing mode, computed for the measured equilibrium of chapter 4, demonstrates the close connection with the linear or quasi-linear theory. For non-resonant radii, of course, such agreement is at least partly to be expected as here the form of the resistive (or ideal) MHD field-eigenfunctions simply depends on a small amplitude helical equilibrium (only partly, since the solution of a small amplitude helical equilibrium in the region between the resonance and the wall depends on the boundary condition at the resonance which is essentially given by Δ').

In this study we have not addressed the stability of pressure driven modes. This is because the pressure profile deduced in chapter 4 is not accurate enough for such a study. Indeed it is very hard to see that further measurements will change this situation. However, it has been shown that the observed m = 1 fluctuations can be adequately interpreted in terms of tearing modes of almost marginal stability. This is consistent with the m = 1 modes not being continuously unstable. In chapter 5 we saw evidence of a cyclic process in which unstable modes grew and then were quasi-linearly stabilised. This process would fit in nicely with the observation of marginal stability. However it is not possible to exclude the g-mode as a possible source of the observed m = 1 fluctuations.

For the case of the m = 0 tearing instability it has been shown that the measured equilibrium is in fact always unstable. Edge coil measurements do

predict a mode of this type although there is a slight uncertainty about the n-number which might possibly be zero as well. In this case the observed m = 0 modes might well be associated with mode-mode coupling effects produced by m = 1. Further investigation will be required to elucidate this.

The second largest process discernable by CMF corresponds to local fluctuations of a correlation length of about 3 cm. This local turbulence is peaked in the central regions of the discharge at an amplitude similar to the dominant global process and falling, within errors, to zero at the plasma edge. At high frequencies (>30 kHz) these fluctuations dominate over the larger correlation length phenomena.

Observation of such local modes has been reported before, notably in ZETA and more recently in ETA-BETA-II. In all cases these observations have been confined to high frequencies where the global instabilities are less apparent. The importance of the observations reported here is that, even at low frequencies, local fluctuations are of a comparable importance to the larger scale lengths.

The final process discernable by CMF is a global mode characterised by $\tilde{B}_r=0$ for some $r>0$ and $<r_w$. The peak amplitude of this process is about 1/2 that of the dominant first process and the frequency dependence is broadly similar. These two facts suggest that this process should obey a small amplitude helical equilibrium given by the linearised forms of $\nabla\times(\underline{J}\times\underline{B})=0$ and $\nabla.\underline{B}=0$ (for $r \neq r_s$) since small frequencies indicate that inertial terms are negligible and the relatively large amplitude in relation to the dominant fluctuations disfavours an origin due to non-linear effects. To test this conjecture figure 6.20 shows $\tilde{B}_\theta(r)$ and $\tilde{B}_\phi(r)$ as calculated by the equations $(\nabla\times(\underline{J}\times\underline{B}))_r=0$ and $\nabla.\underline{B}=0$ given $\tilde{B}_r(r)$ as predicted by CMF. The resemblence to figure 6.14, which shows the radial amplitude vector as deduced by CMF, is clearly apparent. Hence the third process discernable by CMF appears to obey a small amplitude helical equilibrium and thus we may

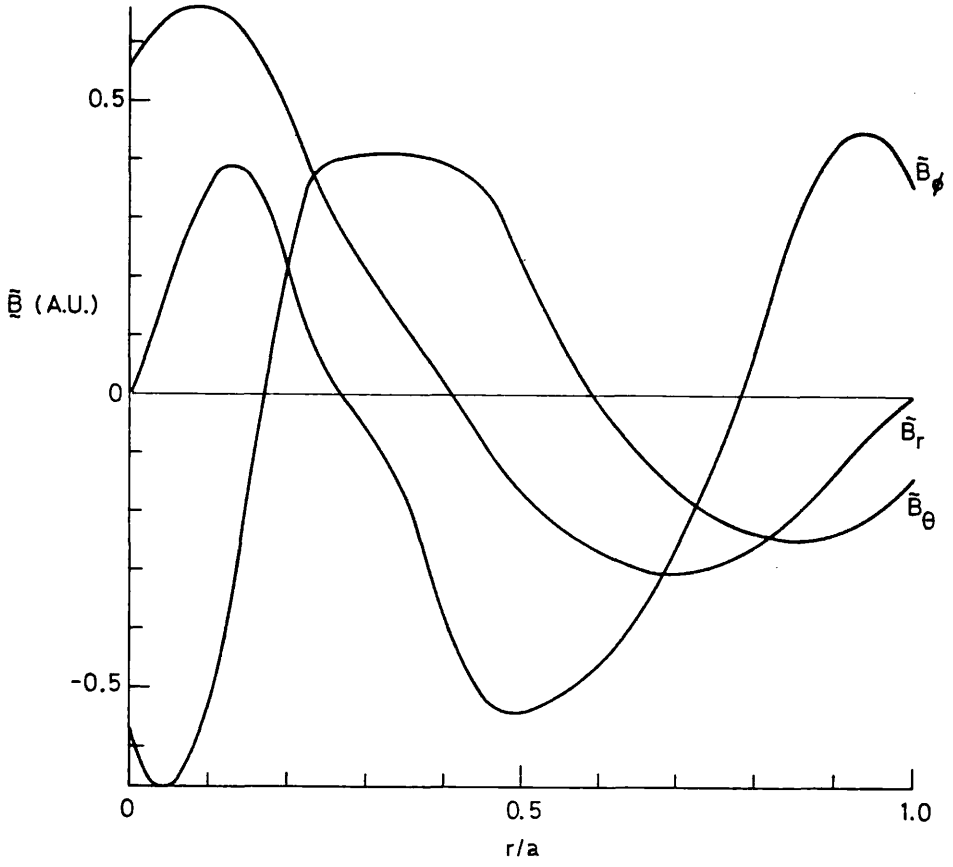

Figure 6.20 Calculated profiles of $\tilde{B}_\phi$ and $\tilde{B}_\theta$ derived from the measured second-process $\tilde{B}_r$ using the equations $\nabla \times (\underline{J} \times \underline{B}) = 0$ and $\nabla \cdot \underline{B} = 0$.

conclude that this mode has a linear or quasi-linear origin in the sense that it need not arise non-linearly from the dominant m = 1 modes.

As we have seen from the ideal stability analysis, at the edge of our error estimates the measured equilibrium is unstable to on-axis current driven modes if we ignore the stabilising effect of the liner. Clearly the radius at which $\tilde{B}_r = 0$ for this third process is not on axis. However, by inspection of the q-profile determined in chapter 4 we see that the nearest integral mode number to the axis is actually n = -6 which is resonant at r = 8 cm. Thus, taking into account the toroidal nature of the pinch, we realise that the most unstable ideal mode will have $\tilde{B}_r = 0$ at precisely the radius observed. Within errors this mode has approximately marginal stability.

The timescales observed are clearly not consistent with direct ideal instability. However we have seen that if the liner is taken as the relevant infinitely conducting wall then there is no instability. The fact that the liner is resistive means that instability can occur [6] but at a timescale

functionally determined by field diffusion through the liner. At low frequencies this timescale may be estimated by matching the value of $(1/\tilde{B}_r)d\tilde{B}_r/dr$ at the liner as computed by the integration of the linearised forms of $\nabla x(\underline{J}x\underline{B})=0$ and $\nabla.\underline{B}=0$ from the resonance to the liner and by the solution of Laplace's equation in the vacuum region between the liner and shell. Such a procedure gives $\omega < 50$ kHz. We would thus conclude that the frequencies of the 3rd process are explicable in terms of a 'liner-liberated' current driven ideal instability.

Since the ideal stability is, within errors, marginal it should be mentioned that there exists another explanation for the observed timescalesof the third CMF process. It has been shown [7] that for the near-marginal case hybrid growth rates can be obtained for a resistive wall. Thus if we consider the shell to be resistive and further that the marginal point for stability is just outside the shell then we might expect 'resistive-shell' hybrid timescales. These timescales would, of course, be modified by the resistive liner. Owing to the critical dependence on the condition of marginal stability we are unable to estimate exact growth rates. However we cannot rule out this shell-hybrid explanation.

Finally we come to the question of radial propagation. Within errors we find that there is no such propagation and hence there is no evidence that energy is directly carried out of the plasma by this mechanism. The observation that there exists an almost $\pi/2$ phase shift between $\tilde{B}_r$ and $\tilde{B}_\theta$ (or $\tilde{B}_\phi$) is indicative of propagation in the toroidal or poloidal directions, which substantiates the more direct observations of such propagation discussed in chapter 5.

6.4 CONCLUSIONS

In this chapter we have discussed results from an analysis of probe and edge coil data designed to elucidate the internal structure of the magnetic

fluctuations. The CMF technique developed in chapter 3 has been applied to the probe data with good results. It is possible, in the sustainment phase of the discharge, to distinguish three types of instability. At low frequencies (4-20 kHz) the dominant internal fluctuations are to be associated with the global $m = 1$ $|n| \approx 8$ resistive kink modes seen by the edge coils. These modes possess a radial structure in agreement with that predicted by a linear tearing mode stability analysis of the measured equilibrium. At similar amplitudes to these modes there is also a short correlation component ($\Lambda_r \approx 3$cm) which is peaked in the central regions of the discharge. At high frequencies this local turbulence dominates over the global modes. Finally at about 1/4 the peak power of the dominant global modes and with a similar frequency dependence, an $m = 1$ mode with some ideal characteristics is observed. Stability calculations show that ideal modes that are either destabilised by a resistive shell or whose growth rates are reduced by a resistive liner would have the same radial structure and timescales as this mode. No evidence is found for radial propagation but phasing of the fluctuating field indicates that toroidal and poloidal propagation occur. The internal structure of fluctuations in the termination and set-up phases have been studied. Results indicate a similar scenario to the sustainment phase but poorer statistics do not allow the clear observation of the resistive wall mode.

CHAPTER 7

SUMMARY

7.1 CONCLUSIONS OF THIS THESIS

This thesis has presented an experimental study of the fluctuation activity in the RFP HBTX1A using arrays of edge coils, an insertable magnetic probe and statistical analysis techniques.

Chapter 5 presented the results concerning edge coil measurements. These measurements give an accurate description of the fluctuation activity at the plasma edge. It has been shown that, in the sustainment phase of discharges, the superficially random signals observed from these edge coils can in fact be attributed almost entirely to global modes of poloidal mode number m = 0 and 1 provided account is taken of the toroidal distortion of these instabilities. For the first time results have been presented from a toroidal array of edge coils which discloses a broad spectrum of toroidal mode numbers with a peak at $|n| \approx 10$ and significant variation with time and frequency. Cross correlation between signals from the poloidal and toroidal edge coil arrays establishes that the $|n| \approx 10$ is m = 1, a set of helical modes resonant inside the reversal surface and also shows the presence of m = 0, $|n| \approx 0$. Further studies indicate that the m = 0 feature is composed of two linearly independent modes, the first being an $n = 0$ $\tilde{B}_\theta$ oscillation and the second, an $|n| \approx 0$ $\tilde{B}_\phi$.

Timescales of the measured fluctuations indicate that the instabilities are probably resistive in character. Estimates of the mode amplitude at the resonant surface, using the approximation of a small amplitude helical equilibrium, indicate island overlap should occur, leading to magnetic field ergodization. The energy confinement time due to stochastic transport, estimated directly from the measured fluctuations, has been

shown to be consistent with that experimentally observed.

Studies of the edge magnetic fluctuations have been applied to discharges of differing conditions and in the termination and current set-up phases. Results have shown that, although systematic trends in the amplitude occur, the general structure of the fluctuations is invarient with respect to changes in plasma current and filling pressure. At high values of Θ however, an $m = 1$, $n \approx -3$ mode becomes of equal significance to the more usual $m = 1$, $n \approx -10$ activity. Estimates of the safety factor indicate that, although the observed timescale of this mode appears resistive, it is not resonant.

The structure of the global fluctuations in the current set-up phase appears very similar to that during sustainment, although the amplitude is higher. If the observed fluctuations are essential to the relaxation process this indicates that the production and sustainment of reversal rely on the same mechanism. In the termination phase the observed fluctuations show several differences in the frequency and mode numbers. However, after reversal is lost the observed frequencies correspond to resistive timescales rather than the Alfven timescale expected for ideal modes.

An investigation of the radial structure of magnetic fluctuations under low current conditions using the insertable probe has been reported in chapter 6. In order to analyse data from the probe in terms of linearly independent modes the technique of correlation matrix fitting has been developed. In the sustainment phase of discharges this technique allows the identification of three simultaneous processes. At low frequencies (4-20 kHz) the dominant process can be shown to be due to resistive modes characterised by $m = 1$ and $n \approx -10$. A stability analysis of the measured equilibrium field profiles predicts a radial structure of the most unstable $m = 1$ tearing mode in good agreement with this process.

At a roughly equal peak amplitude the second process discernable is due

to modes localised in radius. This local turbulence is peaked on axis and falls to zero within errors at the discharge edge. At high frequencies (50-100kHz) this process dominates over the global modes.

The third process discernable, which has a peak power of around 1/4 of the dominant global instabilities, has been shown to possess the same radial structure and timescales as ideal modes of $m = 1$, $n \approx -6$ which are either destabilised by a resistive liner or whose growth rates are reduced by a resistive shell.

In the case of the termination and current set-up phases only the resistive global modes and the local turbulence can be discriminated due to statistical errors. However, the results in these phases are structurally very similar to those of the sustainment phase.

In order to be able to interpret the measurements of fluctuations in terms of equilibrium quantities chapter 4 was devoted to a determination of the equilibrium of low current discharges. While being used throughout the thesis in relation to fluctuations, the results of this chapter have also contributed valuable information on their own. In particular the form of the magnetic equilibrium has been confirmed to be in agreement with an MBFM description, the variation with radius of the flux-surface displacement due to toroidicity appears consistent with Shafranov's theory and pressure profiles have been deduced which appear peaked on axis and show $\beta_\theta \approx 14\%$. In addition an important result concerning stability is that no pitch minima are observed.

As we discussed in chapter 2, previous measurements of global instabilities in the RFP all relied on the observation of coherent modes. The toroidal variation of these instabilities was never studied in depth and the radial structures measured were, in the past, obtained by inspection or at best as the square root of the radial power distribution.

In addition, until recently, measurements on slow pinches were only compared with the ideal MHD theory. The contribution of this thesis is thus principally a systematic study of incoherent global instabilities in the RFP by statistical techniques and a detailed comparison with current MHD theory. In addition some progress, at least, has been made to a better understanding of the two key questions; field reversal and transport.

7.2 FURTHER AREAS OF STUDY

There are principally two areas open for obvious further investigation. These are the continuation of the study of linearly independent modes, with additional comparison to the linear theory, and an investigation into non-linear inter-mode coupling. We will start by listing the more important topics of the first area.

More detailed measurements with the edge coils using a larger toroidal array may be able to elucidate the n number of the m = 0 B_ϕ instabilities. Once this is known an accurate island size may be calculated and the question of whether the stochastic field-line region extends throughout the plasma or whether it is confined to the core could be answered.

In chapter 3 we discussed the large number of problems with the Association spectrum due to linear coupling effects. An obvious way around these problems is to use the technique of correlation matrix fitting on the signals from the poloidal array to disciminate the linearly independent modes. By a mutual orthogonalisation of these poloidal distributions a set of spatial filters could be constructed akin to the fourier filters used in this thesis. Application of these filters to the signals from the poloidal array could then be used to obtain the poloidal eigenmode spectrum and a type of Association spectrum without linear coupling problems. The benefits of such an investigation would be the possible identification of positive helicity kink modes resonant outside the reversal surface and the

accurate determination of how much independent m = 0 activity is present. This would again tie in with the stochasticity estimates.

In this thesis we have discussed the evolution of the n-spectrum in terms of relaxation oscillations which could account for the reversal process. Better time resolved measurements from both the edge coils and other internal diagnostics could shed significant light on the relevant mechanisms.

Concerning linear phenomena, finally we must point out that the resistive g-mode has not been discussed in this thesis. However it is difficult to see how a realistic stability analysis, as has been performed here for the tearing mode, could be carried out as experimental estimates of the pressure profile are unlikely to improve in the foreseeable future.

Turning now to non-linear effects, significant progress may perhaps be made by applying the correlation matrix fitting technique to higher order correlations. From the insertable probe measurements this might answer the question of whether the local turbulence is non-linearly correlated to the global modes. In the context of edge coil measurements the m = 2/m = 1 and m = 0/m = 1 non-linear couplings could be addressed. Such an investigation, if successful, could significantly enhance the understanding of the field-reversal mechanism.

BIBLIOGRAPHY

CHAPTER 1:

/1/ e.g 'Plasma Physics and Nuclear Fusion' Chapter 5 ed R D Gill Academic press (1981).

/2/ Friedberg J P :Reviews of Modern Physics 54 801 (1982).

/3/ Greene J M : Lausanne report LRP 114/76.

/4/ Wesson J A : Nucl. Fusion 18 1 87 (1978).

/5/ Mikhailovskii in 'Reviews of Plasma Physics'ed M A Leontovich (Consultants Bureau New York) 3 p20 (1967).

/6/ Krall and Trivelpiece: 'Principles of Plasma Physics' McGraw-Hill New York (1973).

/7/ Braginskii S I in 'Reviews of Plasma Physics' ed M A Leontovich (Consultants Bureau New York) Vol 1 (1965).

/8/ Furth H P: Nucl. Fusion 15 487 (1975).

/9/ Bartsh R R et al: Phys. Fluids 21 2287 (1978).

/10/ Bateman G: 'MHD instabilities' (MIT Cambridge Mass.) (1978).

/11/ Bodin H A B and Newton A A: Nucl. Fusion 20 1255 (1980).

/12/ Alfven H and Falthammar C G: 'Cosmical Electrodynamics', Clarendon Press, Oxford (1963).

/13/ e.g. Tritton D J: 'Physical Fluid Dynamics' Van Nostrand Reinhold Co New York (1977).

/14/ e.g. Bateman G: 'MHD Instabilities' (MIT cambridge Mass.) p67 (1978).

/15/ Mukhovatov V S, Shafranov V D: Nucl. Fusion 1 605 (1971).

/16/ Artsimovich L A: Nucl. Fusion 12 215 (1972).

/17/ Thomas C L: Culham Report CLM-R133 (1974).

/18/ Shafranov V D in Reviews Of Plasma Physics 2 130 Ed Leontovich M A Consultants Bureau New York.

/19/ Taylor J B: Phys. Rev. Lett. 33 139 (1974).

/20/ Whiteman K J: Plasma Phys. 7 293 (1965).

/21/ Connor J W Hastie R J Taylor J B Phys. Rev. Lett. 40 399 (1979).

/22/ Friedberg J P: Reviews Of Modern Physics 54 801 (p 863) (1982).

/23/ e.g. Bateman G: 'MHD Instabilities' (MIT Cambridge Mass.) p 93 (1978).

/24/ Furth H P, Killeen J, Rosenbluth M N and Coppi B: Culham IAEA Conf. 1 pp103-126 (1965).

/25/ Shafranov V D: Zh. Tech. Fiz. 40 241 (1970).

/26/ Kruskal M D: USAEC Rep. NYO-6045.

/27/ Shafranov V D: Atomnaya Energiya 5 38 (1956)
(English translation: Sov.J.Atom.Energy 1 709)
- 1963 Voprosy Teorii Plazmy 2 Gosatomizdat 317
- 1968 Proc. 3th Int. Conf. on Plasma Physics and controlled Nuclear Fusion Research, Novosibirsk vol 1 (Vienna IAEA) disc. p276.

/28/ e.g Chirgwin B H and Plumpton C: 'A course of Mathematics for Engineers and Scientists' Vol 1 Mathematical Methods p 388 Permagon press First Ed (1961).

/29/ Suydam B R: Proc. UN Conf. on Peaceful uses of Atomic Energy, 2nd Geneva Vol 31 (1958).

/30/ Bateman G: 'MHD Instabilities' (MIT Cambridge Mass.) p 67 (1978).

/31/ Newcomb W A: Ann. Phys. (N.Y.) 10 232 (1960).

/32/ e.g Butkov E: 'Mathematical Physics' Addison-Wesley Pub. Co. (1968).

/33/ Furth H P, Killeen J and Rosenbluth M N: Phys. Fluids 6 459 (1963).

/34/ Coppi B, Greene J M, Johnson J L: Nucl. Fusion 6 (1966) 101.

/35/ Robinson D C: Nucl. Fusion 18 939 (1978).

/36/ Killeen J: 'Physics of Hot Plasmas', Edited by Rye B J and Taylor J L Plenum Press p202 (1970).

/37/ Hosking R J and Robinson D C: Proc. 9th European Conf. on Controlled Nuclear fusion and Plasma Physics, Oxford 1 61 (1979).

/38/ e.g Cook I in 'Plasma Physics and Nuclear Fusion Research' Ed Gill R D Academic press 293 (1981).

/39/ Davidson R C: 'Methods in Nonlinear Plasma Theory' Academic Press (1972).

/40/ Rutherford P H: Phys. Fluids 16 1903 (1973).

/41/ White R B, Monticello D A, Rosenbluth M N, Waddell B V: Phys. Fluids 20 800 (1977).

/42/ Hender T C and Robinson D C: Nucl. Fusion 21 755 (1981).

/43/ Hender T C: PhD thesis London University (1982).

/44/ Rosenbluth M N, Sagdeev R Z, Taylor J B: Nucl. Fusion 6 297 (1966).

/45/ Rechester A B and Rosenbluth M N: Phys. Rev. Lett. 40 38 (1978).

/46/ Cowling T G: Mon. Not. R. Astron. Soc. 94 39 (1933).

/47/ Colgate S A, Ferguson J F, Furth H P in Peaceful Uses of Atomic Energy (Proc. 2nd Int. Conf. UN Geneva 1958) 32 100 (1958).

/48/ Gowers C W, Robinson D C, Sykes A, Verhage A J L, Wesson J A, Watts M R C, Bodin H A B in Plasma Physics and Controlled Nulcear Fusion Research (Proc. 6th Int. Conf. Berchtesgaden 1976) 1 IAEA Vienna 429 (1977).

/49/ Sykes A and Wesson J A in Controlled Fusion and Plasma Physics (Proc. 8th Europ. Conf. Prague 1977) 1 Czechoslovak Academy of Sciences 80 (1977).

/50/ Wesson J A and Sykes A: Phys. Rev. Lett. 37 140 (1976).

/51/ Buffa A, Costa S, Nalesso G F, Malesani G in Controlled Fusion and Plasma Physics (Proc. 7th Europ. Conf. Lausanne 1975) 1 Ecole Polytechnique Federale de Lausanne 40 (1975).

/52/ Buffa A, Costa S, De Angelis R, Nalesso G F, Ortolani S et al in Controlled Fusion and Plasma Physics (Proc. 6th Europ. Conf. Prague 1977) Czechoslovak Academy of Sciences, Prague 81 (1977).

/53/ Butt E P, Firth L, Gribble R F, Yin-An, Li, Newton A A, Verhage A J L : Culham laboratory report CLM-R165 (1977).

/54/ Butt E P, Gowers C W, Mohri A, Newton A A, Robinson D C, Verhage A J, Watts M R C, Yin-An, Li, Bodin H A B in Controlled Fusion and Plasma Physics (Proc. 7th Europ. Conf. Lausanne 1975) 1 Ecole Polytechnique Federale de Lausanne 39 (1975).

/55/ Hutchinson I H: Private communication and submitted to Phys. Fluids.

/56/ Kadomtsev B B: IAEA-CN-35/B1 555.

/57/ Kadomtsev B B: Fiz Plasmy 1 710 (1975).

/58/ Caramana E J, Nebel R A, Schnack D D: Los Alamos Report LA-UR82-2360 and submitted to Phys. Fluids.

/59/ Rusbridge M G: Plasma Phys. 19 499 (1977).

/60/ Rusbridge M G and Saunders P G H: Culham Laoratory Memorandum CLM-M21 (1963).

/61/ Rusbridge M G: Plasma Phys. 22 331 (1980).

/62/ Jacobson A R and Moses R W: Submitted to Physical Review.

CHAPTER 2:

/1/ Butt E P, Carruthers R, Mitchell J T D, Pease R S, Thonemann P C, Bird M A, Blears J, Hartill E R: Proc. Second Int. Conf. on Peaceful Uses of Atomic Energy (United Nations, Geneva, 1958), Vol 32, p.42.

/2/ Burton W M, Butt E P, Cole H C, Gibson A, Mason D W, Pease R S, Whiteman K, Wilson R, Nucl. Fusion Suppl. Pt. 3, 903 (1962).

/3/ Rusbridge M G, Jones H W, Lees D J, Saunders P A H, Witalis E A: J. Nucl. Energy Part C: Plasma Physics 3 98 (1961).

/4/ Rusbridge M G, Lees D J, Saunders P A H: Nucl. Fusion Suppl. Part 3 895 (1962).

/5 / Robinson D C, Rusbridge M G, Saunders P A H: Plasma Physics 10 1005 (1968).

/6/ Robinson D C, Rusbridge M G: Plasma Physics 11 73 (1969).

/7/ Robinson D C, Rusbridge M G: Phys. Fluids 14 2499 (1971).

/8/ Edwards S F: J. Fluid Mech. 18 239 (1964).

/9/ Robinson D C: PhD Thesis University of Manchester 1966.

/10/ Lees D J, Rusbridge M G: Culham Report CLM-P68.

/11/ Wort D J H, Heald M A: Plasma Phys. 7 79 (1965).

/12/ Butt E P, Cole H C, Dellis A N, Gibson A, Rusbridge M G, Wort D: Plasma Physics and Controlled Nuclear Fusion Research (Proc. 2nd Int. Conf. Culham 1965).

/13/ Robinson D C, King R E: ibid. 263 1968.

/14/ Wort D J H: Culham Report CLM-R40 (1965).

/15/ Robinson D C, Boland B C, King R E, Pease R S: Controlled Fusion and Plasma Physics (Proc. 2nd Europ. Conf.. Sweden 1967).

/16/ Butt E P, Newton A A: Pulsed High Beta Plasmas (Proc. 3rd Top. Conf. Abingdon 1975) Pergamon Press, London (1976) 425.

/17/ Taylor J B: Phys. Rev. Lett. 33 139 (1974).

/18/ Butt E P, Firth L, Gribble R F, Yin An Li, Newton A A, Verhage A J L: Culham Report CLM-R165.

/19/ Verhage A J L, Furzer A S, Robinson D C: Nucl. Fusion 18 457 (1978).

/20/ Carolan P G, Gowers C W, Robinson D C, Watts M R C, Bodin H A B: Plasma Physics and Controlled Nuclear Fusion Research (Proc. 7th Int. Conf. Innsbruck 1978) 2 IAEA, Vienna 23 1979.

/21/ La Haye R J et al: General Atomic Report GA-A16945 (1982).

/22/ Antoni V, Ortolani S: Plasma Phys. 25 799 (1983).

/23/ Jacobson A R, Rusbridge M G: Los Alamos Report LA-9589-MS.

/24/ Watt R G, Nebel R A: Phys. Fluids 26 1168 (1983).

/25/ Rusbridge M G and Jacobson A R: submitted to J. Appl. Phys.

/26/ Jacobson A R, Rusbridge M G, Burkhardt L C: J. Appl. Phys. 55 125 (1984).

CHAPTER 3:

/1/ e.g. Muir D: PhD thesis London University (1983).

/2/ e.g. Bleaney B I and Bleaney B: 'Electricity and Magnetism' p129 Oxford Univ. Press (1976).

/3/ Bendat J S: 'Principles and Applications of Random Noise Theory' Wiley New York (1958). Reprinted by Krieger Publishing Co. New York (1977).

/4/ Bendat J S and Piersol A G: 'Random Data: Analysis and Measurement Procedures' Wiley-Interscience (1971).

/5/ Bendat J S and Piersol A G: 'Engineering Applications of Correlation and Spectral Analysis' Wiley-Interscience (1980).

/6/ Hasselman K, Munk W and MacDonald G: 'Bispectra of Ocean Waves' in 'Time Series Analysis' Ed M.Rosenblatt pp125-139 Wiley.

/7/ e.g. Butkov E: 'Mathematical Physics' Addison-Wesley Publishing Co. p198 (1968).

/8/ Gull S F, Daniell G J: Nature 272 686 (1978).

/9/ Skilling J, Strong A W and Bennet K: Mon. Not. R. Astr. Soc. 187 145 (1979).

/10/ Cottrell G A, Clark W H M and Gull S F: Culham Report CLM-P687.

/11/ Skilling J: 'Algorithms and Applications' Workshop On Maximum Entropy Analysis, Laramie, Wyoming (1981).

/12/ 'Handbook of Applicable Mathematics' Ed Ledermann W, Churchhouse F Volume III Chapter 11 Wiley (1981).

CHAPTER 4:

/1/ Shafranov V D in Reviews of Plasma Physics 2 p130 Ed Leontovich M A Consultants Bureau New York.

/2/ Whiteman K J : Plasma Phys. 7 (1965) 293.

/3/ Spitzer L : 'Physics of fully ionised gases', Interscience tracts on Physics and Astronomy, Interscience publishers, John Wiley and sons, New York / London.

/4/ e.g. Moffet H K : 'Magnetic Field Generation In Electrically Conducting Fluids', Cambridge university press (1978).

/5/ La Haye R J, Carlstrom T N, Goforth R R, Jackson G L, Schaffer M J, Tomano T, Taylor P L : General Atomic Report GA-A16945 and submitted to Nucl Fusion.

/6/ Antoni V and Ortalani S : Plasma Physics 25 799 (1983).

/7/ Bodin H A B , Bunting C A , Carolin P G , Guidicotti L , Gowers C W , Hirano Y , Hutchinson I H , Jones P A , Lamb C , Malacarne M , Newton A A , Piotrowicz V A , Shimada T, Watts M R C in plasma physics and controlled nuclear fusion research Proc. conf. Baltimore, 1982, Vol 1, IAEA Vienna 1983 pp641-657.

/8/ Schnack D D, Caramana E J, Nebel R A : Bulletin of APS 28 8 p1229 (1983).

/9/ Gimblett C G , Watkins M L in controlled Fusion and Plasma Physics (proc. 7th Europ. conf. Lausanne,1975) Vol.1. 103 (1975).

/10/ Gimblett C G , Watkins M L in pulsed high β Plasmas (Proc. 3th top. conf. Abingdon, 1975) Permagon press, London 279 (1976).

/11/ Rusbridge M G : Plasma Phys. 19 499 (1977).

CHAPTER 5:

/1/ Bodin H A B et al : Proc.9th Int.Conf. Baltimore 1982 vol 1 641.

/2/ Whiteman K J : Plasma Phys. 7 293 (1965).

/3/ Robinson D C : Plasma Phys. 13 439 (1971).

/4/ e.g Bateman G : 'MHD Instabilities' (MIT Cambridge Mass.) (1978).

/5/ Rochester A B and Rosenbluth M N : Phys. Rev. Lett. 40 38 (1978).

/6/ Rosenbluth M N, Sagdeev R Z, Taylor J B and Zaslavski G M : Nucl. Fusion 6 297 (1966).

/7/ Antoni V and Ortolani S : Plasma Phys. 25 799 (1983).

/8/ Hender T C and Robinson D C : Computer Phys. Comm. 24 413 (1981).

/9/ Rutherford P H : Phys. Fluids 16 1903 (1973).

/10/ Hender T C and Robinson D C : Nucl. Fusion 21 755 (1981).

/11/ Furth H P: in 'Current Disruption in Toroidal devices' Lackner K and Zehrfeld H P (Eds) IPP 3/51. Max Planck Institut fur Plasmaphysik Garching (1979).

CHAPTER 6:

/1/ Antoni V and Ortolani S: Plasma Phys. 25 799 (1983).

/2/ Robinson D C, Nunn-Price J E, Furzer A S, Killeen J, Diabase J A: Culham Report CLMP710 and submitted to Reports on Progress in Physics.

/3/ Furth H P, Killeen J, Rosenbluth M N: Phys. Fluids 6 459 (1963).

/4/ Johnson J L, Greene J M, Coppi B: Phys. Fluids 6 1169 (1963).

/5/ Coppi B, Greene J M, Johnson J L: Nucl. Fusion 6 101 (1966).

/6/ Goedbloed et al: Nucl. Fusion 12 649 (1972).

/7/ Robinson D C: Culham Report CLM-R199 (1979).

APPENDIX A

MAXIMUM ENTROPY ESTIMATION OF THE TOROIDAL MODE POWER SPECTRUM

Measurements from the toroidal array of edge coils can be used to construct the spatial auto-correlation function, $R(\delta\phi)$ for $0 < \delta\phi < \phi_{max}=60°$. In principle the toroidal mode power spectrum P_n can be calculated from this information through an expression of the form:

$$R(\delta\phi) = L(P_{o,...}) \ , \qquad - (AA1)$$

where L is a linear operator. The problem with such direct calculation through 'linear deconvolution' is that R is only known to a certain accuracy. On inversion of equation AA1 large amplitude spurious features in P_n can arise from such errors. Essentially the presence of statistical errors in R may be thought of as generating an infinite family of possible R's each of which map to an element of a similar family in P. The family of possible P's dictate the probability of a certain realisation of P being the 'true' power spectrum given the (gaussian) distributions of R. Clearly what is wanted is an estimation of the most likely P consistent with R within the statistics. The reason why linear deconvolution is not successful is that the most likely P is not the most likely R.

Clearly it would be impractical to estimate the most likely power spectrum by evaluating the mapping of different R realisations to their counterpart P's as this would involve enormous computer time. However it can be argued that the smoothest power spectrum consistent with the measured R is the most likely. This is the basis of the Maximum Entropy Method (MEM).

Maximum Entropy Procedure

Suppose we estimate $R(\delta\phi)$. In practice we only have a finite number of toroidal array coils, N and so we will refer to $R(\delta\phi)$ as R_i. Then we define a 'smoothness function' which is known as the Configurational Entropy as:

$$S \equiv - \sum_i h_i \ln (h_i) \qquad - (AA2)$$

where $h_i \equiv P_i / \sum_i P_i$.

Now consider the quantity:

$$Q \equiv S(P_{o,\ldots}) - \lambda \sum_i \{ R_i - L(P_{o,\ldots})\}^2, \qquad - (AA3)$$

where λ is a Lagrange multiplier. If $\lambda=0$ and we maximise Q we will calculate that $h_i = 1/e$ for all i, which is the smoothest possible solution since there is no variation with respect to i. On the other hand if $\lambda\to\infty$, maximising Q leads to the same result as an exact linear deconvolution. Thus there will exist some λ, intermediate to the two extremes, $\lambda = 0$ and $\lambda\to\infty$, which represents the smoothest possible power spectrum consistent with the measured spatial autocorrelation function (within errors). This will be the most likely power spectrum. The trick with the Maximum Entropy method is to devise algorithms which will maximise $Q(\lambda)$ such that λ effects the correct balance between smoothness and information content in P as determined by the errors in R.

Outline Of Algorithms

Figure AA1 shows a flow diagram of a basic MEM algorithm. Initially a very small value of λ is chosen. Q is then maximised by a non-linear optimisation routine and an error test is performed which dictates if λ is too high to be consistent with the errors in R. If λ is not too high it is

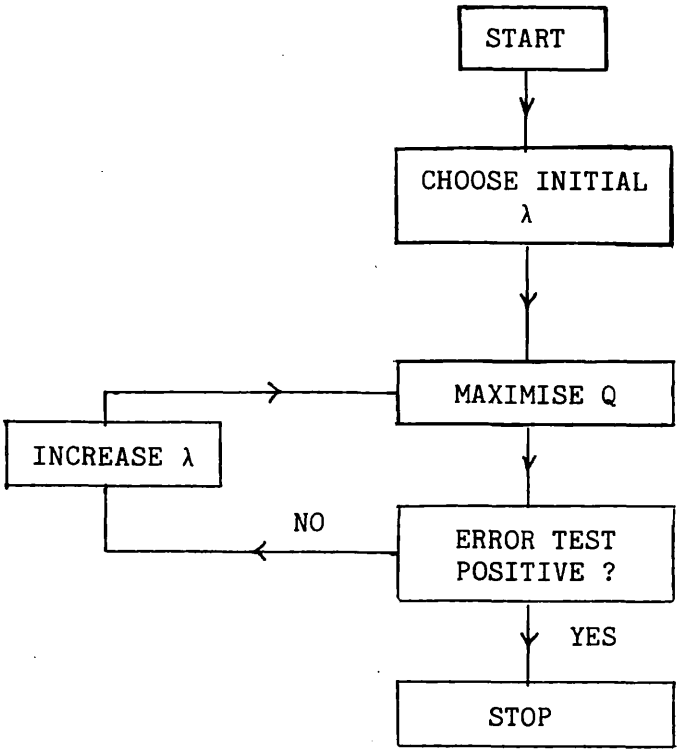

Figure AA1

incremented and the procedure iterates. The error test is simply a χ^2 test. After each Q optimisation a power spectrum P_n is predicted. This is used to calculate a predicted R_i by equation AA1. Denoting the predicted R_i by $R^p{}_i$ and the measured R by $R^m{}_i$ the test is:

$$\sum_i \{ R^p{}_i - R^m{}_i \}^2 / \sigma_i{}^2 < N \ , \qquad \text{- (AA4)}$$

where σ_i is the standard error in R_i. If the test is positive then λ is large enough whereas if it is negative λ should be increased to allow extra information in the predicted power spectrum.

Numerical Schemes

Two principle numerical schemes have been implemented to calculate the Maximum Entropy toroidal mode power spectrum. Both use the type of algorithm outlined in figure AA1 differing only in the method for optimising Q for a given λ. It should be stressed that this numerical

problem is not trivial and for an efficient solution the algorithms become very complicated. Since the problem in hand is relatively small the two algorithms used were constructed with simplicity and not efficiency in mind. This means that instead of taking a few seconds to calculate a toroidal mode power spectrum the programs developed take typically a few minutes.

Scheme One:

We require to optimise the function:

$$Q \equiv -\sum_i \{ \frac{P_i}{\sum_j P_j} \ell n \frac{P_i}{\sum_j P_j} \} - \lambda \sum_i \{ P_i - L(P_1, \ldots) \}^2 \qquad - (AA5)$$

Since Q has only one minimum in the function space $\{P_i\}$ we may reduce the optimisation of Q to the solution of the equations $\partial Q/\partial P_i = 0$. These equations may be written in the form:

$$P_i = \exp\{ Z[P_0, \ldots] \} , \qquad - (AA6)$$

where Z is some non-linear functional. An obvious implicit algorithm is:

$$P_i^{(n+1)} = \exp\{ Z[P_0^{(n)}, \ldots] \}, \qquad - (AA7)$$

where the superscipt n indicates successive iteration. This algorithm has the advantage that P_i must always be positive definite and in addition should be able to cope with large dynamical ranges (due to the exp). However the algorithm as it stands is susceptable to numerical instability. In order to escape this problem a modified form must be used:

$$P_i^{(n+1)} = \alpha P_i^{(n)} + (1-\alpha)\exp\{ Z[P_0^{(n)}, \ldots] \} , \qquad - (AA8)$$

where α is a constant in the interval [0,1]. In highly unstable cases α must be increased to 0.999 making convergence rather slow.

Scheme Two:

The second method that has been used to optimise Q is a steepest ascents algorithm of the form:

$$P_i^{(n+1)} = P_i^{(n)} + \beta \left\{\frac{\partial Q}{\partial P_i}\right\}^{(n)} \quad \text{if } P_i^{(n+1)} > 0 \qquad - (AA9)$$

$$= \text{Small positive number} \quad \text{otherwise ,}$$

where the coefficient β is reduced as n increases to effect convergence.

The main problem with this algorithm is that it spends most of its time adjusting the small values of P_i produced by the second alternative in the above equation.

APPENDIX B

LINER PENETRATION

Because some of our measurements are made outside the liner it is important to estimate the effect of the liner on the observed fluctuations. If we treat the liner as thin with conductivity σ and thickness δ having radius a concentric within a shell, assumed infinitely conducting, of radius b and consider perturbations of the form exp $i(m\theta + n\phi - \omega t)$. Then provided

$$\{ \left(\frac{m}{a}\right)^2 + \left(\frac{n}{R_o}\right)^2 \}(b-a)^2 << 1 \qquad - (AB1)$$

we can treat the outward penetration of magnetic field across the liner (B_0) as related to that inside (B_i) by :

$$B_0 = B_i/(1 + i\omega\tau) \quad , \qquad - (AB2)$$

where $\tau = \mu_0 \sigma \delta (b-a)$.

This shows that the effect of the liner is to integrate the field with a passive time constant τ.

An important complication is that the liner has a bellows construction so that the effective δ is different for currents flowing in the toroidal and poloidal directions. Denote these by δ_θ and δ_ϕ. Then it may be shown that, approximating the liner as thin, we have

$$\delta_{eff} = \frac{\delta_\theta \delta_\phi \{ (m/a)^2 + (n/R_o^2) \}}{\delta_\theta (m/a)^2 + \delta_\phi (n/R_o)^2} \quad . \qquad - (AB3)$$

For the liner of HBTX1A $\tau_\theta = \mu_o \sigma \delta_\theta (b-a) \approx 30$ μs and $\delta_\phi \approx \delta_\theta/16$ from which the penetration time constant of any mode may be calculated. For example, if $m = 0$, $n \neq 0$, then $\tau \approx 30$ μs while for $m = 1$, $n = 8$ $\tau \approx 10$ μs, corresponding to frequencies of ≈ 5 kHz and 15 kHz respectively.

Additional complications arise beacause the convolution depth is not small compared to (b-a); however the above treatment is regarded as sufficient to first order. Finally, for m = 0, n = 0 the shell gaps prevent it from acting as a flux conserver and the penetration time depends on the equivalent flux out to the windings. The penetration times are then estimated as ≈ 100μs for B_ϕ and ≈ 20 μs for B_θ. It should be noted therefore, that m = 0 perturbations (and particularly for n = 0) suffer significantly greater attenuation in general than those for higher m.

APPENDIX C

CORRECTION OF THE FIELD PROFILES FOR A UNIFORM HORIZONTAL PLASMA SHIFT

We have seen that, in the central region of the discharge, the plasma equilibrium may be characterised by a set of concentric magnetic surfaces whose centre is shifted a distance Δ from the geometrical minor axis (GMA). Figure AC1 shows the situation. Our probe is inserted vertically to the GMA, the individual coils measuring $B_{mx}(y)$,$B_{my}(y)$ and $B_{mz}(y)$. The problem we address is to determine the true poloidal and toroidal fields $B_\omega(\rho)$ and $B_Z(\rho)$.

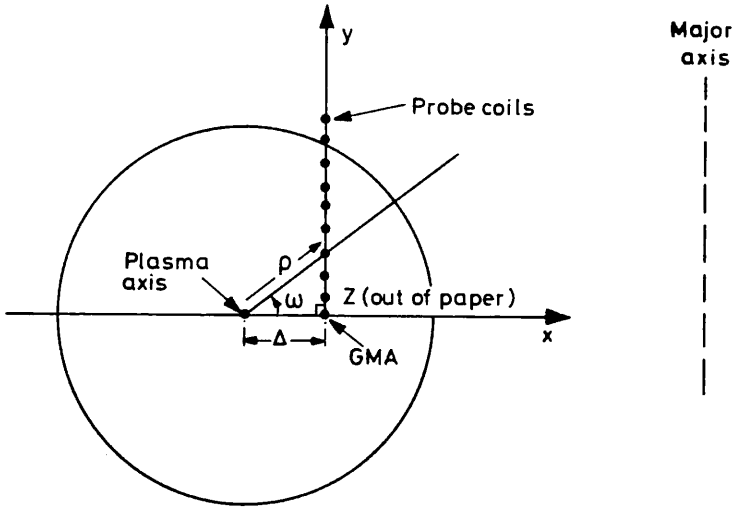

Figure AC1 Diagram showing the shifted plasma equilibrium. The point $\rho=0$ represents the centre of symmetry of the innermost flux surface and the point marked GMA represents the geometrical minor axis.

AC.1 Toroidal Field

By definition we may write

$$B_{mz}(y) = B_z(\rho) = B_z(\sqrt{[y^2 + \Delta^2]}). \qquad - (AC1)$$

And so,on expansion,this yields

$$B_z(\rho) \approx B_z(y + \frac{\Delta^2}{2y}) \approx B_z(y) + \frac{\Delta^2}{2y}\ \frac{dB_z}{d\rho}, \qquad - (AC2)$$

which is valid provided $\Delta^2/y^2 << 1$. Using AC1 again this may be recast in the following form

$$B_z(y) \approx B_{mz}(y) - \frac{\Delta^2}{2y} \frac{dB_{mz}}{dy} \quad . \qquad - (AC3)$$

Obviously, near the axis this formula is not justified. However, in this region we may expand in the following manner :

$$B_z(\rho) \approx B_z(0) + \frac{\rho^2}{2} \frac{d^2 B_z}{d\rho^2}\bigg|_{\rho=0} \qquad - (AC4)$$

$$\approx B_z(y) + \frac{\Delta^2}{2} \frac{d^2 B_{mz}}{dy^2}\bigg|_0 \quad , \qquad - (AC5)$$

$$\text{provided } \left|\frac{\Delta^3}{6B_{mz}} \cdot \frac{d^3 B_{mz}}{dy^3}\right| \ll 1. \qquad - (AC6)$$

Now since near the axis $\frac{d^2 B_{mz}}{dy^2}\Big|_0 \approx \frac{1}{y} \frac{dB_{mz}}{dy}\Big|_y$ we again obtain equation AC3. So this equation in fact holds subject to the condition AC6 which is not difficult to satisfy. Our correction scheme for B_z is therefore to use

$$B_z(y) = B_{mz}(y) - \frac{\Delta^2}{2y} \frac{dB_{mz}}{dy} \quad . \qquad - (AC7)$$

Hence if we expand the measured field as an even polynomial in y so that

$$B_{mz}(y) = \sum_{j=0}^{N} b_j \, y^{2j} \qquad - (AC8)$$

the corrected toroidal field may be written

$$B_z(y) = \sum_{j=0}^{N} b_j \left(1 - \frac{j\Delta^2}{y^2}\right) y^{2j} \quad . \qquad - (AC9)$$

AC.2 Poloidal Field

In the outer region of the discharge we may expand as follows

$$\frac{B_\omega(\rho)}{\rho} = \frac{B_{mx}(y)}{y} \approx \frac{B_{mx}(\rho)}{\rho} - \frac{\Delta^2}{2\rho} \frac{d}{d\rho}\left(\frac{B_{mx}}{\rho}\right) \qquad - (AC10)$$

$$\text{provided } \left|\frac{\Delta^2}{2B_{mx}} \frac{d}{d\rho}\left(\frac{B_{mx}}{\rho}\right)\right| \ll 1 \quad . \qquad - (AC11)$$

Changing variables this gives the following correction scheme:

$$B_\omega(y) = B_{mx}(y) - \frac{\Delta^2}{2} \frac{d}{dy}\left(\frac{B_{mx}}{y}\right) \quad . \qquad - (AC12)$$

However near the axis the condition AC11 will break down and we must then

expand as follows:

$$B_\omega(\rho) \approx \frac{dB_\omega}{d\rho}.\rho + \frac{d^3B_\omega}{d\rho^3}\frac{\rho^3}{3!} \quad . \qquad - (AC13)$$

And so $$B_{mx}(y) \approx \left.\frac{dB_\omega}{d\rho}\right|_0 y + \left.\frac{d^3B_\omega}{d\rho^3}\right|_0 \frac{y\rho^2}{3!} \qquad - (AC14)$$

$$\approx B_\omega(y) + \frac{1}{6}\, y\, \Delta^2 \left.\frac{d^3B_{mx}}{dy^3}\right|_0 . \qquad - (AC15)$$

However in the inner region

$$\frac{\Delta^2}{2y}\frac{d}{dy}\left(\frac{B_{mx}}{y}\right) \approx \frac{1}{6}\Delta^2 \left.\frac{d^3B_{mx}}{dy^3}\right|_0 \qquad - (AC16)$$

since $$\frac{B_{mx}}{y} \approx \left.\frac{dB_{mx}}{dy}\right|_0 + \left.\frac{d^3B_{mx}}{dy^3}\right|_0 \frac{y^2}{3!} \quad . \qquad - (AC17)$$

Hence AC15 leads to the correction scheme of AC12. This is valid provided

$$\left|\frac{\Delta^2}{6}\left.\frac{d^3B_{mx}}{dy^3}\right|_0 \Big/ \frac{dB_{mx}}{dy}\right| << 1 \ . \qquad - (AC18)$$

If we thus expand B_{mx} as an odd polynomial series so

$$B_{mx}(y) = \sum_{j=0}^{N} a_j y^{(2j+1)} \qquad - (AC19)$$

then the true poloidal field is given by

$$B_\omega(y) = \sum_{j=0}^{N} \left(1 - \frac{j\Delta^2}{y^2}\right) y^{(2j+1)} \qquad - (AC20)$$

APPENDIX D

DERIVATION OF THE FIELD-LINE DIFFUSIVITY

When field-lines are thoroughly stochastic one expects that the quantity

$$\langle \Delta r^2/L \rangle \equiv D_{st} \qquad \text{- (AD1)}$$

has a well defined non-zero limit as $L \to \infty$ (here Δr is the radial displacement experienced in following a field-line a distance L).

Now $$\Delta r = \int_0^L \frac{B_r}{|B|}\, d\ell \quad , \qquad \text{- (AD2)}$$

all quantities being evaluated at the resonance $r = r_s$. So assuming $|B|$ and B_r have negligible variation over Δr,

$$D_{st} \equiv \langle \Delta r^2/L \rangle = \left\langle \frac{1}{B^2 L} \int_0^L \int_0^L B_r(\ell')\, B_r(\ell)\, d\ell\, d\ell' \right\rangle \qquad \text{- (AD3)}$$

$$= \frac{1}{B^2 L} \int_0^L \int_0^{L-\ell} \langle B_r(\ell)\, B_r(\ell+s) \rangle\, ds\, d\ell. \qquad \text{- (AD4)}$$

If we now assume that the fluctuations are translationally symmetric so that $\langle B_r(\ell)\, b_r(\ell+s) \rangle$ is independent of ℓ and also L > parallel correlation length, then

$$D_{st} = \frac{1}{B^2} \int_{-\infty}^{+\infty} \langle B_r(0)\, B_r(s) \rangle ds \qquad \text{- (AD5)}$$

$$= \left| \frac{B_r}{B} \right|_{r_s}^2 \Lambda_{\parallel} \quad ,$$

where $\Lambda_{\parallel}$ is the parallel coherence length.

APPENDIX E

THE EFFECT OF THE SHAFRANOV SHIFT ON THE CMF ALGORITHM

Owing to the toroidal nature of the HBTX1A pinch the longitudinal plasma axis does not coincide with the geometrical minor axis (GMA) but is shifted by a distance $\Delta \approx 3$ cm (the Shafranov shift). The magnetic probe refered to in this thesis is inserted into the plasma vertically and the end coil is situated at the GMA. Figure AE1 shows the situation. It is clear that near to the GMA the probe signals measure linear combinations of the various field components rather than single components. In this appendix we address the question of what effect the shafranov shift has on the various m = 1 processes deduced by CMF.

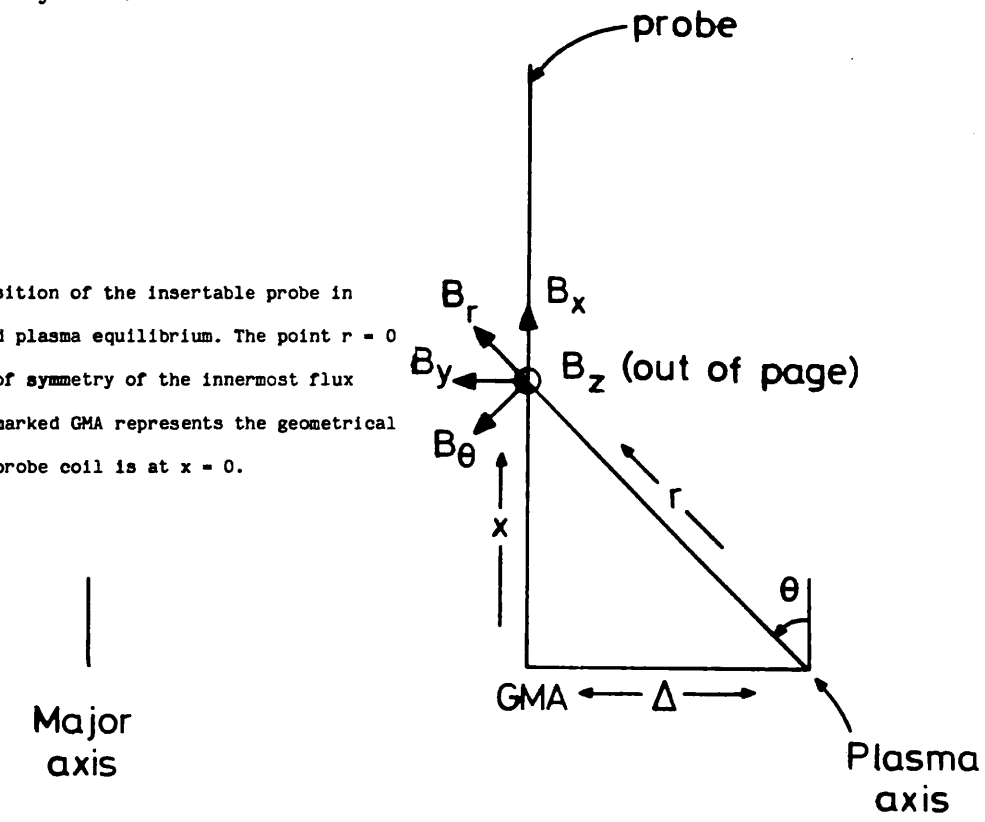

Figure AE1

Diagram showing the position of the insertable probe in relation to the shifted plasma equilibrium. The point r = 0 represents the centre of symmetry of the innermost flux surface and the point marked GMA represents the geometrical minor axis. The first probe coil is at x = 0.

We start by fourier decomposing the 'true' fluctuating fields in a manner consistent with the equation $\nabla.\underline{B} = 0$ and the observation that the temporal phase of B_r is $\pi/2$ out of phase with B_θ and B_ϕ. We assume that there is just one fourier mode present and consider a plane of constant ϕ:

$$\tilde{B}_r(t) = b_r(r) \sum_\alpha \zeta(\omega_\alpha)\cos(m\theta+\omega_\alpha t)$$
$$\tilde{B}_\theta(t) = b_\theta(r) \sum_\alpha \zeta(\omega_\alpha)\sin(m\theta+\omega_\alpha t) \quad - (AE1)$$
$$\tilde{B}_\phi(t) = b_\phi(r) \sum_\alpha \zeta(\omega_\alpha)\sin(m\theta+\omega_\alpha t) \quad .$$

From figure AE1 we see that the probe actually measures (B_x,B_y,B_z). These are related to the true field components by the following expressions:

$$\tilde{B}_x(r,\theta) = \tilde{B}_r(r,\theta)\cos\theta - \tilde{B}_\theta(r,\theta)\sin\theta$$
$$\tilde{B}_y(r,\theta) = \tilde{B}_\theta(r,\theta)\cos\theta + \tilde{B}_r(r,\theta)\sin\theta \quad - (AE2)$$
$$\tilde{B}_z(r,\theta) = \tilde{B}_\phi(r,\theta).$$

For the y-component, using equations AE1 this gives:

$$\tilde{B}_y(r,\theta) = \sum_\alpha \{ b_r(r)\zeta(\omega_\alpha)\sin\theta\cos(m\theta+\omega_\alpha t) + b_\theta(r)\zeta(\omega_\alpha)\cos\theta\sin(m\theta+\omega_\alpha t)\} \quad - (AE3)$$

which, for m = 1, may be written:

$$\tilde{B}_y(r,\theta) = \sum_\alpha \zeta(\omega_\alpha)\{\frac{\sin(\omega_\alpha t)}{r^2}[\, x^2 b_\theta(r) - \Delta^2 b_r(r)] + \cos(\omega_\alpha t)\,\frac{\Delta x}{r^2}\,[\, b_r(r) + b_\theta(r)]\}. \quad - (AE4)$$

Using this expression we may calculate the auto correlation matrix, R^{yy}:

$$R^{yy}(x,x') \propto \int \tilde{B}_y(r,\theta)\tilde{B}_y(r',\theta')dt \quad - (AE5)$$
$$\propto \int \sum_\alpha \sum_\beta \zeta(\omega_\alpha)\zeta(\omega_\beta)\{ \sin(\omega_\alpha t)b_y{}^1(r) + \cos(\omega_\alpha t)b_y{}^2(r)\}$$
$$X \{ \sin(\omega_\beta t)b_y{}^1(r') + \cos(\omega_\beta t)b_y{}^2(r')\}dt$$

where $b_y{}^2(r) \equiv \Delta x\{b_r(r) + b_\theta(r)\}/(r^2)$

and $b_y{}^1(r) \equiv \{x^2 b_\theta(r) - \Delta^2 b_r(r)\}/(r^2)$.

Terms such as $\sin(\omega_\alpha t)\sin(\omega_\beta t)$ will now cancel and we are left with:

$$R^{yy}(x,x') \propto b_y{}^1(x).b_y{}^1(x') + b_y{}^2(x).b_y{}^2(x') \quad - (AE6)$$

If we substitute this form of R^{yy} into equation 10 (section 2 of this paper) assuming two global processes and then proceed to minimise Q, the two processes that we will calculate are simply $b_y{}^1$ and $b_y{}^2$. Thus, assuming that the fluctuations are solely due to m = 1, the Shafranov shift acts to create another process ($b_y{}^2$) and distort the true m = 1 B_θ 'eigenfunction' ($b_y{}^1$).

Away from the centre of the discharge $x \approx r >> \Delta$ and so in this region $b_y{}^1$ is simply the undistorted m = 1 eigenfunction. As we approach the centre of the discharge x becomes comparable to r and Δ. At the GMA x = 0 and $r = \Delta$ and so $b_y{}^1 = -b_r$. However, due to single-valuedness of the magnetic field, in this region (for m = 1) $b_r \approx -b_\theta$ and so $b_y{}^1$ is, to a good approximation, the true m = 1 B_θ eigenfunction for all r.

Regarding $b_y{}^2$, this is a global process of about one third of the amplitude of the true B_r and B_θ eigenfunctions. Figure AE2 shows its general form. By using a four-process CMF fit we are sometimes able to distinguish this process although $\chi^2 < 1$.

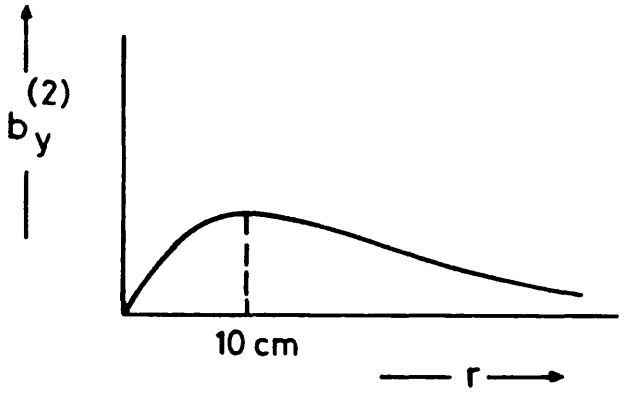

Figure AE2 Form of the shift-induced second (m = 1) process for B_θ.

Exactly similar results may be shown to hold for B_x. For B_z the effect of the Shafranov shift is to create a second-process localised to the first two coils of the probe (nearest to the GMA) and to weight the true B_ϕ eigenfunction in the vicinity of the GMA with a function that goes to zero at x = 0. This latter restriction is relaxed when an m = 0 component is

considered in addition to the m = 1, the two being linearly coupled together.

We should thus conclude that the large diagonal element mismatch for r < a/2 in figure 6.12 is not expicable by the Shafranov shift. However, in figure 6.11 we should interpret nearly all of the mismatch on the first two coils as being due to this shift. In addition, the B_θ and B_r m = 1 eigenfunctions of figures 6.9 and 6.14 are not affected by the shift and the B_ϕ is simply weighted towards zero on the first two coils. The fact that $\tilde{B}_\phi \neq 0$ at x = 0 is indicative of m = 1 being linearly coupled to m = 0 in this region.

APPENDIX F

DPRIME : A DELTA PRIME TEARING MODE STABILITY CODE

In order to investigate the tearing mode stability of the measured equilibrium field profiles (discussed in chapter 5) a delta prime code 'DPRIME' was written (using FORTRAN and implemented on an LSI 11/23 digital equipment computer). In this appendix we will briefly discuss this code and outline the equations it solves.

In the approximation of cylindrical geometry, small but finite resistivity and no equilibrium pressure gradient we consider a perturbation of the form $B_r = b_r(r)\exp(im\theta + ikz + \omega t)$. This perturbation can be shown to satisfy the following second order ODE (obtained from the linearised form of the equations $\nabla x(\underline{J}x\underline{B})=0$ and $\nabla.\underline{B}=0$):

$$\frac{d^2\Psi}{dr^2} + A\Psi = 0 \quad , \qquad \text{- (AF1)}$$

where $\Psi = \dfrac{r^{3/2} b_r(r)}{(m^2 + k^2r^2)^{1/2}}$

and $A = \sigma^2 + \dfrac{2\sigma mk}{m^2 + k^2r^2} + \dfrac{(m^4 + 10\, m^2k^2r^2 - 3k^4r^4)}{4r^2(m^2 + k^2r^2)^2} - \dfrac{m^2 + k^2r^2}{r^2}$

$$- \frac{d\sigma}{dr}\frac{(mB_z - krB_\theta)}{(mB_\theta + krB_z)}$$

and $\sigma = \dfrac{\underline{J}.\underline{B}}{B^2}$.

Close to the singular surface this equation breaks down and a higher order finite resistivity equation must then be used.

In order to determine the tearing mode stability of a given equilibrium (determined by B_θ, B_z) to a helical instability with mode numbers (m,n) we integrate the above equation out from the origin (where $\Psi=0$ and Ψ' determines the scaling) to the resonance, where the last term in the definition of A diverges leading to a logarithmic singularity in $d\Psi/dr$. In this region we use the asymtotic solution:

$$\Psi(x) = C(1 - gx\ln|x|) + B(x - gx^2/2), \qquad - (AF2)$$

where $$g = -\frac{d\sigma}{dr}\frac{(mB_z/r - kB_\theta)}{dF/dr}$$

and $$F = \frac{mB_\theta}{r} + kB_z$$

and $$x = (r - r_s).$$

By matching Ψ and Ψ' just before r_s we can determine the two constants C and B and so fully determine the solution from the axis to the resonance. By choosing another 'B' constant (denote this by D) we can determine the outer solution in the region of the resonance and from this we can integrate the full equation out to the wall. By a shooting iteration we can find the value of this last constant at which we obtain $\Psi(r_w)=0$. Then the mismatch in gradients at the resonance, Δ', is given by

$$\Delta' = \frac{D - C}{B} . \qquad - (AF3)$$

Finite resistivity analysis [1,2,3] shows that the condition for instability is $\Delta' > 0$ with growth rate (in resistive time units) given by

$$W = 0.55\,(\Delta')^{4/5}(\eta/4\pi)^{3/5}(dF/dr)^{2/5}/(4\pi\rho)^{1/5}, \qquad - (AF4)$$

where η is the resistivity, ρ the density and dF/dr is evaluated at the singular surface.

NUMERICAL ASPECTS

Pressure Removal

Since we deal only with current driven instabilities , for consistency, we must remove the pressure from the equilibrium field profiles. DPRIME therefore accepts as input a digitised μ profile (which it then

interpolates using cubic splines). The fields are solved for by using the force-free equation $\nabla x\underline{B} = \mu\underline{B}$. The iterative algorithm used is

$$B_z^{i+1} = B_z^i - \Delta\, \mu^i B_\theta^i \qquad \text{- (AF5)}$$

$$B_\theta^{i+1} = r^{i+1}(\Delta\, \mu^{i+1} B_z^{i+1} + B_\theta^i)/(r^{i+1} + \Delta),$$

the on-axis boundary conditions being $B_\theta = 0$ and $B_z = \frac{2}{\mu}\frac{\partial B_\theta}{\partial r}$. To check the calculation, the program automatically calculates the pressure gradient via $\underline{J}x\underline{B}$ and μ once it has calculated the force-free fields.

Main Integration

For both the inner and outer solutions we use the following algorithm :

$$\psi^{i+1} = \psi^i(2 - A^i\Delta^2) - \psi^{i-1}. \qquad \text{- (AF6)}$$

The boundary condition is $\psi = 0$ at $r = 0$ and we shoot for $\psi = 0$ at $r = r_w$ using a newton-raphson iteration on the coefficient D. Typically we use 500 mesh points, 10 of which comprise the asymtotic solution. We find that in 99% of cases only three shooting iterations are necessary after which we calculate Δ' as above.

Eigenfunction Calculation

When the shooting iteration is complete we have effectively solved for the B_r eigenfunction. In fact we have actually solved for ψ but this is related to b_r as described above. In order to compute the B_θ and B_z eigenfunctions we use the linearised forms of $(\nabla x(\underline{J}x\underline{B}))_r = 0$ and $\nabla.\underline{B} = 0$. These may be written:

$$\frac{m}{r} b_z - k b_\theta = \mu b_r \quad ; \quad \frac{m}{r} b_\theta + k b_z = -\frac{1}{r}\frac{\partial}{\partial r}(r b_r) \text{ .- (AF7)}$$

Facilities of the code

The code has several modes of operation. It can be used to calculate the eigenfunctions and $\Delta'$of a given (m,n) set. Alternatively it may be used to compute a stability diagram. For m = 0 resonances the code will produce a diagram of Δ' against ka. For m > 0 the code will plot Δ' against the resonant radius. In addition to these two modes, the code has an integrated test facility allowing the calculation of stability boundaries using certain analytic pitch profiles. It also has the facility to accept measured B_r perturbation eigenfunctions (say from a magnetic probe) and to compute the other two field eigenfunctions.

DPRIME has been tested by comparing the stability boundaries of certain analytic pitch profiles given in [4]. Also the analytic on-axis criterion

$$\frac{P}{2}\frac{d^2P}{dr^2}\bigg|_{r\to 0} > -\frac{4}{7-2m} \quad (m \neq 0)\,, \qquad \text{- (AF8)}$$

and the marginal point of $\theta = 1.56$ for the BFM have been verified.

APPENDIX OF PUBLISHED PAPERS

PAPERS ALREADY PUBLISHED

The following papers are bound into this thesis:

PAPER 1

'The Structure Of Magnetic Fluctuations In The HBTX1A Reversed Field Pinch': Hutchinson I H, Malacarne M, Noonan P, Brotherton-Ratcliffe D : Nucl Fusion 24 (1984) 59 and Culham report CLMP701.

PAPER 2

'Studies Of Fluctuations In The Reversed Field Pinch HBTX1A':
Malacarne M, Hutchinson I H, Brotherton-Ratcliffe D:
Proc. Varenna Conf. (1983) Italy.

PAPER 3

'Variations Of Magnetic Fluctuations With Plasma Conditions In HBTX1A RFP': Malacarne M and Brotherton-Ratcliffe D: Proc. Int. Conf. Plasma Physics Lausanne 1984.

PAPER 4

'Studies Of X-ray and Magnetic Fluctuations In HBTX1A RFP':
Brotherton-Ratcliffe D and Malacarne M: Proc. Int. Conf. Plasma Physics Lausanne 1984.

PAPERS SUBMITTED FOR PUBLICATION OR ACCEPTED FOR PUBLICATION

PAPER 5

'The Structure Of The Magnetic Equilibrium In the HBTX1A Reversed Field Pinch': Brotherton-Ratcliffe D and Hutchinson I H: To be published as a Culham Report.

PAPER 6

'An Analysis Of The Internal Magnetic Fluctuations In The HBTX1A Reversed Field Pinch': Brotherton-Ratcliffe D, Gimblett C G, Hutchinson I H: Submitted to Plasma Physics and to be published as a Culham Preprint.

THE STRUCTURE OF MAGNETIC FLUCTUATIONS IN THE HBTX-1A REVERSED FIELD PINCH

I.H. HUTCHINSON*, M. MALACARNE**, P. NOONAN,
D. BROTHERTON-RATCLIFFE***
Culham Laboratory,
Abingdon, Oxon,
(Euratom-UKAEA Fusion Association),
United Kingdom

ABSTRACT. Arrays of edge magnetic coils and statistical analysis techniques have been used to investigate the magnetic fluctuation structure in the HBTX-1A reversed field pinch. The superficially random fluctuations can in fact be attributed almost entirely to global modes with poloidal mode number m = 0 and 1, provided account is taken of toroidal distortion of the modes. A toroidal array of coils discloses a broad spectrum of toroidal mode numbers with peak at $|n| \sim 10$ and significant variation with time and frequency. Cross-correlation establishes that $|n| \sim 10$ corresponds to m = 1, a helical mode resonant inside the reversal surface, and also shows the presence of m = 0, $n \sim 0$. The time-scales of the fluctuation indicate that the instabilities are probably resistive in character, and the mode amplitudes are such that island overlap and magnetic field ergodization should occur. The energy confinement time due to stochastic transport, estimated from the measured fluctuations, is consistent with that observed experimentally.

1. INTRODUCTION

In the Reversed Field Pinch (RFP), even during relatively quiescent periods, a significant level of fluctuation in the magnetic field exists. It is widely accepted that the appearance and sustainment of a reversed magnetic field by plasma action requires such magnetic fluctuations, although the detailed mechanisms by which self-reversal occurs are generally not yet understood. It also seems that usually the energy confinement in the RFP is determined by enhanced transport arising from the fluctuations. Detailed study of the fluctuations therefore offers the possibility of elucidating these two vital topics: self-reversal mechanisms and energy transport. We present here a study of magnetic fluctuation in the HBTX-1A RFP using magnetic coils outside the plasma edge.

Magnetic fluctuations have long been observed in stabilized pinch discharges, and in early experiments on ZETA and the Mk-IV torus [1, 2] clear evidence of principally kink (m = 1) modes was obtained. Later ZETA experiments [3] concentrated on higher frequencies and interpretation in terms of fully developed turbulence, and less attention was paid to the larger scale lengths. In fast programmed experiments on HBTX [4], coherent m = 1 kinks were also observed during sustainment; these perturbations appeared to be a mixture of ideal and resistive modes.

More recently, on present-generation pinches, studies have been reported on ETA-BETA II [5] and OHTE [6]. In the latter case, results very similar to those for the early ZETA and the Mk-IV torus were obtained, indicating dominantly m = 1 modes.

The experimental techniques for studying magnetic fluctuations, using magnetic coils of various sorts, are of course well developed. In addition to magnetic probes inserted into the plasma, which have been used both in RFPs [6] and tokamaks [7], coils outside the plasma in the form of discrete coils or coils specially wound to measure Fourier components (sine and cosine coils) prove to be of considerable help in diagnosing plasma instabilities and are now used routinely in tokamaks.

Two important factors distinguish our techniques from those which are most frequently used. The first is that in the RFP the most dangerous MHD instabilities [8, 9] have poloidal mode number m = 0 or 1 and a variety of possible toroidal mode numbers n. This is the converse of the tokamak situation with dominantly n = 1 (or 2) and various m, and implies that it is of considerable interest to have arrays of coils round the toroidal circumference rather than just the poloidal circumference as is more usual. The second factor is

* Present address: Nuclear Engineering Department, Massachusetts Institute of Technology, Cambridge, MA 02139, USA.
** Euratom-supported fellow and Oxford University, UK.
*** Royal Holloway College, London University, UK.

that the majority of RFP fluctuations do not have the obvious periodicities in time which are typically seen in tokamaks; rather, the fluctuations appear to be fairly stochastic and turbulent. The consequence of this is that in many cases it is not possible to distinguish the evolution of particular types of modes simply by inspection. It is therefore usually necessary to adopt statistical forms of analysis in order to extract from the apparently random signals the required information.

Our studies here concentrate on the sustainment phase of the RFP discharge during which the fluctuations are weakest and also typically least coherent. We present a systematic analysis of the poloidal and toroidal mode structure and of helical perturbations. In addition, we present observations of the evolution of the perturbations, very-low-frequency oscillations and some observations of the termination phase. In the final section we discuss the interpretation of our results in terms of the resistive MHD instabilities expected in RFP configurations.

2. TECHNIQUES

Details of the HBTX-1A experiment have been published in Ref.[10]. The magnetic coils used in these studies consist primarily of three sets, illustrated in Fig.1. Outside the vacuum liner, in the interspace between the liner (inner minor radius 0.26 m, major radius R = 0.8 m) and the conducting shell (inner minor radius 0.29 m), we have a poloidal array of coils measuring toroidal and poloidal components of the field (B_ϕ, B_θ) at 16 poloidal angles (θ). Also, adjacent to the poloidal array is a toroidal array measuring B_ϕ and B_θ at 14 toroidal positions covering 60° in toroidal angle. The toroidal array is at a poloidal angle of −40°. Inside the vacuum vessel are poloidal arrays similar to the interspace array but with the coils recessed into special sections of the bellows liner. These internal coils are more sensitive to higher-frequency fluctuations because they do not require the fields to penetrate the liner.

The signals from these coils, either integrated or unintegrated, are digitized typically at 500 kHz sampling frequency, using 10-bit ADCs (LeCroy 8210). Because of the nature of the signals this is fast enough to avoid aliasing problems (except possibly at high frequencies with the unintegrated internal coils) and to cover the frequency band in which virtually all the fluctuation power lies.

A variety of forms of statistical analysis has been applied to the signals obtained which we summarize

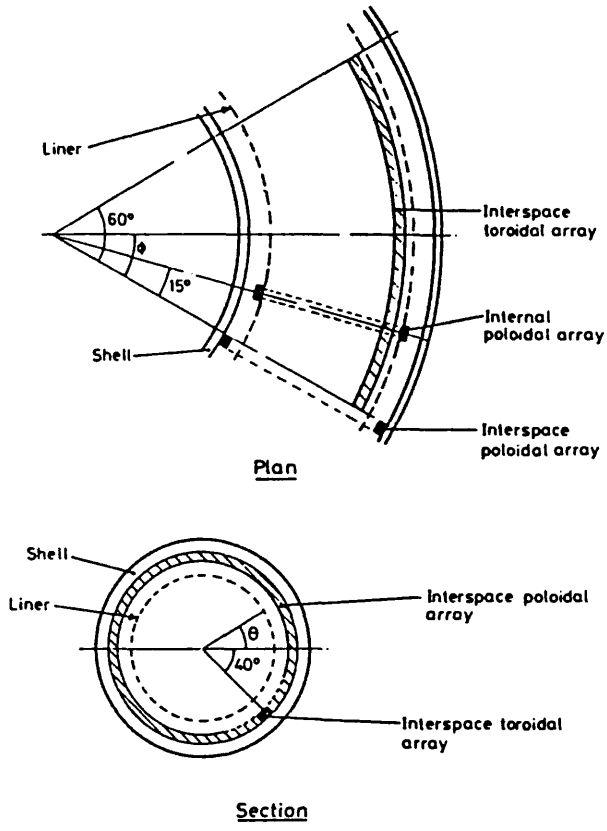

FIG.1. Discrete coil layout.

here. Given signals x(t), y(t) during a finite time period T with Fourier transforms X(ν), Y(ν), which we calculate numerically by FFT programs, the power spectrum of x is

$$P_x(\nu) \equiv \frac{1}{T} \langle |X(\nu)|^2 \rangle \qquad (1)$$

where ⟨⟩ denotes the average over ensembles (i.e. distinct time periods or different shots). The cross-spectrum is given by

$$\Gamma(\nu) = \frac{1}{T} \langle X(\nu)\, Y^*(\nu) \rangle \qquad (2)$$

and $|\Gamma|$ is commonly called the cross-power-spectrum and arg(Γ) the phase spectrum; these are useful for

discovering any systematic phase relationships between the signals x and y. The normalized cross-spectrum

$$\gamma = |\Gamma| / [P_x P_y]^{1/2} \tag{3}$$

is called the coherence.

In the time domain we use the cross-correlation function

$$R_{xy}(\tau) \equiv \left\langle \frac{1}{T} \int x(t)\, y(t+\tau)\, dt \right\rangle \tag{4}$$

which we often normalize to give the cross-correlation coefficient:

$$\rho(\tau) = R_{xy}(\tau) / [R_{xx}(0)\, R_{yy}(0)]^{1/2} \tag{5}$$

We note that for signals which are statistically stationary the Wiener-Kintchine theorem states that $P_x(\nu)$ is the Fourier transform of R_{xx}.

It is often convenient to perform time-domain correlation analysis for signals which are frequency filtered in various ways. For example, this may be used to remove the slow variations due to equilibrium evolution. In order to do this, we multiply the Fourier spectrum $X(\nu)$ by an appropriate filtering function (e.g. a 'box' $f(x) = 1$ for $\nu_1 < \nu < \nu_2$, zero elsewhere) and then transform back to obtain the filtered time history $x'(t)$ which can then be used to obtain correlations. In this way we can concentrate on fluctuations in a limited frequency range, excluding others.

The structure of the fluctuations in the spatial coordinates θ and ϕ is often most easily expressed as an expansion in terms of spatial Fourier harmonics: $\exp i(m\theta + n\phi)$. We can form linear combinations of the discrete coil signals in order to obtain the time histories of various poloidal or toroidal harmonics. These can then be used as input to the various statistical coefficients outlined above. An alternative approach is to investigate the cross-correlation of the magnetic fluctuations at various positions, e.g. forming the autocorrelation in space. In essence, this approach contains the same information as the spatial harmonics; however, it sometimes provides a more transparent interpretation and sometimes allows greater resolution.

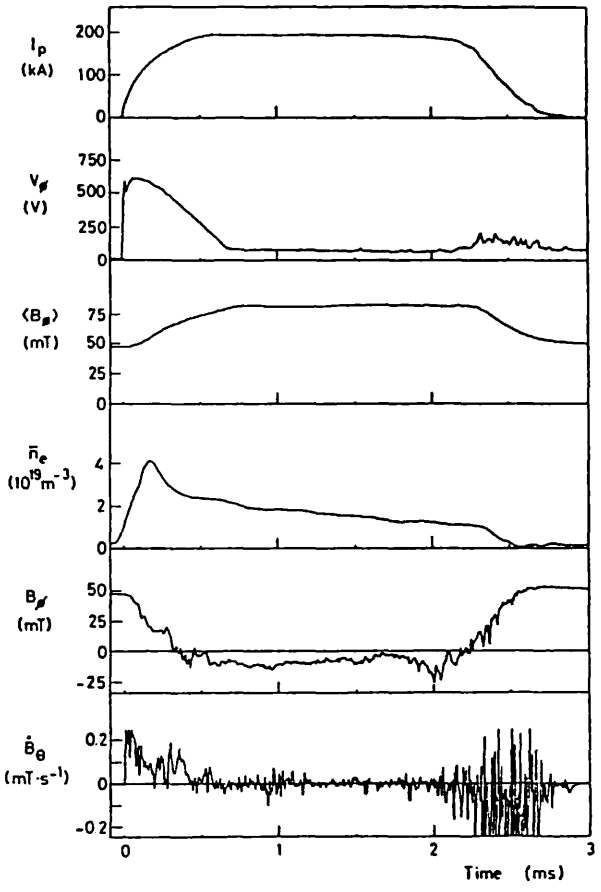

FIG.2. Time history of a typical shot: plasma current (I_p), toroidal loop voltage (V_ϕ), average toroidal magnetic field ($\langle B_\phi \rangle$), average line-of-sight electron density ($\bar{n}_e$), toroidal magnetic field at the liner (B_ϕ), and time derivative of poloidal magnetic field at the liner ($\dot{B}_\theta$).

3. RESULTS

3.1. General

The evolution of the main discharge parameters for a typical shot of interest is shown in Fig.2. We present mostly data for shots such as this whose plasma current is sustained approximately constant at ~200 kA. Brief surveys of other discharges show little substantial change in the character of the fluctuations in shots with decaying currents. Substantial surveys over different current level, pinch parameter or filling pressure have not yet been carried out.

Also shown in Fig.2 are example traces from single coil probes: integrated, giving field B_ϕ, and unintegrated, giving $\dot{B}_\theta$. The apparently stochastic nature of the fluctuations is evident from these traces.

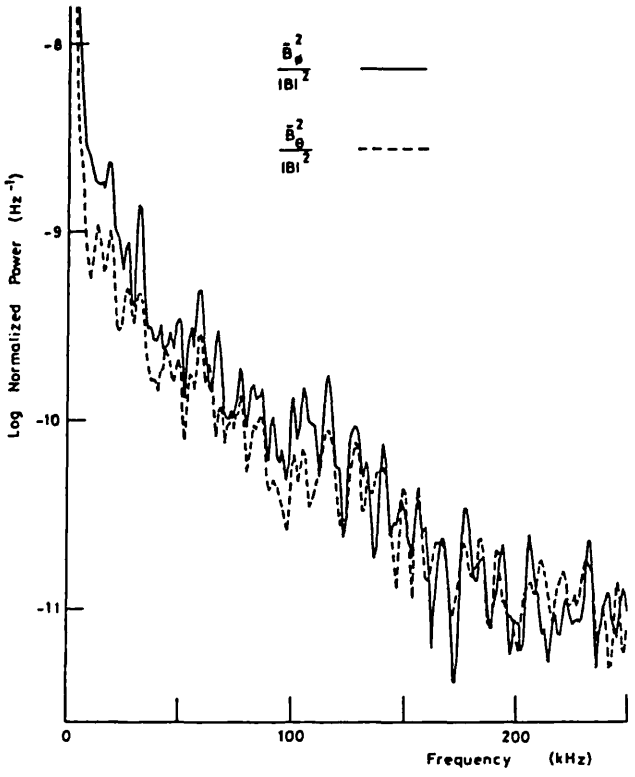

FIG.3. Power spectrum of $\tilde{B}_\phi^2/|B|^2$ and $\tilde{B}_\theta^2/|B|^2$ during the sustainment phase, obtained from the internal coil ensemble averaged over five shots.

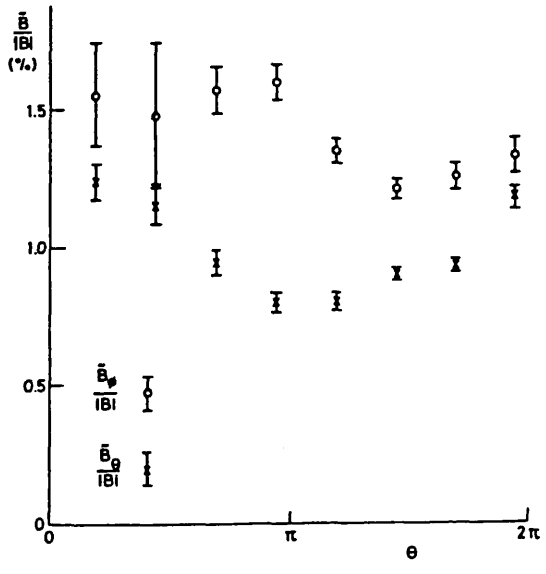

FIG.4. Ensemble-averaged amplitude of $\tilde{B}_\phi/|B|$ and $\tilde{B}_\theta/|B|$ as a function of the poloidal angle during the sustainment phase (frequency band 5–250 kHz).

The power spectrum, $P(\nu)$, during the current sustainment phase of such signals is shown in Fig.3. These spectra are averaged over five shots to illustrate the trends, though substantial variation from shot to shot occurs in the details of the spectra. It is clear that the dominant power is at low frequencies. Above about 40 kHz the spectra fall off approximately as ν^{-2}. As can be observed in the figure, there is little obvious difference in the spectral shape for B_θ and B_ϕ, although the power at the lower frequencies ($\lesssim$ 40 kHz) is systematically slightly higher for B_ϕ.

The total root-mean-square fluctuation levels expressed as a fraction of the (poloidally averaged) total magnetic field, $(B_\phi^2 + B_\theta^2)^{1/2}$, are plotted in Fig.4 as a function of poloidal angle θ. The significant variation particularly in $\tilde{B}_\theta$ is indicative of the importance of toroidicity in HBTX-1A. The mean fluctuation levels are typically 1.5% for B_ϕ and 1% for B_θ during sustainment, and considerably greater, 6–10% for both, during current rise and termination.

3.2. Poloidal mode structure

In order to determine the structure of the fluctuations, we may Fourier decompose in θ by forming the sums over coils k:

$$C_m = \frac{2}{N} \sum_{k=1}^{N} \tilde{B}_k \cdot \cos m\theta_k \tag{6}$$

$$S_m = \frac{2}{N} \sum_{k=1}^{N} \tilde{B}_k \cdot \sin m\theta_k \tag{7}$$

$$P_m = \frac{1}{2} \langle |C_m|^2 + |S_m|^2 \rangle \tag{8}$$

which then gives the total power in each Fourier mode. The resultant poloidal mode power spectra obtained from the internal coil array during the sustainment phase are plotted in Fig.5. The spectrum of $\tilde{B}_\phi$ is dominated by m = 0, 1, with very rapid fall-off at higher m; for $\tilde{B}_\theta$ the spectrum, though similar, shows relatively rather greater levels of m = 2 and less m = 0.

Another approach to the poloidal mode structure is to form the cross-correlation coefficient (initially with zero time delay) between the various coils, thus giving the spatial autocorrelation. This is shown for B_θ in

Fig.6, using coils approximately on the inner (a) and outer (b) equator as reference coils. There is a very clear difference in the autocorrelation obtained with these different reference coils; using reference coils at $\theta \cong \pm 90°$ gives autocorrelations which are asymmetric. These differences indicate that the fluctuations do not possess rotational symmetry in their statistics: i.e. θ is not an ignorable co-ordinate. The nature of the fluctuations may be deduced from inspection of such autocorrelations. To lowest order, disregarding for a moment the lack of rotational symmetry, the autocorrelation is that which would be expected from dominantly m = 0 and m = 1 modes of similar magnitude, i.e. it is the sum of a constant plus a cos θ dependent part. The lack of symmetry indicates that, in fact, the 'm = 1' component is distorted because of toroidicity so that its phase varies more rapidly at the outer equator ($\theta \sim 0$) than at the inner equator ($\theta \sim 180°$).

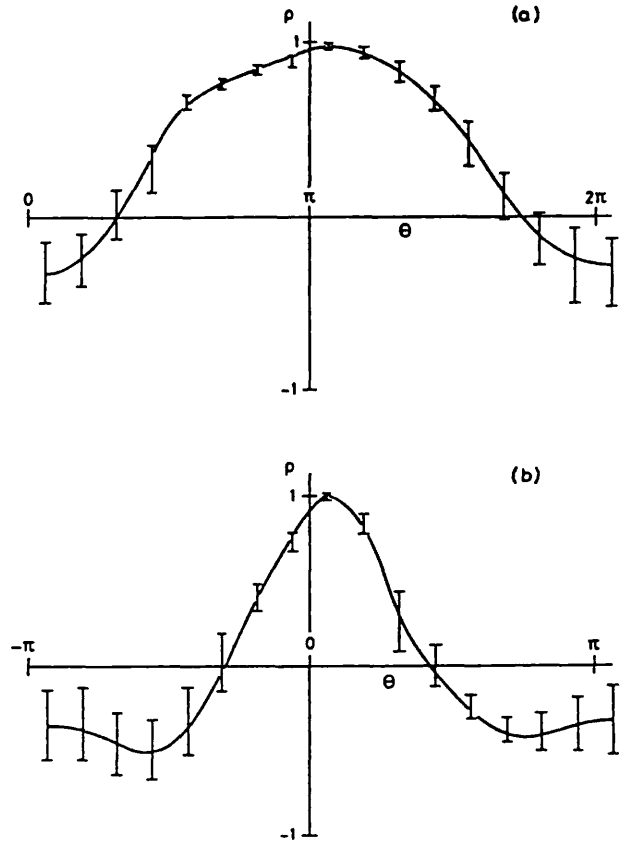

FIG.6. Equal-time cross-correlation coefficient (spatial autocorrelation) for B_θ as a function of displacement in poloidal angle; (a) reference coil at $\theta \cong \pi$; (b) reference coil at $\theta \cong 0$. (Sustainment phase: filter 5–50 kHz.)

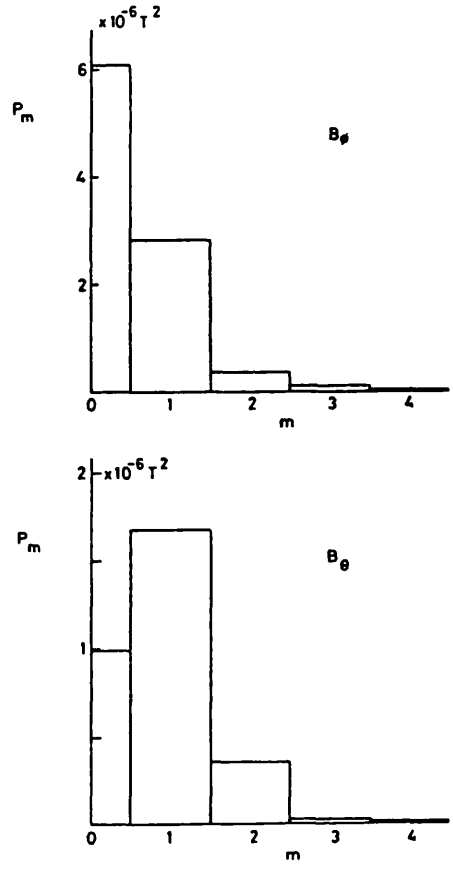

FIG.5. Poloidal mode power spectra for $\tilde{B}_\phi$ and $\tilde{B}_\theta$ during the sustainment phase (frequency band 5–250 kHz).

Expressed in terms of the Fourier decomposition, this means that the fluctuation mode consists of a sum of poloidal Fourier components

$$M_1 = \cos(\theta - \alpha) + \epsilon_2 \cos(2\theta - \alpha) + \ldots \qquad (9)$$

where α is some (random) phase, these Fourier components being coupled (linearly) together. The signature of this linear coupling is that the cos θ and cos 2θ (and also sin θ and sin 2θ) components are always in phase with each other. This characteristic is readily confirmed by forming the cross-spectrum between cos θ and cos 2θ. Figure 7 shows this spectrum. The coherence at lower frequencies is very high ($\gtrsim 0.8$), indicating that about 60% of the power in the modes is linearly coupled. The phase is zero, indicating that cos 2θ and cos θ are in phase at $\theta = 0$ (the outer equator) as expected from the autocorrelation data.

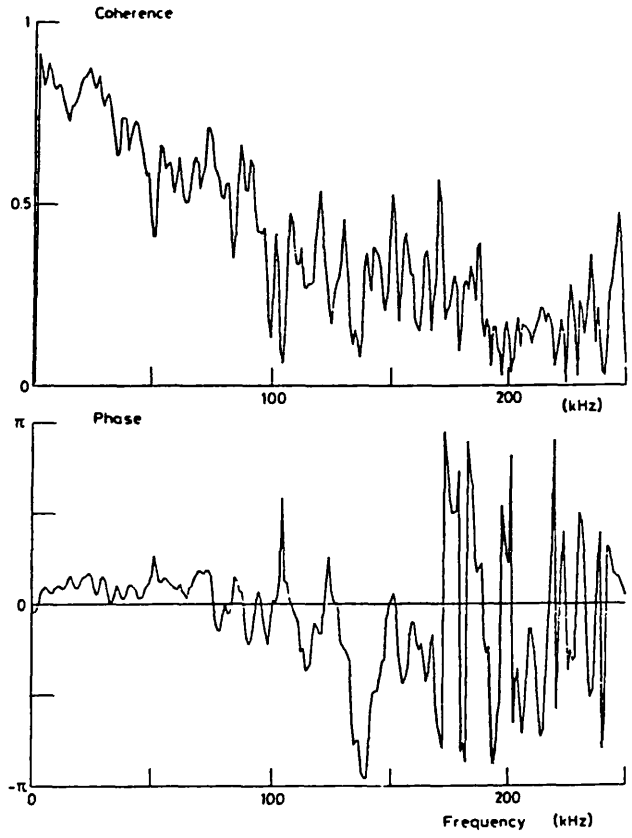

FIG. 7. Coherence and cross-phase spectrum between the m = 1 and m = 2 cosine modes for B_θ (ensemble average over ten shots, sliding averaged over three frequency points during the sustainment phase).

The fall-off of coherence and the accompanying randomization of the phase at higher frequencies for this spectrum appear to be caused by the increasing importance of electronic system noise due to the fall in power. Coherence spectra obtained by using unintegrated $\dot{B}$ signals do not suffer from this problem and coherence is high up to 250 kHz. It is possible also that different modes become important at higher frequency.

The spatial autocorrelation of $\tilde{B}_\phi$ shows less asymmetry than $\tilde{B}_\theta$, although the m = 1, m = 2 coherence spectrum is qualitatively similar, indicating that there is some linear coupling. This is consistent with the mode spectra showing smaller m = 2 power for $\tilde{B}_\phi$ than for $\tilde{B}_\theta$.

Figure 8 illustrates a different type of linear coupling observed in the m = 0, m = 1 cross-spectrum of B_ϕ. In this case, at the higher frequencies the cross-phase is 180°, indicating that the modes add constructively at the inner equator. This is consistent with the toroidal distortion of the m = 0 mode, i.e. $B_\phi \propto 1/R \cong 1 - (a/R_0)\cos\theta$. The lower coherence at low frequencies indicates that the major parts of the m = 0 and m = 1 power there are independent.

Thus, the poloidal mode structure is that there are dominantly only two statistically significant types of modes, M_0 and M_1, which may be identified as the modes corresponding to m = 0 and m = 1 plus their concomitant higher harmonics generated by the toroidal distortions. These linear coupling effects are stronger for $\tilde{B}_\theta$ than $\tilde{B}_\phi$, which is partly why the mode spectra are different. The presence of higher-order modes independent of M_0, M_1 is not established; however, their power is certainly less than 3% of the M_0 and M_1 power.

In order to determine propagation and rotation effects, we examine the time-delayed cross-correlation between coils in the poloidal array. Figure 9(a) shows the result for $\tilde{B}_\theta$ in which evidence of rotation is indeed present. The rotation is in the direction of the ion diamagnetic drift (which is in the direction of electron poloidal current flow) inside the reversal surface. The rapid fall-off with time (or distance) of the maximum

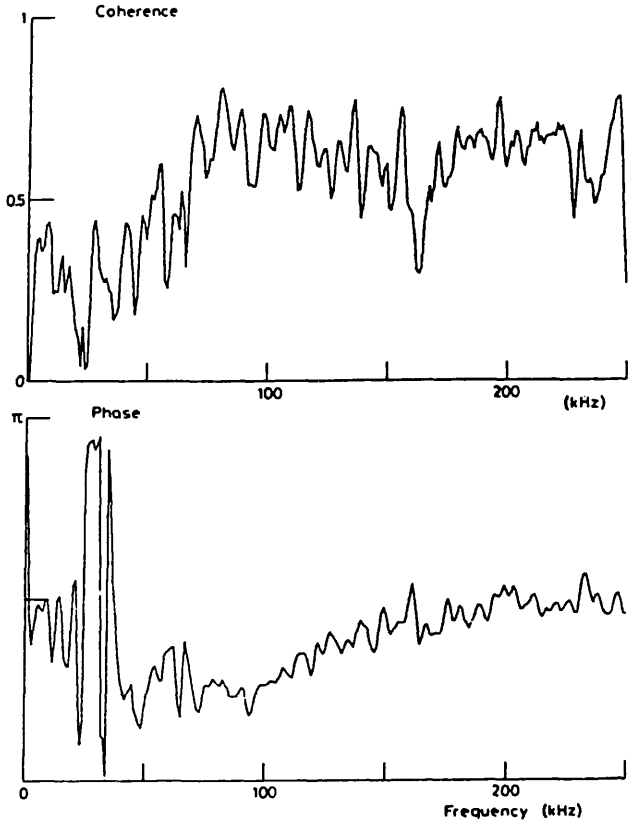

FIG. 8. Coherence and cross-phase spectrum between the m = 0 and m = 1 cosine modes for $\tilde{B}_\phi$ (averaged as in Fig. 7).

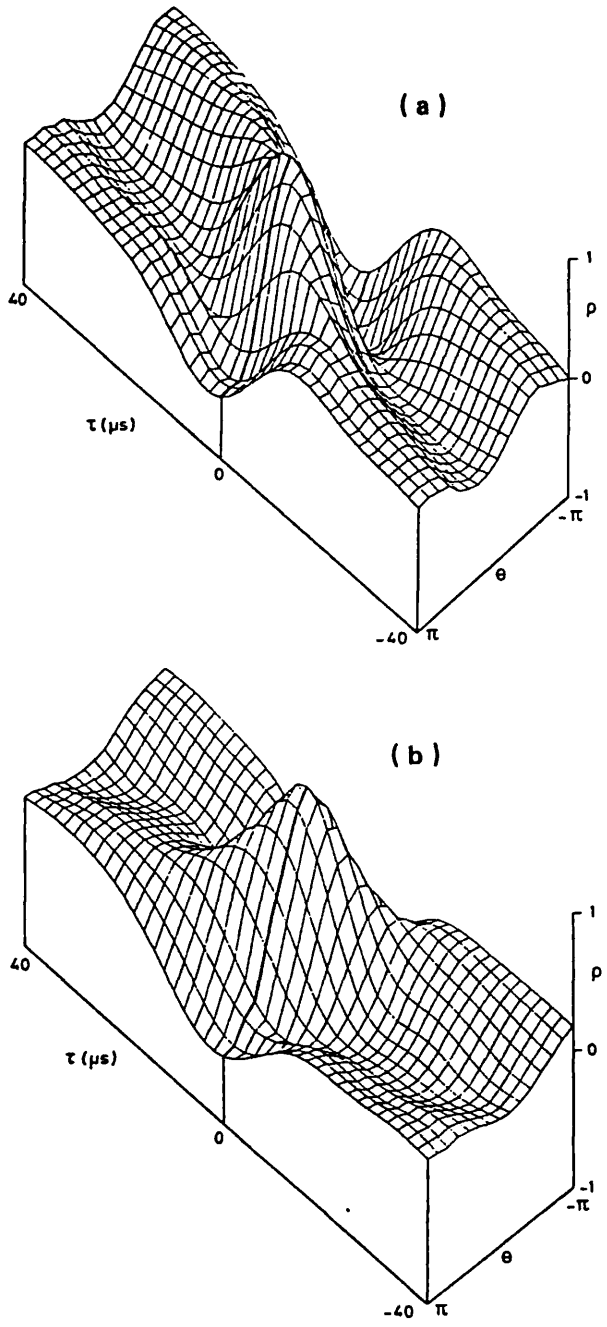

FIG.9. Time-delayed cross-correlation coefficient as a function of θ, ensemble-averaged over the sustainment phase (filter 5–50 kHz): (a) for $\tilde{B}_\theta$, (b) for $\tilde{B}_\phi$; showing evidence of poloidal rotation.

value of the time-delayed correlation coefficient indicates the relative incoherence of the modes due either to a broad spread of rotation rates or to growth and decay rates of the same order of magnitude as the rotation.

That there are different rotation rates is emphatically confirmed by Fig.9(b) in which the time-delayed cross-correlation for $\tilde{B}_\phi$ shows rotation for nominally identical shots in the opposite direction to $\tilde{B}_\theta$ rotation. This is not due to shot-to-shot variation, since it is observed on a single shot, but must presumably be interpreted as an indication that in this case the fluctuations to which $\tilde{B}_\phi$ is most sensitive preferentially rotate in the opposite direction to those to which $\tilde{B}_\theta$ is most sensitive. Other sets of discharges of nominally similar parameters sometimes show almost no significant rotation. The reasons for this are unclear.

3.3. Toroidal mode structure

We have used the toroidal array of coils to determine the toroidal mode structure of the fluctuations initially by forming cross-correlations within the toroidal array to give the toroidal autocorrelation in space. If the machine were completely toroidally symmetric, then ϕ would be an ignorable co-ordinate and the cross-correlation between two angles ϕ_1 and ϕ_2 would depend only on $|\phi_1 - \phi_2|$. Figure 10 shows the spatial autocorrelation averaged over the sustainment phase obtained for $\phi > 0$ using coil 1 of the toroidal array as reference and for $\phi < 0$ using coil 14 as reference. The symmetry obtained is not perfect, indicating that the properties of the fluctuations are not perfectly toroidally symmetric, presumably because of the presence of ports, shell gaps, etc., which introduce asymmetries into the machine.

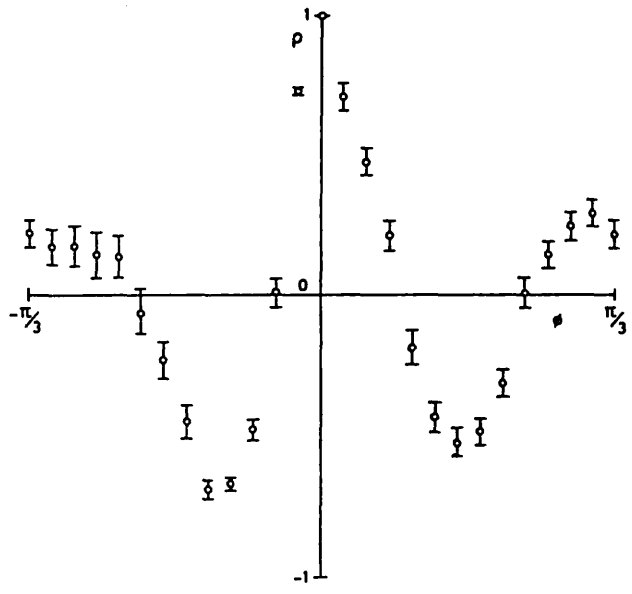

FIG.10. Autocorrelation in space, ρ(φ), for $\tilde{B}_\phi$ (frequency band 5–15 kHz).

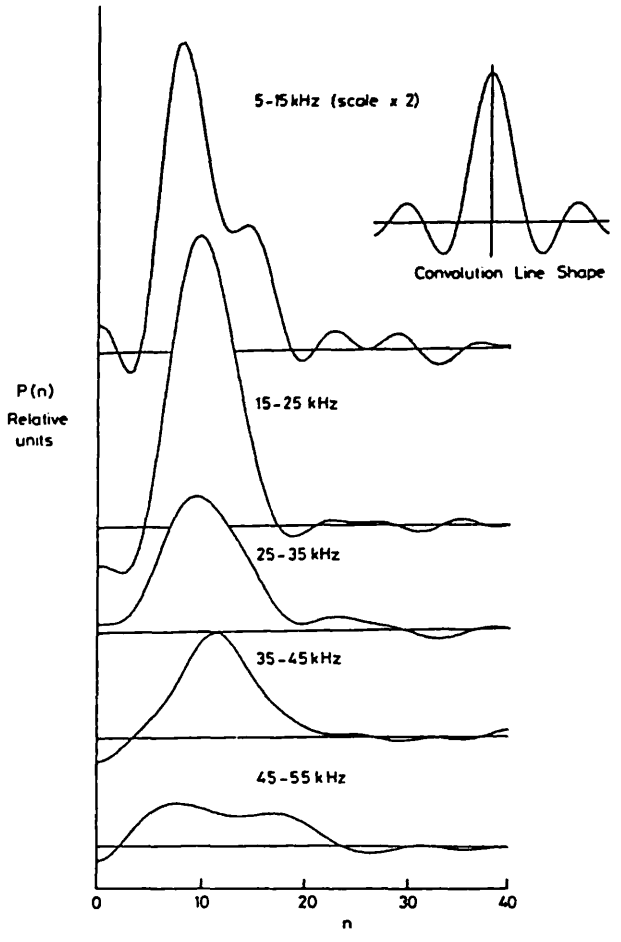

FIG.11. Toroidal mode power spectra of $\tilde{B}_\phi$ for various frequency bands.

The spatial autocorrelation has a rapidly damped form, indicating a fairly broad spectrum of toroidal wavelengths. It is clear that a close-spaced array of the type we use is essential for obtaining a reasonable estimate of the toroidal structure since the correlation length is of the order of or less than the 60° in ϕ which we have available. Thus, it would not be possible to obtain detailed information on the toroidal structure, except with arrays whose spacing is considerably less than this 60° correlation length. It would be preferable to have a toroidal array whose extent is much greater than the correlation length. Unfortunately, the present array does not meet this criterion and the result is that our resolution of toroidal wave number is of the same order as the width of its spectrum. This enforces upon us the need to maximize the resolution in our data analysis.

In order to obtain the toroidal wave number spectrum, which we express in terms of the mode number n ($\equiv 2\pi R k_\phi$), we symmetrize the autocorrelation function by averaging the two sides of Fig.10 and then Fourier transform. This is equivalent to taking the cosine transform only of the unsymmetrized autocorrelation and discarding the sine transform. This process provides nearly twice the resolution obtainable by forming directly weighted sums of coil signals, but requires us to invoke the approximate ignorability of ϕ. The results we obtain are consistent with the direct method.

The resulting n-spectra of B_ϕ are shown in Fig.11. The inset shows the shape function we obtain by this process, the spectra obtained being the convolution of this shape function with the true spectra. We show results for several frequency bands obtained by digital filtering. It may be observed that the detailed shape of the spectrum changes with frequency. The dominant feature at most lower frequencies is at n = 8 – 12, and

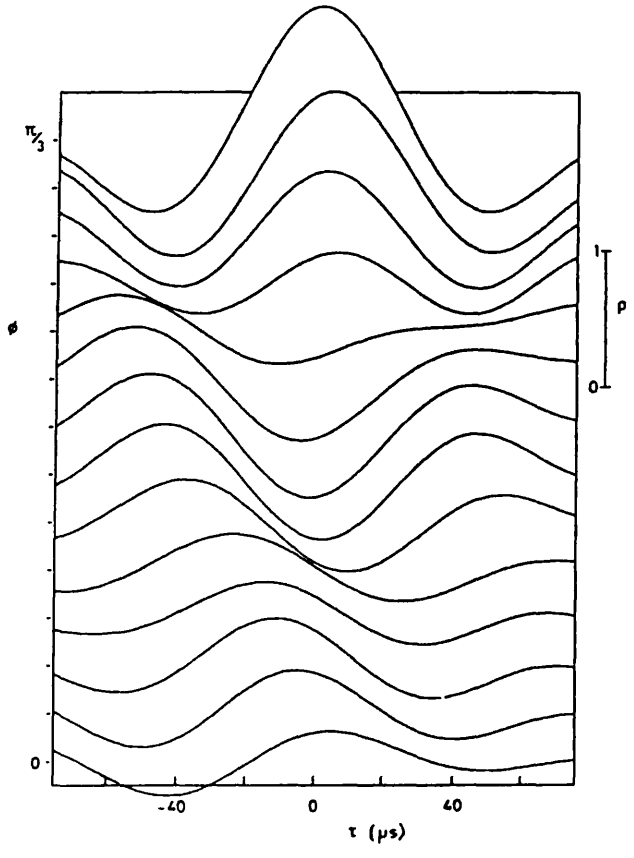

FIG.12. Correlation function ρ versus time delay, τ, and toroidal angle, φ, for $\tilde{B}_\phi$ (frequency band 5–15 kHz), showing evidence of toroidal rotation.

sometimes there appears to be a higher harmonic structure to the spectrum. Generally, very little power appears for $n \lesssim 5$, although some other spectra show power close to $n = 0$.

Propagation in the toroidal direction has been observed from time-delayed cross-correlation coefficients. Figure 12 shows a typical example. The propagation is generally even less pronounced than that observed on the poloidal array in Fig.7, indicating the incoherence of the modes. At the lower frequencies, where the rotation is generally least ambiguous, the observed preferred rotation is in the direction of (conventional) toroidal plasma current (i.e. opposite to the electron flow). The speed is essentially given by the frequency and preferred n, and is typically 10^4 ms^{-1}.

3.4. Helical mode analysis

Although the results presented so far give a general picture of the m and n spectra separately, they do not of themselves allow us to determine the mode structure and to associate given m's with certain n's. This requires in general a two-dimensional array of measurements which can then be decomposed into helical Fourier components of the form $\exp i(m\theta + n\phi)$. Our situation is less complete than this in that we have only two perpendicular one-dimensional arrays.

If we form the 'correlation matrix',

$$Q(\theta, \phi) \equiv \langle x(\theta, \phi_0)\, x^*(\theta_0, \phi) \rangle \qquad (10)$$

by correlating at zero time delay the signals from the poloidal array with those from the toroidal array, we obtain a two-dimensional measure of the statistical properties. In a situation in which θ and ϕ are ignorable, it may be shown that Q is sufficient to determine essentially completely the second-order statistics (i.e. power spectra, etc.). In particular, the Fourier transform of Q

$$A_{mn} = \frac{1}{(2\pi)^2} \iint \exp[-i(m\theta + n\phi)]\, Q(\theta, \phi)\, d\theta\, d\phi \qquad (11)$$

is then equal to the two-dimensional power spectrum.

As we have shown above, toroidal effects are quite strong so that θ is not ignorable and some asymmetries exist even in the ϕ direction. Nevertheless, we can form Q and transform it to obtain A, which we refer to as the 'association spectrum' since it is a measure of the correlation between m and n components. We expect the linear-coupling toroidal effects to generate 'spurious' associations on A in adjacent m numbers, but allowance can be made for this in interpreting the spectra produced.

Figure 13 shows an example of a correlation matrix for $\tilde{B}_\theta$ obtained from the two interspace arrays. Its maximum is near $\theta = -40°$, $\phi = 60°$, at the intersection

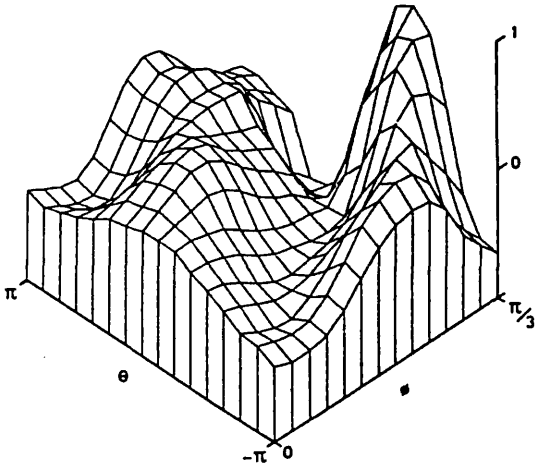

FIG.13. Correlation matrix between the poloidal and toroidal arrays for $\tilde{B}_\theta$ (frequency band 5–50 kHz), indicating a dominantly helical structure.

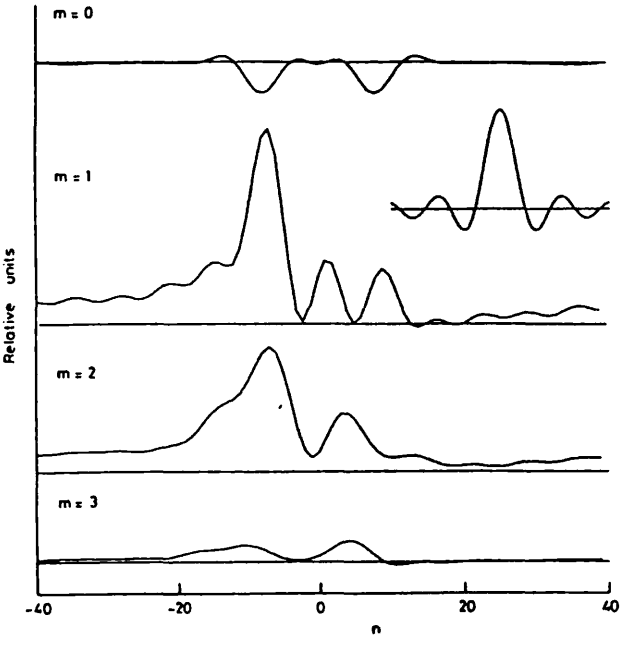

FIG.14. Association spectrum for $\tilde{B}_\theta$. Inset shows convolution line function (frequency band 5–50 kHz).

of the arrays, and it clearly shows a dominantly diagonal correlation profile indicating a helical structure.

Transforming Fig.13, we get the corresponding association spectrum shown in Fig.14. The symmetry $A_{mn} = A^*_{-m-n}$ allows us to adopt the convention that m is taken always non-negative and then n ranges from $-\infty$ to $+\infty$. Our sign convention is that magnetic field lines inside the reversal surface have helicity corresponding to negative n. Since the power is negligibly small for higher m, we show only $m \leqslant 3$; also we plot only the real part of the transform since in the ideal case, where θ, ϕ are ignorable and the ϕ range measured is $0-2\pi$ (neither of which is the case here), the imaginary part is zero. The inset shows the line width (convolution) function.

The dominant feature peaks at $m = 1$, $n \cong -7$, with evidence of a tail extending out to $n \sim -20$. Additional peaks appear near $n = 0$ and $n = +9$ on $m = 1$, and the $m = 2$ spectrum appears to mimic the $m = 1$ spectrum. The $m = 0$ spectrum shows a negative feature coinciding with the main $m = 1$ peak; the $m = 0$ spectrum is, by definition, symmetric in n.

It would be a mistake to interpret all these features as representing independent modes existing in the plasma. Almost certainly, virtually all the $m = 2$ spectra should be regarded as arising from the toroidal linear coupling effects previously discussed. The $m = 0$ feature must also be regarded as spurious for two reasons: first, it is negative, whereas in the idealized case the spectrum would be positive definite; second, there can be no $\tilde{B}_\theta$ component of a true $m = 0$, $n \neq 0$ perturbation outside the plasma since, there, curl $\vec{\tilde{B}} = 0$. Thus the $m = 0$ spectrum here contains little power which we can interpret as 'true'.

The features of $m = 1$ near $n = 0$ and $n \cong +9$ are less certain. Inspection of the correlation matrix reveals little evidence of opposite helicity modes, so probably we should regard the $n \cong +9$ feature as an artifact arising from linear coupling, although we cannot rule out the possibility of its representing an independent mode. The $m = 1$, $n \sim 0$ may well be a true mode, in which case it represents an equilibrium shift type of behaviour. However, it may partly arise from the sidelobes of the convolution function.

Figure 15 shows the association spectrum for $\tilde{B}_\phi$ obtained from the internal poloidal array and the toroidal array. The $m = 1$ component looks similar to that of the $\tilde{B}_\theta$ spectrum, although the peak is now near $n = -10$. This, we believe, should be interpreted as a bias effect in that $\tilde{B}_\phi$ is more sensitive to high $|n|$ and $\tilde{B}_\theta$ is more sensitive to low $|n|$ because of the direction of the perturbed field for a given mode at the

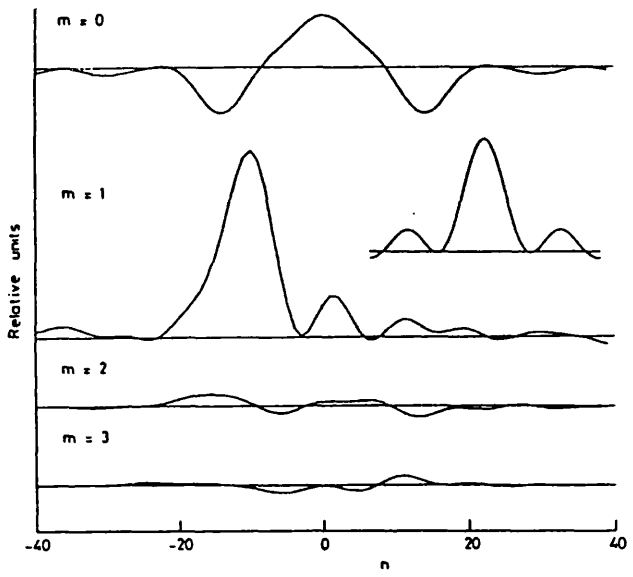

FIG.15. Association spectrum for $\tilde{B}_\phi$. Inset shows convolution line function (frequency band 5–50 kHz).

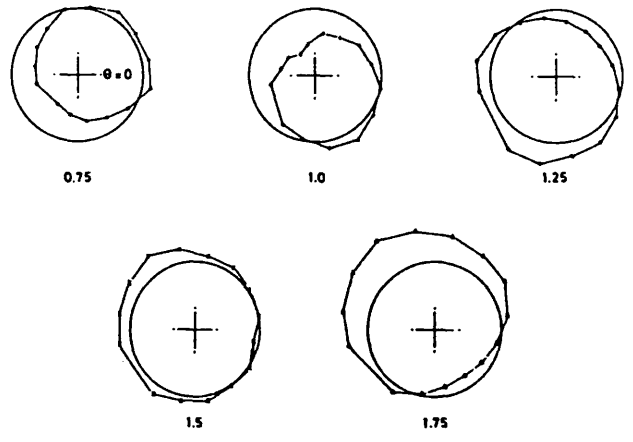

FIG.16. Polar plots of $\tilde{B}_\phi$: evolution in time (ms), showing low-frequency m = 1 rotation.

edge (which is given by curl $\vec{\tilde{B}} = 0$). The $m = 2$ spectrum is much smaller than for $\tilde{B}_\theta$, consistent with a weaker toroidal distortion. There is still a negative feature on $m = 0$, slightly shifted with respect to the $n = -10$ peak; we regard this phase shift as an effect due to incomplete cancellation of liner-induced phase shifts. The $m = 1$, $n = +10$ peak is much less significant than for $\tilde{B}_\theta$, which is consistent with its interpretation as a toroidal distortion artifact. Then there remains the $m = 0$, $n \sim 0$ component, which we take as real and indicating a definite contribution from those modes; and $m = 1$, $n \sim 0$, which is probably mostly a toroidal distortion of $m = 0$, $n \sim 0$.

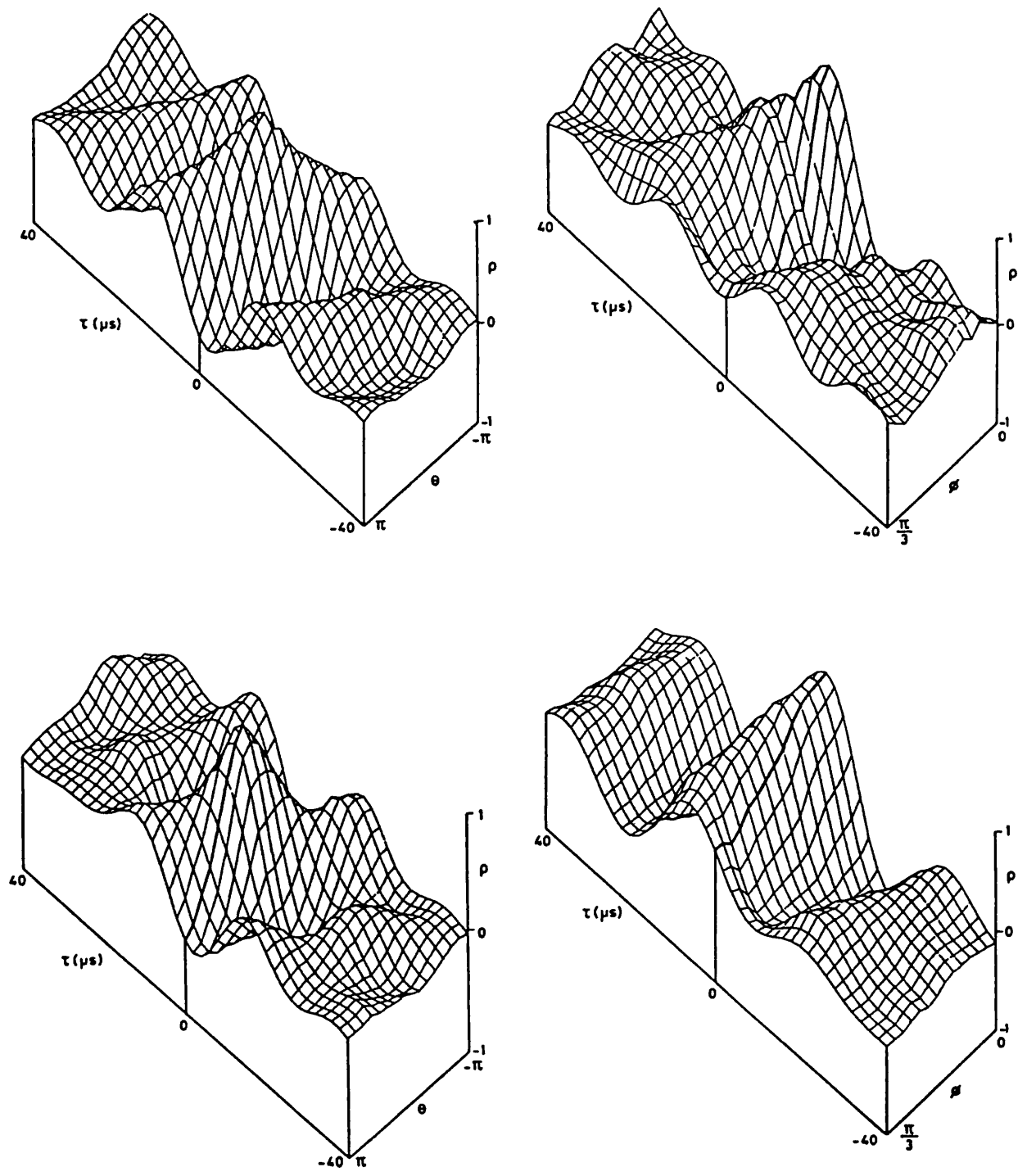

FIG.17. Time evolution of n-spectrum for $\tilde{B}_\phi$ (frequency band 5–50 kHz).

It should be noted that these association spectra are corrected for liner penetration effects only by assuming a single 10 μs penetration time for the liner, whereas the theoretical liner penetration time (see Appendix) is different for different modes. In particular, for m = 0, n = 0, the penetration time is about ten times longer for $\tilde{B}_\phi$, causing attenuation by a factor of ten. If this effect is allowed for, the m = 0, n ~ 0 feature on B_ϕ is significantly enhanced over that shown.

3.5. Evolutionary phenomena

So far, several important phenomena have not been mentioned in our presentation of the results. First, it must be noted that our statistical techniques have concentrated on frequencies above about 5 kHz, which are high enough to exclude the global evolution of the equilibrium plasma parameters, such as current and flux. However, it is observed that on a good proportion of discharges evolutionary phenomena exist at frequencies as low as 1 kHz which justify the designation 'perturbation' since they are not simply evolutions of a quasi-cylindrical equilibrium. Since these turn out to be spatially fairly coherent, even though they exist for typically no more than one time cycle, we can illustrate their characteristics by plotting directly the temporal evolution of the edge field profiles. Figure 16 shows a particularly clear example of polar plots from a single discharge of the toroidal field amplitude as a function of θ, referred to the mean B_ϕ at each θ (over the time plotted) as zero. The clear m = 1 character slowly rotating in azimuth is evident by inspection. Such perturbations as this are also evident on the toroidal array and indicate that it is again a helical perturbation with typical toroidal wave number n ~ −10. The (peak) amplitude of the mode is sometimes as great as $\tilde{B}_\phi/|B| \sim 5\%$, which for typical reversal levels is $\tilde{B}_\phi/|B_\phi|_a \sim 50\%$. These perturbations tend to be present only during the first millisecond or so of the sustainment phase, their amplitude decaying with time.

A second characteristic which must be emphasized under the heading of evolutionary phenomena concerns the various spectra presented earlier. These are time and shot averages over typically 1 ms and 5–10 shots. However, we find that the characteristics of the fluctuations vary with time in a systematic though not reproducible manner. The fluctuations occur in bursts, separated by quieter periods, and are not in the statistical sense stationary random signals. One striking observation is a form of cyclic behaviour in the evolution of the n-spectrum. Figure 17 shows the evolution of the

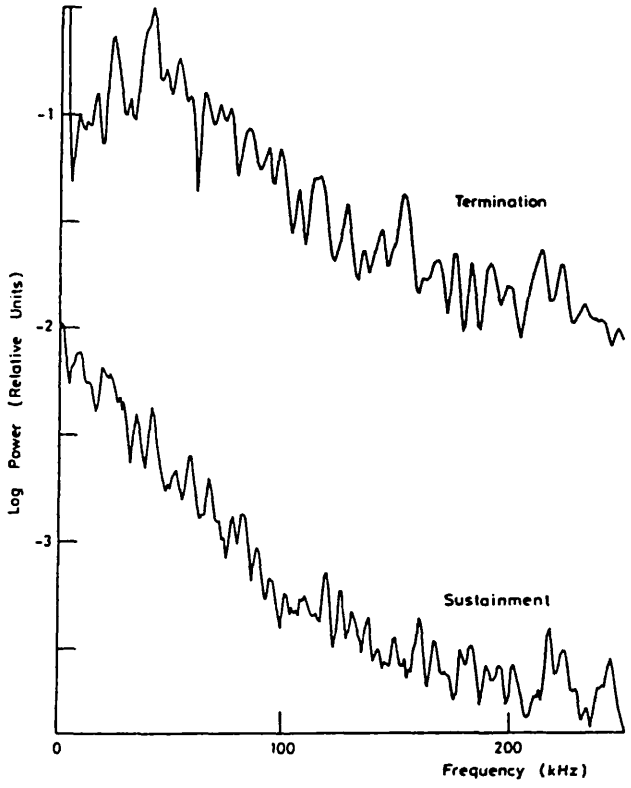

FIG.18. Relative power spectra for $\tilde{B}_\theta$ during the sustainment phase and during termination.

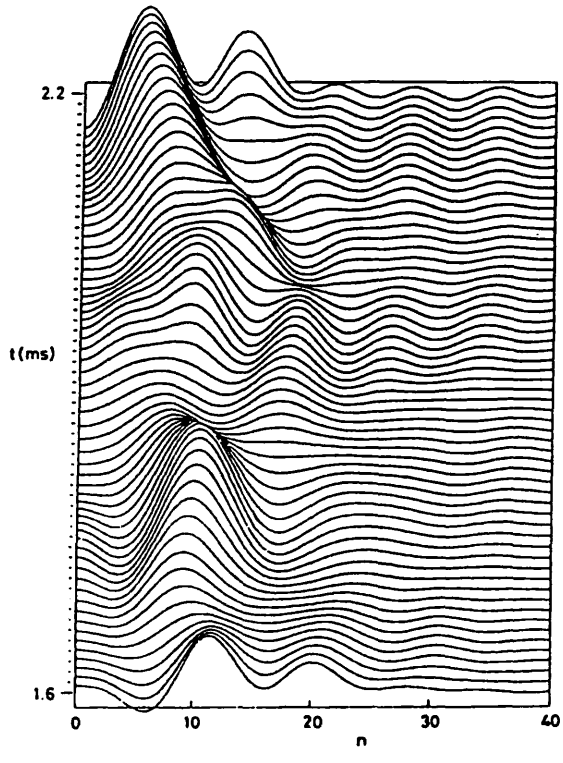

FIG.19. Time-delayed cross-correlation coefficient for $\tilde{B}_\phi$ (top) and $\tilde{B}_\theta$ (bottom), as a function of θ (left) and ϕ (right), during the termination phase (filter 5–50 kHz).

n-spectrum calculated by a sliding average over 128 μs during a period of 0.6 ms in the sustainment phase. During this period the spectrum evolves from single-peaked high power to double-peaked lower power and back again, going through about two cycles in 0.6 ms. The average spectra of Fig.11 are dominated at lower frequencies by the higher-power single-peaked type of spectrum, but it is evident that at some times other wave numbers are dominant.

Finally, we should present some observations concerning the termination phase. As Fig.2 illustrates, the amplitude of fluctuations rises considerably once reversal is lost. Figure 18 shows on a relative scale how the fluctuation power spectrum during termination differs from that during sustainment. The shape is significantly altered, showing a rise up to ~ 50 kHz; thus higher frequencies become more important. Another characteristic of the termination phase is that the rotation is much more coherent. This shows clearly on the time-delayed cross-correlations illustrated in Fig.19. The rotations are always in the same direction during termination, namely toroidally in the direction of electron current flow and poloidally in the electron diamagnetic drift direction (these directions are equivalent for our helical perturbations).

Another effect which shows clearly in Fig.19 is that the toroidal wavelength (and coherence length) increases. This is a progressive effect, but of course our figure only captures one period during the current decay. At the time referred to in Fig.19, θ is about 1.0. The poloidal structure is always dominantly m = 1 and the helicity corresponds to negative n; for Fig.19, n ~ −3 to 4 for B_ϕ and ~ −1 to 2 for B_θ.

4. DISCUSSION

Our measurements show that the overwhelming proportion of the fluctuations observed at the plasma edge is attributable to low poloidal mode numbers M_0 and M_1. Of course, the nature of the measurements tends to favour large-scale perturbations such as these, since fine-scale perturbations originating well inside the plasma will generally fall off more rapidly with radius and would therefore be proportionately smaller at the edge. Nevertheless, the fact that the fluctuation power in Fourier modes m > 2 is only about 3% of that in modes m ≲ 2 for B_ϕ appears to be a quite strong indication that the low m-modes are indeed dominant throughout the plasma.

The difference for m > 0 between the poloidal mode spectra for $\tilde{B}_\theta$ and $\tilde{B}_\phi$ is explicable by consideration of the details of the toroidal distortion effects. Writing the condition curl $\tilde{B} = 0$ in toroidal geometry provides a relationship between the fields outside the plasma for a given helical mode; for example, if $\tilde{B}_\phi$ is purely m = 1, $\tilde{B}_\theta$ has an m = 2 component of amplitude a/R. The outward (Shafranov) shift of the plasma in the shell is at least partly responsible for these toroidal distortions, but this cannot easily be distinguished from departure of the internal mode structure from the quasi-cylindrical approximation.

A major advance in the present results is the detailed information we have obtained on the toroidal mode structure. In order to see its significance we must consider the radial profile of the field line pitch, which we express in terms of the safety factor $q \equiv rB_\phi/RB_\theta$. As is well known, the RFP adopts a field configuration in which the profile may be estimated by using one of the quasi-cylindrical models such as the modified Bessel function model or the Bessel vacuum model. For the HBTX-1A discharges of interest here, such calculations indicate the on-axis q_0 to be about 1/5; q falls to zero at r/a ~ 0.75, the reversal point; at the liner it reaches ≅ −0.04. Internal magnetic probe measurements on different discharges confirm these estimates which are relatively insensitive to the model employed.

Helical perturbations are resonant at the radius where q = − m/n, which for m = 1 is where $q^{-1} = -n$. At this radius, non-zero radial field perturbations will lead to magnetic island formation. Our main peak in the n-spectrum at n ~ −10 is a mode which is resonant at r/a ~ 0.5; the broad spectrum we see, which extends from n ~ −5 to n ~ −20, indicates modes which are resonant at radii from r ~ 0 out to quite close to the reversal surface. We cannot, with our modest resolution, exclude modes which are non-resonant (i.e. $|n| < 5$), but their contribution, if any, is small. In addition to these m = 1 modes, the m = 0 perturbations are always resonant at the reversal surface.

The perturbations we see seem to correspond qualitatively quite well with the expectations of resistive instability theory [9] in that we see m = 1 perturbations resonant from r = 0 outward and also m = 0 perturbations of long toroidal wavelength. For the discharges studied here we have not observed perturbations resonant outside the reversal surface (m = 1, n ≳ +25), although the statistical accuracy of our measurements only allows us to put an upper bound of 5% of the fluctuation power in such modes. This corresponds to a root-mean-square amplitude upper bound of $\tilde{B}/|B| < 0.2\%$.

Our present analysis does not allow us to distinguish whether the m = 0 perturbations arise directly from linearly unstable resistive modes or indirectly as a non-linear consequence of the m = 1 modes. Further studies employing higher-order correlations and focusing on the time non-stationarity may be able to shed further light on this topic. We are also not able to distinguish the driving energy sources for any of the perturbations which provide the usual theoretical distinction between tearing and pressure-driven 'g' modes.

One may obtain an estimate of the growth (and decay) times for these perturbations from the frequency spectra presented. Taking the width of the overall spectrum as the relevant frequency spread, i.e. ~ 30 kHz, one would estimate a growth time of ~5 μs. This might be rather shorter than the required estimate since the relevant frequency width might more appropriately be taken as the width of the individual features on the spectrum, i.e. approximately 5 kHz, leading to ~ 30 μs. This should be compared with the poloidal Alfvén transit time of ~ 0.5 μs for these discharges and the magnetic Reynolds number $S \sim 10^5$. Thus the perturbation lifetime is approximately $S^{-1/3}$ (in resistive time units), although this is only a single measurement, not a scaling. This lifetime suggests that we should take the perturbations as dominantly 'resistive' rather than 'ideal' MHD in character. Of course, the states we are observing are non-linear so that this distinction is of debatable significance, except that we may assume that magnetic reconnection and island formation are occurring. This resistive character has been qualitatively confirmed by observations of radial magnetic field perturbations inside the plasma on HBTX-1A as well as elsewhere [6], i.e. $\tilde{B}_r$ does not reverse sign inside the plasma.

In order to estimate the size of magnetic islands inside the plasma arising from a specific helicity mode, we could in principle integrate the linearized MHD equations inward from the edge until we reach the resonant surface. The island width, W, may then be estimated from the standard formula [11]

$$W = 4\left|\frac{\tilde{B}_r r_s}{mB_\theta}\frac{q}{q'}\right|^{1/2} \tag{12}$$

This would require a detailed knowledge (or assumption) of the equilibrium field profiles in order to carry out the integration. We may instead get an order-of-magnitude estimate by appealing to the observation that theoretical studies [9] of tearing-mode stability perform essentially this integration and indicate that, roughly speaking, the radial derivative of $\tilde{B}_r$ is approximately constant outside the resonant surface for modes whose resonant surface is not too close to the axis. Now we measure the perturbations close to the shell, where $\tilde{B}_r = 0$, so $\nabla\cdot\vec{B} = 0$ gives

$$\left|\frac{\partial \tilde{B}_r}{\partial r}\right| = \left|\frac{m}{r}\tilde{B}_\theta + \frac{n}{R}\tilde{B}_\phi\right| \tag{13}$$

Thus, our estimate is

$$\tilde{B}_r(r_s) = (a - r_s)\left|\frac{m}{r}\tilde{B}_\theta + \frac{n}{R}\tilde{B}_\phi\right|_a \tag{14}$$

For $n \sim -10\,(m = 1)$, typically $|q/q'r_s| \cong 1$ and $B_\theta(r_s) \sim 1.5\,|B(a)|$, so

$$W/r_s \cong 4\left\{(a - r_s)\left|\frac{m}{r}\tilde{B}_\theta + \frac{n}{R}\tilde{B}_\phi\right|_a \Big/ mB_\theta(r_s)\right|^{1/2}$$

$$\sim 4\,|\tilde{B}/B|_a^{1/2} \tag{15}$$

In order to determine the amplitude $|\tilde{B}|$ to be ascribed to each mode, take half of the ~ 2% root-mean-square fluctuation level as being in m = 1 and take this as spread over about six toroidal modes as indicated by the n-spectrum; this then indicates a single-mode root-mean-square level of $2/\sqrt{12} \cong 0.5\%$. Hence the above estimate of island size is $W/r_s \sim 0.3$.

The separation, δ, of (m = 1) resonant surfaces in this region of the plasma is given by

$$\delta = |q^2/q'| \sim q\,r_s \sim 0.1\,r_s \tag{16}$$

Therefore, the island overlap condition [12] $W > \delta$ is easily satisfied. So, if the different helicities are simultaneously present with this typical amplitude, we expect that the magnetic field lines are stochastic throughout the region and magnetic surfaces no longer exist. Strictly, our analysis has not shown unequivocally that the different helicities are truly simultaneous in view of the 'bursting' character of the fluctuations; however, it seems most improbable that the different modes would be sufficiently separated in time for stochasticity to be avoided. Estimates of m = 0 island sizes give similar values for W, though in this case we

are less certain of the resistive MHD mode character. Much of the M_0 mode power may arise non-linearly from the M_1 mode.

Given the mode amplitudes and the fact that field lines are stochastic, we can estimate the energy transport due to stochastic diffusion. The field-line diffusion coefficient [13] is, for our case, typically $\langle \Delta r^2/L \rangle \sim a|\tilde{B}/B|_a^2$, giving effective perpendicular energy diffusivity [12] $\chi_{eff} \sim v_e \langle \Delta r^2/L \rangle$, where v_e is the electron thermal speed. For $|\tilde{B}/B|_a = 0.01$ and $T_e \sim 100$ eV, this leads to an estimate of energy confinement time $\tau_E \sim 50\,\mu$s, assuming that the whole of the plasma experiences this stochastic diffusion. This value is consistent with experimentally observed parameters. However, it should be regarded as an order-of-magnitude estimate only because of the sensitive (squared) dependence on the internal $\tilde{B}_r$ which has been estimated somewhat crudely. Nevertheless, it should be emphasized that this is a direct estimate based on measured longitudinal correlation lengths and field perturbation amplitudes and not, like earlier stochastic transport estimates [5, 14], on theoretical estimates of longitudinal correlation.

It is of interest too to estimate the island size for the large, coherent, slowly rotating perturbations of Fig.16. The linearized estimates are somewhat questionable for such large perturbations; however, taking the peak perturbation amplitude, we obtain $W \sim r_s$, indicating a very large island but not extending to the magnetic axis. More careful non-linear calculations might be appropriate in this case to obtain more reliable estimates.

The rotation speeds observed are of the same order of magnitude as estimates of diamagnetic drifts. However, the ambiguity of direction observed indicates that a simple interpretation in terms of these drifts is hardly adequate. It should be noted also that an electrostatic potential of about 100 V would be sufficient to cause plasma rotation of this order of magnitude.

The rather cyclic behaviour observed in the evolution of the n-spectrum leads one to a rather persuasive picture of the overall behaviour. Suppose that the evolution of the field profiles leads to a situation in which resistive modes at r/a ~ 0.5 are preferentially destabilized. These grow and then stabilize themselves via non-linear modifications to the profiles; their amplitude then decreases. However, the profile modifications tend to destabilize other modes with n greater (and smaller) than those just discussed. Therefore, these other modes tend to become dominant and enforce profile changes which compete with those of the first modes. This competition continues, establishing a quasi-equilibrium in which cyclic variations of mode amplitude maintain the mean profile such that no mode achieves complete dominance. Theoretical ideas of this sort have been proposed [15] in the context of the tokamak disruptive instability. However, here we seem to have direct experimental evidence in the RFP for the importance of this MHD mode competition.

Many further fluctuation topics remain to be investigated; notably, how the amplitudes and the character of the perturbations vary with plasma parameters and also what are the non-linear characteristics, mode coupling and so forth. However, the present study has revealed many interesting and significant characteristics of the magnetic fluctuation structure in the RFP, which should serve as a basis from which to pursue these investigations.

Appendix

Since some of our measurements are made outside the liner, it is important to estimate the effect of the liner on the observed fluctuations. If we treat the liner as being thin, with conductivity σ and thickness δ, having the radius a concentric within a shell (assumed infinitely conducting) of radius b, and consider perturbations of the form $\exp i(m\theta + n\phi - \omega t)$, then, provided

$$\left[\left(\frac{m}{a}\right)^2 + \left(\frac{n}{R}\right)^2\right](b-a)^2 \ll 1 \qquad \text{(A1)}$$

we can treat the outward penetration of magnetic field across the liner (B_0) as related to that inside (B_i) by:

$$B_0 = B_i/(1 + i\omega\tau) \qquad \text{(A2)}$$

where

$$\tau = \mu_0 \sigma \delta (b-a) \qquad \text{(A3)}$$

This shows that the effect of the liner is to integrate the field with a passive time constant τ.

An important complication is that the liner has a bellows construction so that the effective δ is different for currents flowing in the poloidal and toroidal directions. Denote these by δ_θ, δ_ϕ; then it may be shown that, approximating the liner as being thin, we have

$$\delta_{eff} = \frac{\delta_\theta \delta_\phi \, [(m/a)^2 + (n/R)^2]}{\delta_\theta (m/a)^2 + \delta_\phi (n/R)^2} \qquad (A4)$$

For the liner of HBTX-1A, $\tau_\theta = \mu_0 \sigma \delta_\theta (b - a) \cong 30\ \mu s$ and $\delta_\phi \cong \delta_\theta / 16$, from which the penetration time constant of any mode may be calculated. For example, if $m = 0$, $n \neq 0$, $\tau = 30\ \mu s$, while for $m = 1$, $n = 8$, $\tau \cong 10\ \mu s$, corresponding to frequencies of ~ 5 kHz and 15 kHz, respectively.

Additional complications arise because the convolution depth is not small compared with $(b - a)$; however, the above treatment is regarded as sufficient to first order. Finally, for $m = 0$, $n = 0$, the gaps of the shell prevent it from acting as a flux conserver and the penetration time depends on the equivalent flux out to the windings. The penetration times are then estimated as $\sim 100\ \mu s$ for B_z and $\sim 20\ \mu s$ for B_θ. It should be noted, therefore, that $m = 0$ perturbations (particularly for $n = 0$) suffer significantly greater attenuation in general than those for higher m.

ACKNOWLEDGEMENTS

The authors are grateful to the other members of the HBTX-1A team for their co-operation and to J.B. Taylor for helpful discussions.

REFERENCES

[1] RUSBRIDGE, M.G., LEES, D.J., SAUNDERS, P.A.H., in Plasma Physics and Controlled Nuclear Fusion Research (Proc. Conf. Salzburg, 1961), Nucl. Fusion Suppl. Pt.3, IAEA, Vienna (1963) 895.

[2] RUSBRIDGE, M.G., JONES, H.W., LEES, D.J., SAUNDERS, P.A.H., WITALIS, E.A., Plasma Phys. 3 (1961) 98.

[3] ROBINSON, D.C., RUSBRIDGE, M.G., Phys. Fluids 14 (1971) 2499.

[4] CAROLAN, P.G., GOWERS, C.W., ROBINSON, D.C., WATTS, M.R.C., BODIN, H.A.B., in Plasma Physics and Controlled Nuclear Fusion Research 1978 (Proc. 7th Int. Conf. Innsbruck, 1978) Vol.2, IAEA, Vienna (1979) 23.

[5] ANTONI, V., ORTOLANI, S., Plasma Phys. 25 (1983) 799.

[6] TAMANO, T., CARLSTROM, T., CHU, C., GOFORTH, R., JACKSON, G., La HAYE, R., OHKAWA, T., SCHAFFER, M., TAYLOR, P., BROOKS, N., CHASE, R., in Plasma Physics and Controlled Nuclear Fusion Research 1982 (Proc. 9th Int. Conf. Baltimore, 1982) Vol.1, IAEA, Vienna (1983) 609.

[7] HUTCHINSON, I.H., Phys. Rev. Lett. 37 (1976) 338.

[8] ROBINSON, D.C., Nucl. Fusion 18 (1978) 939.

[9] ROBINSON, D.C., Plasma Phys. 13 (1971) 439.

[10] BODIN, H.A.B., BUNTING, C.A., CAROLAN, P.G., GIUDICOTTI, L., GOWERS, C.W., HIRANO, Y., HUTCHINSON, I.H., JONES, P.A., LAMB, C., MALACARNE, M., NEWTON, A.A., PIOTROWICZ, V.A., SHIMADA, T., WATTS, M.R.C., in Plasma Physics and Controlled Nuclear Fusion Research 1982 (Proc. 9th Int. Conf. Baltimore, 1982) Vol.1, IAEA, Vienna (1983) 641.

[11] BATEMAN, G., MHD Instabilities, MIT Press, Cambridge, MA (1978).

[12] RECHESTER, A.B., ROSENBLUTH, M.N., Phys. Rev. Lett. 40 (1978) 38.

[13] ROSENBLUTH, M.N., SAGDEEV, R.Z., TAYLOR, J.B., ZASLAVSKI, G.M., Nucl. Fusion 6 (1966) 297.

[14] HENDER, T.C., ROBINSON, D.C., Comput. Phys. Commun. 24 (1981) 413.

[15] FURTH, H.P., in Current Disruption in Toroidal Devices (LACKNER, K., ZEHRFELD, H.P., Eds), Max-Planck-Institut für Plasmaphysik, Garching, Rep. IPP-3/51 (1979).

(Manuscript received 1 August 1983)

STUDIES OF FLUCTUATIONS IN THE REVERSED FIELD PINCH HBTX1A

M Malacarne[+], I H Hutchinson[*] and D Brotherton-Ratcliffe[≠]

Culham Laboratory, Abingdon, Oxfordshire, OX14 3DB, UK
(Euratom/UKAEA Fusion Association)

ABSTRACT

Profiles of X-ray emissivity have been measured that show an outward displacement and a central region of uniform emissivity. The fluctuations are concentrated in an annular region around the reversal surface. Edge coil measurements indicate the presence of an $m = 0$, $n = 0$ mode on B_ϕ. The B_θ component also shows an $m = 0$, $n = 0$ component and an $m = 1$, $n \sim 8$ kink is the dominant mode. An additional $m = 1$, $n \sim 2$ kink is visible at high values of the pinch parameter.

+ Euratom Supported Fellow and Oxford University, UK
* Present address: Nuclear Engineering Department, MIT, Cambridge, Ma 02139, USA
≠ Royal Holloway College, London University, UK

1. INTRODUCTION

We present here studies of fluctuations which have been undertaken on the RFP HBTX1A at Culham Laboratory (for details of the HBTX1A experiment see Ref [1]). Magnetic field fluctuations have been observed using several arrays of edge coils and X-ray emission monitored by means of an array of Silicon Surface Barrier Diodes (SBD). In section 2 the measurements with the SBD array are described. The major numerical algorithms used in the data analysis are also introduced. The following section (3) is devoted to the measurements with edge coils .

2. MEASUREMENTS OF X-RAY EMISSIVITY

The experimental set-up of the first diagnostic system consists of an array of 24 diodes divided into three pinhole cameras viewing a minor cross section of the plasma through three neighbouring vertical ports (Fig 1 shows details of the central array). To this first group of diodes one or two more can be added at different positions in toroidal angle, although as yet only one has been used. The diodes comprising the array are Silicon Surface Barrier Diodes (ORTEC BA-100-023-50-100). In order to screen unwanted visible light a thin silver foil (3000 A) is placed in front of each detector. This gives a low-energy cut-off in the photon efficiency at 100 eV.

Emission from the plasma is the effect of various atomic processes such as bremsstrahlung, recombination radiation and line emission. Because of the complicated dependence of these processes on density, temperature and impurity, it is difficult to obtain absolute estimates of these parameters from the broad band measurements we are concerned with. Usually therefore one concentrates on the relative variation of the intensity in deducing the nature of various profiles and instabilities, relying on the fact that the intensity is a strong (exponential) function of temperature to ensure that temperature variation is the dominant effect. We adopt essentially this approach.

The discharge is divided into three phases: setting-up, where the loop voltage is high and plasma current is rising fast, followed by a sustainment phase with steady plasma current, steady field reversal and a relatively low level of MHD activity; this eventually leads to the termination where major chaotic disruptions occur; see the example of Fig 6. Here we investigate the sustainment phase.

Profiles of line-of-sight integrated emissivity can be derived from the average signal level of the diodes in the array. Averages are taken over a short time interval (typical discharge duration 3 - 6 msec; averaging time from 50 μsec to 500 μsec) and/or on several consecutive discharges (ensemble averages). In the case of a cylindrical plasma, this can yield the actual radial profile by means of an Abel's inversion [Ref 2]. In our case helical instabilities and plasma shifts play a significant role in modifying this situation. With several arrays at different poloidal angles or with the assumption of uniform rotation of the plasma column (equivalent to an infinite series of poloidal views as time proceeds) the problem could be solved by means of an expansion in poloidal Fourier modes: each mode would be "inverted" separately by a simple extension of the original Abel's algorithm. Unfortunately this is not the case so that the simple approximation must be made that the only dominant distortion to the cylindrical symmetry depends on θ like $\cos\theta$ (which is consistent with the measurements using the edge coils). In this case the symmetric and antisymmetric part of the integrated profile are inverted separately to reconstruct an average two-dimensional plot of the X-ray emissivity.

It is seen from Fig 2 that the discharge is shifted radially outwards by about 3 cm through its time evolution. This was predicted by toroidal equilibrium calculations using Shafranov's formula and confirmed by electrical diagnostics. A new and unexpected feature is that the profile of emissivity tends to become flat soon after the setting-up phase. By frequency filtering each signal (with digital techniques) it is also possible to determine the profile of the fluctuation intensity in different frequency bands. In this case the approximation of a single helical distortion is certainly less rigorous and the results of the inversion must be taken as purely qualitative. What is apparent though is that, whichever frequency band is chosen, the fluctuation are concentrated in a rather narrow annular region of thickness Δ, with $\Delta/a \sim 0.2$ at the edge of the plasma approximately centred, in fact, on the reversal surface (where the toroidal magnetic field is zero (see Fig 3)).

Before we proceed it is convenient to introduce some of the numerical algorithms carried out in the data analysis. The techniques followed here are commonly referred to as spectrum and correlation analysis and they are routinely adopted in the study of random signals (Ref 3). The fundamental idea is that of a Fourier analysis in the independent variable which in most cases is time, but can also be space.

Appendix 1 gives a summary of relevant definitions. These formulae can be regarded as useful only if the condition of stationarity is satisfied, that is, if the quantities do not depend on the choice of time. Ensemble averages can be replaced with time averages if one makes the further assumption of ergodicity. These conditions are not usually satisfied except for very short periods. On the other hand, a short time interval means a poor frequency resolution so that a compromise must be found between the two conflicting requirements. This can become extremely delicate in the case of the setting -up and termination phases which have a very limited duration.

The cross-spectra and cross-correlation functions are but two facets of the same idea and, as the Wiener-Kintchine theorem shows, can be obtained from each other with a Fourier transform. This means that information can be easily exchanged between the two types of analysis we are performing. Cross-spectra of signals from two neighbouring diodes show good coherence only in the region of low frequencies (up to 50 kHz; the high frequency cut-off of the preamplifier being 250 kHz; indeed most of the signals we deal with are sampled and digitized with a frequency of 500 kHz).

We expect to find modes at low frequency that are coherent over a long distance (global modes) whereas fluctuations at higher frequencies can be due to more local turbulence. This is confirmed by measuring the auto-correlation function in space (or its normalised form called the cross-correlation coefficient). It can be done by taking one diode as a reference and correlating at zero time delay with all the others. Filtering the signals in a low frequency band the results one obtains show that the cross-correlation coefficient is always positive and remains at an almost constant level of $\sim$ 30% after an initial rapid decrease when moving away from the reference diode (Fig 4). The correlation length of this more local component decreases rapidly as the frequency increases and the level of background correlation falls rapidly to zero.

Measurements with one diode at 90° away from the fixed array have shown that the global modes observed in the low frequency region maintain a good coherence even at such distance as one meter (the major radius of the machine is 81 cm).

No attempt has been made so far to evaluate transport coefficient associated with the level of fluctuation as this would imply a better knowledge of the emission processes. The overall picture that we can therefore derive from this preliminary study of X-ray emissivity

fluctuations is that symmetric modes (m = 0) are dominant (although at times m = 1 and m = 2 modes are observed) together with a background of more localized turbulence. The fluctuations are concentrated in a narrow region around the reversal surface and the plasma column shows a significant outward shift in agreement with electrical diagnostics.

3. MAGNETIC FLUCTUATION MEASUREMENTS

Several sets of discrete coils are used to measure the poloidal and toroidal components of the magnetic field at the edge of the plasma. Most of these coils are arranged in arrays that encircle the plasma in the θ direction (poloidal arrays) with sixteen sets of coils. There are five of these arrays inside the vacuum vessel and four outside distributed along the toroidal direction. Besides this there is a toroidal array of 28 coils (14 for B_θ and 14 for B_ϕ) spanning 60° in the toroidal direction (see Fig 5) (this is equivalent to a resolution in toroidal mode number of $\Delta n \sim \pm 4$).

By Fourier analysing in θ each poloidal array can provide an expansion of the magnetic fluctuations for a total of eight independent poloidal modes ($0 \lesssim m \lesssim 7$). The toroidal array plus other coils from different poloidal arrays serves the same purpose in the ϕ-direction (although with a broader resolution).

In fact each coil measures the time derivative of B (no analogue integration is applied) but for those coils that lie outside the vacuum vessel an effective integration is provided at frequencies higher than about 5 kHz due to the skin time for the penetration of fluxes through the metal*. In the measurements we describe here data were taken simultaneously from the toroidal array and from one internal poloidal array intersecting it. A systematic analysis of poloidal and toroidal mode structure is presented which derives from the same statistical techniques used for the SBD array; magnetic fluctuations also appear fairly stochastic and turbulent (as it can be observed in the example of Fig 6). Helical structures are also studied by correlating the two arrays together. Some interpretation of these results is discussed in terms of the resistive MHD instabilities expected in RFP configuration.

In order to determine the structure of the fluctuations we may Fourier decompose in θ or ϕ by forming sums over coils with a weighting function $\cos m\theta$ and $\sin m\theta$ (similarly for ϕ). The sum of the squares of these two components gives the total power in each Fourier mode.

* (A more detailed calculation shows that this time is different for modes with different helicities.)

The poloidal mode-spectra are dominated by the m = 0 and m = 1 component both for B_θ and B_z (see Fig 7). The toroidal mode-spectra on the other hand show variations according to the frequency band the signals are filtered within. In general, the dominant feature at the lower frequencies is at n = 8 - 12. At higher frequencies there is some evidence for harmonic structure.

Another approach to the poloidal mode structure is to form the cross correlation coefficient (initially with zero time delay) between the various coils thus giving the spatial autocorrelation. For the case of B_θ, if the coil on the inner and outer equator are used as a reference there is a clear difference in the auto-correlation obtained although both are symmetric (see Fig 8). Using references at $\theta \simeq \pm 90°$ gives auto-correlations which are asymmetric. These differences indicate that the fluctuations do not possess rotational symmetry in their statistics: i.e. θ is not an ignorable coordinate. The nature of the fluctuations may be deduced from inspection of such autocorrelations. To lowest order, disregarding for a moment the lack of rotational symmetry, the autocorrelation is that which would be expected from dominantly m = 0 and m = 1 of similar magnitude. The lack of symmetry indicates that in fact the "m = 1" component is distorted due to toroidicity so that its phase varies more rapidly at the outer equator ($\theta \sim 0$) than the inner ($\theta \sim 180°$). Expressed in terms of the Fourier decomposition, this means that the fluctuation mode consists of a sum of poloidal Fourier components:

$$M_1 = \cos(\theta - \alpha) + \varepsilon_2 \cos(2\theta - \alpha) + \ldots$$

where α is some (random) phase, these Fourier components being coupled (linearly) together. The $\cos\theta$ and $\cos 2\theta$ (and also $\sin\theta$ and $\sin 2\theta$) components are always in phase with each other. This characteristic is readily confirmed by forming the cross-spectrum between $\cos\theta$ and $\cos 2\theta$ The coherence at lower frequencies is very high ($\gtrsim 0.8$) indicating that about 60% of the power in the modes is linearly coupled. The phase is zero indicating that the $\cos 2\theta$ and $\cos\theta$ are in phase at $\theta = 0$. The spatial autocorrelation of $\tilde{B}_\phi$ shows less asymmetry than $\tilde{B}_\theta$ although the m = 1 on m = 2 coherence spectrum is qualitatively similar in the two cases. The poloidal mode structure is thus that there are dominantly just two statistically significant types of mode M_0 and M_1 which may be identified as the modes corresponding to m = 0 and m = 1 plus their concomitant higher harmonics generated by the toroidal distortions.

In the toroidal direction the auto-correlation in space is almost truly independent of the choice of origin. This reflects the axisymmetry of the torus, apart from small imperfections due to field errors (ports, iron core coils etc.). The spatial autocorrelation has a rapidly damped form indicating a fairly broad spectrum of toroidal wavelengths. It is clear that a closely spaced array of the type we are using is essential for obtaining a reasonable estimate of the toroidal structure since the correlation length is of the order of or less than the 60° in ϕ which we have available. It would be preferable to have a toroidal array whose extent was much greater than the correlation length. Unfortunately the present array does not meet this criterion and the result is that our resolution of toroidal wave number is of the same order as the width of its spectrum.

In order to determine propagation and rotation effects we examine the time delayed cross correlation between coils in the poloidal array and in the toroidal array. In the former case evidence of rotation is indeed present. In the latter it is less clear but nevertheless can be shown to exist.

So far an independent analysis of the poloidal and toroidal structure has been performed. If a correlation is carried out between the two arrays it is possible to reconstruct the actual helical pattern of the instabilities. From the time delayed cross-correlation coefficient for pairs of coils in the two arrays it is possible to deduce the presence of a dominant $m = 1$, $n \sim 8 - 12$ helical perturbation. A more precise calculation involving a double Fourier transform was carried out [Ref 5]. In what we refer to as the "association spectrum" each poloidal mode (mostly $m = 0, 1, 2$) has an associated n-spectrum. The main features of this spectrum confirm the presence of the $m = 1$ $n \sim 8 - 12$ mode and indicate the presence of an $m = 0$ $n = 0$ mode for B_ϕ. The n-spectrum of the $m = 2$ mode on the other hand is mostly due to linear coupling from the $m = 1$ whose shape it reproduces.

Now helical perturbations are resonant at the radius where the safety factor $q = \frac{rB_\phi}{RB_\theta}$ is given by $q = -m/n$ [ref 4]. At this radius, non zero radial field perturbations will lead to magnetic island formation. All the helical perturbations found in the association spectrum of $m = 1$ correspond to resonant surfaces inside the reversal surface. In addition to this $m = 1$ mode, the $m = 0$ perturbations are always resonant at the reversal surface (for $n \neq 0$). A comparison with known theoretical calculations [4] permits us to deduce the presence of island overlapping and consequent stochastic behaviour. An estimate of the transport coefficient that results from this agrees with measured values of confinement times (Ref [5]). It can also be shown [5] that the perturbations that we see seem to correspond qualitatively quite well with the expectations of resistive instability theory in that we see $m = 1$ perturbations resonant from $r = 0$ outward up to the reversal surface and also $m = 0$ perturbations of long toroidal wavelength.

Our present analysis does not allow us to distinguish whether the m = 0 perturbations arise directly from linearly unstable resistive modes or indirectly as a non-linear consequence of the m = 1 modes. Further studies employing higher order correlations and focusing on the time non-stationarity may be able to shed further light on this topic. Nor are we able to distinguish the driving energy sources for any of the perturbations which might indicate whether the modes are tearing or pressure driven 'g' modes.

Finally a scan was carried out in the pinch parameter, θ, (where $\theta = 2\pi a I_\phi/\Phi$, I_ϕ being the toroidal current and Φ the toroidal flux) to study how the MHD activity changes its structure. Fig 9 shows the variation with θ of the relative RMS fluctuation level (after filtering in the frequency band 3 - 250 kHz) At the value of $\theta \sim 1.7$ * the B_θ toroidal spectrum (computed for the frequency band 5 - 50 kHz) shows a peak at $n \sim 8$ and also some power for $n \sim 0$ (Fig 10). B_z shows only the peak at $n \sim 8$. As we vary θ two trends become apparent:

(a) As θ is increased, the $n \sim 0$ component of B_θ becomes stronger, until at $\theta \sim 2.4$ this mode is equal to the $n \sim 8$ and

(b) At higher values of θ, the $n \sim 8$ peak becomes narrower on both B_θ and B_ϕ.

The poloidal spectra confirm that for each value of θ the power is confined to the m = 0 and m = 1 modes, as it can be seen in Fig 11 and 12. The m = 2 mode, especially for B_θ, is shown to be due to a toroidal distortion of the m = 1 to which it is strongly linearly coupled for all θ values except the very lowest.

We have also calculated cross-spectra between poloidal and toroidal modes (this is equivalent to the technique of the association spectra, but is more detailed in the frequency domain once the relevant poloidal and toroidal modes have been identified). The results of this study of helical structure confirm the presence of an m = 1, $n \sim 8$ kink, visible on both B_θ and B_ϕ, and two m = 0, n = 0 modes for both B_θ and B_ϕ (the latter is not seen on the toroidal spectrum for B_ϕ because of its absorption by the liner: for this mode in fact, the penetration time, necessary to reach the interspace toroidal array, is much longer than for the other modes and is estimated to be $\sim$ 100 μs). Furthermore, it is possible to detect a significant correlation between m = 1 and n = 2 (mainly for B_θ), which becomes stronger as θ is increased. This mode is non resonant by its nature and could be an interchange mode due to a pressure profile peaked on axis.

4. ACKNOWLEDGEMENTS

We would like to thank Mr J P Webber and Mr P Noonan for their help in the numerical analysis and Dr J B Taylor for many helpful discussions. We also thank the rest of the HBTX1A team for their kind support.

Oct 1983

* The value of θ is measured outside the liner.

APPENDIX

Given the time history of two signals

$$k_{x(t)} \, , \, k_{y(t)} \qquad \text{(index k is for an element of the ensemble)}$$

we can Fourier transform to obtain

$$k_{X(f)} \quad k_{Y(f)}$$

The "power Spectrum" is defined

$$P_x(f) = \langle \left| k_X(f) \right|^2 \rangle \qquad P_y(f) = \langle \left| k_Y(f) \right|^2 \rangle ;$$

Given the function $\Gamma_{xy} = \langle k_X(f) \; k_Y(f)^* \rangle$

we define the "cross spectrum" as: $\left| \Gamma_{xy} \right|$ and the "phase spectrum" as: $\arg(\Gamma_{xy})$. The "coherence" is as follows

$$\gamma = \frac{\left| \Gamma_{xy}(f) \right|}{\{ P_x(f) \; P_y(f) \}^{1/2}}$$

The "cross-correlation function" is given by $R_{xy}(\tau) = \int_{t_o}^{t_o+T} \langle k_x(t) k_y(t+\tau) \rangle dt$ where the two signals are previously filtered to eliminate the influence of the D.C level. The Wiener-Kintchine theorem links spectra with correlation functions

$$R_{xy}(\tau) = 2 \int_0^\infty df \; \Gamma_{xy}(f) \; e^{i2\pi f\tau}$$

Finally we can normalize R_{xy} to give the "cross-correlation coefficient":

$$\rho_{xy}(\tau) = R_{xy} / \left\{ \int_{t_o}^{t_o+T} \langle k_x^2(t) \rangle \, dt \int_{t_o}^{t_o+T} \langle k_y^2(t) \rangle \, dt \right\}^{1/2}$$

If x = y "cross" is replaced by "auto".

REFERENCES

[1] H A B Bodin, RFP Experiments: Results from HBTX1A, this course.

[2] N R Sauthoff, S Von Goeler: Techniques for the re-construction of two-dimensional images from projections; Princeton Plasma Physics Laboratory Report PPPL 1447

[3] J S Bendat, A G Piersol: Random Data; Analysis and measurement procedures (Wiley-Interscience, 1971).

[4] G Bateman: MHD Instabilities (MIT Press, 1978).

[5] I H Hutchinson, M Malacarne, P Noonan, D Brotherton-Ratcliffe: The Structure of Magnetic Fluctuations in HBTX1A Reversed Field Pinch Culham Laboratory Report CLM P-701 (and submitted to Nuclear Fusion).

FIGURE CAPTIONS

Fig 1 Geometry of Surface Barrier Diodes array (details of central array only).

Fig 2 Chord integrated and "Abel inverted" radial profile of X-ray emission.

Fig 3 Profile of the fluctuation level (filtered in the frequency band 5 - 50 kHz).

Fig 4 Cross-correlation coefficient at zero time delay for X-ray diodes, taking SBD 4 as a reference. (frequency band 5 - 50 kHz).

Fig 5 Geometry of discrete coil arrays.

Fig 6 Time history of a typical discharge: plasma current (I_p); toroidal loop voltage (V_ϕ); average toroidal magnetic field ($<B_\phi>$); average line-of-sight electron density ($\bar{n}_e$); toroidal magnetic field at the liner (B_ϕ); time derivative of poloidal magnetic field at the liner ($\dot{B}_\theta$).

Fig 7 Poloidal mode power spectrum for $\tilde{B}_\theta$ and $\tilde{B}_\phi$ for $\theta \sim 1.7$ (filtered in the band 5 - 50 kHz).

Fig 8 Equal time cross-correlation coefficient (spatial autocorrelation) for B_θ as a function of displacement in poloidal angle; (a) reference coil at $\theta \simeq \pi$; (b) reference coil at $\theta \simeq 0$. (5 - 50 kHz)

Fig 9 RMS relative fluctuation level for B_θ and B_ϕ as a function of θ. (high-pass filter from 3. kHz)

Fig 10 Toroidal mode power spectrum for $\tilde{B}_\theta$ and $\tilde{B}_\phi$ for $\theta \sim 1.7$. (5 - 50 kHz)

Fig 11 Evolution of power in the poloidal modes for $\tilde{B}_\theta$ as a function of θ (5 - 50 kHz).

Fig 12 Evolution of power in the poloidal modes for $\tilde{B}_\phi$ as a function of θ (5 - 50 kHz).

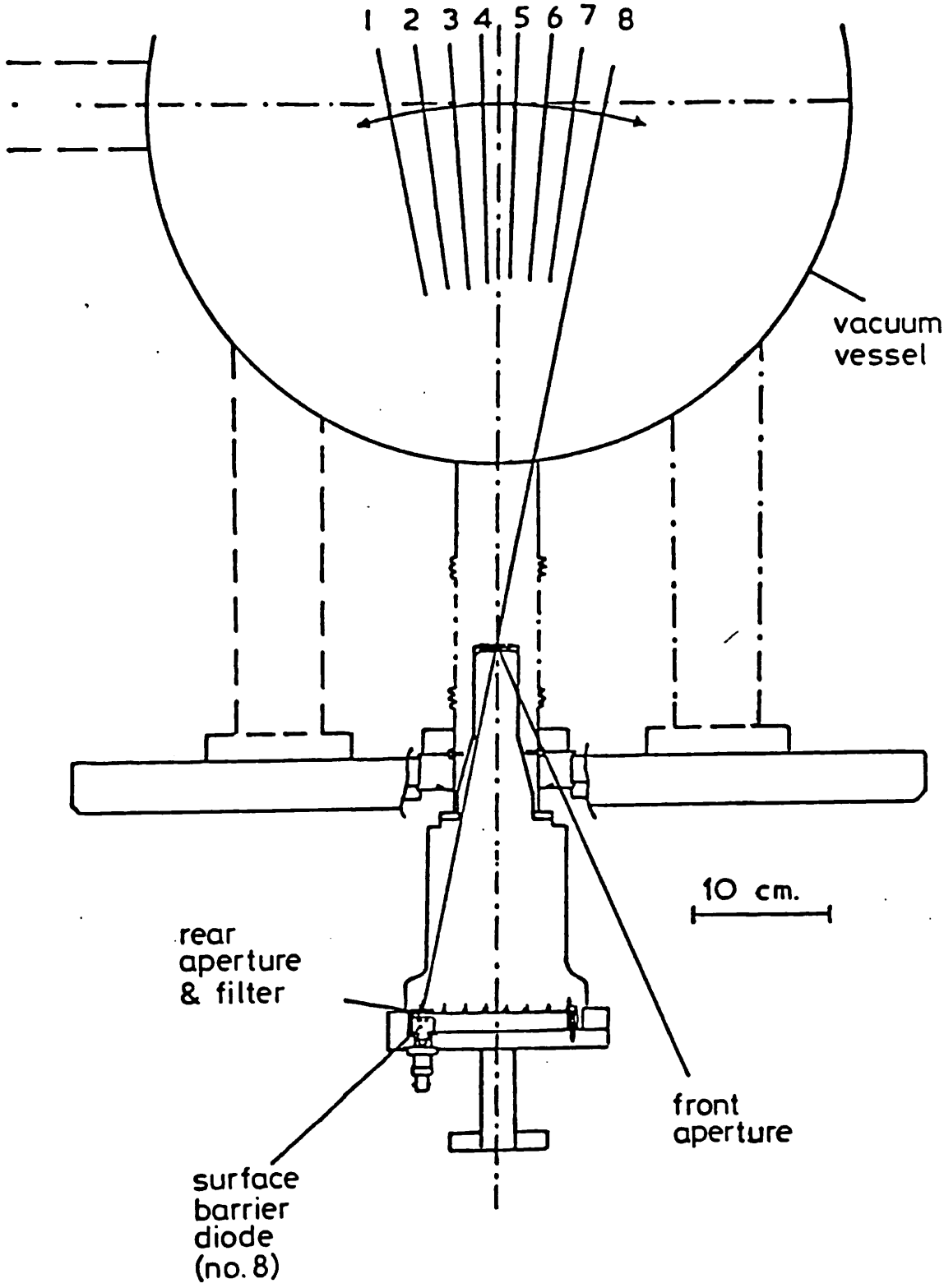
1 2 3 4 5 6 7 8
vacuum vessel
10 cm.
rear aperture & filter
front aperture
surface barrier diode (no. 8)

Fig. 1

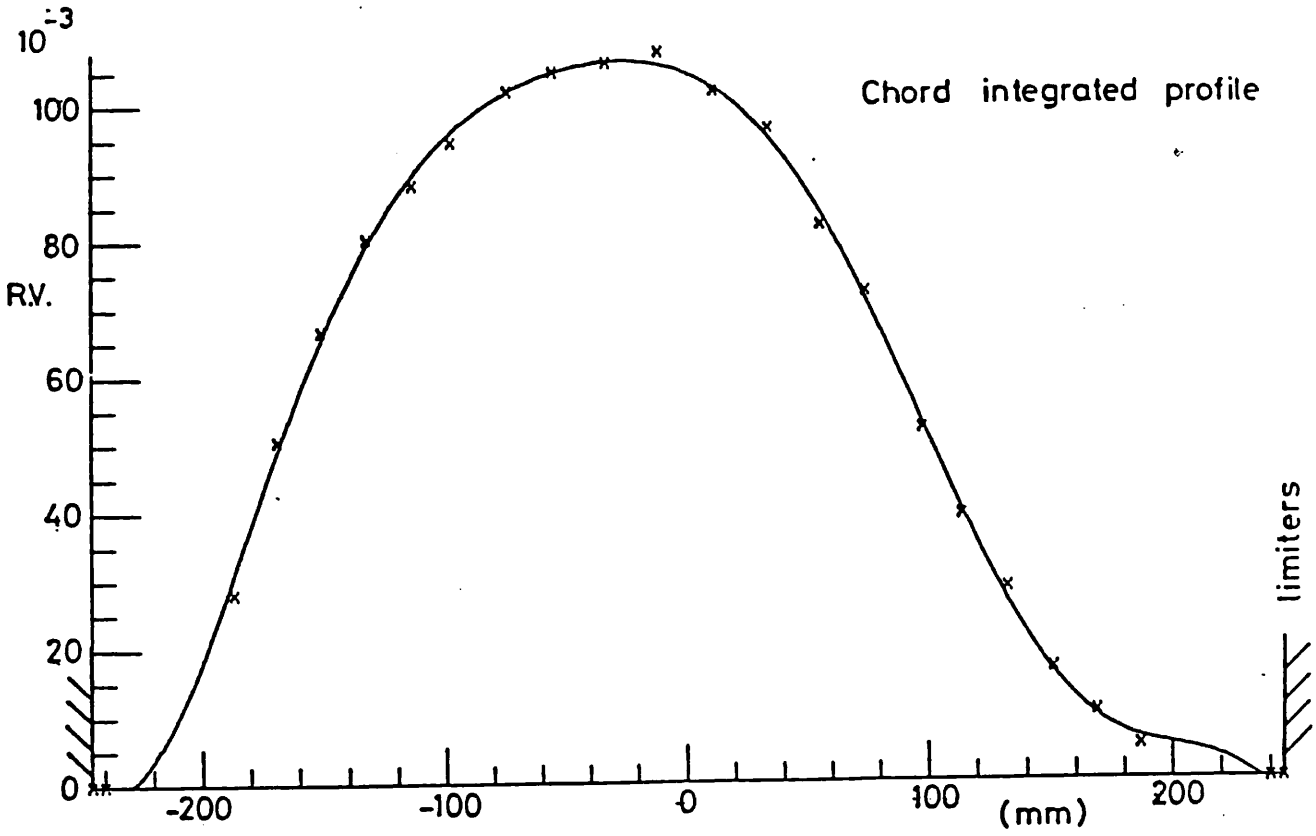
10^{-3}
100
80
R.V.
60
40
20
0
Chord integrated profile
limiters
-200
-100
0
100
200
(mm)

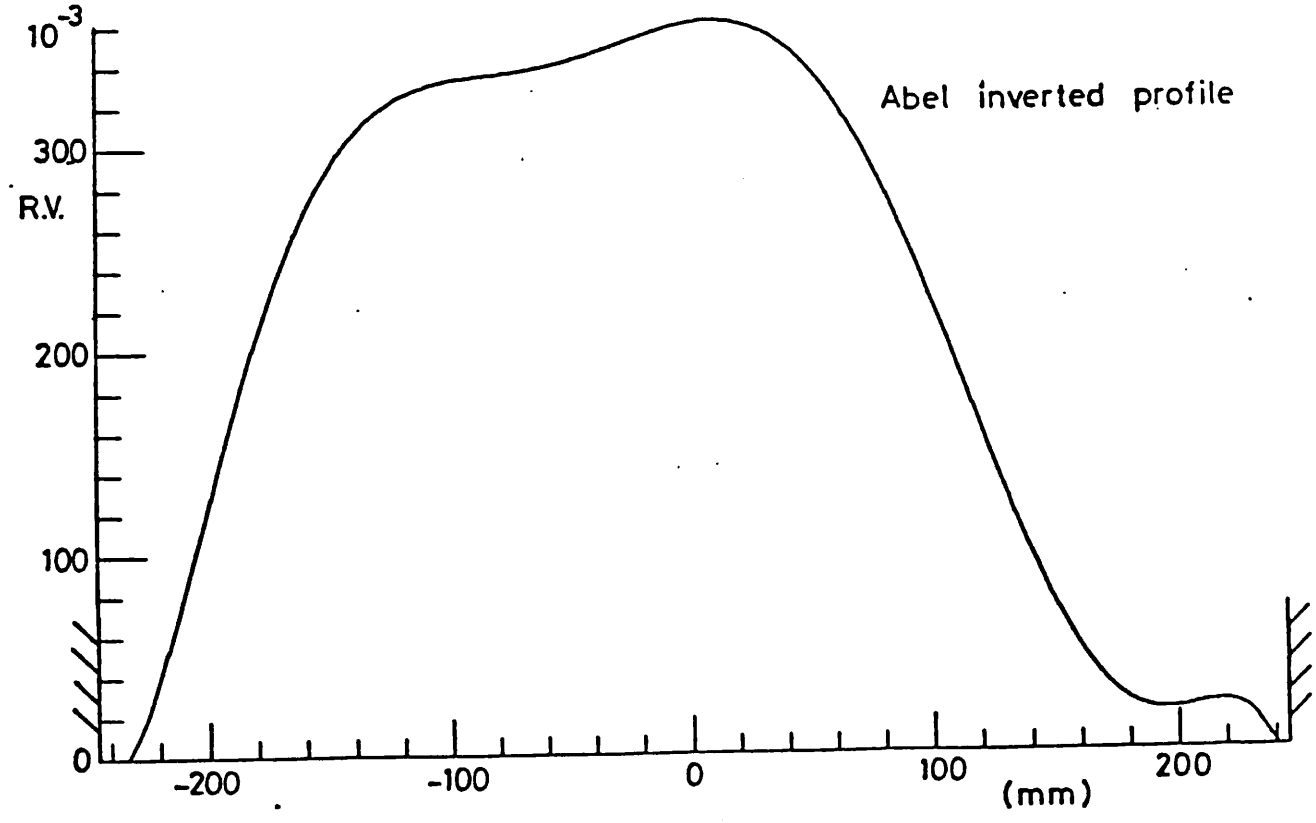
10^{-3}
300
R.V.
200
100
0
Abel inverted profile
-200
-100
0
100
200
(mm)

Fig. 2

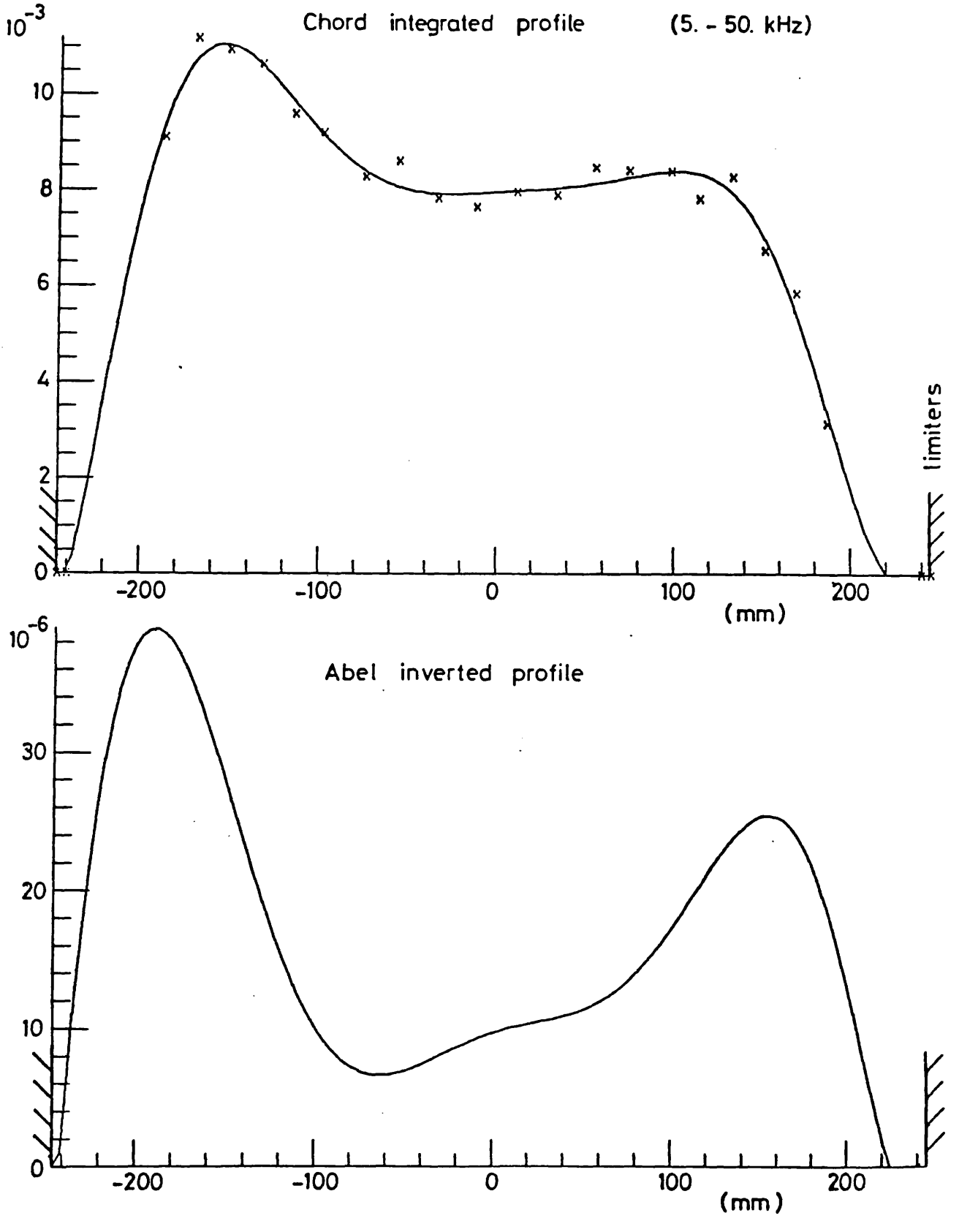
FLUID LEVEL
Chord integrated profile
(5. - 50. kHz)
10^{-3}
10
8
6
4
2
0
-200
-100
0
100
200
(mm)
limiters
10^{-6}
Abel inverted profile
30
20
10
0
-200
-100
0
100
200
(mm)

Fig. 3

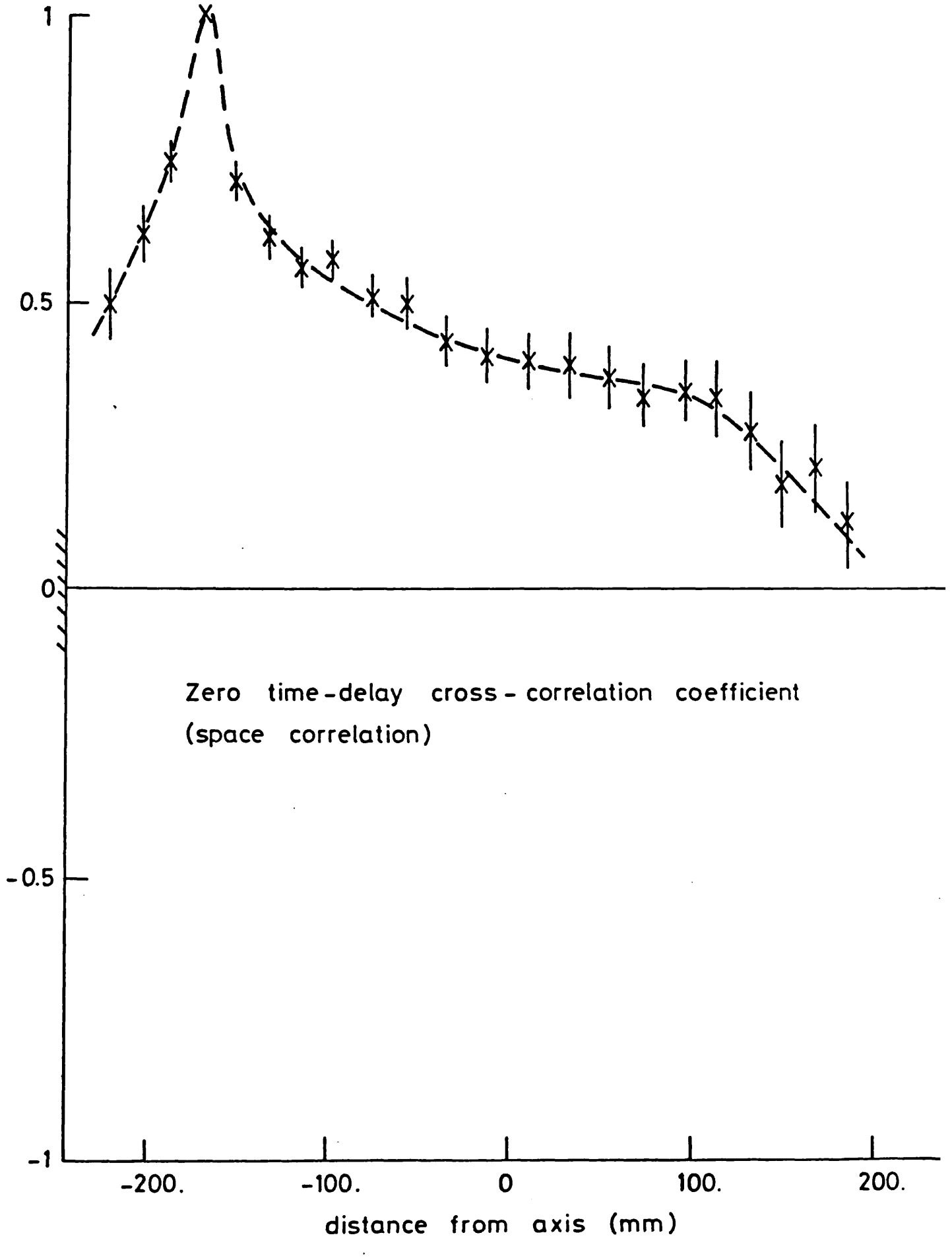
1
0.5
0
-0.5
-1
-200.
-100.
0
100.
200.
Zero time-delay cross-correlation coefficient
(space correlation)
distance from axis (mm)

Fig. 4

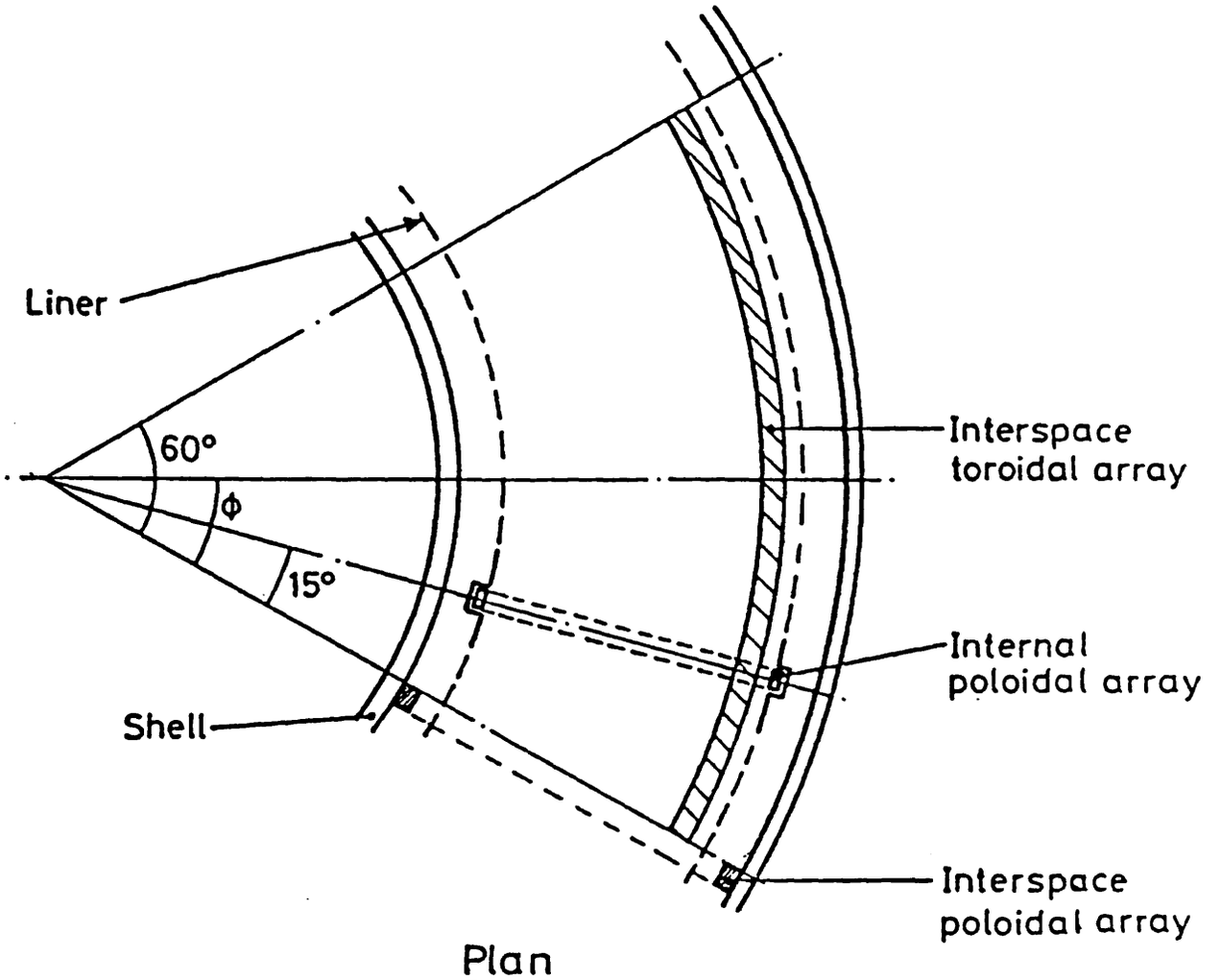

Plan

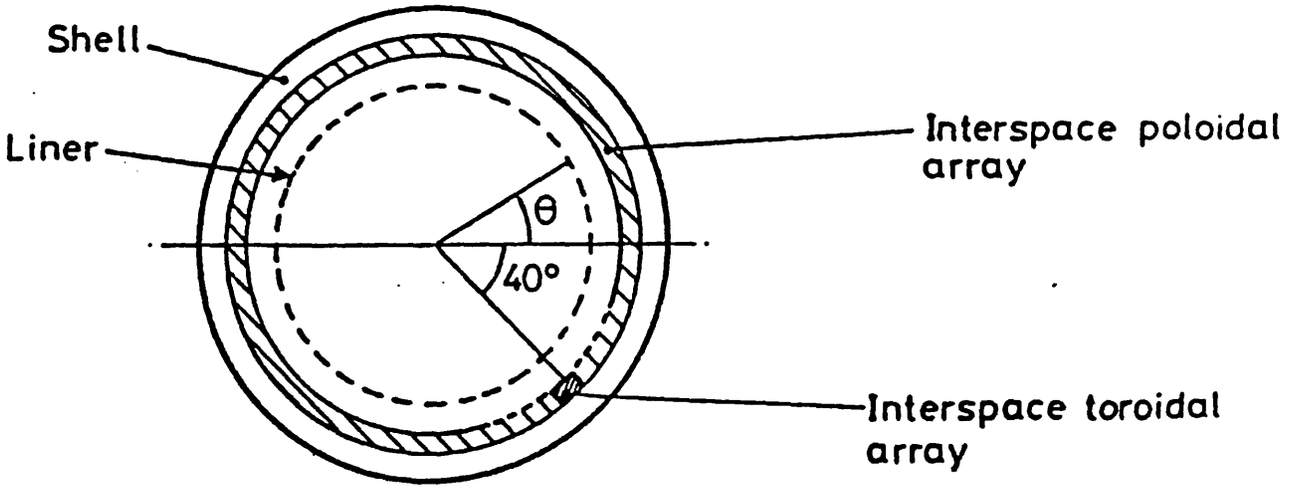

Section

Fig. 5

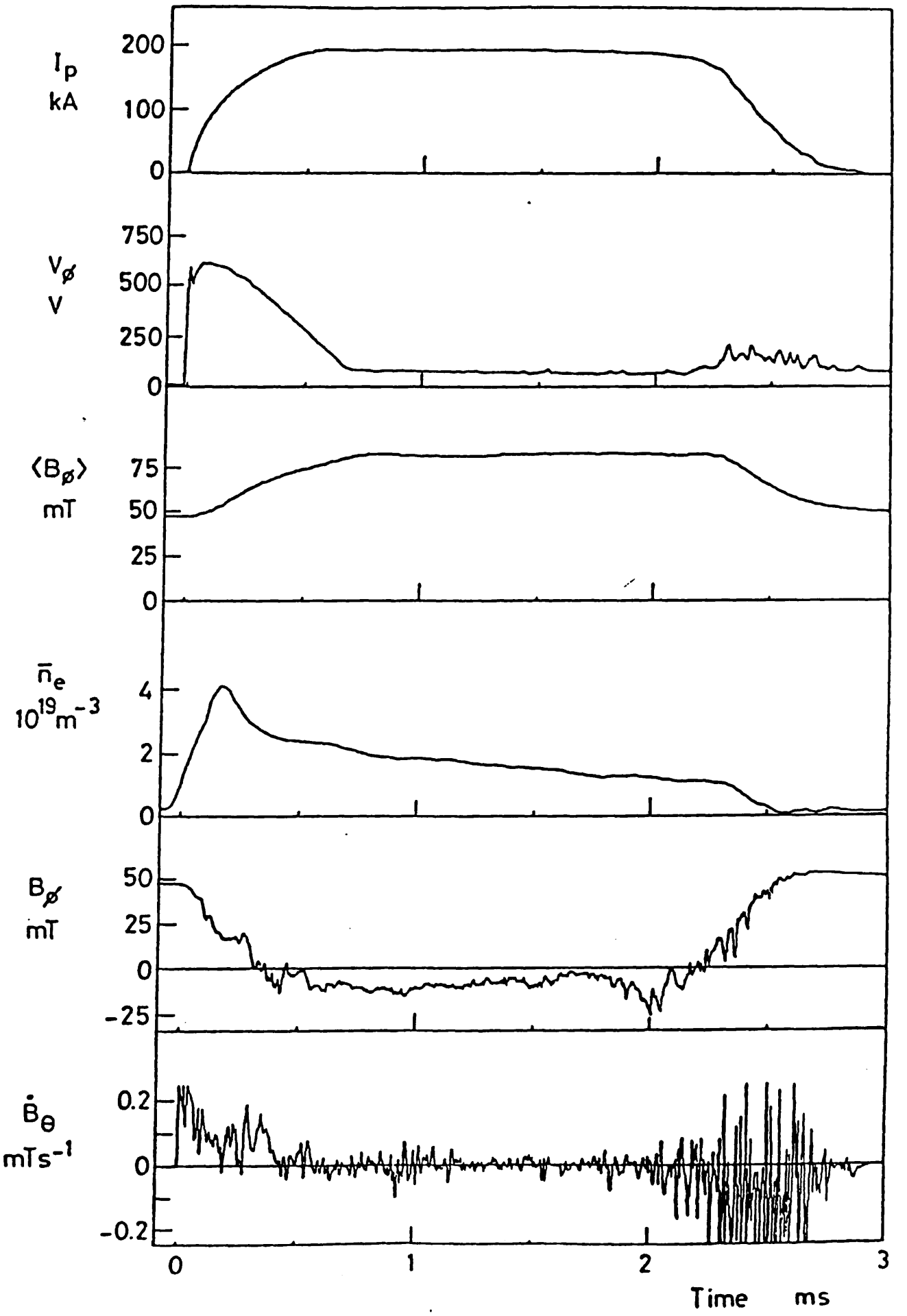
I_p
kA
200
100
0
V_ϕ
V
750
500
250
0
$\langle B_\phi \rangle$
mT
75
50
25
0
$\bar{n}_e$
$10^{19} m^{-3}$
4
2
0
B_ϕ
mT
50
25
0
-25
$\dot{B}_\theta$
mTs^{-1}
0.2
0
-0.2
0
1
2
3
Time ms

Fig. 6

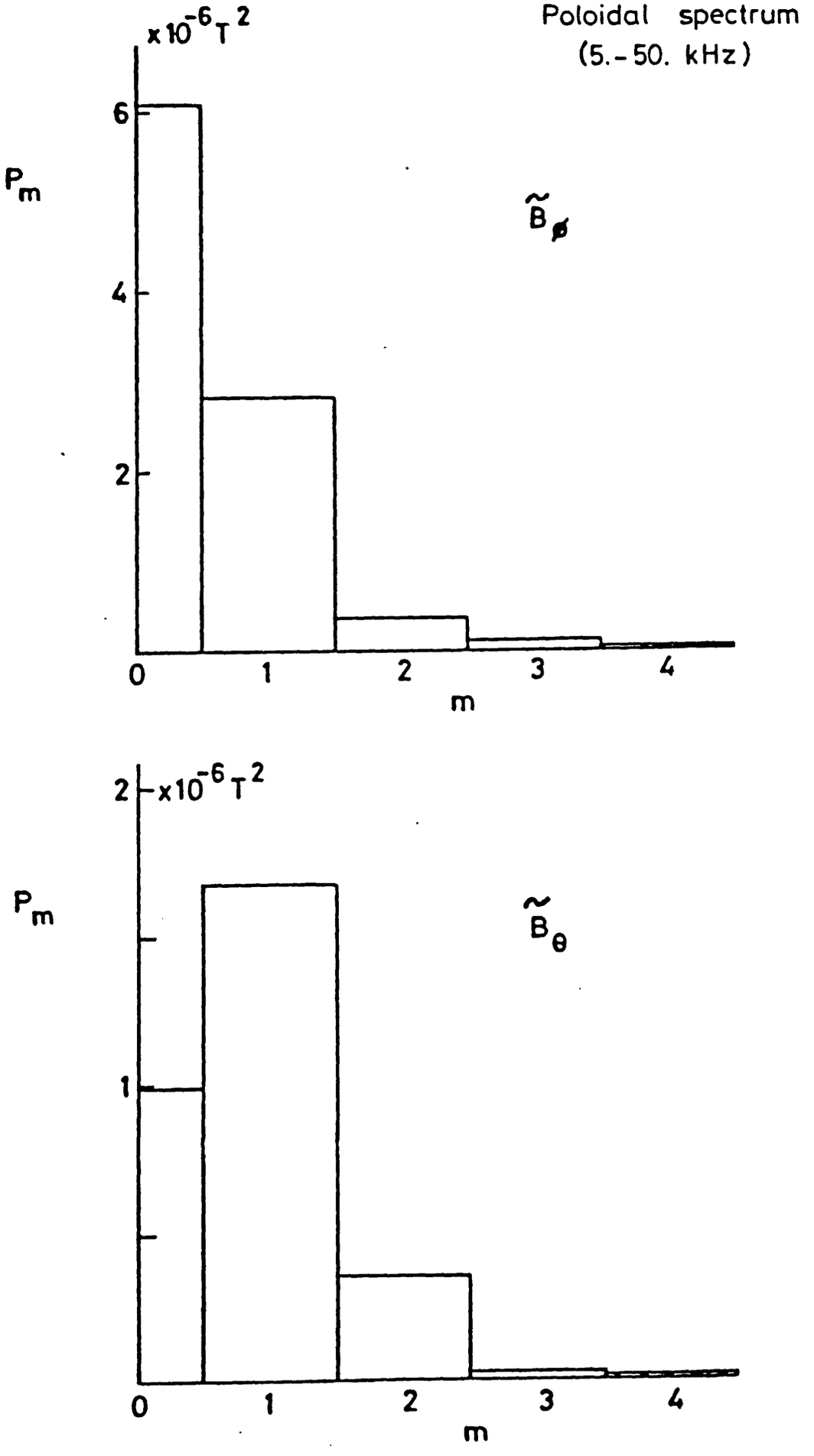
Poloidal spectrum
(5.-50. kHz)
x10⁻⁶T²
6
4
2
Pm
B̃φ
0
1
2
3
4
m
2
x10⁻⁶T²
1
Pm
B̃θ
0
1
2
3
4
m

Fig. 7

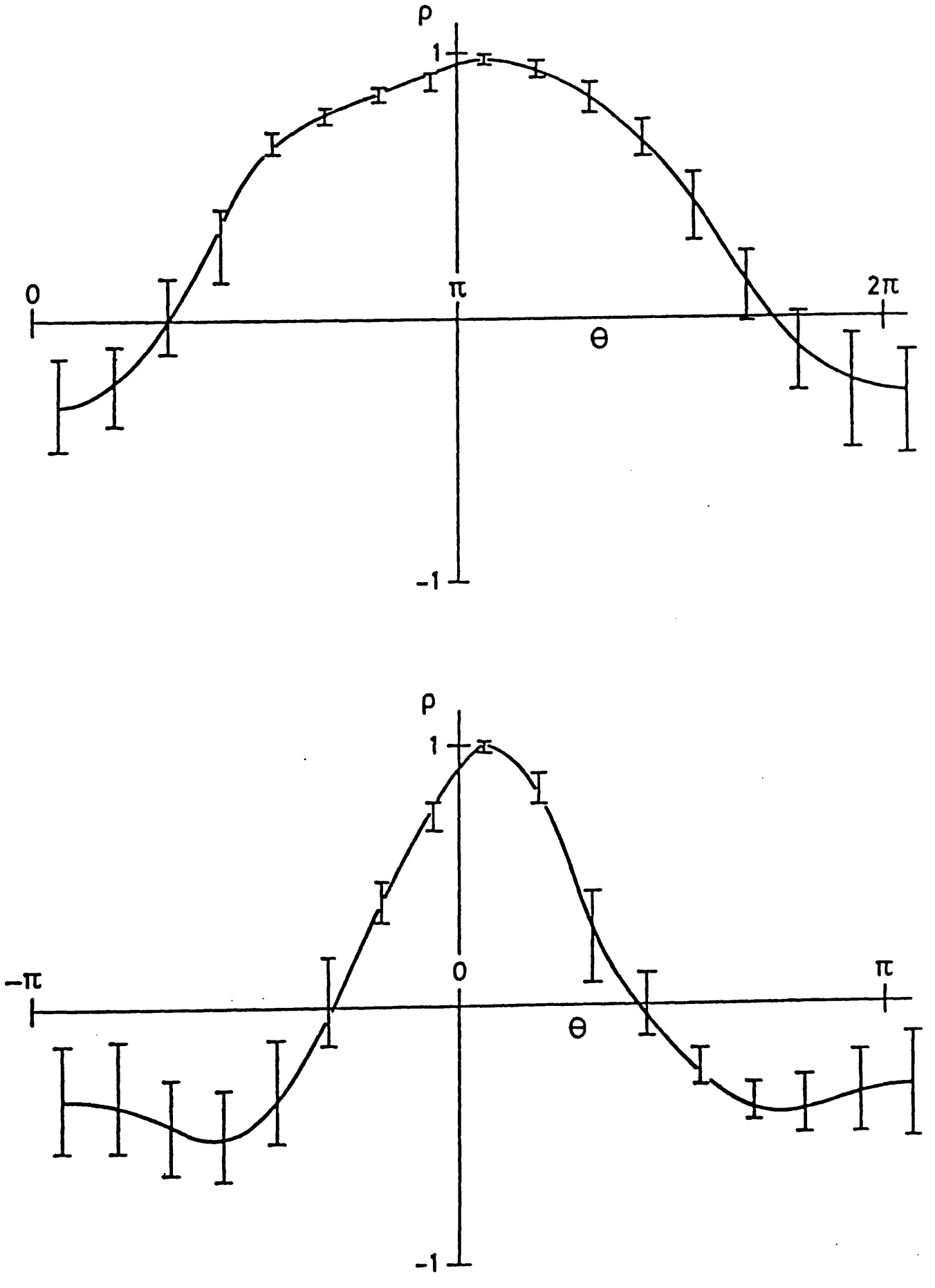

Fig. 8

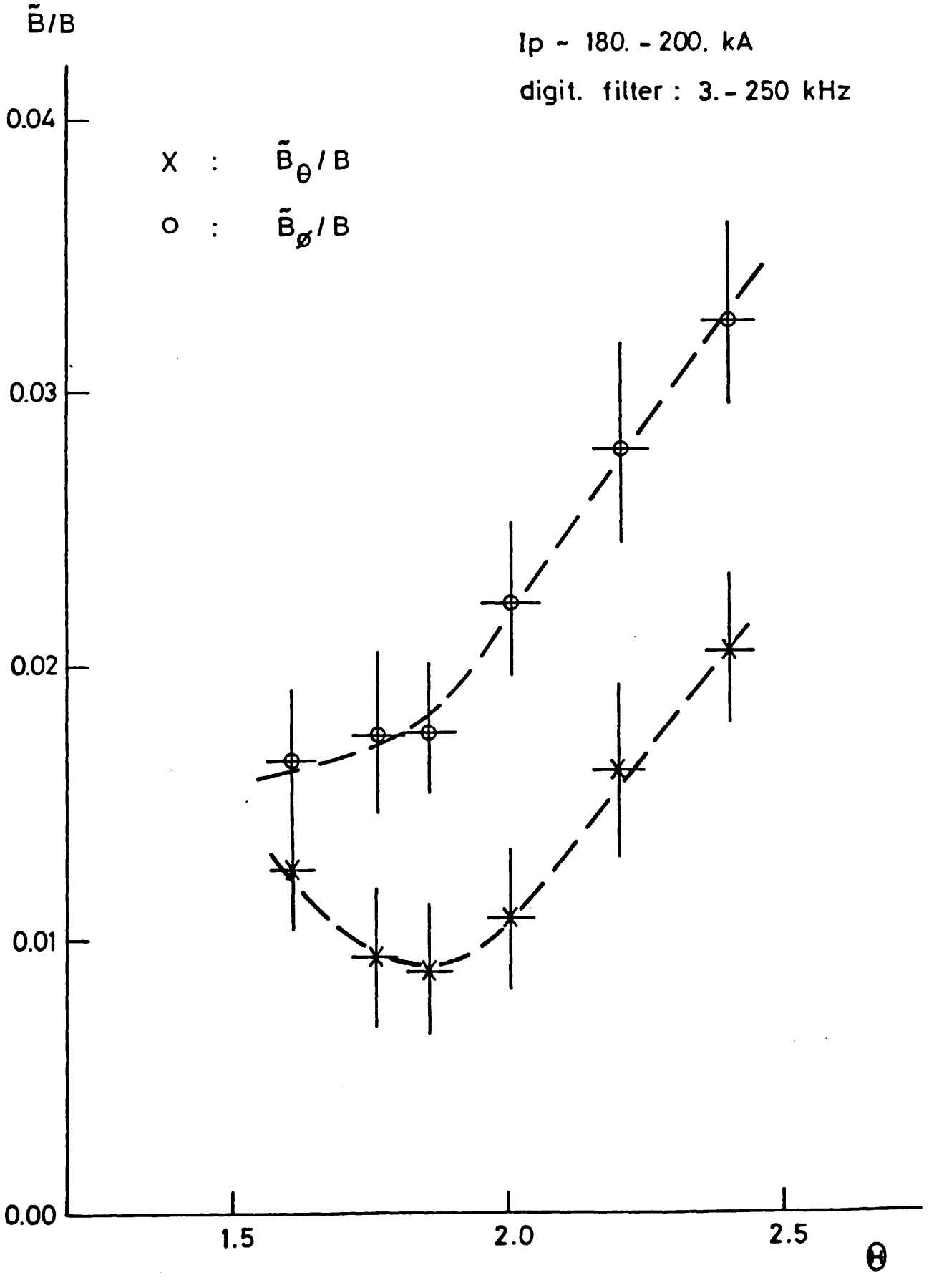
$\tilde{B}/B$
Ip ~ 180. - 200. kA
digit. filter : 3. - 250 kHz
X : $\tilde{B}_\theta / B$
o : $\tilde{B}_\phi / B$
0.04
0.03
0.02
0.01
0.00
1.5
2.0
2.5
θ

Fig.9

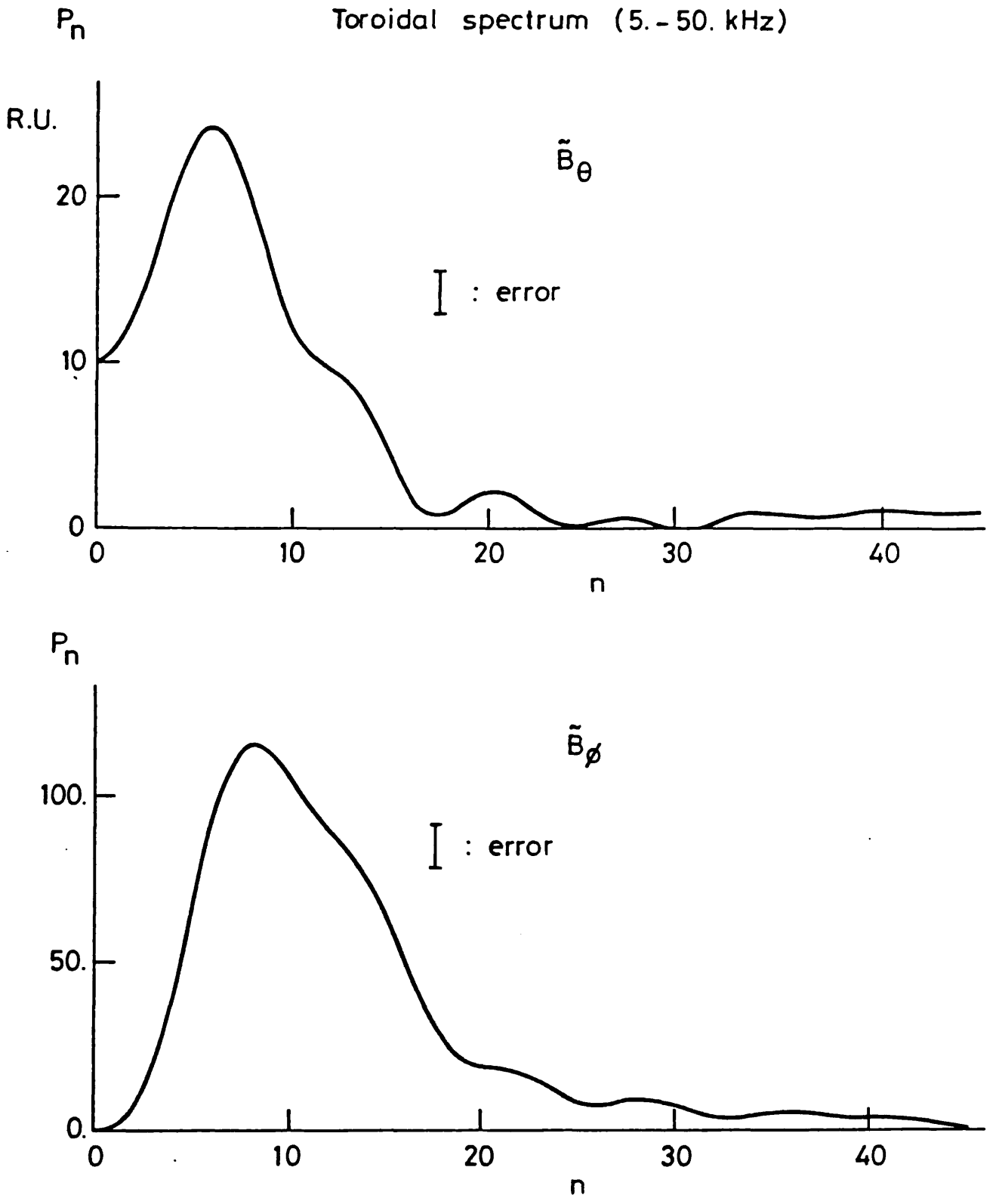
P_n
Toroidal spectrum (5.-50. kHz)
R.U.
20
10
0
$\tilde{B}_\theta$
I : error
0
10
20
30
40
n
P_n
100.
50.
0.
$\tilde{B}_\phi$
I : error
0
10
20
30
40
n

Fig. 10

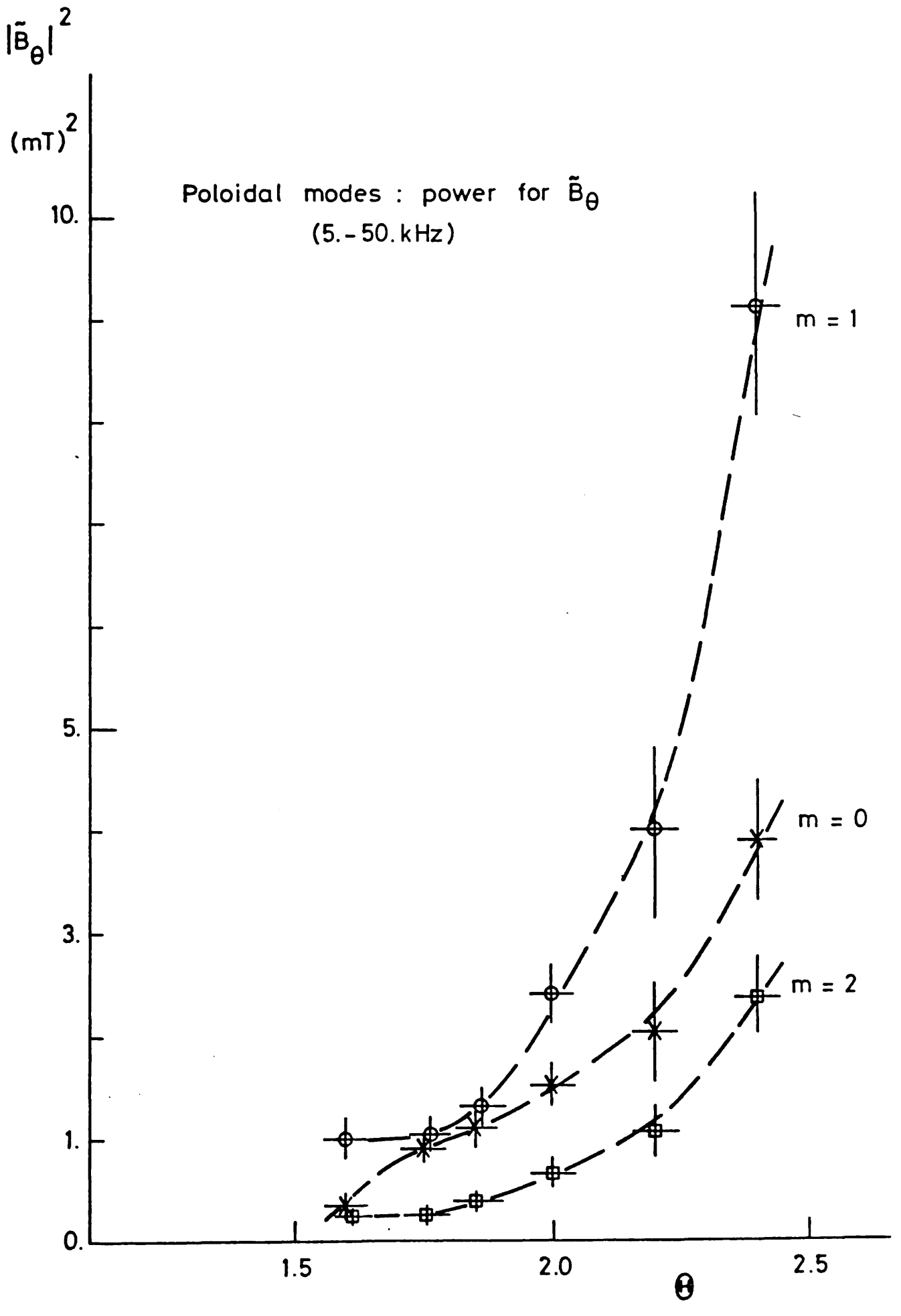
$|\tilde{B}_\theta|^2$
$(mT)^2$
Poloidal modes : power for $\tilde{B}_\theta$
(5. - 50. kHz)
10.
5.
3.
1.
0.
m = 1
m = 0
m = 2
1.5
2.0
2.5
θ

Fig. 11

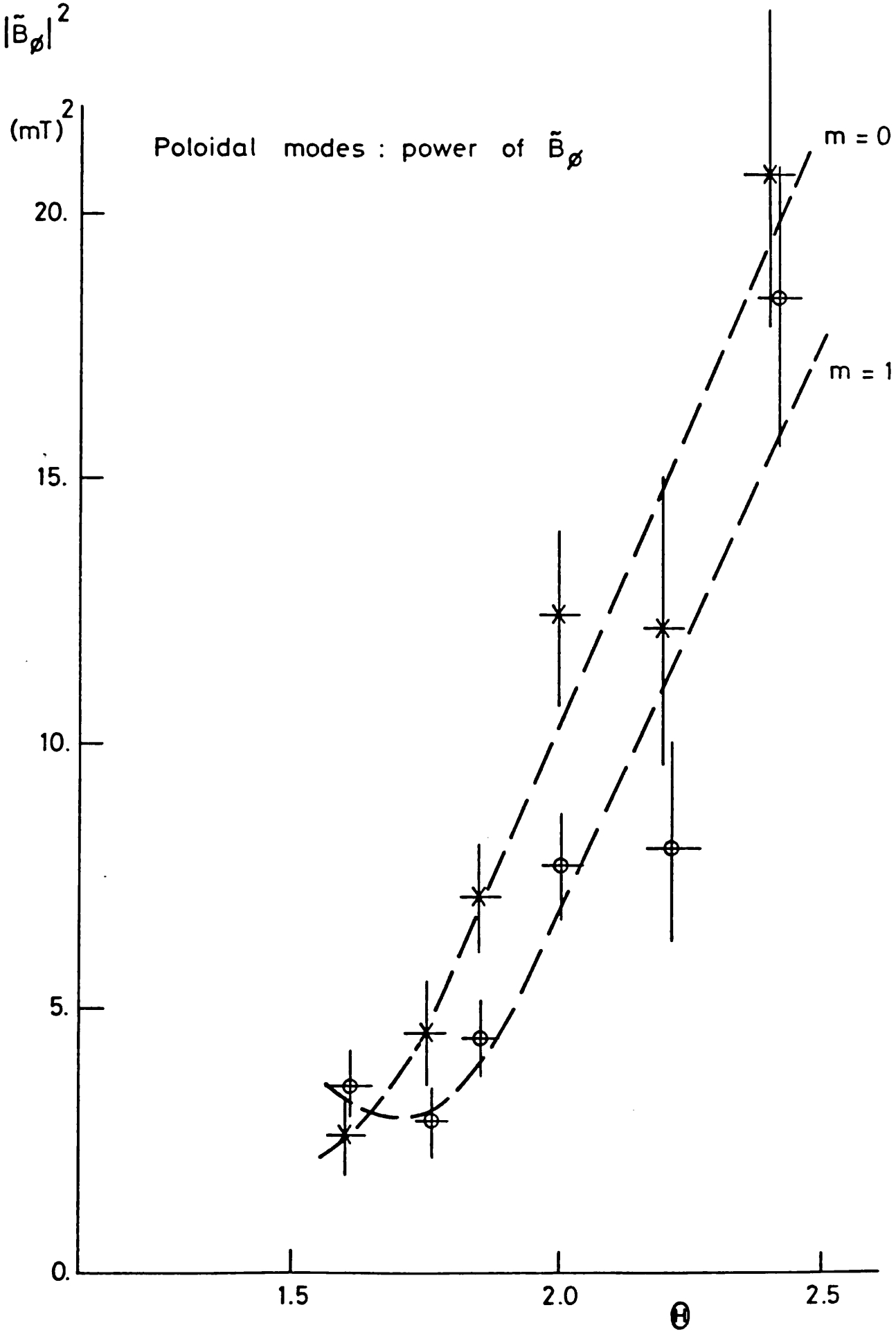
$|\tilde{B}_\phi|^2$
$(mT)^2$
Poloidal modes : power of $\tilde{B}_\phi$
m = 0
m = 1
20.
15.
10.
5.
0.
1.5
2.0
2.5
θ

Fig. 12

VARIATIONS OF MAGNETIC FLUCTUATIONS WITH PLASMA CONDITIONS IN HBTXIA RFP

M Malacarne** and D Brotherton-Ratcliffe*
Culham Laboratory, Abingdon, Oxon, OX14 3DB
(Euratom/UKAEA Fusion Association)
*Royal Holloway College, University of London
**Euratom supported Fellow and University of Oxford

ABSTRACT: Arrays of edge magnetic coils have been used to study the structure of fluctuations in the HBTXIA Reversed Field Pinch in the sustainment phase of discharges in a variety of plasma conditions: variations in relative amplitude are observed but no change in the mode numbers, except at high values of the pinch parameter. The current rise and the termination phases have been considered and it is found that only in termination are the fluctuation frequency and mode numbers different from sustainment.

1. INTRODUCTION

It has previously been shown[1] that the dominant global instabilities in the sustainment phase of standard discharges in the HBTXIA Reversed Field Pinch (RFP) ($\Theta \sim 1.8$, $I_p \sim 200$kA, $p_o \sim$ 1.5 mTorr) (the value of Θ is measured at the liner) are a broad band of m=1 kink modes centred on $|n| \sim 7$ and resonant inside the reversal surface. In addition, two independent m=0 modes have been observed with $|n| \sim 0$. In this paper we extend the previous analysis to study the differences in the global fluctuations for discharges of different conditions (varying I_p, p_o and Θ) and in the current rise and termination phases.

2. RESULTS

By forming weighted sums of signals from arrays of edge coils in the θ and ϕ directions we are able to evaluate the power associated with poloidal and toroidal Fourier modes, m and n. Figure 1 shows two examples of these spectra for b_θ (frequency band 5-50 kHz) in the sustainment phase of discharges with $\Theta \sim 1.8$ and 2.4 (I_p=200 kA, p_o= 1.5 mTorr). By correlating signals from the two arrays it is possible to identify the peaks at $|n| \sim 7$ in this figure as m=1. At high values of Θ part of the $n \sim 0$ features is ascribable to m=1 modes, in addition to the

to the usual m=0, n~0 activity; detailed studies show $|n|$=2-3 for these modes. By carrying out a similar analysis for discharges with different I_p and different p_o, we find no changes from the modal structure of fluctuations in standard discharges. Figure 2 shows how b/B varies with I_p, p_o and Θ (other parameters constant), for frequencies >3 kHz.

Figure 3 defines three time intervals in the termination phase for which Fig 4 shows how the b_θ n-spectrum evolves (frequency band 5-50kHz). In the first interval (end of sustainment) the dominant activity is at $|n|$~7. This remains the same until the third time interval, after the loss of reversal. Here the n-spectrum shows the presence of low n kinks; further studies indicate $|n|$=2-3. Power spectra in the frequency domain show that during sustainment the dominant modes are approximately in the region 5-15 kHz. However, in the second time interval there is an increase in power in the region 20-50 kHz, followed by a return to low frequency dominance as soon as reversal is lost. At no time are significant fluctuations observed at frequencies higher than 70 kHz. In the current rise phase, as in termination, the amplitude of the fluctuations is 6 to 10 times higher than in the sustainment phase. However, a detailed spectrum analysis shows the same power distribution, both in frequency and in mode number, as in the sustainment phase; in particular no low n kinks ($|n|$~2) are observed.

3. DISCUSSION AND CONCLUSION

That the mode numbers and frequency distribution of the fluctuations are the same with respect to changes in plasma parameters is indicative of the fundamental nature of these instabilities. At high values of Θ the presence of an m=1, $|n|$~3 instability with resistive time scales is interesting as estimates of the safety factor indicate that this mode would be non-resonant, suggesting that it should be ideal. The scaling of the relative fluctuation amplitude with Θ shows an optimum value at about 1.8. Variation with plasma current agrees with previous measurements[2] which showed two regimes, one at low current where b/B scales approximately like 1/I, and another at high current where the

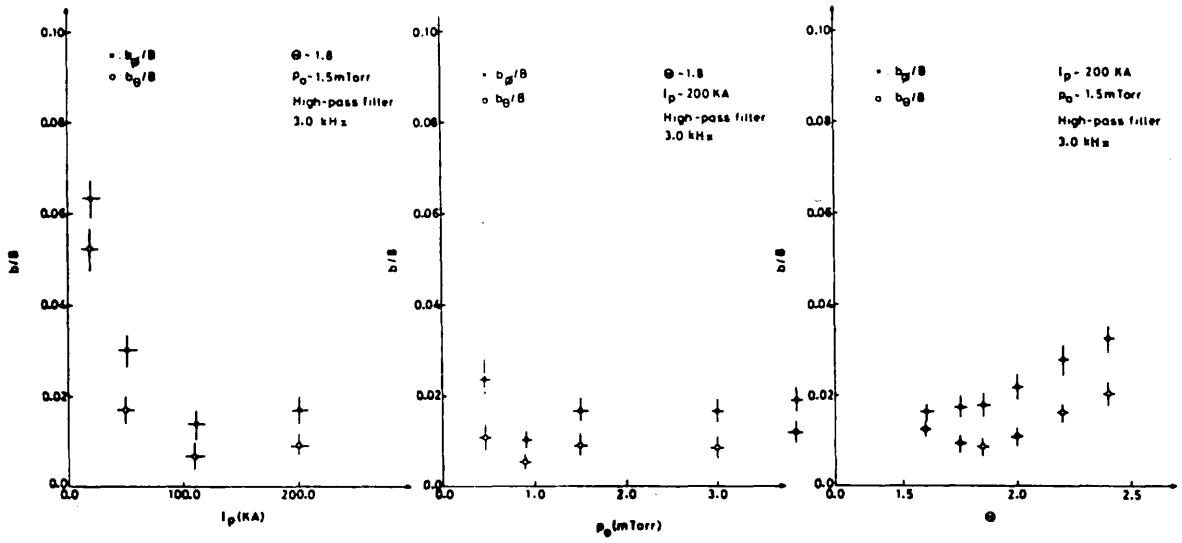

Fig. 2. Variation of b/B with I_p , p_o and Θ.

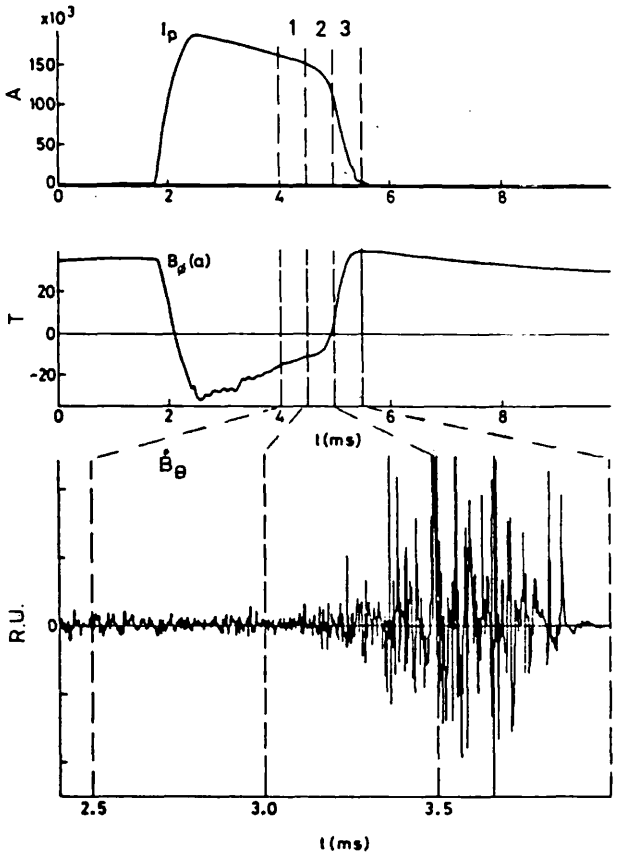

Fig. 3. Magnetic fluctuations in termination.

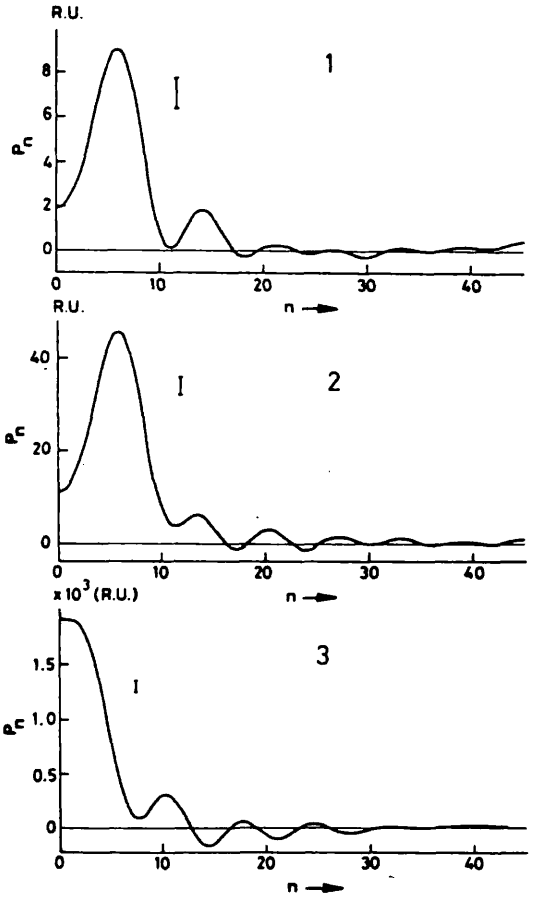

Fig. 4. Evolution of the n spectrum for b_θ in termination.

REFERENCES

[1] HUTCHINSON I H et al, Nuclear Fusion 24 (1984) 59

[2] HUTCHINSON I H, Proc. 11th Euro Conf. Aachen (1983)

scaling is much weaker. Pressure variations, on the other hand, do not seem to alter strongly the relative fluctuation level.

The structure of the global fluctuations in the current rise phase is very similar to that during sustainment, although the amplitude is higher. If these modes are essential to the relaxation process, this indicates that the production and sustainment of reversal rely on the same mechanism. In the termination phase of the discharge the fluctuations have larger amplitudes and show several differences in the frequency and mode numbers. However, after reversal is lost the observed frequencies correspond to resistive timescales rather than the Alfven timescale expected for ideal modes.

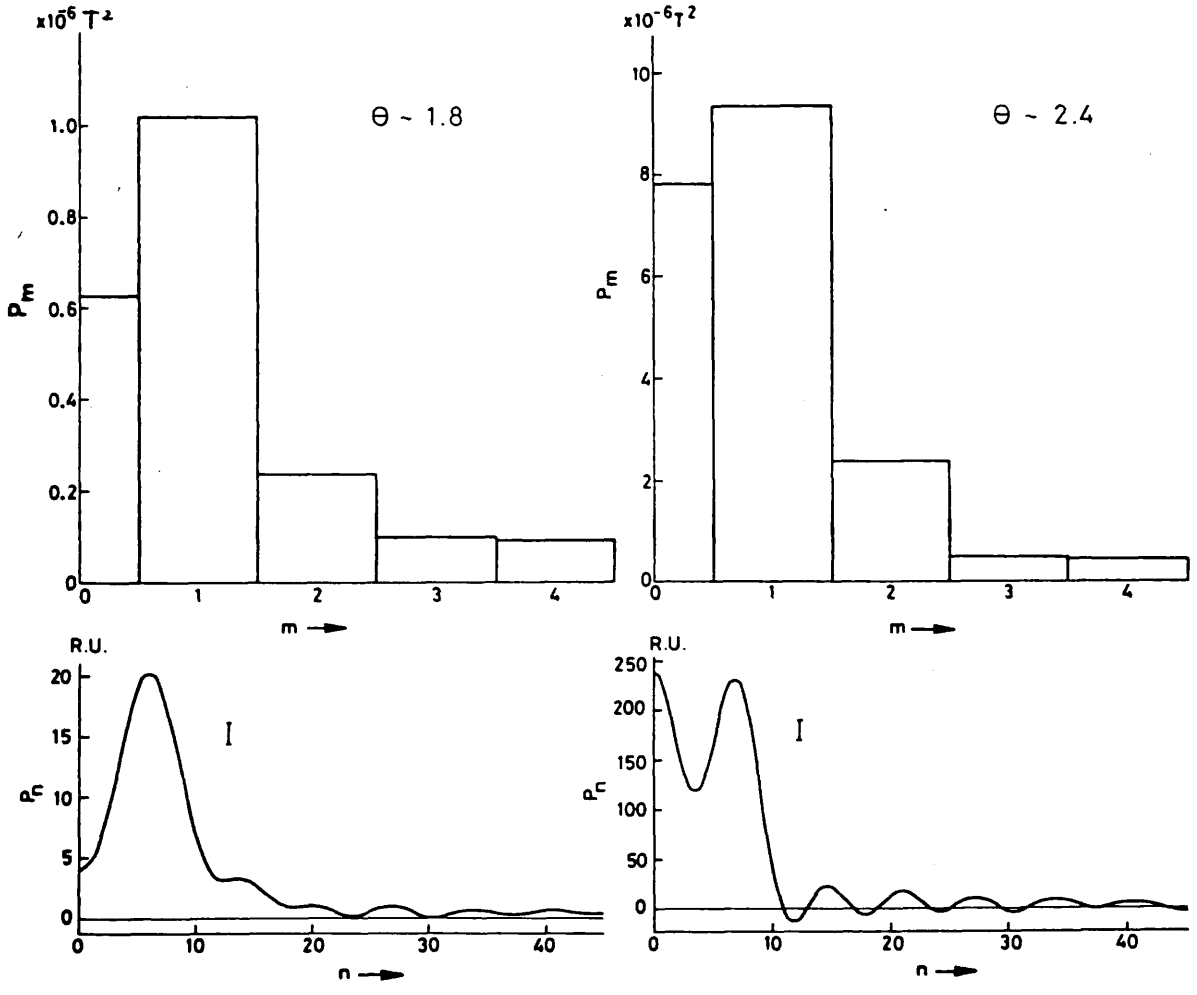

Fig.1. m and n spectra for b_θ

STUDIES OF X-RAY AND MAGNETIC FLUCTUATIONS IN HBTXIA RFP

D Brotherton-Ratcliffe* and M Malacarne**
Culham Laboratory, Abingdon, Oxon, OX14 3DB
(Euratom/UKAEA Fusion Association)
*Royal Holloway College, University of London
**University of Oxford and Euratom Research Fellow

ABSTRACT: X-ray detectors, magnetic insertable probes and edge coils have been used to study the global fluctuations in the HBTXIA Reversed Field Pinch. The results are compared and in both cases several independent m=0 and m=1 modes are observed and their toroidal and radial structure is analysed.

1. INTRODUCTION

A Reversed Field Pinch (RFP) discharge[1] is characterised by the presence of random MHD-type fluctuations. Indeed, the generation and sustainment of a reversed toroidal field and the energy transport observed in the RFP are believed to be related to such fluctuations. In this paper we present and compare results from X-ray and magnetic measurements concerning the detailed structure of the dominant global instabilities observed in the HBTXIA RFP[2]. Statistical techniques (spectrum and correlation analysis)[3] have to be applied in order to identify coherent phenomena out of apparently featureless data.

2. RESULTS

By forming weighted sums of signals from arrays of edge coils in the θ and ϕ directions it is possible to evaluate the power distribution in poloidal and toroidal Fourier mode numbers (m and n, respectively). Figure 1 shows these spectra (calculated by maximum entropy techniques) for $\tilde{B}_\theta$ and $\tilde{B}_\phi$ in the current sustainment phase of the discharge (I_p=200kA, p_o=1.5mTorr, Θ=1.8) in the frequency band 5-50kHz. By cross correlating signals from the two arrays we conclude that the dominant modes are m=1 kinks with a broad band of toroidal numbers centered on $|n|$=7 and two independent m=0 modes, one for $\tilde{B}_\theta$(n=0) and one for $\tilde{B}_\phi$

$(n\sim0)^4$. By using the technique of correlation matrix fitting,[5] we are able to interpret data from the insertable probe in terms of the radial magnetic field profile of the dominant global instabilities. We can distinguish two independent modes, shown in Fig 2 and 3 (frequency band 4-20kHz). Results from a linear tearing mode stability analysis[5] show similar field eigenfunctions to the first mode which corresponds to the m=1 kink. The nature of the second mode is more uncertain, although symmetry considerations indicate it to be m=1. The change in sign of $\tilde{B}_r$ suggests an ideal origin; however the characteristic time scales are resistive.

An analysis of data from an array of 24 Surface Barrier Diodes (SBD) viewing a minor cross section of the discharge, using the same technique as above, shows the amplitude of the dominant global fluctuations in X-ray emissivity as a function of radius. This is shown in Fig 4 for the chord integrated profiles (i) and the corresponding Abel inverted profiles (ii). Symmetry indicates that modes a and b are m=0 while c is m=1; data from single detectors displaced toroidally indicate that the two m=0 modes are $n\sim0$ whereas the m=1 mode is $|n|>>0$. It has not been possible so far to measure directly a significant correlation between the m=1 activity from the edge coils and the SBDs. However a good correlation is shown to exist between X-ray fluctuations and fluctuations in plasma current; Figure 5 shows the zero time delay correlation between the time history of the $\tilde{B}_\theta$ m=0 component and the diodes (frequency band 5-50 kHz).

4. DISCUSSION AND CONCLUSIONS

The overall picture deduced from edge magnetic measurements indicates the presence of a broad band of m=1 helical instabilities resonant inside the reversal surface augmented by m=0 activity. Values of $\tilde{B}_r/B$ at the resonant surface of the m=1 modes confirm earlier estimates[4] that magnetic islands should overlap and stochastic transport ensue. A mode with m=1 resonant inside the reversal is also observed with the insertable probe and its measured radial amplitude variation

agrees with linear theory; this favours a quasi-linear description of the mode evolution. The presence of a second mode with some ideal features is not yet fully understood. The X-ray fluctuations indicate modes with the same values of m and n as from the magnetic fluctuations; however, the absence of significant correlation between the m=1 X-ray and magnetic components suggests that independent fluctuations with the same helicity occur simultaneously.

REFERENCES

[1] BODIN H A B, NEWTON A A, Nuclear Fusion 20 (1980) 1255

[2] BODIN H A B et al: Proc.9th Int.Conf. Baltimore 1982, Vol.1,641.

[3] BENDAT J S, PIERSOL A G, "Random Data; Analysis and Measurement Procedures" Wiley-Interscience.

[4] HUTCHINSON I H et al, Nuclear Fusion 24 (1984) 59.

[5] BROTHERTON-RATCLIFFE D, GIMBLETT C G, to be published.

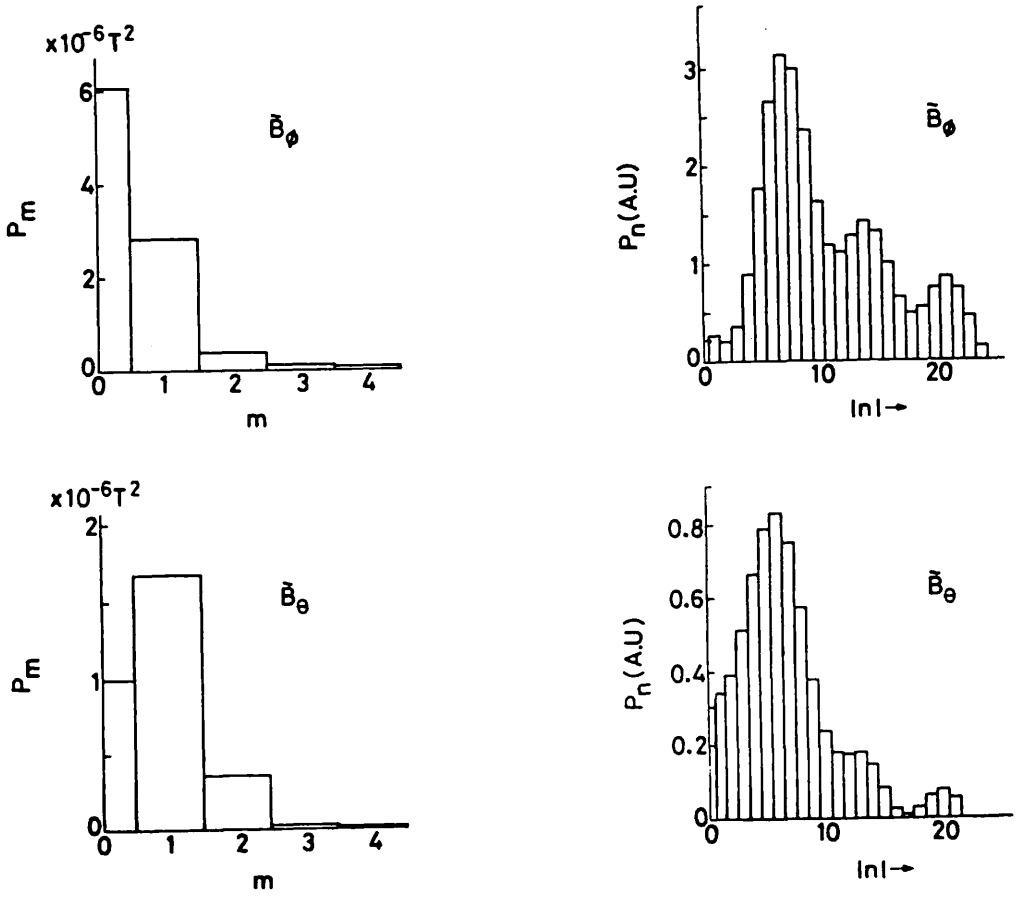

Fig. 1. m and n spectra in sustainment.

R.H.C. LIBRARY

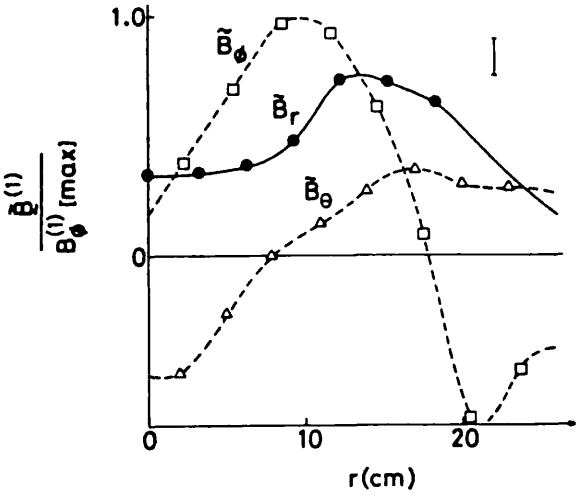

Fig. 2. Field profile of magnetic fluctuations (1st mode)

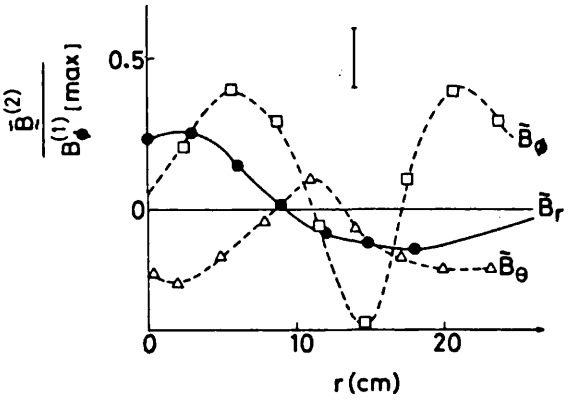

Fig. 3. Field profile of magnetic fluctuations (2nd mode)

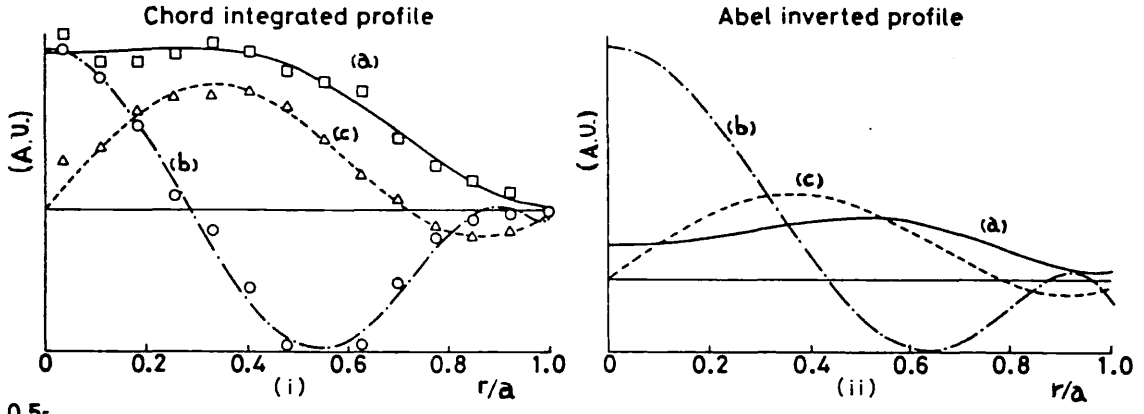

Fig. 4. X-ray fluctuations : 3 independent modes.

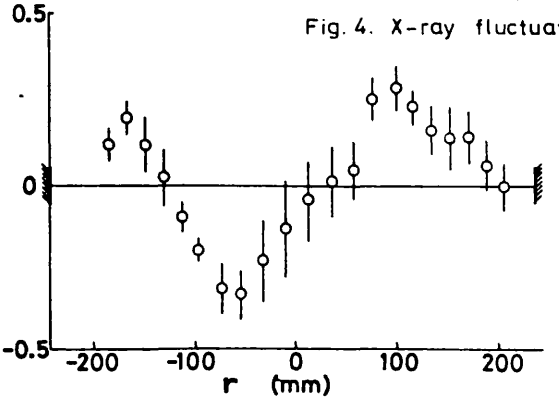

Fig. 5. Correlation between plasma current and X-ray detectors.